UNIVERSITAT ROVIRA I VIRGILI

SYNTHESIS, CHARACTERIZATION AND THEORETICAL CALCULATIONS OF ZNTIO3 FOR THE ADSORPTION AND PHOTOCATALYTIC REMOVAL OF METHYLENE BLUE DYE

Ximena Verónica Jaramillo Fierro

ADVERTIMENT. L'accés als continguts d'aquesta tesi doctoral i la seva utilització ha de respectar els drets de la persona autora. Pot ser utilitzada per a consulta o estudi personal, així com en activitats o materials d'investigació i docència en els termes establerts a l'art. 32 del Text Refós de la Llei de Propietat Intel·lectual (RDL 1/1996). Per altres utilitzacions es requereix l'autorització prèvia i expressa de la persona autora. En qualsevol cas, en la utilització dels seus continguts caldrà indicar de forma clara el nom i cognoms de la persona autora i el títol de la tesi doctoral. No s'autoritza la seva reproducció o altres formes d'explotació efectuades amb finalitats de lucre ni la seva comunicació pública des d'un lloc aliè al servei TDX. Tampoc s'autoritza la presentació del seu contingut en una finestra o marc aliè a TDX (framing). Aquesta reserva de drets afecta tant als continguts de la tesi com als seus resums i índexs.

ADVERTENCIA. El acceso a los contenidos de esta tesis doctoral y su utilización debe respetar los derechos de la persona autora. Puede ser utilizada para consulta o estudio personal, así como en actividades o materiales de investigación y docencia en los términos establecidos en el art. 32 del Texto Refundido de la Ley de Propiedad Intelectual (RDL 1/1996). Para otros usos se requiere la autorización previa y expresa de la persona autora. En cualquier caso, en la utilización de sus contenidos se deberá indicar de forma clara el nombre y apellidos de la persona autora y el título de la tesis doctoral. No se autoriza su reproducción u otras formas de explotación efectuadas con fines lucrativos ni su comunicación pública desde un sitio ajeno al servicio TDR. Tampoco se autoriza la presentación de su contenido en una ventana o marco ajeno a TDR (framing). Esta reserva de derechos afecta tanto al contenido de la tesis como a sus resúmenes e índices.

WARNING. Access to the contents of this doctoral thesis and its use must respect the rights of the author. It can be used for reference or private study, as well as research and learning activities or materials in the terms established by the 32nd article of the Spanish Consolidated Copyright Act (RDL 1/1996). Express and previous authorization of the author is required for any other uses. In any case, when using its content, full name of the author and title of the thesis must be clearly indicated. Reproduction or other forms of for profit use or public communication from outside TDX service is not allowed. Presentation of its content in a window or frame external to TDX (framing) is not authorized either. These rights affect both the content of the thesis and its abstracts and indexes.

UNIVERSITAT
ROVIRA i VIRGILI

Synthesis, characterization and theoretical calculations of $ZnTiO_3$ for the adsorption and photocatalytic removal of Methylene Blue dye

---

XIMENA VERÓNICA JARAMILLO FIERRO

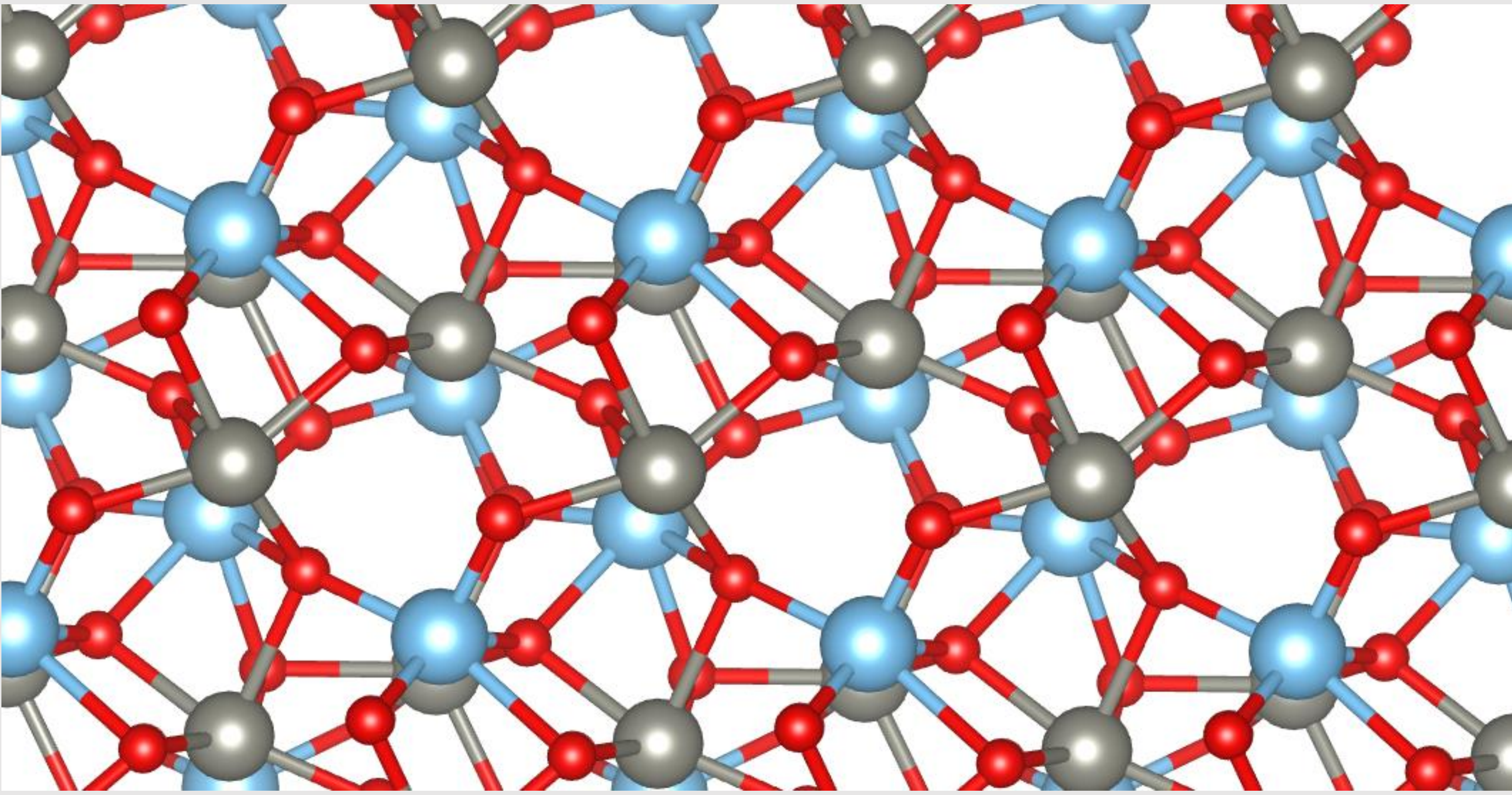

DOCTORAL THESIS

2022

Ximena Verónica Jaramillo Fierro

Synthesis, characterization and theoretical calculations of $ZnTiO_3$ for the adsorption and photocatalytic removal of Methylene Blue dye

Doctoral Thesis

Supervised by:

Dr. Francesc Medina

Departament d'Enginyeria Química, Universitat Rovira i Virgili (Spain)

Dra. Silvia González

Departamento de Química, Universidad Técnica Particular de Loja (Ecuador)

UNIVERSITAT ROVIRA i VIRGILI

Tarragona (Spain)

2022

UNIVERSITAT
ROVIRA i VIRGILI

DEPARTMENT OF CHEMICAL ENGINEERING
ESCOLA TÈCNICA SUPERIOR D'ENGINYERIA QUÍMICA
Av. Països Catalans, 26, 43007, Tarragona (Spain)
Tel. +34 977 55 96 03 / 04 Fax +34 977 55 96 21
e-mail: secdeq@etseq.urv.es
http://www.etseq.urv.es/DEQ/

Dr. Francesc Medina Cabello and Dra. Silvia González Pérez

CERTIFY:

That the present study, entitled "Synthesis, characterization and theoretical calculations of $ZnTiO_3$ for the adsorption and photocatalytic removal of Methylene Blue dye", presented by Ximena Verónica Jaramillo Fierro for the award of the degree of Doctor, has been carried out under our supervision at the Departament d'Enginyeria Química, Universitat Rovira i Virgili (Spain) and Departamento de Química, Universidad Técnica Particular de Loja (Ecuador).

Tarragona, 10th of January 2022

Doctoral Thesis Supervisors

Francisco
Medina Cabello
- DNI
24152174N
(AUT)

Firmado digitalmente por Francisco Medina Cabello - DNI 24152174N (AUT)
Nombre de reconocimiento (DN): c=ES, o=Universitat Rovira i Virgili, 2.5.4.97=VATES-Q9350003A, ou=Treballador públic de nivell alt d'autenticació, title=Vicerector/a d'Innovació i Transferència del Coneixement, sn=Medina Cabello - DNI 24152174N, givenName=Francisco, serialNumber=IDCES-24152174N, cn=Francisco Medina Cabello - DNI 24152174N (AUT)
Fecha: 2022.01.11 16:28:56 +01'00'

SILVIA
GONZALEZ
PEREZ

Fecha:
2022.01.10
09:44:39 -05'00'

Dr. Francesc Medina Cabello

Dra. Silvia González Pérez

“Nothing in life is to be feared,

it is only to be understood.

Now is the time to understand more,

so that we may fear less.”

Marie Curie

Acknowledgements

I would like to express my sincere gratitude to all those who, with their personal and professional support, made the development and completion of this thesis possible.

First of all, I want to thank my supervisor, Dr. Francisco Medina Cabello, for his trust, his unconditional support, and for allowing me to develop my thesis as part of the CATHETER research group at the Rovira i Virgili University (Spain).

Also, thank Dr. Silvia González from the Universidad Técnica Particular de Loja (Ecuador), for her friendship, patience and for allowing me to be part of the Computational Chemistry group where she opened the doors of knowledge in this area of study.

My special thanks also to Dr. Sandra Contreras for her correct suggestions, to Dr. Mariana Stefanova, and to Dr. Francesc Gispert Guirado for helping me with each of the analyzes that made the development of my research possible.

I also want to thank Susana Domínguez, Núria Juanpere, Margarita Jiménez, and Raiana Tomazini for all their help in administrative, operational, and technical matters, but above all for always being aware of me and offering me their friendship.

In the same way, my sincere thanks to the Universidad Técnica Particular de Loja, for granting me the scholarship to carry out my doctoral studies and providing me with the necessary facilities to continue with my personal and professional training.

Finally, my eternal thanks to all my family, my parents, my husband, and my children for encouraging me at all times, for sharing my dreams, and above all for helping me make them come true. And how could it be otherwise, my deep gratitude to God for giving me the grace to understand that his plans are always perfect.

List of Abbreviations

AOP:	Advanced Oxidation Processes
BET:	Brunauer-Emmet-Teller
CB:	Conduction Band
EDX:	Energy Dispersive X-ray
DFT:	Density Functional Theory
DE:	Diatomaceous Earth
DRS:	Diffuse Reflectance Spectroscopy
FAU:	Faujasite
GGA:	Generalized Gradient Approximation
LTA:	Linde Type A
MB:	Methylene Blue
PBE:	Perdew-Burke-Ernzerhof
VASP:	Vienna Ab initio Simulation Package
VB:	Valencia Band
SEM:	Scanning Electron Microcopy
XRD:	X-ray Diffraction
XRF:	X-ray Fluorescence

Index of Contents

Index of Figures

Index of Tables

SUMMARY

Nanoscience, as well as nanotechnology, have merged as a dynamic research field in recent years [1]. The exponential growth in this interdisciplinary research field is due to the improved characteristics of nanomaterials and their various applications. Currently, nanomaterials have aroused great interest for environmental applications, such as the removal of colorants in wastewater. To this end, various nanomaterial architectures have been designed to allow their practical use in adsorption and photocatalysis processes. Zinc (Zn) and titanium (Ti) oxides are widely used photocatalysts for contaminant removal due to their unique properties. On the other hand, clay materials have proven to be excellent sources of raw material for the synthesis of zeolites, as well as effective supports for photocatalysts. Both clays and zeolites have important adsorbent properties and, together with photocatalytic materials, allow the preparation of materials with improved properties for the practical and effective treatment of wastewater.

The purpose of this thesis was the preparation of structured materials with adsorbent and photocatalytic properties for the removal of the cationic methylene blue (MB) dye in aqueous solutions. To do this, initially, 12 Ecuadorian clays were collected and characterized, which were used as supports for photocatalysts prepared based on zinc and titanium. The photocatalysts $ZnTiO_3/TiO_2$, $ZnTiO_3/TiO_2/La$ and TiO_2 (anatase phase) were synthesized by the sol-gel method setting a calcination temperature of 500 °C. $ZnTiO_3/TiO_2$ and $ZnTiO_3/TiO_2/La$ were obtained with a particle size less than 100 nm, setting a $ZnO:TiO_2$ molar ratio of 1:3. Photocatalysts were evaluated in methylene blue photocatalytic degradation tests, and as a result, it was obtained that $ZnTiO_3/TiO_2$ and $ZnTiO_3/TiO_2/La$ had a better degradation capacity than TiO_2 (anatase phase).

The photocatalysts were impregnated in the 12 Ecuadorian clays and then structured in the form of pellets of 0.2 cm (diameter) and 1.0 cm (length). The materials thus prepared were again evaluated regarding their photocatalytic activity and their adsorption capacity. The tests were carried out at room temperature, using a Bach-type reactor, both in the presence of solar light and UV light. The removal of methylene blue by adsorption and photocatalysis was verified from the discoloration of the solution and quantified by UV-Vis spectrophotometry at 623 nm. $Clay_{12}$ (or R-Clay, due to its red color) impregnated with TiO_2 showed the best photocatalytic activity. The X-ray Fluorescence (XRF) results showed that this clay had TiO_2 and Fe_2O_3 in its composition, which could improve its photocatalytic activity. $Clay_6$ (or G-Clay, due to its gray color) had the best methylene blue adsorption capacity. The results of the X-ray Diffraction (XRD) allowed concluding that the presence of the metahalloysite phase improved the adsorption capacity of the clay. In addition, this clay contained several oxides with exchange cations that could also contribute to its high adsorption capacity.

Both clays, G-Clay and R-Clay, were used as raw material sources to synthesize FAU and LTA zeolites, respectively. The zeolites were synthesized by alkaline fusion and hydrothermal method, presenting good textural and morphological characteristics, suitable for adsorption processes. The zeolites were combined with their precursor clays and with $ZnTiO_3/TiO_2$ to prepare pellets that were successfully used as adsorbents in MB removal tests in aqueous solutions. The experimental isotherms were adjusted to the Langmuir model and the experimental kinetics to the pseudo-second-order model, which showed monolayer adsorption on a surface that contained an infinite number of identical sites, maintaining a constant adsorption rate during the process.

Finally, a comparative study was carried out using computational simulation to determine the MB adsorption mechanism on the surfaces (101) of $ZnTiO_3$ and TiO_2 (anatase phase). The DFT (Density Functional Theory) calculations were developed using the VASP code (Vienna Ab initio Simulation Package) with the Perdew-Burke-Ernzerhof (PBE) functional in the generalized gradient approximation (GGA). The results showed that the adsorption of MB on the surface (101) of $ZnTiO_3$ is stronger than on the surface (101) of TiO_2. Furthermore, the semi-perpendicular orientation was the most likely molecular approach for the surfaces of both oxides. Our theoretical study verified that $ZnTiO_3$ has better MB adsorption energy than TiO_2 in the anatase phase, which is important to enhance a subsequent degradation process. The large bandgap obtained by DFT calculations also showed that $ZnTiO_3$ can potentially be used as a photocatalyst, which would allow complete degradation of MB after being adsorbed. Therefore, considering only the structure of the band, $ZnTiO_3$ fully meets the necessary requirements to be a photocatalyst. But, as already mentioned, in addition to the band structure, the adsorption capacity is also very important for photocatalytic materials. In this way, the feasibility of using $ZnTiO_3$ as an adsorbent and photocatalytic material for the removal of methylene blue in aqueous systems was experimentally and computationally corroborated. Therefore, $ZnTiO_3$ constitutes an efficient alternative material for various technological and environmental applications.

RESUMEN

La nanociencia, así como la nanotecnología, se han fusionado como un campo de investigación dinámico durante los últimos años [1]. El crecimiento exponencial en este campo de investigación interdisciplinario se debe a las características mejoradas de los nanomateriales y sus diversas aplicaciones. Actualmente, los nanomateriales han despertado gran interés para aplicaciones ambientales, como la remoción de colorantes en aguas residuales. Con este fin, varias arquitecturas de nanomateriales han sido diseñadas para permitir su uso práctico en procesos de adsorción y fotocatálisis. Los óxidos de zinc (Zn) y de titanio (Ti) son fotocatalizadores ampliamente utilizados para la remoción de contaminantes debido a sus propiedades únicas. Por otra parte, los materiales arcillosos han demostrado ser excelentes fuentes de materia prima para la síntesis de zeolitas, así como soportes efectivos de fotocatalizadores. Tanto las arcillas como las zeolitas presentan importantes propiedades adsorbentes y, junto con los materiales fotocatalíticos, permiten la preparación de materiales con propiedades mejoradas para el tratamiento práctico y efectivo de aguas residuales.

La presente tesis tuvo por finalidad, la preparación de materiales estructurados con propiedades adsorbentes y fotocatalíticas para la remoción del colorante catiónico azul de metileno (MB) en soluciones acuosos. Para ello, inicialmente se recolectaron y caracterizaron 12 arcillas ecuatorianas que fueron utilizadas como soportes de fotocatalizadores preparados a base de zinc y titanio. Los fotocatalizadores $ZnTiO_3/TiO_2$, $ZnTiO_3/TiO_2/La$ y TiO_2 (fase anatasa) fueron sintetizado mediante el método sol-gel fijando una temperatura de calcinación de 500 °C. $ZnTiO_3/TiO_2$ y $ZnTiO_3/TiO_2/La$ fueron obtenidos con un tamaño de partícula menor a 100 nm fijando una relación molar $ZnO:TiO_2$ de 1:3. Los fotocatalizadores fueron evaluados en pruebas de degradación fotocatalítica de azul de metileno, y como resultado, se obtuvo que $ZnTiO_3/TiO_2$ y $ZnTiO_3/TiO_2/La$ tenían una mejor capacidad de degradación que TiO_2 (fase anatasa).

Los fotocatalizadores fueron impregnados en las 12 arcillas ecuatorianas y luego estructurados en forma de pellets de 0.2 cm (diámetro) y 1.0 cm (largo). Los materiales así preparados fueron nuevamente evaluados respecto a su actividad fotocatalítica y su capacidad de adsorción. Los ensayos se realizaron a temperatura ambiente, utilizando un reactor de tipo Bach, tanto en presencia de luz solar como de luz UV. La remoción de azul de metileno por adsorción y fotocatálisis fue verificada a partir de la decoloración de la solución, y cuantificada mediante espectrofotometría UV-Vis a 623 nm. La arcilla $Clay_{12}$ (o R-Clay, debido a su color rojo) impregnada con TiO_2 mostró la mejor actividad fotocatalítica. Los resultados de Fluorescencia de Rayos X (XRF) mostraron que esta arcilla presentaba TiO_2 y Fe_2O_3 en su composición, lo que podría mejorar su actividad fotocatalítica. La arcilla $Clay_6$ (o G-Clay, debido a su color gris) tuvo la mejor capacidad de adsorción de azul de metileno. Los resultados de la Difracción de Rayos X (DRX) permitieron concluir que la presencia de la fase metahalloysita mejoraba la capacidad de adsorción de la arcilla. Además, esta arcilla contenía varios óxidos con cationes de intercambio que también podrían contribuir a su elevada capacidad de adsorción.

Ambas arcillas, G-Clay y R-Clay fueron utilizadas como fuentes de materia prima para sintetizar zeolitas FAU y LTA, respectivamente. Las zeolitas fueron sintetizadas mediante fusión alcalina y método hidrotermal, presentando buenas características texturales y morfológicas, aptas para procesos de adsorción. Las zeolitas se combinaron con sus arcillas precursoras y con $ZnTiO_3/TiO_2$ para preparar pellets que fueron utilizados exitosamente como adsorbentes en pruebas de remoción de MB en soluciones acuosas. Las isotermas experimentales se ajustaron al modelo de Langmuir y las cinéticas experimentales al modelo de pseudo-segundo orden, lo cual evidenció una adsorción de monocapa en una superficie que contenía un número infinito de sitios idénticos, manteniendo una tasa de adsorción constante durante el proceso.

Finalmente, se realizó un estudio comparativo utilizando simulación computacional para determinar el mecanismo de adsorción del MB en las superficies (101) de $ZnTiO_3$ y TiO_2 (fase anatasa). Los cálculos DFT (Density Functional Theory) fueron desarrollados usando el código VASP (Viena Ab initio Simulation Package) con el funcional Perdew-Burke-Ernzerhof (PBE) en la aproximación de gradiente generalizado (GGA). Los resultados mostraron que la adsorción de MB en la superficie (101) de $ZnTiO_3$ es más fuerte que en la superficie (101) de TiO_2. Además, la orientación semiperpendicular fue el enfoque molecular más probable para las superficies de ambos óxidos. Nuestro estudio teórico verificó que el $ZnTiO_3$ tiene mayor energía de adsorción de MB que el TiO_2 en la fase anatasa, lo cual es importante para potenciar un proceso de degradación posterior. La gran banda prohibida obtenida por los cálculos de DFT también demostró que el $ZnTiO_3$ se puede usar potencialmente como fotocatalizador, lo que permitiría la degradación completa del MB después de ser adsorbido. Por lo tanto, considerando solo la estructura de la banda, $ZnTiO_3$ cumple completamente con los requisitos necesarios para ser un fotocatalizador. Pero, como ya se mencionó, además de la estructura de la banda, la capacidad de adsorción también es muy importante para los materiales fotocatalíticos. De esta forma, se corroboró experimental y computacionalmente la viabilidad de usar $ZnTiO_3$ como material adsorbente y fotocatalítico para la remoción de azul de metileno en sistemas acuosos. Así, el $ZnTiO_3$ constituye un material alternativo eficiente para diversas aplicaciones tecnológicas y ambientales.

RESUM

La nanociència, així com la nanotecnologia, s'han fusionat com un camp de recerca dinàmic durant els últims anys [1]. El creixement exponencial en aquest camp de recerca interdisciplinari es deu a les característiques millorades dels nanomaterials i les seves diverses aplicacions. Actualment, els nanomaterials han despertat gran interès per a aplicacions ambientals, com la remoció de colorants en aigües residuals. Amb aquesta finalitat, diverses arquitectures de nanomaterials han estat dissenyades per permetre el seu ús pràctic en processos d'adsorció i fotocatàlisi. Els òxids de zinc (Zn) i de titani (Ti) són fotocatalitzadors àmpliament utilitzats per a la remoció de contaminants per les seves propietats úniques. D'altra banda, els materials argilosos han demostrat ser excel·lents fonts de matèria primera per a la síntesi de zeolites, així com suports efectius de fotocatalitzadors. Tant les argiles com les zeolites presenten importants propietats adsorbents i, juntament amb els materials fotocatalítics, permeten la preparació de materials amb propietats millorades per al tractament pràctic i efectiu d'aigües residuals.

La present tesi va tenir per finalitat, la preparació de materials estructurats amb propietats adsorbents i fotocatalítiques per a la remoció del colorant catiònic blau de metilè (MB) en solucions aquoses. Per a això, inicialment es van recol·lectar i van caracteritzar 12 argiles equatorianes que van ser utilitzades com a suports de fotocatalitzadors preparats a base de zinc i titani. Els fotocatalitzadors $ZnTiO_3/TiO_2$, $ZnTiO_3/TiO_2/La$ i TiO_2 (fase anatasa) van ser sintetitzat mitjançant el mètode sol-gel fixant una temperatura de calcinació de 500 °C. $ZnTiO_3/TiO_2$ i $ZnTiO_3/TiO_2/La$ van ser obtinguts amb una mida de partícula menor a 100 nm fixant una relació molar $ZnO:TiO_2$ 1:3. Els fotocatalitzadors van ser avaluats en proves de degradació fotocatalítica de blau de metilè, i com a resultat, es va obtenir que $ZnTiO_3/TiO_2$ i $ZnTiO_3/TiO_2/La$ tenien una millor capacitat de degradació que el TiO_2 (fase anatasa).

Els fotocatalitzadors van ser impregnats en les 12 argiles equatorianes i després estructurats en forma de pellets de 0.2 cm (diàmetre) i 1.0 cm (longitud). Els materials així preparats van ser novament avaluats respecte a la seva activitat fotocatalítica i la seva capacitat d'adsorció. Els assajos es van realitzar a temperatura ambient, utilitzant un reactor de tipus Batch, tant en presència de llum solar com de llum UV. La remoció de blau de metilè per adsorció i fotocatàlisi va ser verificada a partir de la decoloració de la solució, i quantificada mitjançant espectrofotometria UV-Vis a 623 nm. L'argila $Clay_{12}$ (o R-Clay, degut al seu color vermell) impregnada amb TiO_2 va mostrar la millor activitat fotocatalítica. Els resultats de Fluorescència de Raigs X (XRF) van mostrar que aquesta argila presentava TiO_2 i Fe_2O_3 en la seva composició, el que podria millorar la seva activitat fotocatalítica. L'argila $Clay_6$ (o G-Clay, degut al seu color gris) va tenir la millor capacitat d'adsorció de blau de metilè. Els resultats de la Difracció de Raigs X (XRD) van permetre concloure que la presència de la fase metahalloysita millorava la capacitat d'adsorció de l'argila. A més, aquesta argila contenia diversos òxids amb cations d'intercanvi que també podrien contribuir a la seva elevada capacitat d'adsorció.

Les dues argiles, G-Clay i R-Clay van ser utilitzades com a fonts de matèria primera per a sintetitzar zeolites FAU i LTA, respectivament. Les zeolites van ser sintetitzades mitjançant fusió alcalina i mètode hidrotermal, presentant bones característiques texturals i morfològiques, aptes per a processos d'adsorció. Les zeolites es van combinar amb les seves argiles precursores i amb $ZnTiO_3/TiO_2$ per preparar pèl·lets que van ser utilitzats amb èxit com adsorbents en proves de remoció de MB en solucions aquoses. Les isotermes experimentals es van ajustar al model de Langmuir i les cinètiques experimentals al model de pseudo-segon ordre, la qual cosa va evidenciar una adsorció de monocapa en una superfície que contenia un nombre infinit de llocs idèntics, mantenint una taxa d'adsorció constant durant el procés.

Finalment, es va realitzar un estudi comparatiu utilitzant simulació computacional per determinar el mecanisme d'adsorció de l'MB en les superfícies (101) de $ZnTiO_3$ i TiO_2 (fase anatasa). Els càlculs DFT (Density Functional Theory) van ser desenvolupats usant el codi VASP (Viena Ab ini-tio Simulation Package) amb el funcional Perdew-Burke-Ernzerhof (PBE) en l'aproximació de gradient generalitzat (GGA). Els resultats van mostrar que l'adsorció de MB a la superfície (101) de $ZnTiO_3$ és més forta que en la superfície (101) de TiO_2. A més, l'orientació semiperpendicular va ser l'enfocament molecular més probable per a les superfícies de tots dos òxids. El nostre estudi teòric va verificar que el $ZnTiO_3$ té una major energia d'adsorció de MB que en el TiO_2 en fase anatasa, la qual cosa és important per potenciar un procés de degradació posterior. La gran banda prohibida obtinguda pels càlculs de DFT també va mostrar que el $ZnTiO_3$ es pot fer servir potencialment com fotocatalitzador, el que permetria la degradació completa de l'MB després de ser adsorbit. Per tant, considerant només l'estructura de la banda, $ZnTiO_3$ compleix completament amb els requisits necessaris per ser un fotocatalitzador. Però, com ja es va esmentar, a més de l'estructura de la banda, la capacitat d'adsorció també és molt important per als materials fotocatalítics. D'aquesta manera, es va corroborar experimental i computacionalment la viabilitat d'usar $ZnTiO_3$ com a material adsorbent i fotocatalític per a la remoció de blau de metilè en sistemes aquosos. Per tant, el sistema $ZnTiO_3$ constitueix un material alternatiu eficient per a diverses aplicacions tecnològiques i ambientals.

CHAPTER 1

OBJECTIVES & STRUCTURE OF THE THESIS

1.1. Objectives of the thesis

The main objective of this thesis was to develop materials with absorbent and photocatalytic properties for the removal of dyes in aqueous systems. In this way, the following specific objectives were established:

- Establish the best synthesis conditions to obtain different Zn and Ti oxides using the sol-gel method.
- Synthesize the nanocomposites $ZnTiO_3/TiO_2$, $ZnTiO_3/TiO_2/La$ and TiO_2 (anatase phase) and characterize them using X-Ray Diffraction (XRD), Scanning Electron Microscopy (SEM), Diffuse Reflectance Spectrum (DRS).
- Determine the photocatalytic activity of $ZnTiO_3/TiO_2$, $ZnTiO_3/TiO_2/La$ and TiO_2 by means of methylene blue removal tests in aqueous solutions, under sunlight and UV-C light.
- Collect twelve clays in different locations in southern Ecuador, purify, and characterize them using XRD and XRF.
- Prepare photocatalyst-clay composites and adapt them to the shape of cylinders 0.2 cm in diameter and 1.0 cm long.
- Evaluate the adsorption capacity and photocatalytic activity of the composites prepared by means of methylene blue removal tests in aqueous solutions, under solar light and UV-C light.
- Test the feasibility of using at least one of the Ecuadorian clays as raw material for the synthesis of FAU and/or LTA zeolites, using the hydrothermal method.
- Characterize the synthesized zeolites using X-Ray Fluorescence (XRF), X-Ray Diffraction (XRD), Scanning Electron Microscopy (SEM), and determination of the specific surface area using the BET equation.
- Prepare photocatalyst-clay-zeolite composites and adapt them to the shape of cylinders 0.2 cm in diameter and 1.0 cm long.

- Evaluate the adsorption capacity of the composites prepared by means of methylene blue removal tests in aqueous solutions, establishing the kinetic and isotherm models that best explain the behavior of the composites.
- Evaluate the reuse capacity of all the composites prepared using a minimum of three treatment cycles.
- Apply quantum mechanical studies (DFT) using the VASP code to determine the electronic properties of $ZnTiO_3$ and TiO_2 (anatase phase), as well as the MB adsorption mechanism on the surface (101) of both oxides.

In this way, this thesis aims to contribute to the development of alternative materials for technological and environmental applications.

1.2. Structure of the thesis

This thesis has been structured in seven chapters. The main and specific objectives are given in **Chapter 1**. **Chapter 2** presents an introduction on water pollution and the technologies for its treatment. It also includes a brief description of the methods and materials that are currently used to eliminate pollutants from aqueous systems, the advantages of using adsorption and photocatalysis have been shown. Furthermore, as technological processes for the economic and efficient treatment of wastewater have been demonstrated. This chapter also describes the properties of adsorbent materials, such as clays and zeolites, and Zn and Ti photocatalysts. As well as, the importance of the design of structured materials for practical applications. Finally, a brief introduction to computational chemistry is presented, as a tool to study and solve chemical problems through computational simulation.

Chapter 3 details the results of the synthesis of the $ZnTiO_3/TiO_2$ nanocomposite supported in Ecuadorian clays for the adsorption and photocatalytic removal of methylene blue dye. This chapter includes the optimal parameters for the synthesis of $ZnTiO_3/TiO_2$ and TiO_2 (anatase phase), the clays with the best MB removal capacity are also determined; and the characterization of all the compounds is included, by means of different techniques.

Chapter 4 describes the structuring of $ZnTiO_3/TiO_2$ adsorbents for the removal of methylene blue, using zeolite precursor clays as natural additives. The clays used in this study were chosen from the twelve clays analyzed in Chapter 3. The results of the zeolitization and the respective characterization of the zeolites are included in this chapter, as well as the adsorption and kinetic models that best describe the extruded materials studied.

Chapter 5 displays the preparation of the La-doped $ZnTiO_3/TiO_2$ nanocomposite supported in ecuadorian diatomaceous earth as a highly efficient photocatalyst driven by solar light. In this chapter, the adsorption capacity and photocatalytic activity of the synthesized composites are demonstrated using methylene blue dye removal as a reaction model.

Chapter 6 focuses on the DFT study of the adsorption of methylene blue on surfaces of $ZnTiO_3$ and TiO_2 (101), to determine the adsorption mechanism of the dye and clarify the experimental results obtained in the two previous chapters. In this comparative study, the electronic properties of $ZnTiO_3$ and TiO_2 were first calculated, and later the adsorption mode and the best orientation of the MB molecule on both surfaces were determined.

Chapter 7 presents the main conclusions obtained through the studies carried out in the previous chapters; and, finally, the publications and communications derived from these studies are presented in **Chapter 8**.

CHAPTER 2

INTRODUCTION

2.1. Contamination of water

In recent years, environmental pollution has become one of the most important global concerns [2]. In fact, there are often a wide variety of compounds in water and wastewater today. These compounds are called emerging pollutants and have attracted a lot of attention due to their potential environmental and health impacts. Most of these pollutants are quite resistant to chemical oxidation treatments and their toxicity makes biological degradation difficult, so discharge to the environment represents a very worrying problem [3].

Currently, one of the attractive solutions in response to water scarcity problems is the implementation of wastewater recovery and reuse projects to ensure sustainable water development and management. However, there is concern that emerging pollutants could still be present in the treated water [4]. Therefore, the removal of emerging pollutants from water systems is an urgent problem that must be solved [5].

2.2. Contamination by dyes

With the growing revolution in science and technology, the demand for novel chemicals that could be used in various industrial processes has increased enormously [6]. Among several new chemicals, dyes are the most widely used in many industrial activities. Therefore, these products have become an integral part of all industrial effluents.

At present, there are more than 1000 types of commercial dyes available and more than $7x10^5$ tons of dyes are produced annually with a considerable fraction discharged from the textile, leather, paper, rubber, plastics, and other industries such as cosmetics, pharmaceuticals and food [7–9]. During production, up to 2% of the dyes are discharged directly as affluent and approximately 10% are lost in the coloring process [10]. Effluents from these industries are considered the most polluting among all other industrial effluents due to their complex composition [11].

The dyes have an important molecular weight and complex structure, so they resist biodegradation and accumulate in water currents [8,10,12]. These waters are characterized by a high biochemical oxygen demand and a high chemical oxygen demand [13], in addition, they present a potential risk for aquatic organisms since they cause eutrophication [14] and make it difficult for light to pass by, inhibiting photosynthesis [15,16]. Most of the dyes are toxic, they can cause allergies and irritation of the skin and intestinal walls, they are also mutagenic and carcinogenic [13,17,18].

Dyes can be classified into three types based on their core structures: anionic dyes (acidic and reactive), nonionic dyes (disperse), and cationic dyes (basic). The toxicity of dyes depends on their chemical form [10]. The cationic organic dyes are considered more toxic than the anionic ones [7]. Coloring pigments such as anthraquinone or the azo groups present in anionic, cationic, or non-ionic dyes, which have a complex chemical structure, are very difficult to degrade under environmental conditions [19].

In order to protect humans and recover the ecosystem from contamination, the dyes must be removed from the wastewater containing the dyes before being released into the environment. This is why dye removal has become an important and challenging area of research on wastewater treatment and other environmental issues [20].

2.3. Methylene blue dye

Methylene blue (MB) is one of the best known basic/cationic dyes and has been widely used in the wool, silk, cotton and pharmaceutical industries [21]. This dye, also known as methylthioninium chloride, is a basic cationic dye with the molecular formula $C_{16}H_{18}N_3SCl$.

At room temperature, MB is a dark green powder that gives a blue solution when dissolved in water [22]. Figure 2.1 shows the chemical structure of Methylene blue (MB).

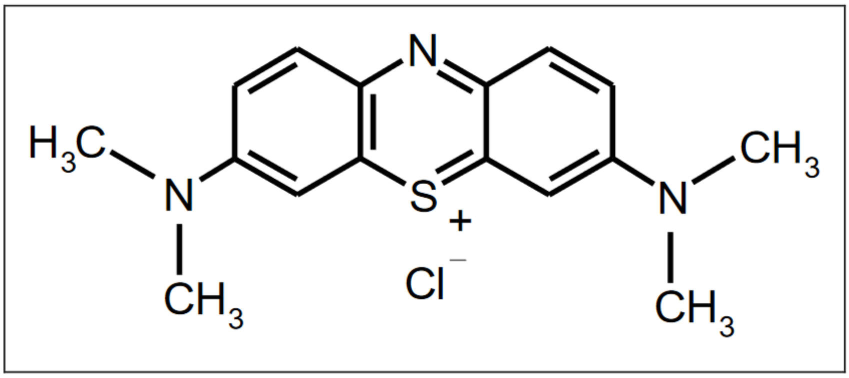

Figure 2. 1. Chemical structure of Methylene blue [23]

Due to the existence of multiple aromatic rings in its molecular structure, this dye is very stable and its biodegradation is very difficult. Therefore, its release into the environment can cause substantial contamination and pose a serious risk to living organisms [24]. In fact, MB can cause some health problems, such as eye burns, which can be responsible for permanent injury to the eyes of humans and animals. On inhalation, it can produce short periods of rapid or difficult breathing, while ingestion by mouth produces a burning sensation and can cause nausea, vomiting, profuse sweating, mental confusion, and methemoglobinemia [25,26].

2.4. Treatment of wastewater

Many dyes and other organic pollutants are difficult to break down in nature and require more advanced techniques for their removal. The bleaching of dyes in effluents has received much attention, therefore, various chemical, physical and biological treatment methods have been developed for the removal of dyes from aqueous solutions. These treatments include adsorption, precipitation, coagulation-flocculation, reverse osmosis, catalytic chemical degradation, oxidation with ozone, chlorine or hydrogen peroxide, electrolysis, use of anion exchange membranes, biological treatment, and other processes [16], [22], [27]. Figure 2.2 shows some processes for wastewater treatment.

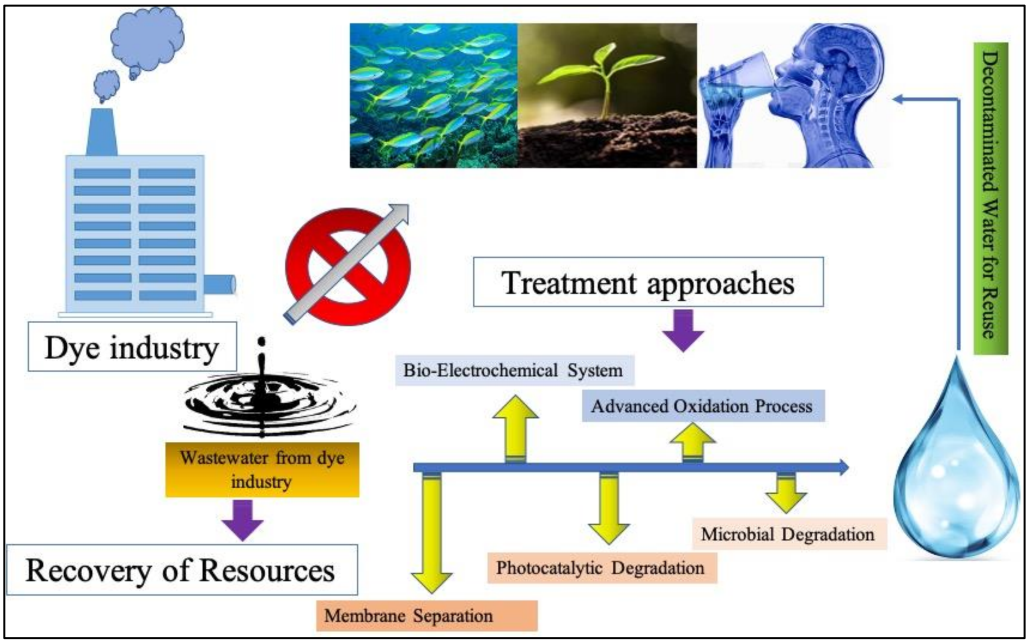

Figure 2. 2. Approaches to wastewater treatment [28]

Biological treatment is currently considered one of the best available technologies for wastewater treatment, but there are many pollutants that are toxic, chemically stable, or resistant to biodegradation [3]. For this reason, greater attention has been paid to the study of the removal of dyes and pigments from industrial effluents and wastewater through adsorption processes using nanostructured materials [5,19]. However, this method only transfers the polluting phase to another phase instead of eliminating it [29], being necessary to incorporate secondary remediation steps [30] to achieve the complete elimination of dyes from industrial wastewater [12].

For this reason, other methods have been proposed, such as advanced oxidation processes (AOPs) for the removal of recalcitrant organic pollutants, especially for those with low biodegradability [4]. Photodegradation is an important process in which toxic materials can degrade in the presence of sunlight to benefit human health and the environment [31]. In fact, the photocatalytic degradation of natural pollutants in air and water through the use of semiconductors has attracted extraordinary attention in the last two decades [32].

It is important to mention that the efficiency of photocatalytic degradation can be improved by anchoring the photoactive catalysts on a suitable support, particularly that of a large surface area. The adsorption of pollutants on large surface supports increases their concentration around supported photocatalysts; its diffusion to photocatalysts and, therefore, promotes the photocatalytic process [33]. In this way, adsorption in combination with photocatalysis represents an efficient alternative for wastewater treatment. Figure 2.3 shows the classification of wastewater treatments. Here it can be seen that adsorption and photocatalysis belong to the group of tertiary treatments.

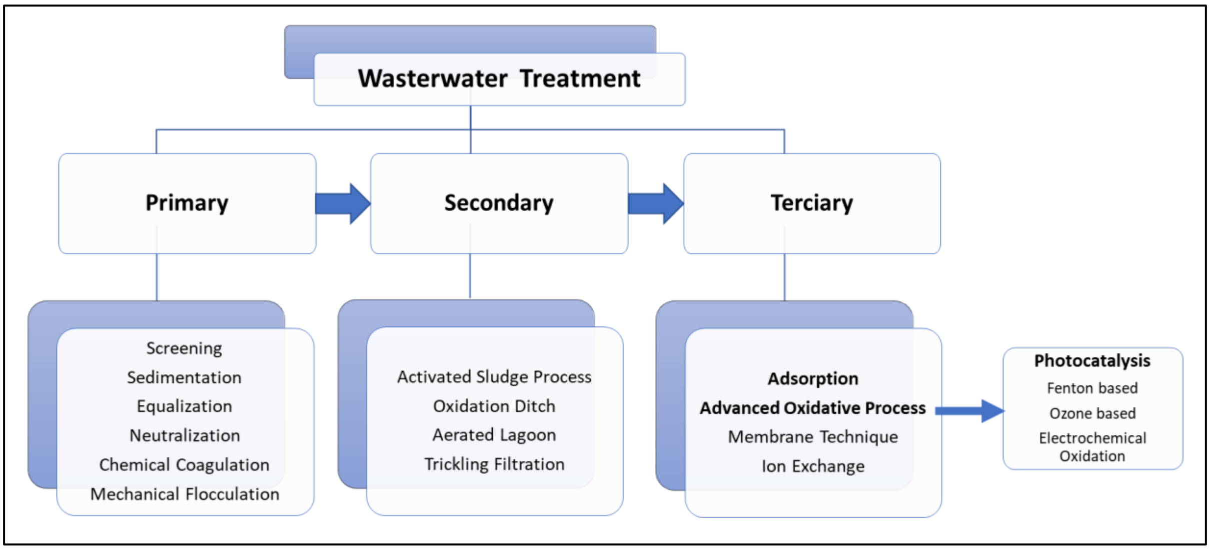

Figure 2. 3. Classification of wastewater treatments [28]

2.5. Adsorption

Adsorption is an attractive method of removing pollutants from effluents, because if the adsorption system is designed correctly, then the treated effluent will reach a high-quality [34]. Adsorption allows more flexibility than other processes in terms of simplicity of design, ease of operation, and produces contaminant-free effluents that are suitable for reuse. Also, since adsorption is usually reversible, the adsorbent can be regenerated, resulting in significant cost savings [35].

Adsorption can occur by different mechanisms, including electrostatic interaction, a chemical reaction such as complexation, or an ion exchange between the adsorbate and the adsorbent [10]; however, pore structure and adsorbent surface chemistry have the greatest influence on the adsorption process, while pore size distribution affects adsorption efficiency and selectivity. Several studies have shown that although adsorption occurs mainly in the micropores of the adsorbent, the mesopores facilitate the adsorption of adsorbates in internal and narrow micropores, since the adsorption capacity increases with the volume of the mesopore for surface areas and volumes of similar micropores. Furthermore, the influence of mesopore volume on adsorption capacity has been shown to be more pronounced for larger than smaller adsorbates [34].

Adsorption is an excellent way to remove dye particles from effluents and different adsorbents have been used for this purpose, such as clays, zeolites, polymeric membranes, xerogels, titanium oxide nanotubes, carbon nanotubes, graphene, chitosan nanoparticle, carbon. activated, ash, chitin, and others [18,36]. Adsorbents must have a high specific surface area, sorption capacity, and active sites on their surfaces [10]. Furthermore, adsorbents must meet the requirements and standards of the water treatment industry and also be environmentally friendly, highly efficient, inexpensive, and available in large quantities [8]. Consequently, the most promising materials and candidates for alternative adsorbents are clay minerals [22].

2.6. Clays

Clays are minerals that are widely distributed in nature, being produced by the erosion of rocks. Chemically they are hydrated alumina silicates, whose formula is:

$$Al_2O_3 \bullet 2SiO_2 \bullet 2H_2O$$

The color, texture, and chemical composition of clays are very varied, depending on the presence of organic and inorganic impurities, as well as the geological origin of the clays. Although particle size is a key parameter in all definitions of clay, there is no generally accepted upper limit, however various authors have suggested that the term "clay" should only be used in the textural sense to indicate material that is finer than 4 µm. These minerals are made up of sheets of tetrahedra with a general chemical composition of Si_2O_5, where each tetrahedron (SiO_4) is joined by its corners to three others forming a hexagonal network, as shown in Figure 2.4. Aluminum and iron atoms can partially replace silicon in the structure. The oxygen atoms located at the apexes of the tetrahedra of these sheets can, at the same time, form part of another parallel sheet composed of octahedra. These octahedra are usually coordinated by cations of Al, Mg, Fe^{3+}, and Fe^{2+}, and less frequently, by atoms of Li, V, Cr, Mn, Ni, Cu, or Zn [11].

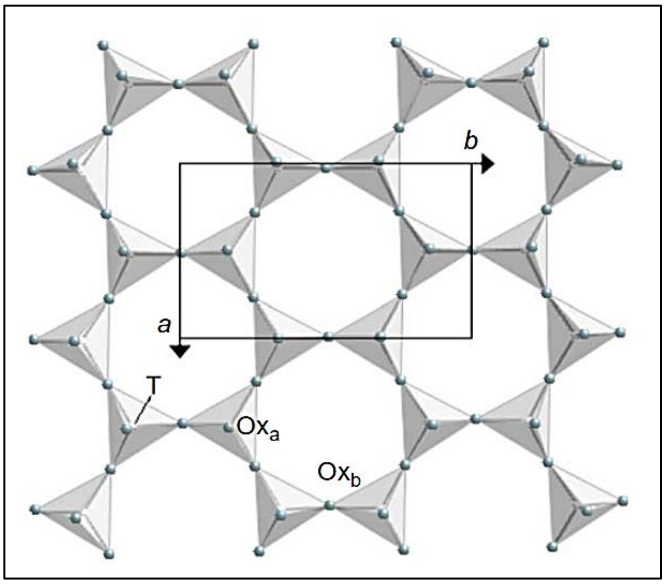

Figure 2. 4. Hexagonal network formed by sheets of tetrahedra in clays [37]

In industrial applications of clays, one distinguishes four types of clays: (i) bentonites with montmorillonite as the principal clay mineral constituent, (ii) kaolins containing kaolinite, (iii) palygorskite and sepiolite, and (iv) "common clays" which often contain illite/smectite mixed-layer minerals, and are largely used for ceramics.

Clays have interesting physicochemical properties such as a large specific surface area, high porosity, low permeability, and high cation exchange capacity, which allows efficient molecular adsorption on their surface. The permanent negative charge related to the isomorphic substitution in the interlaminar space of clays improves the adsorption capacity of cationic elements, such as methylene blue dye. Whatever the type of clay, the electrostatic interaction between the adsorbate and the adsorbent is an important parameter that determines the efficiency of adsorption [10].

Remediation methods based on nanomaterials include the use of clays for the detoxification and transformation of pollutants, therefore, various types of clays have become important targets for applications in environmental industries and bioremediation [38]. The adsorption of dyes on clays is generally attributed to an ion-exchange mechanism and is linked to the specific surface area of the clay [11]. In fact, the adsorption of MB in natural clay is dominated by the cation exchange between this colorant and the cations of the intermediate layer of the clay. For this, methylene blue is ionized in an aqueous medium producing a negatively charged Cl^- ion and a delocalized positively charged aromatic structure that forms aggregates in the intermediate layer of the clay, leading to the adsorption process [10].

2.7. Zeolites

The term "*zeolite*" comes from the Greek *zeo* which means "*to boil*" and *lithos*, which means "*stone*". Crude zeolite forms naturally in the earth's crust under particular hydrothermal and geological conditions, but is rarely pure, as it is contaminated by other minerals, metals, quartz, or other zeolite structures [39].

Zeolites are microporous and microcrystalline inorganic materials capable of complexing or adsorbing small and medium-sized organic molecules. Typical particle sizes are in the range of 0.1 to 10 mm and possess regular periodic structures that can be thought of as a sponge-like material with interconnected channels and cages that periodically and regularly extend throughout its entire structure. Generally, zeolite micropores have diameters of up to 2 nm, and due to their regular size aperture, they allow small molecules to diffuse directly, but trap larger ones, acting as molecular sieves [40]. Normally, zeolites due to their precise pore size and shape, molecular polarity, and chemical composition have developed selective adsorption properties, based on surface molecular-scale phenomena in which the molecules are attracted to the volume Z of the porous solid [40].

The adsorption of organic compounds on zeolites can occur on both external and internal surfaces. Internal complexation or intracrystalline adsorption occurs by host diffusion into channels and cages within the zeolite crystal and is size and shape-selective. Although the inner surface areas far exceed the outer surfaces, intracrystalline adsorption can occur only if the kinetic diameter of the host is less than the diameter of the intracrystalline cavities [41]. The structure of zeolites is built by associating TO_4 tetrahedra, most commonly $[SiO_4]^{4-}$ and $[AlO_4]^{5-}$ linked by shared oxygen atoms, to form a three-dimensional network [40]. Instead of the tetrahedrally bonded Si and Al atoms, so-called "*T atoms*", such as P, Ga, Ge, B, Be, Ti or Fe, can also be part of the structure [42]. The negative charge of the three-dimensional lattice is compensated by the positive charge of the cations located in specific positions of the zeolite structure [40]. Figure 2.5 shows the structural units of zeolites.

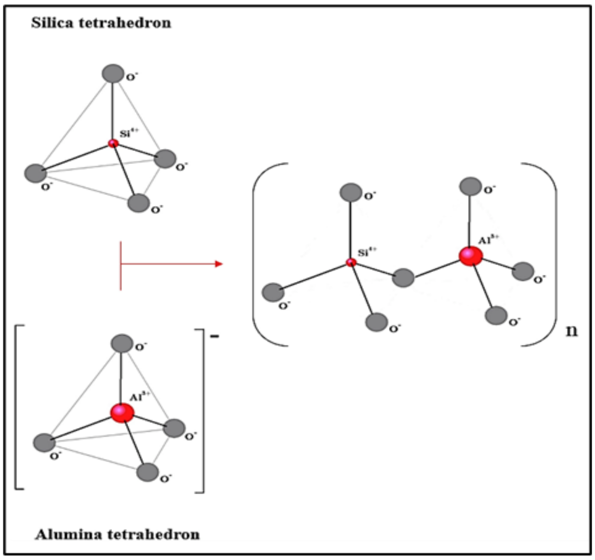

Figure 2. 5. Structural units of zeolites [43]

In most zeolites, the compensating cations are usually monovalent and bivalent metal ions and/or their combinations, which allow compensating the negative charges generated by the presence of Al, giving rise to the general formula,

$$M_{x/n}(AlO_2)_x \bullet (SiO_2)_y \bullet ZH_2O$$

Where M is the compensating cation of the negatively charged structure (such as H^+ or Na^+), y/x the Si/Al ratio, and Z the number of water molecules. According to Löewenstein's rule, there are no Al-O-Al bonds in zeolite aluminosilicate structures, hence $y/x \geq 1$ [39].

Currently, more than 235 different zeolite structures are known that possess peculiar physical and chemical properties. These types are based on the Si/Al ratio [39] as shown Figure 2.6. Natural zeolites have better resistivity and thermal stability in different environments. Its thermal stability and chemical resistance increase with the increase of the Si/Al ratio, as well as in the presence of alkali cations in the zeolite structure [44]. Synthetic zeolites have many additional advantages. For example, synthetic zeolite are extremely pure and with uniform size form along with better ion exchange capabilities [39].

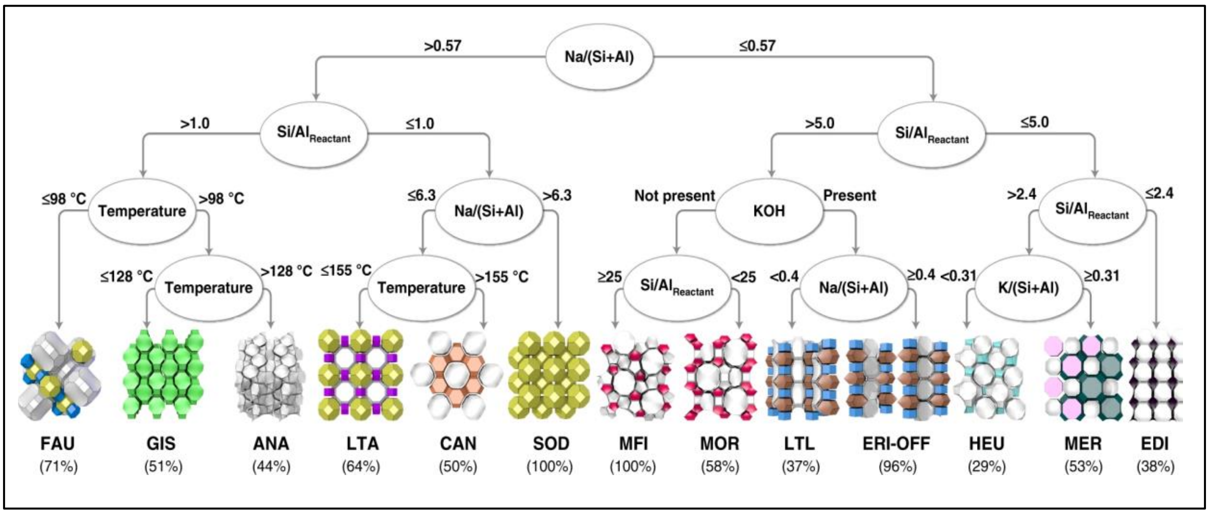

Figure 2. 6. Types of zeolites according to the Si/Al ratio [45]

Commercially, synthetic zeolites are used in massive amounts than natural zeolites due to the high purity of the crystalline products and the uniformity of the particle sizes. In addition, synthetic zeolites are manufactured commercially for specific uses including technical, environmental, industrial, commercial, agricultural, cracking and alkylation, and biomedical processes due to their porous character and ion exchange properties [39,44].

The successful development of zeolites and their innovative application in refineries and separation processes have further renewed industrial catalysis. In particular, zeolites with FAU (X and Y zeolites) and LTA (zeolite-A) topologies have potential applications in various industrial processes. These types of zeolites differ mainly due to the content of aluminum (as alumina), which can influence the crystal structure and ion exchange selectivity of the zeolite molecule [44].

2.7.1. Linde Type A (LTA) zeolite

This zeolite is normally synthesized in sodium form with a Si/Al ratio equal to 1. It belongs to the cubic system and when fully hydrated and in sodium form it has a unit cell parameter equal to 24.60 Å. The chemical formula of zeolite A can be expressed as:

$$Na_{12}(AlO_2)_{12}(SiO_2)_{12}\bullet 27H_2O$$

The crystalline structure of zeolite A belongs to groups 4-4. This structure can be described through the union of two types of polyhedra: (a) a simple cube, 4-4, formed by the union of two rings of four tetrahedra (D4R); and, (b) a truncated octahedron formed by the combination of 24 tetrahedra, better known as the β box or sodalite cage. Figure 2.7 shows the structure of LTA zeolite [46].

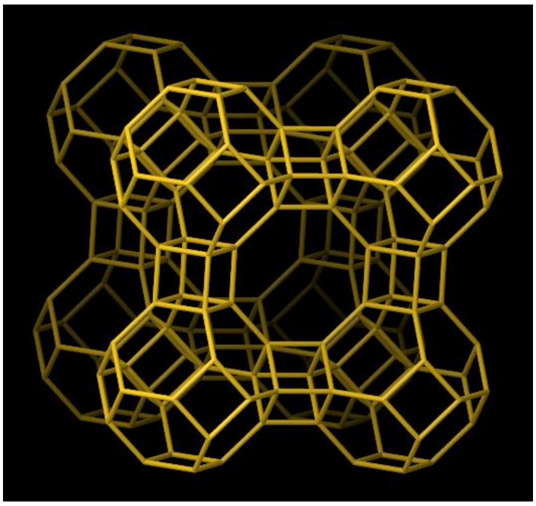

Figure 2. 7. Structure of Linde Type A (LTA) zeolite [47]

The union of sodalite cages, by four of their square faces, with the two rings of four tetrahedrons leads to a polyhedron, which encloses a large cavity known as "super-cages α" with an internal diameter equal to 11.4 Å. The combination of these α super cages with each other with the β cages, gives rise to the final structure of the zeolite, which presents two systems of interconnected three-dimensional channels: (i) a system formed by the union of α super cages, to which it is it enters through circular openings formed by rings of 8 oxygen atoms with a diameter equal to 4.2 Å; and, (ii) a system of channels formed by the alternate connection of sodalite cages and α super cages which are penetrated by openings formed by 6 oxygen atoms, with a diameter equal to 2.2 Å. Access to the first channel system (formed by rings of 8 oxygen atoms) is limited to molecules with kinetic diameters less than 4.5 Å, such as linear alkanes, water, CO_2, etc. In contrast, the channel system is inaccessible to organic and inorganic molecules with kinetic diameters greater than 2.5 Å. Of the 192 Na ions in this zeolite, 67% are located near the axial positions of the six-membered ring, but within the super cages. The remaining ions are found within the α super cages, coordinated to water molecules, which join together to form pentagonal dodecahedral structures [46].

2.7.2. Zeolites X and Y type faujasite

Although with different names, these zeolites topologically present the same crystalline structure. The differences lie in the intrareticular Si/Al ratio, while zeolite X has a Si/Al ratio between 1.0 and 1.5, zeolite Y has a ratio greater than 1.5. The chemical formulas of both zeolites can be expressed as:

Type X: $M_{86}(AlO_2)_{86}(SiO_2)_{106}\bullet 264H_2O$

Type Y: $M_{56}(AlO_2)_{56}(SiO_2)_{136}\bullet 253H_2O$

These zeolites belong to the cubic system; hydrated and in sodium form present cell parameters that vary between 25.0 and 24.18 Å, depending on the Si/Al ratio of the crystalline structure. This makes it present 192 tetrahedra per unit cell. The crystalline structure of these zeolites can be described basically in the same way as zeolite A. The difference is that, instead of secondary units of construction 4-4, they are double rings of six 6-6 tetrahedra, which are used to join the sodalite cages. The union of these 6-6, with four of the hexagonal faces of the sodalite cages or β cages, (as in zeolite A) form a polyhedron, which encloses a large cavity, the super cage α, but now with an internal diameter equal to 12.4 Å and which is entered through openings or pores delimited by rings of 12 oxygen atoms, with a free opening close to 8 Å. Figure 2.8 shows the structure of FAU zeolite [46].

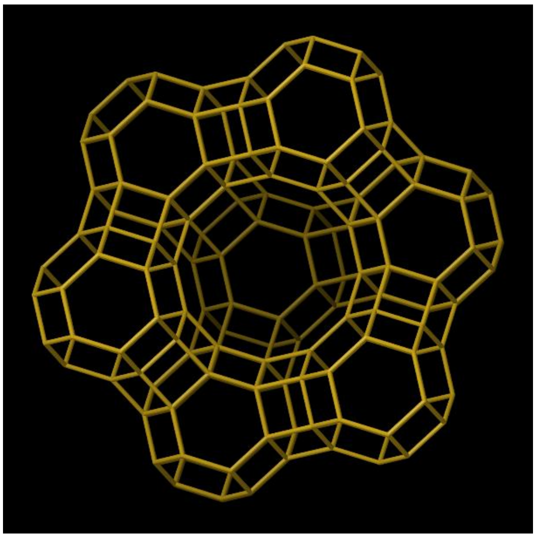

Figure 2. 8. Structure of Faujasite (FAU) zeolite [48]

As in zeolite A, the combination of the α super cages with each other and with the sodalite cages give rise to the final structure of the zeolite. It has two interconnected three-dimensional channel systems: (i) a system formed by the union of α super cages which is entered through openings formed by rings of 12 oxygen atoms with a diameter equal to 7.8 Å; and (ii) a channel system formed by the alternate connection of sodalite cages and α super cages, which is penetrated by openings formed by 6 oxygen atoms with a diameter equal to 2.2 Å. If this second channel system, due to its small pore size, is inaccessible to organic and inorganic molecules, the first is large enough to allow access for most of the organic molecules used as reagents [46].

With regard to compensating cations, various nomenclatures have been proposed to designate their location within the structure. The oldest is the one that distinguishes four different positions:

- The S(I) sites located in the center of the hexagonal prisms (16 S(I) sites per mesh).
- The S(I') sites located inside the sodalite cages and near the base of the hexagonal prisms (32 S(I') sites per mesh, 4 per sodalite cage).

- The S(II) sites located on the same axis as the previous ones, but located in the super cages (32 S(II) sites per mesh).
- The S(II') sites symmetrical to the preceding ones, in relation to the plane of the hexagonal faces of the socket cages (32S(II') sites per mesh).

These zeolites exchanged with multivalent cations and/or in the proton form are used in numerous refining and petrochemical processes, especially in catalytic cracking [44]

2.8. Synthesis of zeolites

Synthetic zeolites have versatile applications ranging from environmental to medicinal applications. Therefore, more emphasis is placed on a basic understanding of the chemistry of zeolite structures and the different preparation routes. Natural zeolites take several days to decades to create, while synthetic zeolites can be prepared in the laboratory from a few hours to a few days. Although zeolites can be synthesized from different raw materials that can be natural or artificial, not all raw materials are suitable for synthesis from an economic point of view. However, costs can be reduced by using clay minerals, volcanic glasses (perlite and pumice), rice husks, diatoms, fly ash, and others as starting materials [42].

The raw materials used for the synthesis of zeolites (zeolitization) must have some properties, including being easily available and inexpensive, have adequate content of alumina and silica, few impurities, and also allow high production performance and selectivity. The literature shows that clays are commonly used as sources of Al and Si for the synthesis of Linde type A (LTA), sodalite, faujasite (FAU), and other types of zeolites. Although the synthesized products contain quartz phases as impurities from natural clay samples, the zeolitization of clay materials has great potential for versatile applications, especially for environmental applications [44].

The zeolitization process involves numerous metastable phases that make the synthesis susceptible to various parameters, including temperature, precursor concentration, stirring speed, etc. In particular, the nucleation and crystallization process for FAU and LTA-type structures are more complex than for structures with high silica content. The aluminosilicate species can spontaneously polymerize while mixing the silica and alumina precursors resulting in the rapid formation of pre-crystalline nuclei with irregular dimensions. Such unevenly sized particles have different growth kinetics and can result in the rapid growth of large crystals. The non-covalent interactions typical of supramolecular self-assembly cannot support such rapid crystal growth and thus the mesostructure collapses. Therefore, tailoring the crystallization process to achieve the desired pore architecture in zeolites remains a major challenge [49].

2.8.1. Hydrothermal method for the synthesis of zeolites

Until now, various physicochemical and solvothermal methods have been adopted and developed to produce synthetic zeolites such as hydrothermal method, alkaline melting method, sol-gel method, and alkaline leaching method. However, the choice of the synthesis method depends on the type of zeolite that is produced. Each method has some advantages and few limitations [44].

The hydrothermal method is considered the main route of synthesis of zeolites. In this method, water is used as a solvent and a base is used as a mineralizer at different temperatures and pressures. Conventionally, hydrothermal synthesis needs to use a sealed container generally made of polypropylene and a Teflon-lined steel autoclave. In this method, a lower temperature is required, because it is very simple and cheaper compared to other methods [44]. The hydrothermal method has several advantages, including low energy consumption, the high reactivity of the reagents, easy maintenance on the solution, less air pollution, formation of metastable phases, and unique condensed phases. There are many factors that can affect the performance of any hydrothermal method, for example, temperature and pressure, batch composition, silica to aluminum ratio, reactive materials, general alkalinity, aging time, condition of the template, and seeding. Therefore, to overcome the limitations of the conventional hydrothermal strategy for the synthesis of zeolites, researchers have developed various means of sustainable ways to synthesize strategies, such as the microwave-assisted hydrothermal method, the alkaline fusion hydrothermal method, the hydrothermal method. assisted by microwave-digested alkaline fusion and the ultrasound-assisted hydrothermal method [44].

2.9. Advanced Oxidation Processes (AOPs)

Advanced oxidation processes (AOPs) are a group of chemical treatment techniques useful for removing organic (and sometimes inorganic) substances from water and wastewater through oxidative degradation reactions [27]. AOPs are based on the *in situ* production of hydroxyl radicals (•OH), which react rapidly in a non-selective way once formed. These radicals are generated with the help of one or more primary oxidants (e.g., O_3, H_2O_2, O_2) and/or energy sources (e.g., UV light) or catalysts (e.g., TiO_2), which are applied in precise amounts and combinations to achieve maximum yield of •OH. Hydroxyl radicals are capable of oxidizing organic compounds mainly by hydrogen abstraction or by electrophilic addition to double bonds, generating free organic radicals (R°) that in turn react with oxygen molecules to form a peroxy radical, initiating a series of oxidative degradation reactions, leading to complete mineralization of contaminants. Due to this mineralization, polluting materials are largely converted into stable inorganic compounds, such as water, carbon dioxide, and salts [4].

Table 2. 1. Classification of Advanced Oxidation Processes [50]

Non-photochemical	Photochemical
Ozonation	Photocatalytic oxidation, UV/Catalyst
Ozonation with hydrogen peroxide (O_3/H_2O_2)	UV/H_2O_2
Fenton (Fe^{2+} or Fe^{3+}/H_2O_2)	UV/O_3
Wet air oxidation (WAO)	UV/O_3/H_2O_2
Electrochemical oxidation	Photo-Fenton (Fe^{3+}/H_2O_2/UV)

AOPs are particularly useful for degrading biologically toxic or non-degradable materials such as aromatics, pesticides, petroleum components, and volatile organic compounds in wastewater. Additionally, AOPs can be used to treat secondarily treated wastewater effluent, which is later referred to as tertiary treatment [27]. As shows Table 2.1, AOPs includes various processes, including ozonation, Fenton and photo-Fenton process, UV-based photolysis, electrochemical oxidation processes, and photocatalysis [20]. However, among the above methods, photocatalysis as a green technology has received attention for the treatment of wastewater contaminated with different compounds since this process offers a lower cost compared to other AOP treatments. In addition, other important advantages of photocatalytic treatment include the environmental operating conditions, the complete destruction of water contaminants without the generation of secondary contaminants [51,52], and the use of the synergistic reaction between some contaminants to simultaneously remove a variety of pollutants. Based on the above advantages, photocatalytic technology has promising applications in the removal of aqueous organic pollutants and heavy metals, water separation, selective oxidation of organic compounds, carbon dioxide conversion, hydrogen peroxide production, etc., which can not only solve the problem of wastewater pollution but also develop and use new energy and other high value-added products [2].

2.10. Heterogeneous Photocatalysis

Heterogeneous photocatalysis is a promising AOP for the treatment of contaminated wastewater since it allows the complete mineralization of different organic and inorganic compounds, using semiconductor catalysts that are activated by natural or artificial light [51–56]. The photocatalytic activity of semiconductors is influenced by a wide variety of factors such as morphology, specific surface area, adsorption affinity and capacity for organic pollutants, intensity and spectral distribution of illuminating light, pH of solutions, among others [57].

The photocatalytic process comprises several reactions that occur on the surface of semiconductor particles, where the reaction rates depend on the efficiency and rate of charge transfer between the photocatalyst and the substrate. Also, this depends on the type of bond between the photocatalysts and the adsorbate. Weak substrate adsorption leads to indirect charge transfer and low photocatalytic activity. On the other hand, a strong and specific bond (adsorption) result in a direct charge transfer that induces higher photocatalytic activity [30]. Figure 2.9 shows a schematic diagram of the principle of photocatalysis.

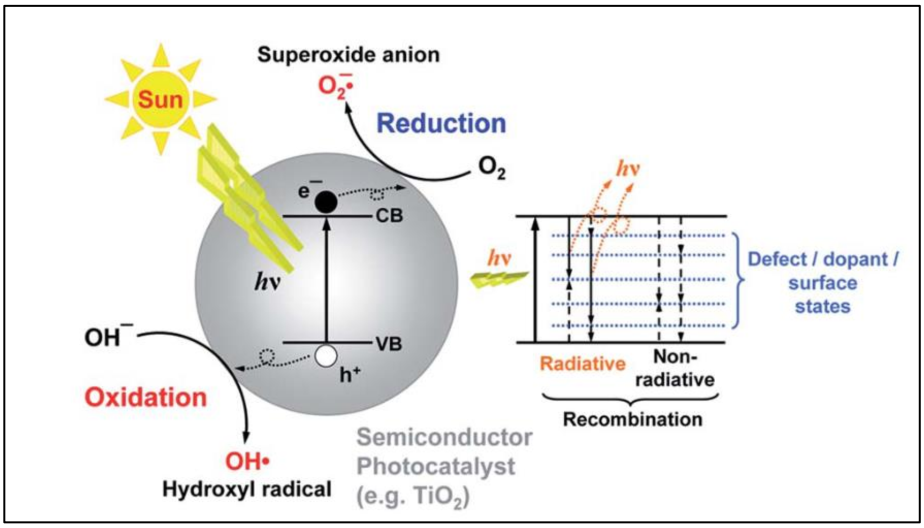

Figure 2. 9. Schematic diagram of the principle of photocatalysis [50]

Photocatalytic reactions begin when a photon of the appropriate energy (*hv*) is absorbed by a semiconductor, it promotes an electron from the valence band (VB) to conduction band (CB), generating an electron-hole pair (e^-, h^+) and leaving a hole (h^+) in the VB (reaction 1). The electron-hole pairs can recombine immediately (less than 1 ns) (reaction 2), but some of them can also migrate to the surface of the catalyst and react separately with other species adsorbed on the surface such as H_2O, OH^-, O_2, and other molecules (R). The holes at the semiconductor VB can oxidize adsorbed water or hydroxyl ions to form highly reactive hydroxyl radicals (reactions 3 and 4). On the other hand, the generated electrons at the CB can react with adsorbed oxygen molecules to produce oh radicals via a succession of reactions (reactions 5-8). These formed hydroxyl radicals have a strong ability to degrade organic dyes such as methylene blue (MB) (reaction 9). Furthermore, a direct oxidation of organic dyes can occur by reaction with holes (reaction 10). These reactions are expressed by the following equations [53,54,57,58]:

$$(semiconductor) \overset{UV}{\rightarrow} semiconductor + e_{CB}^- + h_{VB}^+ \quad \textbf{(1)}$$

$$e_{CB}^- + h_{vb}^+ \rightarrow heat \quad \textbf{(2)}$$

$$H_2O_{ads} + h_{VB}^+ \rightleftharpoons (H^+ + OH^-)_{ads} + h_{VB}^+ \rightarrow OH_{ads}^{\bullet} \quad \textbf{(3)}$$

$$OH_{ads}^- + h_{VB}^+ \rightarrow OH_{ads}^{\bullet} \quad \textbf{(4)}$$

$$(O_2)_{ads} + e_{BC}^- \rightarrow O_2^{\bullet -} \quad \textbf{(5)}$$

$$O_2^{\bullet -} + H^+ \rightarrow HO_2^{\bullet} \quad \textbf{(6)}$$

$$2HO_2^{\bullet} \rightarrow H_2O_2 + O_2 \quad \textbf{(7)}$$

$$H_2O_2 + e^- \rightarrow OH^{\bullet} + OH^- \quad \textbf{(8)}$$

$$R + OH_{ads}^{\bullet} \rightarrow R_{ads}^{\prime\bullet} + H_2O \rightarrow degradation\,products \quad \textbf{(9)}$$

$$R_{ads} + h_{VB}^+ \rightarrow R_{ads}^{\bullet +} \rightarrow degradation\,products \quad \textbf{(10)}$$

Most of the trapped electron-hole pairs (e^-, h^+) recombine indirectly at surface or volume defects and directly from band to band. The lack of these charge carriers causes defects by trapping electrons-holes in the surface and then releasing heat. The efficiency of the generation of electron-holes is related to some factors, such as the competition of different surface conduction processes that consist of the disappearance of electron-holes during the recombination process, the potential location of the bandgap, and the properties of the surface [59]. Consequently, during the last decade, a variety of strategies have been employed to improve the efficiencies of photocatalysts, for example, through proper texture design, doping, and formation of a semiconductor heterojunction by combining them with metals and/or other semiconductors. Among these, the construction of a *p-n* type semiconductor-semiconductor heterojunction has attracted much attention due to its perfect effectiveness in enhancing photocatalytic activity. This effectiveness is because the p-n junction generates a region of space charge at the interface due to the diffusion of electrons and holes, and therefore creates a built-in electric potential that can direct electrons and holes to travel in the opposite direction [60].

2.11. Photocatalyst

Semiconductor oxides are one of the most studied materials, due to their remarkable physical, optical and optoelectronic properties [51]. That is why a variety of semiconductors have been explored in modern photo-assisted techniques, including metal oxides (TiO_2, ZnO, WO_3, Fe_2O_3) and chalcogenides (ZnS, CdS, CdSe) [55,57]. These compounds are characterized by different bandgap energies and oxidizing power and also by destroying organic pollutants [20].

Among semiconductors, zinc (Zn) and titanium (Ti) oxides have been extensively exploited for various photodegradation applications because they are efficient, inexpensive, non-toxic, harmless, and exhibit chemical and thermal stability [61–65]. However, these oxides also have certain disadvantages such as the high recombination rate of the photogenerated carriers and the wide bandgap that only allows them to adsorb ultraviolet light [1, 2,29]. Considering the efficiency of solar energy in the photocatalytic process, it is necessary to design a photocatalysis with a bandgap energy value lower than 2.7 eV [9].

Zn and Ti oxides can be presented as binary compounds (ZnO and TiO_2), ternary ($ZnTiO_3$, Zn_2TiO_4, and $Zn_2Ti_3O_8$), or as mixed compounds, all being attractive alternatives in various scientific and technological applications, such as wastewater decontamination, generation of hydrogen, solar cells, gas sensors, pigments, photocatalysts, photoelectrochemical devices, and UV protection materials, etc. [66–70].

2.11.1. Zinc oxide (ZnO)

Zinc oxide is an inorganic compound with the formula ZnO. ZnO is a white, water-insoluble powder and is formed naturally in the mineral zincite, although most of the ZnO is produced synthetically. ZnO can form a crystal in three different forms: hexagonal wurtzite, cubic zincblende, and cubic rock salt [71]. Hexagonal wurtzite ZnO is thermodynamically the most stable under ambient conditions. However, cubic zincblende can be stabilized by growing ZnO on cubic substrates. ZnO exists in rock salt structure only at relatively high pressure (~10 GPa) [4]. The crystal structures of ZnO are shown in Figure 2.10.

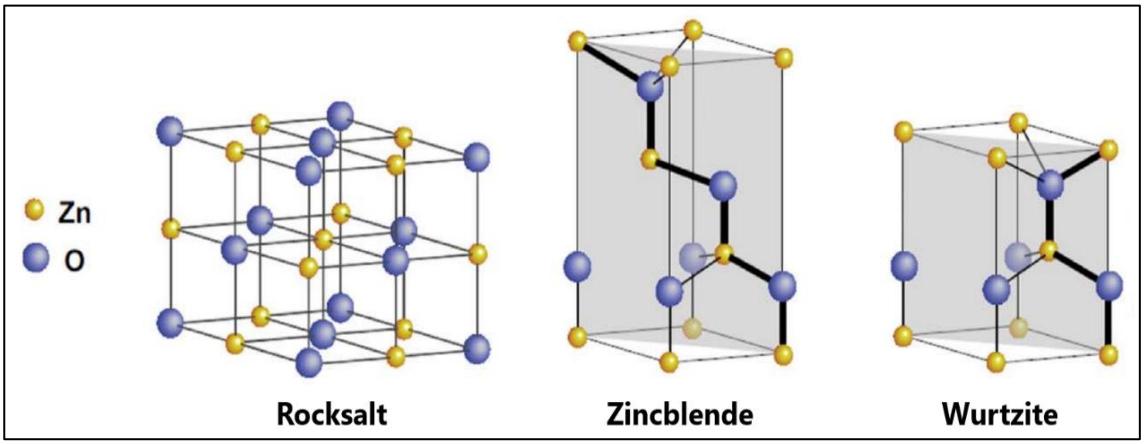

Figure 2. 10. ZnO crystal structures: (a) Rocksalt, (b) Zincblende and (c) Wurtzite [4]

The lattice constants of rocksalt, zincblende and wurtzite are presented in Table 2.2.

Table 2. 2. Lattice constants of Rocksalt, Zincblende and Wurtzite [71] [72].

Parameters	Rocksalt	Zincblende	Wurtzite
Space Group	$F\bar{4}3m$	$F\bar{4}3m$	$P6_3mc$
Structure	Cubic	Cubic	Hexagonal
a (Å)	4.2825	4.4200	3.2488
c (Å)	-	-	5.2058

ZnO is generally an intrinsically n-type semiconductor with the presence of intrinsic defects such as interstitial zinc, oxygen vacancies, and zinc vacancies, which affect its optical properties and electrical behavior [4]. ZnO has a tetrahedral bond configuration and has high ionicity at the border between that of ionic and covalent semiconductors. As a result, ZnO possesses a wide direct bandgap (3.37 eV) [59], a high bond excitation energy (60 meV) [68], as well as a deep violet/borderline ultraviolet (UV) absorption at room temperature [4].

At present, ZnO has attracted intensive research effort due to its unique properties, such as high chemical stability, high electrochemical coupling coefficient, high refractive index, high thermal conductivity, antibacterial bonding properties, and UV protection [55]. Due to these properties, ZnO has versatile applications in conductive films, wave guides, solar cells, ultraviolet (UV) light emitters, piezoelectric devices, and chemical sensors [65]. Furthermore, ZnO is one of the materials that has been used on a large scale as an efficient, inexpensive and non-toxic photocatalytic semiconductor for the photocatalytic degradation of a wide range of organic pollutants [53,73].

Although ZnO is widely used in photocatalysis, the rapid recombination of electron pairs and photogenerated holes that occur on the surface of this oxide results in low quantum efficiency [53]. Likewise, the narrow spectral range of absorption is another factor that limits its photocatalytic use. To address these problems, other semiconductors such as TiO_2 have been widely used which, through doping and deposition methods, improve the photogenerated charge separation and transport of ZnO structures [14].

2.11.2. Titanium dioxide (TiO_2)

Titanium dioxide (TiO_2) is an *n*-type semiconductor, with a bandgap energy range of 3.0-3.2 eV, depending on its crystalline structure [12]. TiO_2 has three main crystal structures; anatase (tetragonal), rutile (tetragonal), and brookite (orthorhombic). Anatase is the phase that is normally synthesized in the sol-gel process, and brookite is mainly found as a by-product when precipitation takes place in an acidic medium at low temperatures. Rutile is a stable structure, while both brookite and anatase are metastable and can generally transition to the stable rutile phase when heated [74]. The crystal structures of TiO_2 are shown in Figure 2.11.

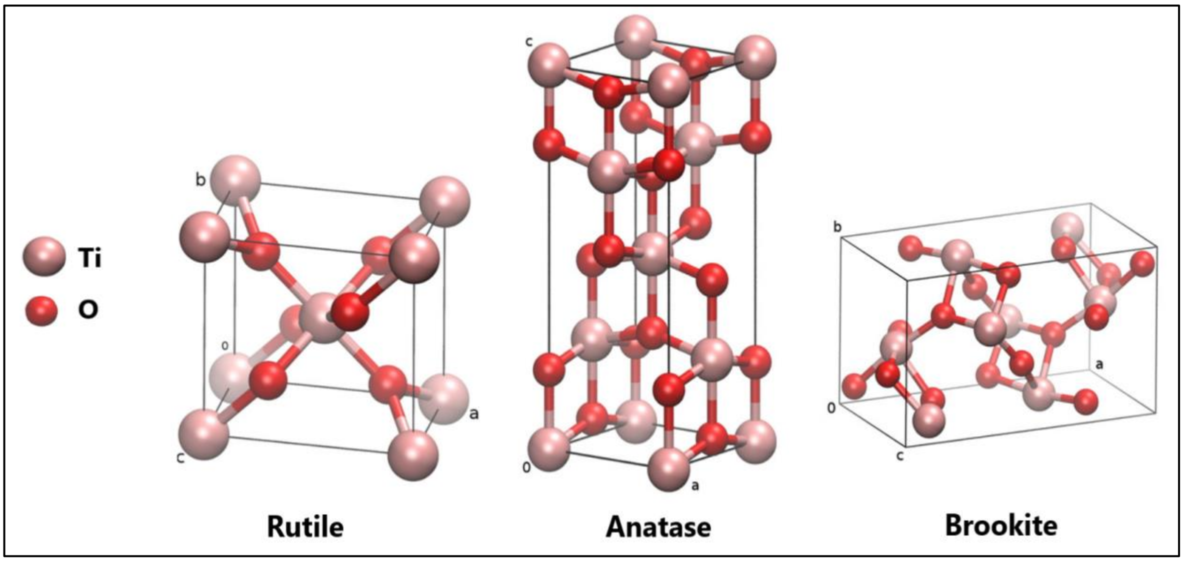

Figure 2. 11 TiO_2 crystal structures: (a) Rutile, (b) Anatase and (c) Brookite [75]

The lattice constants of rutile, anatase and brookite are presented in Table 2.3

Table 2. 3. Lattice constants of Rutile, Anatase and Brookite [76].

Parameters	Rutile	Anatase	Brookite
Space Group	$P4_2/mnm$	$I4_I/amd$	$Pbca$
Structure	Tetragonal	Tetragonal	Orthorhombic
a (Å)	4.594	3.785	5.436
b (Å)	4.594	3.785	9.166
c (Å)	2.959	9.514	5.436

TiO_2 is the most widely used metal oxide for environmental applications, paints, electronic devices, gas sensors, and solar cells [22,55,58], due to its exceptional optical and electronic properties, as well as its excellent performance, abundance, low cost, non-toxicity, photochemical stability, and insolubility in most reaction environments [73,77,78]. This semiconductor is well known for its excellent photocatalytic property which has been widely used in the removal of environmental pollutants, antibacterial additives, self-cleaning buildings, etc. [65]. Unfortunately, TiO_2 tends to show a lower photocatalytic efficiency at low concentrations of pollutants due to its small surface area and low adsorption capacity [3].

Although rutile is activated by visible light itself, its photocatalytic activity is lower than that of anatase, which is excited by UV-A light, however, the photocatalytic activities of both structures are highly influenced by types of substrates applied [79,80]. The combination of anatase with rutile has a higher photocatalytic activity due to a synergistic effect between both phases. In this way, the charges produced in the rutile phase under visible light are stabilized by a rapid transfer of electrons to the anatase phase, which extends the photocatalytic activity to the visible region [81]. On the other hand, brookite is more reactive than anatase; however, the preparation of pure brookite without rutile or anatase is quite difficult and therefore has not been extensively investigated.

2.11.3. ZnO-TiO$_2$ coupling

In recent years, the degradation of polluting dyes in water by photocatalysis, using semiconductors such as TiO$_2$ and ZnO, has attracted great interest due to their very similar physicochemical properties including high photocatalytic efficiency, insolubility in water, thermal and chemical stability, low cost, non-toxic nature and environmentally friendly characteristics [52,55,82]. Despite these advantages, both photocatalysts exhibit low charge transfer efficiency due to the high recombination rate of photoinduced electron pairs and holes [6,77,78,82]. Likewise, both semiconductors have functionality limits due to the fact that they exhibit values of the bandgap (TiO$_2$ = 3.0-3.2 eV and ZnO = 3.37 eV) and of the optical band (TiO$_2$ = 385 nm and ZnO = 425 nm), which allows them to use only a small percentage of solar energy [52,54,64,77].

Since visible light with a spectral wavelength between 400 and 700 nm represents approximately 45% of the total energy of solar radiation, while ultraviolet light occupies less than 10%, it is of great interest to improve the photocatalytic activity and the quantum efficiency of TiO$_2$ and ZnO for practical photocatalytic applications under visible light [63,64,69]. Therefore, several alternatives have been tested, the main ones being the use of dopants and the coupling of photocatalysts [58].

In the doping process, fast charge recombination is delayed and absorption of visible light is enabled, creating defect states in the bandgap [12]. In the former case, recombination is inhibited and interfacial charge transfer is enhanced by trapping VB holes or CB electrons at defect sites. In the second case, electronic transitions from the defect states to the CB or from the VB to the defect state are allowed under forbidden sub-band irradiation. Metal ions (transition metals and noble metals) and non-metallic ions are the two main categories of dopants. Selective metals are generally preferred as they have the potential to transfer electrons and lower the energy level of the bandgap. Among the different metallic doping elements, Cu, Au, and Ag have been shown to be effective dopants to enhance the absorption of visible light [12].

Considering the high price and limited mineral sources of noble metals, researchers have paid more attention to the coupling or heterojunction of two semiconductors that possess different levels of redox energy for their corresponding conduction (CB) and valence (VB) bands. This coupling has proven to be an attractive approach to compensate for the disadvantages of individual components and leads to more efficient charge separation, longer life of charge carriers, and improved interfacial charge transfer to adsorbed substrates [14,51,69]. Several semiconductors have been reported for the potential coupling of TiO_2, including SiO_2, MoO_3, CdS, MgO, WO_3, SnO_2, ZrO_2, CuO, Fe_2O_3, and ZnO [52,58,73,82]. The characteristics and compatibility of the coupling semiconductor are important for the physicochemical properties and stability of the hybrid semiconductor. Each semiconductor substantially affects the surface charge of the material and, therefore, increases or weakens its photocatalytic capacity [55].

Among the numerous semiconductor combinations, the integration of ZnO with TiO_2 is one of the most promising alternatives [6,65,77,83]. The physical and chemical properties of ZnO-TiO_2 are greater than those of the individual ones, which results from the modification of its electronic states [14,62]. In the ZnO-TiO_2 coupling, an energy potential polarization is formed that facilitates the transport of photoinduced electrons by injecting conduction band electrons from ZnO to TiO_2. In this way, by separating the electrons and photoinduced holes, recombination of the charge carriers can be avoided, which improves the photocatalytic activity [55,73,78,84,85]. The schematic diagram of the principle of photocatalysis on the ZnO-TiO_2 coupling is shown in Figure 2.12.

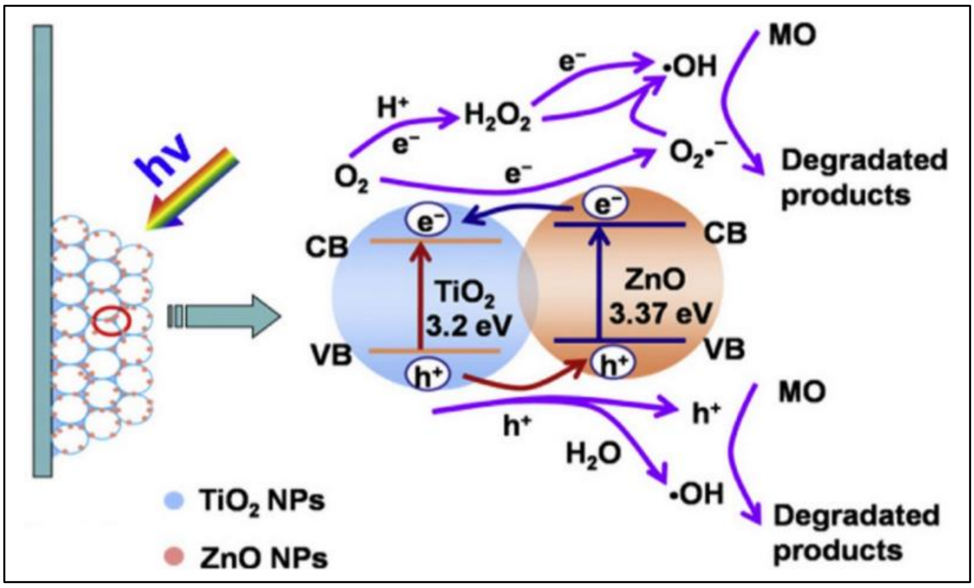

Figure 2. 12. Schematic diagram of the principle of photocatalysis on the ZnO-TiO_2 coupling [86]

2.11.4. Zn-Ti-O system

Several authors report that there are five existing compounds in the ZnO-TiO_2 binary system, including zinc ortho-titanate with a cubic and tetragonal crystalline structure (Zn_2TiO_4), zinc meta-titanate with a cubic and hexagonal crystalline structure ($ZnTiO_3$), and polytitanate of zinc with a cubic crystalline structure ($Zn_2Ti_3O_8$) that is considered as the form of $ZnTiO_3$ at low temperature ($T < 820$ °C) [69,70,87,88]. Furthermore, these three crystalline phases can be converted to each other under certain conditions [2]. Numerous reports on the formation of the Zn-Ti-O system have shown that the composition can change delicately subject to synthetic methods. This implies that the chemical and structural stability of the three zinc titanate structures would change delicately depending on the chemical environment [89].

Among the three different crystalline phases of zinc titanate, $Zn_2Ti_3O_8$ has a relatively high reducing potential. Furthermore, the valence band of $Zn_2Ti_3O_8$ is more positive and the conduction band is more negative than the respective TiO_2 bands (anatase phase). On the other hand, nano-sized crystalline $ZnTiO_3$ is a very significant material that has been used as an absorbent for dyes in wastewater [19,66]. $ZnTiO_3$ is an ABO_3 type of perovskite that has

BO_6 octahedra with A^{2+} cations embedded in the structure [32]. This zinc titanate is normally synthesized and crystallized by the solid-state reaction of a ZnO-TiO_2 mixture at high temperatures (600-900 °C) [90]. However, the synthesis that involves a titanium precursor in the presence of an excess of zinc precursor forms $Zn_2Ti_3O_8$ at temperatures of 700-900 °C. Both $ZnTiO_3$ and $Zn_2Ti_3O_8$ are directly transformed into Zn_2TiO_4 and rutile at temperatures above 945 °C [91].

To achieve pure titanate phases, different preparation techniques have been extensively studied, including wet and dry techniques. For example, Al-hajji *et al.* (2019) developed a comparative study on the microstructure of zinc metatitanate using solvothermal and ball milling methods. The mechanical pathway resulted in the formation of $ZnTiO_3$ as the main product accompanied by $ZnTi_3O_8$ as the secondary product. The solvothermal pathway, instead, resulted in the formation of $Zn_2Ti_3O_8$ accompanied by traces of zincite [92]. Likewise, other authors have proposed that the formation of Zn_2TiO_4 and $Zn_2Ti_3O_8$ is restricted by the presence of anatase and that $ZnTiO_3$ is formed exclusively in the presence of rutile due to structural similarities [89,93–96]. This limitation of solid-state synthesis produces titanates with large grain size, with uncontrolled and irregular morphologies, as well as contamination of different crystallographic phases [92,97,98]. Therefore, it remains a challenge to find new routes to prepare high purity titanate particles at low temperatures [97,99,100].

2.11.5. Zinc titanate ($ZnTiO_3$)

Recently, noncentrosymmetric compounds (NCS) have attracted great interest in materials science due to their symmetry-dependent non-linear second-order ferroelectric, piezoelectric, and optical properties, etc. Consequently, researchers are currently looking for new polar oxides, specifically, those that include distorted cations Jahn-Teller of the second-order (SOJT) (Te^{4+}, Sn^{4+}, Ti^{4+}, Mo^{6+}, Nb^{5+}, V^{5+}, etc.) and cations with stereo active lone pair electrons of ns^2 (Bi^{3+}, Pb^{2+}, Se^{4+}, etc.). The NCS compounds exhibit two famous structures: perovskite-type (Pv-type) and $LiNbO_3$-type (ln-type) phases. Taking into account the structural relationship between the two previous ones, the $LiNbO_3$ type structure can be considered as the derivative of the perovskite structure [101].

Perovskite oxides (ABO_3) are an important family of materials for various technological applications [9]. To date, many perovskite oxides such as $NaTaO_3$, $KTaO_3$, $BaZrO_3$, $SrTiO_3$, $BaTiO_3$, $CaTiO_3$, $LaFeO_3$, etc. have been synthesized, which have good optical, electrical, structural, and catalytic properties [9]. Compared to simple metal oxides, perovskite oxides are more stable and reliable [102,103]. $ZnTiO_3$ is a perovskite-type oxide whose structure allows it to adapt to change the arrangement of sites A and B, as well as to incorporate a combination of cations to these sites. In fact, the electronic properties of perovskite-type oxides vary with changes in stoichiometry or doping with a cation of a different valence state [104].

$ZnTiO_3$ has high thermal and chemical stability, a wide energy gap, high electron mobility, high reduction potential, and low oxidation potential, plus it is cost-effective and environmentally friendly [61,70,105,106]. In recent years, $ZnTiO_3$ has been investigated for application in many fields, such as regenerable sorbent for desulfurization of hot coal gases, gas sensor, humidity sensor, paint pigment, microwave dielectric material, antibacterial agent, and as photocatalyst [19,31,107–111].

The $ZnTiO_3$ structure is formed only at high temperatures and normally crystallizes into a rhombohedral ilmenite (Il) structure, with Zn^{2+} ($3d^{10}$) and Ti^{4+} ($3d^0$) sites [101]. These sites in the crystal structure of $ZnTiO_3$ occupy 2/3 octahedron gaps and the rest of the 1/3 octahedron gaps are completely empty. The existence of the so-called "columbic repulsion" between the Zn^{2+} and Ti^{4+} ion sites cause the slight movement of each ion towards the adjacent unoccupied octahedral sites along the trigonal axis c, thus producing a spontaneous polarization that is seen reinforced by a second-order Jahn-Teller distortion (SOJT), due to Ti^{4+} (d^0) [101,112–114].

ZnTiO$_3$ in the LiNbO$_3$-type (ln) phase is an interesting candidate for nonlinear and ferroelectric optical applications. Under ambient conditions, Il-ZnTiO$_3$ (hexagonal space group $r\bar{3}$), is the most stable polymorph, while ln-ZnTiO$_3$ (cubic space group $3m$) can be obtained as the recovered phase after transforming pure Il-ZnTiO$_3$ at a pressure of ~16.5 GPa and ~1150 K in its polymorph perovskite-type ZnTiO$_3$ (orthorhombic space group *pnma*) [110]. Both ln-type and Il-type structures are related by a zone-center ferroelectric mode involving cation displacement. However, the transformation from type ln to type II requires octahedral rotations that are hampered due to anion-anion contacts for compounds with small tolerance factors. Instead, ln-type ZnTiO$_3$ undergoes a phase transition to an orthorhombic Pv-type phase via an order-disorder phase transition [114]. Figure 2.13 shows the crystallographic structures of LiNbO$_3$ (LN)-type ZnTiO$_3$ and ilmenite (IL)-type ZnTiO$_3$ along the z-axis.

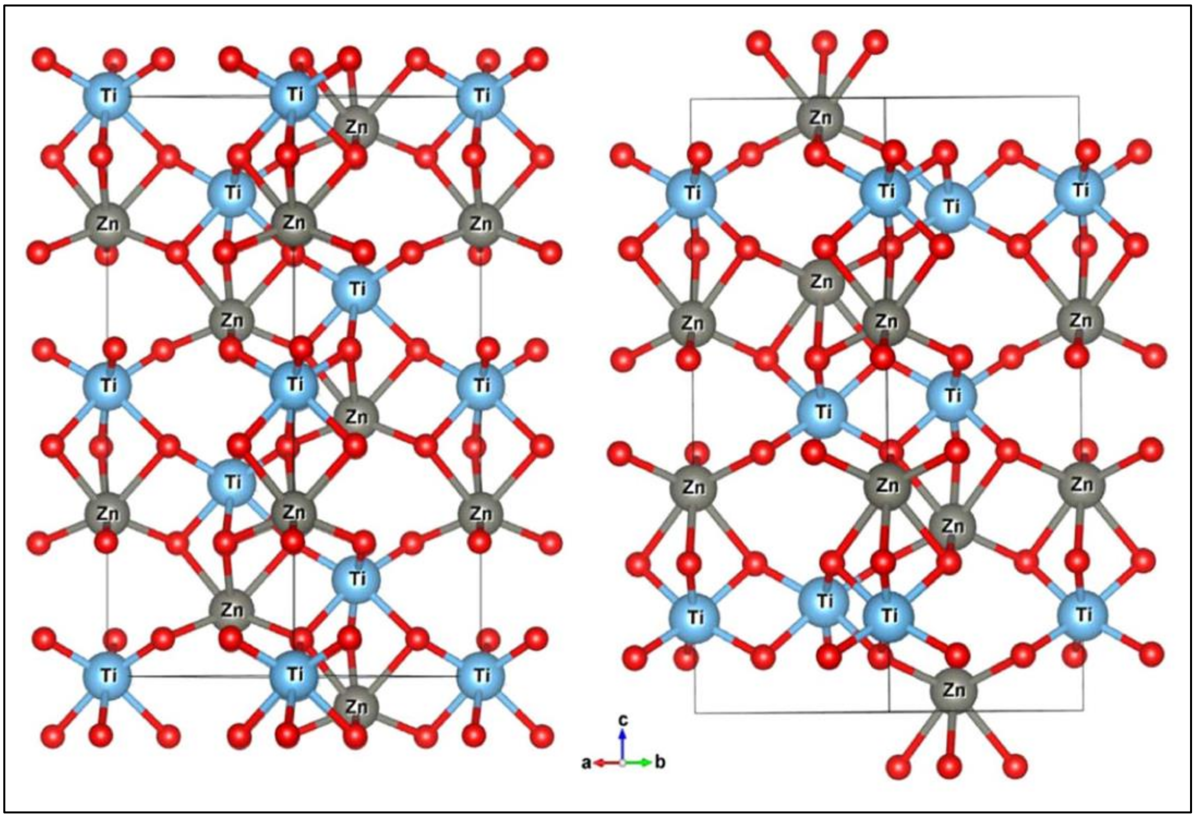

Figure 2. 13. Crystallographic structures of LiNbO$_3$ (LN)-type ZnTiO$_3$ (left, space group R3c) and ilmenite (IL)-type ZnTiO$_3$ (right, space group R$\bar{3}$) [113]

Currently, $ZnTiO_3$ has attracted the interest of numerous researchers due to its photocatalytic properties. However, similar to pure TiO_2 and ZnO, $ZnTiO_3$ is a broadband semiconductor that cannot be activated by visible light. Therefore, to expand the absorption of $ZnTiO_3$ to the visible light region or to improve the photocatalytic efficiency, several alternatives have been studied, among them doping of the $ZnTiO_3$ structure with metals or the $ZnTiO_3/TiO_2$ heterojunction [69].

Compared with $ZnTiO_3$ or TiO_2 pure, the heterojunction of both oxides has excellent stability, large surface areas, and specific capacity, satisfactory load capacity, etc., which is beneficial for the design of potential materials with photocatalytic applications [115].

2.11.6. Sol-gel method for the synthesis of $ZnTiO_3/TiO_2$

It is well known that the photocatalytic activity of semiconductors is closely related to physical properties such as crystalline phase, particle size, crystallinity, and morphology [48][60]. Therefore, at present, several methods have been used to obtain $ZnTiO_3$ of controlled shape and size with high purity and low cost [116]. However, despite the number of methods available, the preparation of pure $ZnTiO_3$ remains a challenge in materials chemistry as this mixed oxide decomposes into Zn_2TiO_4 and TiO_2 at high temperature [110].

To synthesize $ZnTiO_3$ particles, various techniques have been reported, including conventional solid-state reaction, spin coating, chemical vapor deposition, spray pyrolysis, sputtering, laser sintering, sonochemistry, co-precipitation, hydrothermal/ion exchange process, sol-gel process, chemical bath deposition and Pechini method [9,31,78,95,96]. Among these methods, the sol-gel process is a well-established green chemistry technique for the manufacture of ceramic materials [51,52]. This method allows obtaining nanocrystalline structures with regular morphology, suitable for easier control of the kinetics of the chemical reaction [74,100,108,117].

Several authors have systematically investigated the crystalline and phase transformation behaviors of sol-gel synthesized zinc titanates with respect to different molar ratios of Ti: Zn precursors and calcination temperatures [90,99]. Metal alkoxides are generally used as starting materials in the sol-gel synthesis of zinc titanates. These alkoxides are sensitive to moisture and readily hydrolyze to form metal hydroxides and their respective alcohols [118]. The microwave-assisted sol-gel or sol-gel method requires controlled hydrolysis of metal alkoxides in anhydrous alcohol to obtain a uniform particle size distribution [97]. Next, the reactions that occur during the synthesis of $ZnTiO_3$ through the sol-gel process using dehydrated zinc acetate and titanium alkoxide as precursors are described [90].

When dehydrated zinc acetate is added to deionized water, it dissociates into zinc ion, Zn^{2+}, and acetate ion, CH_3COO^-, as shown in reaction (1). CH_3COO^- ions can be further hydrolyzed and release OH^- ions as shown in reaction (2). When an ammonia solution is added, it hydrolyzes into ammonium ions, NH_4^+, and hydroxide ions, OH^-, as shown in reaction (3)

$$Zn(CH_3COO)_2 \rightarrow 2CH_3COO^- + Zn^{2+} \quad \textbf{(1)}$$

$$CH_3COO^- + H_2O \rightarrow OH^- + CH_3COO^- + Zn^{2+} \quad \textbf{(2)}$$

$$NH_3 + H_2O \rightarrow NH_4^+ + OH^- \quad \textbf{(3)}$$

The Zn^{2+} ions will react with the OH^- and NH_4^+ ions and lead to the formation of tetraaminesyncate ions $[Zn(NH_3)_4]^{2+}$, zinc hydroxide $[Zn(OH)_2]$ or tetrahydroxozincate $Zn(OH)_4^{2-}$ ions, which have an octahedral geometry, agglomerated in solution. These aggregates usually contain less than 50 ions. Once the aggregates reach about 150 ions, the wurtzite-structured ZnO domains nucleate in the central region of the aggregates, as shown in reactions (5) and (6). Therefore, the nucleus of the aggregate comprises Zn^{2+} and OH^- ions. Therefore, when more ammonia is added to the solution, there are more OH^- ions and NH_4^+ ions available for the formation of ZnO.

$$Zn(NH_3)_4^{2+} + 2OH^- \rightarrow ZnO + 4NH_3 + H_2O \quad \textbf{(4)}$$

$$Zn(OH)_4^{2-} \rightarrow ZnO + H_2O + 2OH^- \quad \textbf{(5)}$$

$$Zn(OH)_2 + 2OH^- \rightarrow Zn(OH)_4^{2-} \quad \textbf{(6)}$$

During the sol-gel reaction of titanium alkoxides, the OR groups are preferentially hydrolyzed, as shown in reaction (7), while the ligands remain tightly bound during the condensation process (8). In this way, the formation of linear chains of Ti-O polymers composed of octahedra that share edges is promoted. The formation of these octahedral stabilizes TiO_2 as anatase, which reduces the transformation temperature of anatase to rutile.

$$Ti[OCH(CH_3)_2]_4 + 4H_2O \rightarrow Ti(OH)_4 + 4(CH_3)_2CHOH \quad \textbf{(7)}$$

$$2Ti(OH)_4 \rightarrow 2TiO_2{\bullet}H_2O + 3H_2O \quad \textbf{(8)}$$

2.12. Nanocomposites

Nanotechnology products are considered very effective tools for environmental cleaning. Therefore, the use of many types of nanoparticles/nanocomposites and methods to clean up natural resources and improve the quality of life of the population has been widely described [11].

Nanocomposites are heterogeneous materials that consist of two or more components/phases that are chemically/physically different, and at least one of their phases is nano-sized. In general, the size of nano-objects ranges between 1 and 100 nm. Although the size of nanoparticles is between 1 and 100 nm in all three dimensions, nanofibers only have two dimensions at the nanoscale [24]. Due to their small size, high surface area, and the interface between phases, nanocomposites have unique characteristics, such as electronic, magnetic, optical, chemical, and mechanical properties that differ from bulk materials [93]. For this reason, nanocomposites are highly efficient materials in the fields of catalysis and photocatalysis, for the degradation of azo dyes, and have shown a higher photocatalytic performance than pristine samples [9,119].

2.13. Supported and structured materials

The main drawback of using semiconductors as photocatalysts is their susceptibility to aggregation, thus reducing their specific surface area, as well as their efficiency. On the other hand, the practical applications of photocatalysts in the form of powders suspended in an aqueous solution are limited due to the additional cost of separation and recovery [22]. Thus, recent studies have suggested alternatives to solve these problems, for example, by assembling nanostructured semiconductors on porous supports [120,121].

Porous materials have porosities in the microporous (less than 2 nm), mesoporous (between 2 and 50 nm), and microporous (greater than 50 nm) ranges [122]. Of these, the micro and mesoporous materials have wide applications in ion exchange, separation, and catalysis [123], [124]. In particular, porous materials with a higher quantity of surface hydroxyl groups and a large specific surface area are the most suitable for housing nanoparticles of photocatalysts [120,122]. Several porous materials have been investigated as potential supports, including zeolites, clay minerals, activated carbon, silica, glass spheres, perlite, fly ash, and organometallic structures [125]. Among the different porous materials, clays and clay-based materials represent a very promising alternative due to their high mechanical and chemical stability, high surface area, and high adsorption capacity. In addition, clays are environmentally friendly, inexpensive, and offer an interesting route for the revaluation of local resources [12].

Clay minerals have been widely used as supports in heterogeneous catalysis, in fact, TiO_2-clay composites have long been the most studied clay-based materials in photocatalysis. In these composites, the adsorption capacity of the clay and the photocatalytic capacity of the semiconductor are combined synergistically [121]. Furthermore, these composites have been shown to have a large specific surface area, and a porous network mainly composed of micro and mesopores due to the creation of oxide anchored to the layers of stratified clay (montmorillonite) or fibrous (sepiolite, halloysite) [126].

The effective use of micro and mesoporous materials in catalytic applications requires that these porous powders be structured in a macroscopic way. This structured shape must have a morphology that promotes high flow rates and rapid heat and mass transfer, as well as sufficient mechanical, chemical, and wears resistance. The high mechanical integrity of structured porous materials is essential for performance in processes where pressure variations are large and rapid, or when thermal cycling induces stress since these conditions can affect the useful life of the adsorbent and catalyst [122].

Structuring is often accomplished by using techniques that have a lot in common with ceramic processing. The main processing steps involve: (i) mixing the porous powder with inorganic and organic additives, (ii) shaping the powder into the desired engineered shape, and (iii) removing temporary additives and creating a mechanically robust structure by heat treatment. Porous powders are processed to produce structured bodies by a variety of shaping processes such as extrusion, slip and tape casting, foaming, gel casting, coating, spray drying, and dry pressing. Among these, extrusion is probably the most widely used manufacturing method to structure and shape porous powder for adsorption and catalytic applications. Post heat treatment is primarily performed to increase bond in the molded powder body but can be combined with a burn-out step for removal of the organic additives used to facilitate the molding process. Inorganic binders such as clays and silica are typically added to impart the desired mechanical strength [122].

Although binders impart mechanical strength and wear resistance, the incorporation of inactive binder dilutes the active component, i.e., the porous powder, resulting in a reduction in performance per unit mass (or volume) of the structured adsorbent or catalyst [122]. The use of inexpensive inorganic binders, such as SiO_2, Al_2O_3, and clay for catalyst bodies, is common in industrial processes, but several reports indicate that catalyst-binder interactions can influence the reactivity, selectivity, and stability of the overall catalyst material. In addition, the binder can coat the surface of the adsorbent or catalyst powder and cause pore blockage [127].

Traditionally, the structuring of catalysts and adsorbents has been developed by dominant companies and maintained as internal know-how or only disclosed in patents. However, the growing interest in porous materials for emerging applications has led to a greater number of open investigations related to the structuring of adsorbents and catalysts with large surface area, with high capacity and high volumetric efficiency, and easy recovery and recycling at the end of the process [84,122].

2.14. Theoretical and computational chemistry.

Computational chemistry is a division of theoretical chemistry, which is based on the use of natural laws, mathematical calculations, physical methods, among others, to solve problems that allow contrasting and complementing experimental data [128,129]. The methods used in computational chemistry are usually divided according to the classification shown in Figure 2.14.

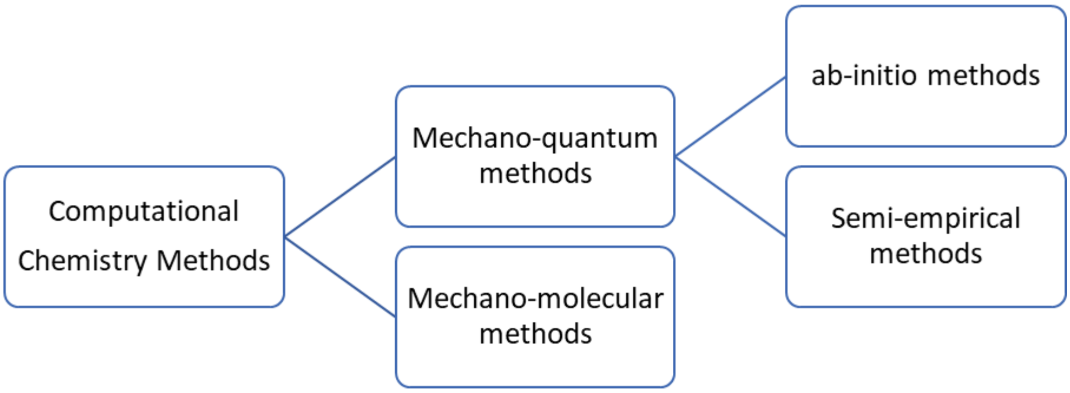

Figure 2. 14. Computational chemistry methods.

2.15. Quantum mechanics and the Schrödinger equation

In quantum mechanics, a system is defined by the particles that constitute it, by the interactions given between said particles and the relevant external fields that act on it. The so-called *ab-initio* methods are quantum-mechanical methods used to describe a system by solving the Schrödinger equation [130].

$$\hat{H}\psi = E\psi \qquad \textbf{(2.1)}$$

Where ψ is the wave function, E is the energy associated with the particular state of the system and $\hat{H}$ is the non-relativistic Hamiltonian operator, which includes both the kinetic contributions ($\hat{T}$) of electrons, with coordinates ***r***, and those of the nuclei atomic, with ***R*** coordinates; in addition to the potential interactions ($\hat{V}$) existing between said particles [131,132].

$$\hat{H}(r,R) \equiv \hat{T}(\dot{r}) + \hat{T}(\dot{R}) + \hat{V}(r) + \hat{V}(R) + \hat{V}(r,R) \qquad \textbf{(2.2)}$$

Multi-electronic systems are characterized by having a large number of electrons interacting with each other, which is why the above equation is extremely difficult to solve analytically. To approach the solution of these systems, it is necessary to include certain approximations, such as the Born-Oppenheimer approximation. This approximation considers the great difference between the relative mass of the nuclei and that of the electrons, with which it is possible to consider the fixed nuclei in certain positions and to simplify the calculations to solve only the electronic equation [133].

$$\hat{H}_{electr} \equiv \hat{T}_e + V_{ee} + V_{Ne} \qquad \textbf{(2.3)}$$

Despite this simplification, the problem remains complex, due to potential electron-electron interactions (V_{ee}), therefore, other additional approaches are required to try to solve polyelectronic systems. Methods based on quantum mechanics allow us to approach the solution of polyelectronic systems. These methods can be grouped into two types [130]:

- Methods based on obtaining the wave function, such as the Hartree-Fock (HF) method.
- Methods based on the calculation of electron density, such as the DFT (Density Functional Theory) method.

2.15.1. The Hartree-Fock (HF) method

Hartree-Fock (HF) methods is the starting point for the majority of computational work on the electronic structure of atoms and molecules. This approach is based on the construction of approximate poly-electronic functions as a product of monoelectronic functions (Slater determinants). The Hartree-Fock (HF) approximation is equivalent to the orbital approximation. The Hartree-Fock wave function is described as an anti-symmetrized spin-orbital product, and uses a single determinant as a test function. The HF method is the basis of current *ab initio* methods, it is an interactive process, applicable to isolated molecules, both in excited and fundamental states. The fact that this approximation uses a single determinant to describe the wave function, and the overestimation of the inter-electronic repulsion, generates many limitations because it is insufficient to describe those systems that include unpaired electrons, such as those involving breakdown of links [134]. This, added to the computational cost, has influenced the creation of new methods

2.15.2. Density functional theory (DFT)

This approach is based on two theorems, formulated by Hohenberg and Kohn:

- *"Any observable magnitude of a stationary non-degenerated ground-state can be calculated exactly from its electronic density"*
- *"The electronic density of a stationary non-degenerated ground-state can be calculated exactly by determining the density that minimizes the energy of the ground-state"*

The DFT method takes as initial data the type of atoms, the number of electrons, and the effects of the electronic correlation in the solution of the Schrödinger equation, which now expresses the energy of the system as a function of the electron density:

$$E_{(\rho)} = T_{(\rho)} + V_{(\rho)} + W_{CL(\rho)} + W_{NCL(\rho)} \qquad \textbf{(2.4)}$$

where T is the kinetic energy, V is the nucleus-electron potential, W is the coulombic (CL) and non-coulombic (NCL) electron-electron potential and ϱ is the electronic density [135].

The DFT method calculates the energy from the electron density taking as a reference a fictitious system of n electrons not interacting with each other, moving under an external potential. The precise mathematical equation that relates to energy and electron density is not currently known, therefore approximations are used that provide acceptable results [136].

2.16. Correlation and exchange functions

As mentioned earlier, the DFT incorporates all the correlation energy and uses an approximate Hamiltonian to generate a final electron density equal to that of the real system. Therefore, it is favorable to have a good functional and potential for represent the correlation and exchange. In the following equations it is possible to appreciate the relationship between the correlation and exchange potential and the correlation and exchange energy:

$$E_{xc}[\rho] = \int \rho\,(\vec{r})\,v_{xc}(\vec{r})d(\vec{r}) \qquad \textbf{(2.5)}$$

$$v_{xc}(\vec{r}) = \frac{\delta E_{xc}[\rho]}{\delta\rho(\vec{r})} \qquad \textbf{(2.6)}$$

The equations (i) and (ii) relate the energy and the total correlation and exchange potential, with the correlation and exchange energy per particle E_{xc} and with the correlation energy and exchange per unit volume v_{xc} [137,138]. The most useful approximations include the local density approximation (LDA) and the generalized gradient approximation (GGA).

2.16.1. Local density approximation (LDA)

LDA is a simple approximation that is available to describe the electron density by means of a correlation and exchange functional. Hohenberg-Kohn proposed an equation to describe the system.

$$E_{xc}^{LDA}[\rho] = \int \rho(r)\varepsilon_{xc}(\rho)dr \qquad \textbf{(2.7)}$$

Where $E_{xc}^{LDA}[\rho]$ represents the exchange-correlation energy functional, $[\rho]$ refers to the electron density that does not change much in relation to (r); and ε_{xc} corresponds to the correlation and exchange energy functional for each electron present in a homogeneous electron gas. The electron density of a homogeneous electron gas is considered to be continuous throughout the system. The density $[\rho]$ of any real point of the system can be replaced by a fictitious system called jellium, ignoring the changes of this variable due to its non-homogeneity [137].

For the approximation, ε_{xc} is a density-dependent functional and is written as the addition or summation of the exchange and correlation:

$$\varepsilon_{xc}\ (\mathrm{P}) = \varepsilon_x(\rho) + \varepsilon_c(\rho) \qquad \textbf{(2.8)}$$

$$\varepsilon_{xc}\ (\mathrm{P}) = -\ \frac{3}{4}\left(\frac{3}{\pi}\right)^{1/3}\ (p(r))^{1/3} \qquad \textbf{(2.9)}$$

The contributions of correlation and exchange are usually treated separately. In LDA, the effects of the correlation in exchange are local and depend exclusively on the value of the electron density at each point. The results obtained with the LDA method are highly reliable, obtaining reasonable values of energy and vibration frequencies as well as the density of charges with the exception of the regions close to the nucleus. However, it does not predict weakly bonded systems well or generates a thermodynamically reliable prediction [139].

2.16.2. Generalized gradient approximation (GGA)

To improve the calculation of the system obtained with the local density approximation, which considers an invariance of the density with respect to position, the effects of the density gradient are integrated into the generalized gradient approximation (GGA). It is a correction to the LDA methods, which includes the variations of the electron density with respect to the position, therefore it is considered a semilocal approximation. In the generalized gradient approximation, within the mathematical formula of the correlation and exchange functional, both the local density approximation and the electron density gradient are included [139].

$$E_{xc}^{GGA}[\rho(r)] = \int f(\rho(r), \nabla\rho(r))d\vec{r} \quad \textbf{(2.10)}$$

Currently, there are a series of functionals that are based on GGA, whose function is to help describe the exchange and correlation energy, such as Perdew-Wang 86 (PW86), Becke-Perdew (bp), Lee-Yang-Parr (LYP), Perdew-Wang 91 (PW91), Perdew-Burke-Ernzerhof (PBE), revised Perdew-Burke-Emzerhof (RPBE), among others [140].

2.17. Pseudopotentials

The valence electrons are in the last layer or energy level, and through electrostatic interactions between the valence electrons of one atom and another form chemical bonds; while the internal electrons also called core, electrons do not contribute to the formation of bonds. In many of the systems, because the core electrons do not participate in bond formation, their energy is affected only by an average electrostatic potential, and their wave functions are slightly modified [141].

The use of pseudopotentials consists in the replacement of the effect of the core electrons by a function of potential energy and an effective nuclear charge. Thus, the pseudopotential replaces the nucleus-electron interaction potential. The approach in the use of pseudopotentials was initially proposed by Philips and Kleinman; and since then, several pseudopotentials have been developed, thus improving their effectiveness and adaptation to the different theoretical methods. The elimination of electrons from the layers prior to the valence shell (core electrons) in computational calculations has allowed to save resources and reduce calculation costs, in addition, calculations based on plane and pseudopotential waves have become precise tools. and powerful in the study of the electronic structure of both atoms and molecules [141].

2.18. Augmented wave projector (PAW)

Among the pseudopotentials, the augmented wave projector (PAW) is an approximation that improves the speed and precision of calculations, giving way to the description of systems that include a large number of atoms and other complexities. The pseudopotential PAW was created by Blöchl, who combines different wave functions for each region of the atom, and describes the core region with more precise calculations, for example, the method of interaction of configurations. Additionally, by using a smoothed wave function to solve the valence region, it is able to adapt to the electronic environment. Through these methods, complex computational problems can be solved reducing their cost [142].

2.19. Model building

Within the framework of what could be called condensed phase systems are the different types of solids and their more or less regular surfaces of atoms or ions that make up the crystal lattice. In materials science, quantum-mechanical models use two different ways to model the adsorption of a substrate, these are the cluster model and the periodic model. The periodic method is described in more detail below. Unlike the cluster method, it allows the study of some properties of solids that are not local [129].

2.19.1. Periodic model

The periodic model contemplates the use of a unit cell with translational symmetry and made up of several atoms to simulate the surface. It uses Bloch's theorem, which considers that, if the potential to which an electron is subjected is periodic, then the monoelectronic wave function complies with the following equation:

$$\psi_{n,k}(r+\tau) = \psi_{n,k}\,(r)e^{ik\tau} \qquad \textbf{(2.11)}$$

Where τ is a translational vector [141]. Both the wave function and the energy value depend on the value of each point *k* in the reciprocal space in which it is calculated. The calculation of the average of the energy of all the points *k* provides the energy of the system, and by integrating the entire Brillouin zone and adding all the occupied bands, the electron density is obtained. There are indeterminate points *k* in the Brillouin zone, but in practice, the wave function is calculated with a finite number of points k. It is necessary to calculate the wave function with enough points *k* to obtain a suitable value of the energy since the number of points *k* is proportional to the precision of the energy; hence the importance of checking that the energy is converged with respect to the number of points *k* [139].

2.20. References

[1] H. Ullah, K. A. Khan, and W. U. Khan, “ZnO/TiO2 nanocomposite synthesized by sol gel from highly soluble single source molecular precursor,” *Chinese J. Chem. Phys.*, vol. 27, no. 5, pp. 548-554+i, 2014, doi: 10.1063/1674-0068/27/05/548-554.

[2] F. Chen *et al.*, “Fabrication and characterization of ZnTiO3/Zn2Ti3O8/ZnO ternary photocatalyst for synergetic removal of aqueous organic pollutants and Cr(VI) ions,” *Sci. Total Environ.*, vol. 706, p. 136026, 2020, doi: 10.1016/j.scitotenv.2019.136026.

[3] M. Tobajas, C. Belver, and J. J. Rodriguez, “Degradation of emerging pollutants in water under solar irradiation using novel TiO 2 -ZnO / clay nanoarchitectures,” *Chem. Eng. J.*, no. June, 2016, doi: 10.1016/j.cej.2016.10.002.

[4] C. Boon, L. Yong, and A. Wahab, “A review of ZnO nanoparticles as solar photocatalysts : Synthesis , mechanisms and applications,” *Renew. Sustain. Energy Rev.*, vol. 81, no. August 2017, pp. 536–551, 2018, doi: 10.1016/j.rser.2017.08.020.

[5] Q. Zhao *et al.*, “Simultaneous efficient adsorption and photocatalytic degradation of methylene blue over iron(III)-based metal–organic frameworks: a comparative study,” *Transit. Met. Chem.*, vol. 44, no. 8, pp. 789–797, 2019, doi: 10.1007/s11243-019-

00349-9.

[6] X. Zou, X. Dong, L. Wang, H. Ma, X. Zhang, and X. Zhang, "Preparation of ni doped ZnO-TiO2 composites and their enhanced photocatalytic activity," *Int. J. Photoenergy*, vol. 2014, 2014, doi: 10.1155/2014/893158.

[7] O. Sakin Omer, M. A. Hussein, B. H. M. Hussein, and A. Mgaidi, "Adsorption thermodynamics of cationic dyes (methylene blue and crystal violet) to a natural clay mineral from aqueous solution between 293.15 and 323.15 K," *Arab. J. Chem.*, vol. 11, no. 5, pp. 615–623, Jul. 2018, doi: 10.1016/j.arabjc.2017.10.007.

[8] Y. Chen, Z. Xiang, D. Wang, J. Kang, and H. Qi, "Effective photocatalytic degradation and physical adsorption of methylene blue using cellulose/GO/TiO2hydrogels," *RSC Adv.*, vol. 10, no. 40, pp. 23936–23943, 2020, doi: 10.1039/d0ra04509h.

[9] T. Tavakoli-Azar, A. R. Mahjoub, M. S. Sadjadi, N. Farhadyar, and M. H. Sadr, "Improving the photocatalytic performance of a perovskite ZnTiO3 through ZnTiO3@S nanocomposites for degradation of Crystal violet and Rhodamine B pollutants under sunlight," *Inorg. Chem. Commun.*, vol. 119, no. July, p. 108091, 2020, doi: 10.1016/j.inoche.2020.108091.

[10] H. Nourmoradi, A. R. Ghiasvand, and Z. Noorimotlagh, "Removal of methylene blue and acid orange 7 from aqueous solutions by activated carbon coated with zinc oxide (ZnO) nanoparticles: equilibrium, kinetic, and thermodynamic study," *Desalin. Water Treat.*, vol. 55, no. 1, pp. 252–262, 2015, doi: 10.1080/19443994.2014.914449.

[11] G. Cavallaro *et al.*, "Organic-nanoclay composite materials as removal agents for environmental decontamination," *RSC Adv.*, vol. 9, no. 69, pp. 40553–40564, 2019, doi: 10.1039/c9ra08230a.

[12] H. B. Hadjltaief *et al.*, "Photocatalytic degradation of methyl green dye in aqueous solution over natural clay-supported ZnO – TiO2 catalysts," *J. Photochem. Photobiol. A Chem.*, vol. 315, pp. 25–33, 2016, doi: 10.1016/j.jphotochem.2015.09.008.

[13] S. Sahoo, Uma, S. Banerjee, and Y. C. Sharma, "Application of natural clay as a potential adsorbent for the removal of a toxic dye from aqueous solutions," *Desalin.*

Water Treat., vol. 52, no. 34–36, pp. 6703–6711, 2014, doi: 10.1080/19443994.2013.816872.

[14] L. Lin *et al.*, "A highly efficient TiO2@ZnO n-p-n heterojunction nanorod photocatalyst," *Nanoscale*, vol. 5, no. 2, pp. 588–593, 2013, doi: 10.1039/c2nr33109h.

[15] S. Kang *et al.*, "Enhanced removal of methyl orange on exfoliated montmorillonite/chitosan gel in presence of methylene blue," *Chemosphere*, vol. 238, Jan. 2020, doi: 10.1016/j.chemosphere.2019.124693.

[16] M. A. Ahmed, E. E. El-Katori, and Z. H. Gharni, "Photocatalytic degradation of methylene blue dye using Fe2O 3/TiO2 nanoparticles prepared by sol-gel method," *J. Alloys Compd.*, vol. 553, pp. 19–29, 2013, doi: 10.1016/j.jallcom.2012.10.038.

[17] J. Ma, S.-Y. Tian, S.-L. Mu, S.-L. Xie, and R.-J. Ying, "Adsorption Properties of Methylene Blue on ODA-Hectorite: Equilibrium, Kinetic Studies," vol. 104, no. Icmcm, pp. 441–446, 2016, doi: 10.2991/icmse-16.2016.11.

[18] J. J. Salazar-Rabago, R. Leyva-Ramos, J. Rivera-Utrilla, R. Ocampo-Perez, and F. J. Cerino-Cordova, "Biosorption mechanism of Methylene Blue from aqueous solution onto White Pine (Pinus durangensis) sawdust: Effect of operating conditions," *Sustain. Environ. Res.*, vol. 27, no. 1, pp. 32–40, 2017, doi: 10.1016/j.serj.2016.11.009.

[19] R. S. Raveendra *et al.*, "Synthesis, structural characterization of nano ZnTiO 3 ceramic: An effective azo dye adsorbent and antibacterial agent," *J. Asian Ceram. Soc.*, vol. 2, no. 4, pp. 357–365, 2014, doi: 10.1016/j.jascer.2014.07.008.

[20] Y. Hanifehpour, N. Hamnabard, B. Khomami, S. W. Joo, B. K. Min, and J. H. Jung, "A novel visible-light Nd-doped CdTe photocatalyst for degradation of Reactive Red 43: Synthesis, characterization, and photocatalytic properties," *J. Rare Earths*, vol. 34, no. 1, pp. 45–54, 2016, doi: 10.1016/S1002-0721(14)60576-7.

[21] S. O. Cigdem, "Adsorption and desorption kinetics behaviour of methylene blue onto activated carbon," *Physicochem. Probl. Miner. Process.*, vol. 48, no. 2, pp. 441–454, 2012, doi: 10.5277/ppmp120210.

[22] L. Laysandra *et al.*, "Adsorption and photocatalytic performance of bentonite-

titanium dioxide composites for methylene blue and rhodamine B decoloration," *Heliyon*, vol. 3, no. 12, p. e00488, 2017, doi: 10.1016/j.heliyon.2017.e00488.

[23] Y. Kuang, X. Zhang, and S. Zhou, "Adsorption of Methylene Blue in Water onto Activated Carbon by Surfactant Modification," *Water 2020, Vol. 12, Page 587*, vol. 12, no. 2, p. 587, Feb. 2020, doi: 10.3390/W12020587.

[24] S. Kurajica, I. Minga, R. Blazic, K. Muzina, and P. Tominac, "Adsorption and Degradation Kinetics of Methylene Blue on As-prepared and Calcined Titanate Nanotubes," *Athens J. Sci.*, vol. 5, no. 1, pp. 7–22, 2018, doi: 10.30958/ajs.5-1-1.

[25] B. Purevsuren *et al.*, "Investigation of adsorption of methylene blue from aqueous phase onto coal-based activated carbons," *J. Chinese Inst. Eng. Trans. Chinese Inst. Eng. A*, vol. 40, no. 4, pp. 355–360, 2017, doi: 10.1080/02533839.2017.1308273.

[26] H. Li, M. Dai, S. Dai, X. Dong, and F. Li, "Methylene blue adsorption properties of mechanochemistry modified coal fly ash," *Hum. Ecol. Risk Assess.*, vol. 24, no. 8, pp. 2133–2141, 2018, doi: 10.1080/10807039.2018.1440527.

[27] M. Shahid *et al.*, "Adsorption and photocatalytic degradation of methylene blue using potassium polytitanate and solar simulator," *J. Nanosci. Nanotechnol.*, vol. 16, no. 5, pp. 4342–4349, 2016, doi: 10.1166/jnn.2016.10998.

[28] T. Shindhal *et al.*, "A critical review on advances in the practices and perspectives for the treatment of dye industry wastewater," *https://doi.org/10.1080/21655979.2020.1863034*, vol. 12, no. 1, pp. 70–87, 2020, doi: 10.1080/21655979.2020.1863034.

[29] M. Faisal, M. Jalalah, F. A. Harraz, A. M. El-Toni, J. P. Labis, and M. S. Al-Assiri, "A novel Ag/PANI/ZnTiO3 ternary nanocomposite as a highly efficient visible-light-driven photocatalyst," *Sep. Purif. Technol.*, vol. 256, no. September 2020, p. 117847, 2021, doi: 10.1016/j.seppur.2020.117847.

[30] A. B. Makama, A. Salmiaton, E. B. Saion, T. S. Y. Choong, and N. Abdullah, "Synthesis of CdS Sensitized TiO2 Photocatalysts: Methylene Blue Adsorption and Enhanced Photocatalytic Activities," *Int. J. Photoenergy*, vol. 2016, 2016, doi:

10.1155/2016/2947510.

[31] S. Perween and A. Ranjan, "Improved visible-light photocatalytic activity in ZnTiO3 nanopowder prepared by sol-electrospinning," *Sol. Energy Mater. Sol. Cells*, vol. 163, no. August 2016, pp. 148–156, 2017, doi: 10.1016/j.solmat.2017.01.020.

[32] R. Abirami, C. R. Kalaiselvi, L. Kungumadevi, T. S. Senthil, and M. Kang, "Synthesis and characterization of ZnTiO3 and Ag doped ZnTiO3 perovskite nanoparticles and their enhanced photocatalytic and antibacterial activity," *J. Solid State Chem.*, vol. 281, no. October 2019, p. 121019, 2020, doi: 10.1016/j.jssc.2019.121019.

[33] E. A. El-Sharkawy, A. Y. Soliman, and K. M. Al-Amer, "Comparative study for the removal of methylene blue via adsorption and photocatalytic degradation," *J. Colloid Interface Sci.*, vol. 310, no. 2, pp. 498–508, 2007, doi: 10.1016/j.jcis.2007.02.013.

[34] A. Gil, F. C. C. Assis, S. Albeniz, and S. A. Korili, "Removal of dyes from wastewaters by adsorption on pillared clays," *Chem. Eng. J.*, vol. 168, no. 3, pp. 1032–1040, 2011, doi: 10.1016/j.cej.2011.01.078.

[35] C. Mahamadi and E. Mawere, "Kinetic Modeling of Methylene Blue and Crystal Violet Dyes Adsorption on Alginate-Fixed Water Hyacinth in Single and Binary Systems," *Am. J. Anal. Chem.*, vol. 04, no. 10, pp. 17–24, 2013, doi: 10.4236/ajac.2013.410a3003.

[36] M. N. Subramaniam, P. S. Goh, N. Abdullah, W. J. Lau, B. C. Ng, and A. F. Ismail, "Adsorption and photocatalytic degradation of methylene blue using high surface area titanate nanotubes (TNT) synthesized via hydrothermal method," *J. Nanoparticle Res.*, vol. 19, no. 6, 2017, doi: 10.1007/s11051-017-3920-9.

[37] M. F. Brigatti, E. Galán, and B. K. G. Theng, "Structure and Mineralogy of Clay Minerals," *Dev. Clay Sci.*, vol. 5, pp. 21–81, Jan. 2013, doi: 10.1016/B978-0-08-098258-8.00002-X.

[38] L. Lisuzzo, G. Cavallaro, S. Milioto, and G. Lazzara, "Layered composite based on halloysite and natural polymers: A carrier for the pH controlled release of drugs," *New J. Chem.*, vol. 43, no. 27, pp. 10887–10893, 2019, doi: 10.1039/c9nj02565k.

[39] R. Bingre, B. Louis, and P. Nguyen, "An overview on zeolite shaping technology and solutions to overcome diffusion limitations," *Catalysts*, vol. 8, no. 4. 2018, doi: 10.3390/catal8040163.

[40] A. L. Velosa, A. S. Silva, F. Rocha, E. Ferraz, and S. Andrejkovic, "Synthetic zeolite pellets incorporated to air lime – metakaolin mortars : Mechanical properties," vol. 69, pp. 243–252, 2014, doi: 10.1016/j.conbuildmat.2014.07.030.

[41] V. Ramamurthy, "Controlling photochemical reactions via confinement: Zeolites," *J. Photochem. Photobiol. C Photochem. Rev.*, vol. 1, no. 2, pp. 145–166, 2000, doi: 10.1016/S1389-5567(00)00010-1.

[42] M. Gougazeh and J.-C. Buhl, "Synthesis and characterization of zeolite A by hydrothermal transformation of natural Jordanian kaolin," *J. Assoc. Arab Univ. Basic Appl. Sci.*, vol. 15, pp. 35–42, Apr. 2014, doi: 10.1016/J.JAUBAS.2013.03.007.

[43] S. K. Masoudian, S. Sadighi, and A. Abbasi, "Synthesis and Characterization of High Aluminum Zeolite X from Technical Grade Materials," *Bull. Chem. React. Eng. Catal.*, vol. 8, no. 1, pp. 54–60, Jun. 2013, doi: 10.9767/bcrec.8.1.4321.54-60.

[44] R. Belaabed, S. Elabed, A. Addaou, A. Laajab, M. A. Rodríguez, and A. Lahsini, "Synthesis of LTA zeolite for bacterial adhesion," *Bol. la Soc. Esp. Ceram. y Vidr.*, vol. 55, no. 4, pp. 152–158, 2016, doi: 10.1016/j.bsecv.2016.05.001.

[45] K. Muraoka, Y. Sada, D. Miyazaki, W. Chaikittisilp, and T. Okubo, "Linking synthesis and structure descriptors from a large collection of synthetic records of zeolite materials," *Nat. Commun.*, vol. 10, no. 1, pp. 1–11, Dec. 2019, doi: 10.1038/s41467-019-12394-0.

[46] G. Giannetto, "Zeolitas - Caracteristicas, Propiedades Y Aplicaciones Industriales," *Editor. Innovación Tecnológica*, pp. 3–163, 2000, Accessed: Jul. 11, 2021. [Online]. Available: https://books.google.com/books/about/Zeolitas.html?hl=es&id=xArCPAAACAAJ.

[47] "LTA: 3D Drawing." https://asia.iza-structure.org/IZA-SC/framework_3d.php?STC=LTA (accessed Jul. 04, 2021).

[48] "FAU: 3D Drawing." https://asia.iza-structure.org/IZA-SC/framework_3d.php?STC=FAU (accessed Jul. 04, 2021).

[49] R. K. Parsapur and P. Selvam, "Rational design, synthesis, characterization and catalytic properties of high-quality low-silica hierarchical FAU- and LTA-type zeolites," *Sci. Rep.*, vol. 8, no. 1, pp. 1–13, Dec. 2018, doi: 10.1038/s41598-018-34479-4.

[50] A. B. Djurišić, Y. H. Leung, and A. M. C. Ng, "Strategies for improving the efficiency of semiconductor metal oxide photocatalysis," *Mater. Horizons*, vol. 1, no. 4, pp. 400–410, Jun. 2014, doi: 10.1039/C4MH00031E.

[51] G. K. Upadhyay, J. K. Rajput, T. K. Pathak, V. Kumar, and L. P. Purohit, "Synthesis of ZnO:TiO2 nanocomposites for photocatalyst application in visible light," *Vacuum*, vol. 160, pp. 154–163, 2019, doi: 10.1016/j.vacuum.2018.11.026.

[52] K. Pengkalsinan, Z. Tio, and F. Melalui, "EFFECT OF CALCINATION TEMPERATURE ON ZnO / TIO 2 COMPOSITE IN PHOTOCATALYTIC TREATMENT OF PHENOL UNDER VISIBLE LIGHT," vol. 21, no. 1, pp. 173–181, 2017.

[53] M. Irani, T. Mohammadi, and S. Mohebbi, "Photocatalytic degradation of methylene blue with zno nanoparticles; a joint experimental and theoretical study," *J. Mex. Chem. Soc.*, vol. 60, no. 4, pp. 218–225, 2016, doi: 10.29356/jmcs.v60i4.115.

[54] B. Ozturk and G. S. P. Soylu, "Promoting role of transition metal oxide on ZnTiO3-TiO2 nanocomposites for the photocatalytic activity under solar light irradiation," *Ceram. Int.*, vol. 42, no. 9, pp. 11184–11192, 2016, doi: 10.1016/j.ceramint.2016.04.027.

[55] K. S. Stefańska *et al.*, "TiO 2 -ZnO Binary Oxide Systems : Comprehensive Characterization and Tests of Photocatalytic Activity," pp. 1–19, 2018, doi: 10.3390/ma11050841.

[56] C. Belver *et al.*, "Ag-Coated heterostructures of ZnO-TiO2/delaminated montmorillonite as solar photocatalysts," *Materials (Basel).*, vol. 10, no. 8, 2017, doi: 10.3390/ma10080960.

[57] I. Daou, O. Zegaoui, and A. Elghazouani, "Physicochemical and photocatalytic

properties of the ZnO particles synthesized by two different methods using three different precursors," *Comptes Rendus Chim.*, vol. 20, no. 1, pp. 47–54, 2017, doi: 10.1016/j.crci.2016.04.003.

[58] M. R. Delsouz Khaki, M. S. Shafeeyan, A. A. A. Raman, and W. M. A. W. Daud, "Enhanced UV–Visible photocatalytic activity of Cu-doped ZnO/TiO2 nanoparticles," *J. Mater. Sci. Mater. Electron.*, vol. 29, no. 7, pp. 5480–5495, 2018, doi: 10.1007/s10854-017-8515-9.

[59] H. Mohammadi and M. Ghorbani, "Synthesis photocatalytic TiO2/ZnO nanocomposite and investigation through anatase, wurtzite and ZnTiO3 phases antibacterial behaviors," *J. Nano Res.*, vol. 51, pp. 69–77, 2018, doi: 10.4028/www.scientific.net/JNanoR.51.69.

[60] H. Wang *et al.*, "Semiconductor heterojunction photocatalysts: Design, construction, and photocatalytic performances," *Chemical Society Reviews*, vol. 43, no. 15. Royal Society of Chemistry, pp. 5234–5244, Aug. 07, 2014, doi: 10.1039/c4cs00126e.

[61] S. J. Mofokeng, L. L. Noto, R. E. Kroon, O. M. Ntwaeaborwa, and M. S. Dhlamini, "Up-conversion luminescence and energy transfer mechanism in ZnTiO3: Er3+,Yb3+ phosphor," *J. Lumin.*, vol. 223, no. March, p. 117192, 2020, doi: 10.1016/j.jlumin.2020.117192.

[62] A. D. Bachvarova-Nedelcheva, R. S. Iordanova, A. M. Stoyanova, R. D. Gegova, Y. B. Dimitriev, and A. R. Loukanov, "Photocatalytic properties of ZnO/TiO2 powders obtained via combustion gel method," *Cent. Eur. J. Chem.*, vol. 11, no. 3, pp. 364–370, 2013, doi: 10.2478/s11532-012-0167-2.

[63] R. Liu, H. Ye, X. Xiong, and H. Liu, "Fabrication of TiO2/ZnO composite nanofibers by electrospinning and their photocatalytic property," *Mater. Chem. Phys.*, vol. 121, no. 3, pp. 432–439, Jun. 2010, doi: 10.1016/j.matchemphys.2010.02.002.

[64] K. S. Ranjith and T. Uyar, "ZnO-TiO2 composites and ternary ZnTiO3 electrospun nanofibers: the influence of annealing on the photocatalytic response and reusable functionality," *CrystEngComm*, vol. 20, no. 38, pp. 5801–5813, 2018, doi:

10.1039/c8ce00920a.

[65] A. Stoyanova, H. Hitkova, R. Iordanova, N. Ivanova, and M. Sredkova, "SYNTHESIS AND ANTIBACTERIAL ACTIVITY OF TiO 2 / ZnO NANOCOMPOSITES PREPARED VIA NONHYDROLYTIC ROUTE a) b)," pp. 154–161, 2013.

[66] C. Wattanawikkam, T. Kansa-ard, and W. Pecharapa, "X-ray absorption spectroscopy analysis and photocatalytic behavior of ZnTiO 3 nanoparticles doped with Co and Mn synthesized by sonochemical method," *Appl. Surf. Sci.*, vol. 474, pp. 169–176, 2019, doi: 10.1016/j.apsusc.2018.03.175.

[67] K. Saeed Baamran and M. Tahir, "Thermodynamic investigation and experimental analysis on phenol steam reforming towards enhanced H2 production over structured Ni/ZnTiO3 nanocatalyst," *Energy Convers. Manag.*, vol. 180, no. October 2018, pp. 796–810, 2019, doi: 10.1016/j.enconman.2018.10.099.

[68] M. Vishnu Chittan, C. Mani Kumar, and B. Rajesh Kumar, "X-ray Peak Profile Analysis and Microstructural Characterization of Solid State Sintered TiO2 doped ZnO Ceramics," *Mater. Today Proc.*, vol. 4, no. 2, pp. 2879–2886, 2017, doi: 10.1016/j.matpr.2017.02.168.

[69] R. Fu *et al.*, "Effect of different processes and Ti/Zn molar ratios on the structure, morphology, and enhanced photoelectrochemical and photocatalytic performance of Ti3+ self-doped titanium-zinc hybrid oxides," *J. Power Sources*, vol. 285, pp. 449–459, 2015, doi: 10.1016/j.jpowsour.2015.03.070.

[70] Y. Chi, Q. Yuan, S. Hou, and Z. Zhao, "Synthesis and characterization of mesoporous ZnTiO3 rods via a polyvinylpyrrolidone assisted sol-gel method," *Ceram. Int.*, vol. 42, no. 4, pp. 5094–5099, 2016, doi: 10.1016/j.ceramint.2015.12.024.

[71] R. S. Koster, C. M. Fang, M. Dijkstra, A. van Blaaderen, and M. A. van Huis, "Stabilization of Rock Salt ZnO Nanocrystals by Low-Energy Surfaces and Mg Additions: A First-Principles Study," *J. Phys. Chem. C*, vol. 119, no. 10, pp. 5648–5656, Mar. 2015, doi: 10.1021/JP511503B.

[72] Y. C. Cheng, X. L. Wu, J. Zhu, L. L. Xu, S. H. Li, and P. K. Chu, "Optical properties of

rocksalt and zinc blende AlN phases: First-principles calculations," *J. Appl. Phys.*, vol. 103, no. 7, p. 073707, Apr. 2008, doi: 10.1063/1.2903138.

[73] K. C. . L. Khang, M. H. M. Hatta, S. L. Lee, and L. Yuliati, "Photocatalytic removal of phenol over mesoporous ZnO/TiO2 composites," *J. Teknol.*, vol. 2, no. 80, pp. 153–160, 2018, doi: 10.11113/jt.v80.11209.

[74] I. Daou, R. Chfaira, O. Zegaoui, Z. Aouni, and H. Ahlafi, "Physico-Chemical Characterization and Interfacial Electrochemical Properties of Nanoparticles of Anatase-TiO2 Prepared by the Sol-Gel Method," *Mediterr. J. Chem.*, vol. 2, no. 4, pp. 569–582, 2013.

[75] J. Moellmann, S. Ehrlich, R. Tonner, and S. Grimme, "A DFT-D study of structural and energetic properties of TiO2 modifications," *J. Phys. Condens. Matter*, vol. 24, no. 42, p. 424206, Oct. 2012, doi: 10.1088/0953-8984/24/42/424206.

[76] L. E. Oi, M.-Y. Choo, H. V. Lee, H. C. Ong, S. B. A. Hamid, and J. C. Juan, "Recent advances of titanium dioxide (TiO2) for green organic synthesis," *RSC Adv.*, vol. 6, no. 110, pp. 108741–108754, Nov. 2016, doi: 10.1039/C6RA22894A.

[77] J. Wang, W. Mi, J. Tian, J. Dai, X. Wang, and X. Liu, "Effect of calcinations of TiO2/ZnO composite powder at high temperature on photodegradation of methyl orange," *Compos. Part B Eng.*, vol. 45, no. 1, pp. 758–767, 2013, doi: 10.1016/j.compositesb.2012.09.053.

[78] J. Lee, H. Ahn, J. Youn, Y. Kim, S. Suh, and H. Oh, "Synthesis and Characterization of ZnO / TiO 2 Photocatalyst Decorated with PbS QDs for the Degradation of Aniline Blue Solution," vol. 56, no. 12, pp. 900–909, 2018, doi: 10.3365/KJMM.2018.56.12.900.

[79] Y. Du and J. Rabani, "The Measure of TiO2 Photocatalytic Efficiency and the Comparison of Different Photocatalytic Titania," *J. Phys. Chem. B*, vol. 107, no. 43, pp. 11970–11978, Oct. 2003, doi: 10.1021/jp035491z.

[80] J. Ryu and W. Choi, "Substrate-specific photocatalytic activities of TiO2 and multiactivity test for water treatment application," *Environ. Sci. Technol.*, vol. 42, no. 1, pp. 294–300, Jan. 2008, doi: 10.1021/es071470x.

[81] C. Karunakaran, G. Abiramasundari, P. Gomathisankar, G. Manikandan, and V. Anandi, "Preparation and characterization of ZnO–TiO2 nanocomposite for photocatalytic disinfection of bacteria and detoxification of cyanide under visible light," *Mater. Res. Bull.*, vol. 46, no. 10, pp. 1586–1592, Oct. 2011, doi: 10.1016/J.MATERRESBULL.2011.06.019.

[82] H. Chorf, M. Saadoun, L. Bousselmi, and B. Bessais, "TiO2-ITO and TiO2-ZnO nanocomposites: Application on water treatment," in *EPJ Web of Conferences*, 2012, vol. 29, doi: 10.1051/epjconf/20122900015.

[83] G. Lakshminarayana, J. Qiu, M. G. Brik, G. A. Kumar, and I. V. Kityk, "Spectral analysis of Er3+-, Er3+/Yb3+- and Er3+/Tm3+/Yb3+-doped TeO2-ZnO- WO3-TiO2-Na2O glasses," *J. Phys. Condens. Matter*, vol. 20, no. 37, Sep. 2008, doi: 10.1088/0953-8984/20/37/375101.

[84] C. Yu, W. Zhou, H. Liu, Y. Liu, and D. D. Dionysiou, "Design and fabrication of microsphere photocatalysts for environmental purification and energy conversion," *Chemical Engineering Journal*, vol. 287. Elsevier, pp. 117–129, Mar. 01, 2016, doi: 10.1016/j.cej.2015.10.112.

[85] M. Pérez-González, S. A. Tomás, M. Morales-Luna, M. A. Arvizu, and M. M. Tellez-Cruz, "Optical, structural, and morphological properties of photocatalytic TiO2-ZnO thin films synthesized by the sol-gel process," in *Thin Solid Films*, Nov. 2015, vol. 594, pp. 304–309, doi: 10.1016/j.tsf.2015.04.073.

[86] X. Zheng *et al.*, "Construction of ZnO/TiO2 photonic crystal heterostructures for enhanced photocatalytic properties," *Appl. Catal. B Environ.*, vol. 168–169, pp. 408–415, Jun. 2015, doi: 10.1016/J.APCATB.2015.01.001.

[87] E. Koufakis, G. N. Mathioudakis, A. C. Patsidis, and G. C. Psarras, "ZnTiO3/epoxy resin nanocomposites: Development, dielectric behaviour and functionality," *Polym. Test.*, vol. 77, no. April, 2019, doi: 10.1016/j.polymertesting.2019.04.017.

[88] Y. C. Lee and P. S. Chen, "Effect of Cu dopant on microstructure and phase transformation of ZnTiO 3 thin films prepared by radio frequency magnetron

sputtering," *Thin Solid Films*, vol. 520, no. 7, pp. 2672–2678, 2012, doi: 10.1016/j.tsf.2011.11.035.

[89] M. Lee, A. Y. Mohamed, D. Kim, D. H. Kim, T. J. Park, and D. Y. Cho, "Identification of ZnTiO3 nanostructures in oxidized TiN/ZnS thin films using X-ray absorption spectroscopy," *Appl. Surf. Sci.*, vol. 494, no. December 2018, pp. 63–71, 2019, doi: 10.1016/j.apsusc.2019.07.188.

[90] M. T. Thein, S.-Y. Pung, A. Aziz, and M. Itoh, "The role of ammonia hydroxide in the formation of ZnO hexagonal nanodisks using sol–gel technique and their photocatalytic study," *J. Exp. Nanosci.*, vol. 10, no. 14, pp. 1068–1081, Sep. 2015, doi: 10.1080/17458080.2014.953609.

[91] M. Jose, M. Elakiya, and S. A. M. B. Dhas, "Structural and optical properties of nanosized ZnO/ZnTiO3 composite materials synthesized by a facile hydrothermal technique," *J. Mater. Sci. Mater. Electron.*, vol. 28, no. 18, pp. 13649–13658, 2017, doi: 10.1007/s10854-017-7207-9.

[92] L. Al-Hajji, "A Comparative Study on the Zinc Metatitanate Microstructure by Ball Milling and Solvothermal Approaches," *J. Struct. Chem.*, vol. 60, no. 5, pp. 830–837, May 2019, doi: 10.1134/S0022476619050172.

[93] M. Salavati-Niasari, F. Soofivand, A. Sobhani-Nasab, M. Shakouri-Arani, A. Yeganeh Faal, and S. Bagheri, "Synthesis, characterization, and morphological control of ZnTiO3 nanoparticles through sol-gel processes and its photocatalyst application," *Adv. Powder Technol.*, vol. 27, no. 5, pp. 2066–2075, 2016, doi: 10.1016/j.apt.2016.07.018.

[94] J. Lu *et al.*, "Rational design and preparation of nanoheterostructures based on zinc titanate for solar-driven photocatalytic conversion of CO2 to valuable fuels," *Appl. Catal. B Environ.*, vol. 256, no. May, pp. 2–11, 2019, doi: 10.1016/j.apcatb.2019.117800.

[95] Y. H. Yu and M. Xia, "Preparation and characterization of ZnTiO 3 powders by sol-gel process," *Mater. Lett.*, vol. 77, pp. 10–12, 2012, doi: 10.1016/j.matlet.2012.02.113.

[96] P. K. Jain, M. Salim, and D. Kaur, "Effect of phase transformation on optical and dielectric properties of pulsed laser deposited ZnTiO3 thin films," *Superlattices*

Microstruct., vol. 92, pp. 308–315, 2016, doi: 10.1016/j.spmi.2016.02.018.

[97] L. Budigi, M. R. Nasina, K. Shaik, and S. Amaravadi, "Structural and optical properties of zinc titanates synthesized by precipitation method," *J. Chem. Sci.*, vol. 127, no. 3, pp. 509–518, 2015, doi: 10.1007/s12039-015-0802-5.

[98] E. Li, P. Zhang, S. Duan, J. Wang, Y. Yuan, and B. Tang, "Low temperature sintering of low-loss ZnTiO3 microwave dielectric ceramics with Zn-B-Si glass," *J. Alloys Compd.*, vol. 647, pp. 866–872, 2015, doi: 10.1016/j.jallcom.2015.06.172.

[99] N. T. Nolan, M. K. Seery, and S. C. Pillai, "Crystallization and phase-transition characteristics of sol-gel-synthesized zinc titanates," *Chem. Mater.*, vol. 23, no. 6, pp. 1496–1504, 2011, doi: 10.1021/cm1031688.

[100] I. Bobowska, A. Opasińska, A. Wypych, and P. Wojciechowski, "Synthesis and dielectric investigations of ZnTiO 3 obtained by a soft chemistry route," *Mater. Chem. Phys.*, vol. 134, no. 1, pp. 87–92, 2012, doi: 10.1016/j.matchemphys.2012.02.033.

[101] Y. Inaguma *et al.*, "High-pressure synthesis, crystal structure, and phase stability relations of a LiNbO3-type polar titanate ZnTiO3 and its reinforced polarity by the second-order Jahn-Teller effect," *J. Am. Chem. Soc.*, vol. 136, no. 7, pp. 2748–2756, Feb. 2014, doi: 10.1021/ja408931v.

[102] H. JIANG and Y. ZHANG, "Ethanol sensing properties of Bi3.15Nd0.85Ti3O12 films at low operating temperatures," *Trans. Nonferrous Met. Soc. China (English Ed.*, vol. 26, no. 12, pp. 3189–3195, 2016, doi: 10.1016/S1003-6326(16)64451-5.

[103] T. Farahmand, S. Hashemian, and A. Sheibani, "Efficient one-pot synthesis of pyrano[2,3-d]pyrimidinone and pyrido [2,3-d] pyrimidine derivatives by using of Mn-ZIF-8@ZnTiO3 nanocatalyst," *J. Mol. Struct.*, vol. 1206, p. 127667, 2020, doi: 10.1016/j.molstruc.2019.127667.

[104] H. Eskandarloo, A. Badiei, M. A. Behnajady, A. Tavakoli, and G. M. Ziarani, "Ultrasonic-assisted synthesis of Ce doped cubic-hexagonal ZnTiO3 with highly efficient sonocatalytic activity," *Ultrason. Sonochem.*, vol. 29, pp. 258–269, 2016, doi: 10.1016/j.ultsonch.2015.10.004.

[105] P. Zhang *et al.*, "Bi 2MoO 6 ultrathin nanosheets on ZnTiO 3 nanofibers: A 3D open hierarchical heterostructures synergistic system with enhanced visible-light-driven photocatalytic activity," *J. Hazard. Mater.*, vol. 217–218, pp. 422–428, 2012, doi: 10.1016/j.jhazmat.2012.03.046.

[106] M. C. Han, J. H. Zhang, P. Cui, Y. R. Zhu, and T. F. Yi, "Construction of spherical ZnTiO3/MWCNTs composites as anode material for high-performance Li-ion batteries," *Sustain. Mater. Technol.*, vol. 25, p. e00207, 2020, doi: 10.1016/j.susmat.2020.e00207.

[107] T. Zhong, W. Zhao, F. Jiang, and X. Liang, "Toluene sensor combining NASICON with ZnTiO3 electrode," *Sensors Actuators, B Chem.*, vol. 202, pp. 1103–1108, 2014, doi: 10.1016/j.snb.2014.06.073.

[108] X. Liu, "Molten salt synthesis of ZnTiO 3 powders with around 100 nm grain size crystalline morphology," *Mater. Lett.*, vol. 80, pp. 69–71, 2012, doi: 10.1016/j.matlet.2012.04.048.

[109] Y. L. Chai, Y. S. Chang, K. T. Liu, and L. G. Teoh, "The structure and PTCR effects of Mg-doped ZnTiO 3 ceramics," *Ceram. Int.*, vol. 38, no. 5, pp. 3613–3618, 2012, doi: 10.1016/j.ceramint.2011.12.078.

[110] T. Bernert, J. Ruiz-Fuertes, L. Bayarjargal, and B. Winkler, "Synthesis and high (pressure, temperature) stability of ZnTiO3 polymorphs studied by Raman spectroscopy," *Solid State Sci.*, vol. 43, pp. 53–58, 2015, doi: 10.1016/j.solidstatesciences.2015.03.014.

[111] Y. Yan, H. Gao, J. Tian, F. Tan, H. Zheng, and W. Zhang, "Ferromagnetic Enhancement in ZnTiO 3 films induced by Co doping," *Ceram. Int.*, vol. 45, no. 9, pp. 11309–11315, 2019, doi: 10.1016/j.ceramint.2019.02.208.

[112] S. J. Mofokeng, L. L. Noto, and M. S. Dhlamini, "Photoluminescence properties of ZnTiO3:Eu3+ phosphor with enhanced red emission by Al3+ charge compensation," *J. Lumin.*, vol. 228, no. July, p. 117569, 2020, doi: 10.1016/j.jlumin.2020.117569.

[113] J. Zhang, B. Xu, Y. S. Wang, Z. Qin, and S. H. Ke, "First-principles investigation of the

ferroelectric, piezoelectric and nonlinear optical properties of LiNbO3-type ZnTiO3," *Sci. Rep.*, vol. 9, no. 1, pp. 1–14, 2019, doi: 10.1038/s41598-019-53986-6.

[114] J. Ruiz-Fuertes *et al.*, "Ferroelectric soft mode of polar ZnTiO3 investigated by Raman spectroscopy at high pressure," *Phys. Rev. B - Condens. Matter Mater. Phys.*, vol. 91, no. 21, 2015, doi: 10.1103/PhysRevB.91.214110.

[115] C. Bao *et al.*, "A signal-off type photoelectrochemical immunosensor for the ultrasensitive detection of procalcitonin: Ru(bpy)32+ and Bi2S3 co-sensitized ZnTiO3/TiO2 polyhedra as matrix and dual inhibition by SiO2/PDA-Au," *Biosens. Bioelectron.*, vol. 142, no. May, 2019, doi: 10.1016/j.bios.2019.111513.

[116] I. Udom *et al.*, "Optimization of Photocatalytic Degradation of Phenol Using Simple Photocatalytic Reactor," *Am. J. Anal. Chem.*, vol. 05, no. 11, pp. 743–750, Aug. 2014, doi: 10.4236/ajac.2014.511083.

[117] Y.-L. Chai, Y.-S. Chang, G.-J. Chen, and Y.-J. Hsiao, "The effects of heat-treatment on the structure evolution and crystallinity of ZnTiO3 nano-crystals prepared by Pechini process," *Mater. Res. Bull.*, vol. 43, no. 5, pp. 1066–1073, May 2008, doi: 10.1016/J.MATERRESBULL.2007.06.002.

[118] X. Chen and S. S. Mao, "Titanium Dioxide Nanomaterials : Synthesis , Properties , Modifications , and Applications," 2007, doi: 10.1021/cr0500535.

[119] K. R. M. Macedo, G. A. C. Oliveira, K. A. B. Pereira, L. C. Mendes, A. S. Araújo, and R. J. Cassella, "Titanium-zinc polycitrate precursor: Influence of thermal treatment on structural, thermal, optical characteristics of zinc titanates," *Mater. Chem. Phys.*, vol. 236, no. May, p. 121768, 2019, doi: 10.1016/j.matchemphys.2019.121768.

[120] Z. Zhang, L. Hu, H. Zhang, L. Yu, and Y. Liang, "Large-sized nano-TiO2/SiO2 mesoporous nanofilmconstructed macroporous photocatalysts with excellent photocatalytic performance," *Front. Mater. Sci.*, vol. 14, no. 2, pp. 163–176, Jun. 2020, doi: 10.1007/s11706-020-0506-8.

[121] K. Sahel *et al.*, "Photocatalytic degradation of anionic and cationic dyes over TiO2 P25, and Ti-pillared clays and Ag-doped Ti-pillared clays," *Appl. Clay Sci.*, vol. 95, pp. 205–

210, Jun. 2014, doi: 10.1016/j.clay.2014.04.014.

[122] F. Akhtar, L. Andersson, S. Ogunwumi, N. Hedin, and L. Bergström, "Structuring adsorbents and catalysts by processing of porous powders," *J. Eur. Ceram. Soc.*, vol. 34, no. 7, pp. 1643–1666, 2014, doi: 10.1016/j.jeurceramsoc.2014.01.008.

[123] C. Belver, J. Bedia, and J. J. Rodriguez, "Applied Catalysis B : Environmental Titania – clay heterostructures with solar photocatalytic applications," *"Applied Catal. B, Environ.*, vol. 176–177, pp. 278–287, 2015, doi: 10.1016/j.apcatb.2015.04.004.

[124] M. Akkari, P. Aranda, H. Ben Rhaiem, A. Ben Haj, and E. Ruiz-Hitzky, "ZnO/clay nanoarchitectures: Synthesis , characterization and evaluation as photocatalysts," *Appl. Clay Sci.*, pp. 1–9, 2015, doi: doi.org/10.1016/j.tsf.2011.08.095.

[125] K. Rajeshwar and W. Chanmanee, "Bioinspired photocatalyst assemblies for environmental remediation," *Electrochim. Acta*, vol. 84, pp. 96–102, Dec. 2012, doi: 10.1016/j.electacta.2012.04.072.

[126] J. Liu and G. Zhang, "Recent advances in synthesis and applications of clay-based photocatalysts: A review," *Physical Chemistry Chemical Physics*, vol. 16, no. 18. Royal Society of Chemistry, pp. 8178–8192, May 14, 2014, doi: 10.1039/c3cp54146k.

[127] G. T. Whiting, A. D. Chowdhury, R. Oord, P. Paalanen, and B. M. Weckhuysen, "The curious case of zeolite–clay/binder interactions and their consequences for catalyst preparation," *Faraday Discuss.*, vol. 188, no. 0, pp. 369–386, Jul. 2016, doi: 10.1039/C5FD00200A.

[128] E. G. Lewars, *Computational chemistry: Introduction to the theory and applications of molecular and quantum mechanics*. Springer Netherlands, 2011.

[129] R. J. Boyd, "Theoretical and Computational Chemistry," in *Reference Module in Chemistry, Molecular Sciences and Chemical Engineering*, Elsevier, 2019.

[130] I. B. Djordjevic, "Quantum Mechanics Fundamentals," in *Quantum Information Processing, Quantum Computing, and Quantum Error Correction*, Elsevier, 2021, pp. 31–95.

[131] J. Morrison, "The Schrödinger wave equation," in *Modern Physics with Modern*

Computational Methods, Elsevier, 2021, pp. 19–36.

[132] A. Popa, "Connection Between Schrődinger and Hamilton–Jacobi Equations in the Case of Stationary Atomic and Molecular Systems," in *Theory of Quantum and Classical Connections in Modeling Atomic, Molecular and Electrodynamical Systems*, Elsevier, 2014, pp. 1–21.

[133] C. Yu, N. Fu, C. Dai, H. Wang, G. Zhang, and J. Yao, "Time-dependent Born-Oppenheimer approximation approach for Schrödinger equation: Application to H2+," *Opt. Commun.*, vol. 300, pp. 199–203, Jul. 2013, doi: 10.1016/j.optcom.2013.02.056.

[134] S. M. Blinder, "Introduction to the hartree-fock method," in *Mathematical Physics in Theoretical Chemistry*, Elsevier, 2018, pp. 1–30.

[135] J. B. Condon, "Density functional theory (DFT)," in *Surface Area and Porosity Determinations by Physisorption*, Elsevier, 2020, pp. 335–360.

[136] Y. A. Wang and P. Xiang, "From the Hohenberg-Kohn Theory to the Kohn-Sham Equations," 2013, pp. 3–12.

[137] S. Śmiga, A. Buksztel, and I. Grabowski, "Density-Dependent Exchange-Correlation potentials derived from highly accurate Ab initio calculations," in *Advances in Quantum Chemistry*, vol. 68, Academic Press Inc., 2014, pp. 125–151.

[138] V. N. Staroverov and E. Ospadov, "Unified construction of Fermi, Pauli and exchange-correlation potentials," in *Advances in Quantum Chemistry*, vol. 79, Academic Press Inc., 2019, pp. 201–219.

[139] J. Andrés Bort and J. Beltrán Comulada, *Química teórica y computacional*, 1st ed. Universitat Jaume I. Servei de Comunicació i Publicacions, 2001.

[140] J. P. Perdew, K. Burke, and M. Ernzerhof, "Generalized gradient approximation made simple," *Phys. Rev. Lett.*, vol. 77, no. 18, pp. 3865–3868, Oct. 1996, doi: 10.1103/PhysRevLett.77.3865.

[141] I. Levine, *Physical Chemistry*. Brooklyn, New York: McGraw-Hill, 2001.

[142] A. R. Tackett, N. A. W. Holzwarth, and G. E. Matthews, "A Projector Augmented

Wave (PAW) code for electronic structure calculations, Part II: pwpaw for periodic solids in a plane wave basis," *Comput. Phys. Commun.*, vol. 135, no. 3, pp. 348–376, Apr. 2001, doi: 10.1016/S0010-4655(00)00241-1.

CHAPTER 3

SYNTHESIS OF THE $ZnTiO_3$/TiO_2 NANOCOMPOSITE SUPPORTED IN ECUADORIAN CLAYS FOR THE ADSORPTION AND PHOTOCATALYTIC REMOVAL OF METHYLENE BLUE DYE

3.1. Introduction

The presence of pollutants in wastewater has a dangerous potential impact on the environment and on health. In fact, water and wastewater treatment is a major problem in our society [1]. Several industries use large amounts of dyes for their end-products. For instance, the textile industry uses more than 10,000 types of dyes. This industry discharges 2% to 20% of its dyes as aqueous effluents [2]. Many of these substances are not biodegradable and pollute the aquatic environment [3], and some of them have a carcinogenic effect [4]. Hence, it is necessary to treat the effluents before discarding them.

There are several technological processes to remove persistent pollutants from water [1,5–8]. Among these processes, photocatalysis is appreciated for its effectivity [9,10]. Photocatalysis is an Advanced Oxidation Process (AOP) that requires a semiconductor [11] that interacts with photons and the adsorbed composite through surface charges. The interaction produces radical species that decompose the adsorbed composite through redox reactions [12].

Titanium dioxide (TiO_2) is a widely used semiconductor for photocatalytic applications. TiO_2 has low toxicity, low cost, is chemically stable, and is an excellent oxidant [13]. TiO_2 is a photocatalyst with a band gap value of 3–3.2 eV, which depends on its crystalline structure. Furthermore, TiO_2 is interesting due to its efficiency in wastewater treatment [14].

On the one hand, TiO_2 is the most popular photocatalyst; nevertheless, it has low sensitivity to the visible light spectrum. On the other hand, zinc oxide (ZnO) is also inexpensive, but has high activity as a photocatalyst in visible light [15]. This oxide has a band gap energy (3.2 eV) similar to that of TiO_2. Both oxides can improve their own photocatalytic activity through TiO_2-ZnO coupling [16]. This improvement is due to a reduced recombination of electron holes. Besides, the greater migration of photogenerated carriers also improves this activity [17].

Synthesis using the sol-gel method of coupled ZnO-TiO_2 [18] can generate some Ti-Zn mixed oxides, such as Zn_2TiO_4, $Zn_2Ti_3O_8$, and $ZnTiO_3$, among the main derived products [19,20]. Some impurity phases can also appear in the final products [21,22]. During the synthesis, the transformation of the crystalline phases presents different products, which depend on the initial molar ratio of the reactants and the calcination temperatures. The presence of anatase and rutile can also affect the behavior of the phases [23].

Ti-Zn mixed oxides are low-cost materials and harmless to the environment [21]. These materials are important due to their technological applications [24]. Ti-Zn mixed oxides can act as pigments, photodetectors, dielectric materials, sensors, and light emitting diodes [25]. Several studies also show their wide use for the photocatalytic decomposition of organic compounds since their band gap has a value of 3.06 eV [26–29].

Although the use of photocatalysts is an interesting alternative for wastewater treatment, their recovery at the process-end limits their practical use. The structured supports offer an alternative to keep the photocatalyst on its surface [30]. Thus, the separation stage becomes unnecessary. The literature shows various materials that serve as supports [31]. Among them are silica, ash, zeolites, active carbon, and clays [32,33]. Clays and materials derived from clay represent a potential alternative. These materials have high chemical and mechanical stability [34]. Besides, they have a great adsorption capacity due to their high surface area [35]. Clays are low-cost materials and offer an interesting route to revalue local resources [36].

The present study reports the synthesis of the $ZnTiO_3/TiO_2$ composite supported in several Ecuadorian natural clays, as well as its efficiency in the adsorption and photocatalytic degradation of methylene blue (MB) in aqueous effluents. The adsorption and photocatalytic degradation of methylene blue were determined by the decolorization of the dye and were quantified by UV-Visible spectrophotometry. The synthesized composites were characterized using X-Ray Diffractometry (XRD), X-Ray Fluorescence (XRF), Diffuse Reflectance Spectroscopy (DRS), and Scanning Electron Microscopy (SEM) techniques.

3.2. Materials and Methods

3.2.1. Materials

All of the reagents used in this study were of analytical grade and used without additional purification: C_3H_8O (Sigma Aldrich, St. Louis, MO, USA, ≥99.5%), $Ti(OC_3H_7)_4$ (Sigma Aldrich, 98%), CH_3COOH (Sigma Aldrich, 99.8%), HCl (Fisher Scientific, Waltham, MA, USA, 37%), cetyl-trimethyl ammonium chloride ($C_{19}H_{42}NCl$) (Sigma Aldrich, 25%), H_2O_2 (Sigma Aldrich, 35%), $AgNO_3$ (Sigma Aldrich, >99.8%), HNO_3 (Sigma Aldrich, 69%), $Zn(CH_3COO)_2{\cdot}2H_2O$ (ACS, St. Louis, MO, USA, ≥98%), and $C_{16}H_{18}ClN_3S{\cdot}nH_2O$ (Sigma Aldrich, ≥95%).

3.2.2. Clay Purification

The raw clays were collected from southern Ecuador. The clay samples were ground and sieved to No. 200 ASTM mesh (0.075 mm size). Carbonates of magnesium and calcium were removed using a hydrochloric acid solution (0.1 N) at the ratio of 10 mL/g. The organic matter in the clay samples was removed by oxidation using H_2O_2 (33%) in the proportion of 10 mL of H_2O_2 for each gram of clay. The samples were constantly stirred for 2 h at room temperature. Subsequently, the samples were centrifuged and washed with distilled water to eliminate Cl^- ions, which was verified with a test with $AgNO_3$. The clay adsorption sites were activated with nitric acid (0.8 N) using a ratio of 10 mL/g. Activation is a process through which a partially dissolved material is obtained, which has greater surface acidity, porosity, and surface area [37]. The activated clay samples were centrifuged, washed with distilled water, and dried at 60 °C for 24 h.

3.2.3. Synthesis of the $ZnTiO_3/TiO_2$-Clay Composite

The $ZnTiO_3/TiO_2$ photocatalysts were synthesized following a modified sol-gel method described for other nanocomposites [38,39]. Several TiO_2/ZnO molar ratios were tested (9:1, 4:1, 3:1, and 2:1). Different calcination temperatures (500, 600, 700, 800, 900, and 1000 °C) were also tested to obtain the optimal photocatalyst synthesis conditions. Afterwards, the synthesis process was repeated in a clay solution as follows: Clay (1 g) was dispersed in isopropyl alcohol (iPrOH) (10 *w*/*w*%) under stirring for 24 h to achieve homogenous solution. Subsequently, a quantity of titanium (IV) isopropoxide (TiPO) in iPrOH (70 *v*/*v*%) was added to the solution at room temperature, using a ratio of 10.5 mmol of Ti per gram of clay. Previously, a solution formed by Zn(acet), water, and iPrOH was slowly added, using the optimal ZnO/TiO_2 molar ratio. The amount of water had a 50 *v*/*v*% iPrOH/water ratio and was determined by stoichiometry, being the amount necessary to hydrolyze the TiPO molecules. The synthesis was performed at room temperature. The reaction system was additionally stirred for 30 min. The mixture was kept under stirring at room temperature for another 30 min after the formation of a precipitate. The precipitate was dried at 60 °C for 24 h and calcined at the optimum temperature for 4 h. Finally, the products were cooled at room temperature. To obtain clay supported TiO_2, the procedure described above was repeated for a final ratio of 10.5 mmol Ti per gram of clay but without the addition of ZnO.

3.2.4. Preparation of the Supported Photocatalysts

For the evaluation of the solid materials, cylindrical extrudates with approximate dimensions of 0.2 cm in diameter and 1.0 cm in length were prepared. The preparation of these solids was carried out by mixing the solid materials with water (approximately 35%) to form a mixture with good plasticity. This mixture was extruded with a 2.5 mm diameter syringe. The extrudates were dried at 90 °C for 2 h and finally calcined at 500 °C for 8 h.

3.2.5. Characterization

The synthetized materials were characterized using a JEOL JSM 6400 scanning electron microscope (SEM) (JEOL, Peabody, MA, USA). X-Ray Fluorescence (XRF) measurements were recorded in a Bruker S1 Turbo SDR portable spectrometer (Bruker Handheld LLC, Kennewick, WA, USA), using the Mining Light Elements measurement method. The X-ray diffraction (XRD) measurements were recorded in a Bruker-AXS D8-Discover diffractometer (Bruker AXS, Karlsruhe, Germany) equipped with a vertical θ-θ goniometer, a parallel incident beam (Göbel mirror), and a HI-STAR General Area Diffraction Detection System (GADDS) (Bruker AXS, Karlsruhe, Germany). The X-ray diffractometer was operated at 40 kV and 40 mA to produce the Cu Kα radiation (1.5406 Å). Data were recorded from 5–70° in the 2θ range. The identification of the crystal phases was obtained by comparison of the XRD profile with the ICDD (International Centre for Diffraction Data, release 2018) database. The determination of the specific surface area of the solids (m^2/g) was carried out in the ChemiSorb 2720 equipment (Micromeritics, Norcross, GA, USA), by nitrogen adsorption at the temperature of liquid nitrogen (−196 °C) with a 30% gas mixture of N_2 diluted in He. UV-Vis diffuse reflectance spectrum (DRS) of the photocatalysts were obtained on an UV-Vis spectrophotometer Thermo model: Nicolet Evolution 201/220 (ThermoFisher, Waltham, MA, USA), equipped with an integration sphere unit using $BaSO_4$ as reference. The Chemisoft TPx System (version 1.03; Data analysis software; Micromeritics, Norcross, GA, USA, 2011) allowed to calculate the specific surface area using the BET equation and the single point method.

3.2.6. Adsorption and Photocatalytic Degradation

Heterogeneous photocatalysis experiments were firstly performed at free pH = 8.0 during 150 min, varying the methylene blue solution concentrations (50, 25, 10, and 5 mg/L) and catalyst concentrations (100, 250, and 500 mg/L). In addition, the effect of the ZnO:TiO_2 molar ratio was examined to select the best catalyst. All the experiments were started with a 30 min adsorption step under dark conditions to obtain the adsorption-desorption equilibrium.

The photocatalytic activity of the compounds was evaluated by the photocatalytic degradation of methylene blue under solar light radiation. Solar light was simulated by a solar box equipped with an air-cooled 1500-W Xenon lamp (Atlas Material Testing Technology, Mount Prospect, Il, USA), which allows 300–800 nm wavelengths to pass through (ATLAS, SUNTEST CPS+). Irradiance was set to 250 W/m^2. The photocatalytic activity of the compounds was also evaluated by the decolorization of methylene blue under UV-C (254 nm) light radiation to improve the photocatalytic degradation of MB [40].

Typically, 25 mg of catalyst were magnetically stirred in a methylene blue aqueous solution (MB) (100 mL of water containing 5 mg/L methylene blue). The solution was maintained in dark conditions for 30 min. Then, the suspensions were irradiated using solar or UV-C light (100 W germicidal UV-C). The temperature of the photoreactor (25 °C) was controlled throughout the reaction using a cooling circulator air system. The tests were carried out without adjusting the pH = 8.0. The remaining concentrations of methylene blue were determined at 623 nm using a Jenway 7350 spectrophotometer (Cole-Parmer, Staffordshire, UK). The MB removal rate was calculated by absorbance according to the Beer–Lambert law. Samples were drawn at 5 min intervals with a syringe and filtered through a 0.45 μm membrane filter to remove any solid particles interfering with the measurement. All tests were carried out in triplicate using a methylene blue solution blank irradiated with solar or UV-C light to eliminate any photolysis effect due to the light. The decolorization rate was better when using UV-C light for the selected operating conditions; in this way, the tests with the photocatalysts supported on clays were carried out under UV-C light.

The adsorption capacity of the synthetized materials was evaluated by the removal of methylene without light irradiation, using the same protocol that was used during the photocatalytic test.

3.2.7. Reuse of the Supported Photocatalysts

A recycle experiment on photocatalytic degradation of MB by $ZnTiO_3/TiO_2$-Clay, and TiO_2/Clay was designed to determine the recycling property of these composites. After completing a treatment cycle, the catalysts extrudates were left in quiescent conditions for 60 min to achieve their precipitate. Then, the clear solution was removed from the reaction system and 100 mL fresh MB solution (5 mg/L) was injected into the reaction system, starting the next cycle. The recycle experiment was carried out for five cycles. Each cycle lasted 150 min under UV-C irradiation.

3.3. Results

3.3.1. Characterization of the Samples

3.3.1.1. XRD Analysis

Figure 3.1 shows Ti-Zn mixed oxides synthesized at 500 °C with different TiO_2/ZnO molar ratios. The diffraction peaks of $ZnTiO_3$ at 2θ values of 23.92°, 32.79°, 35.31°, 40.45°, 48.93°, 53.44°, 56.82°, 61.79°, and 63.39° which are assigned to planes (0 1 2), (1 0 4), (1 1 0), (1 1 3), (0 2 4), (1 1 6), (0 1 8), (2 1 4), and (3 0 0), respectively. Similarly, the diffraction peaks of anatase ($TiO_{2\text{-}a}$) at 2θ values of 25.28°, 36.95°, 37.80°, 38.58°, 48.05°, 53.89°, 55.06°, 62.12°, 62.69°, and 68.76° are assigned to planes (1 0 1), (1 0 3), (0 0 4), (1 1 2), (2 0 0), (1 0 5), (2 1 1), (2 1 3), (2 0 4), and (1 1 6), respectively. Finally, the diffraction peaks of rutile ($TiO_{2\text{-}r}$) at 2θ values of 27.45°, 36.09°, 41.23°, 54.32°, 56.64°, and 69.01° are assigned to planes (1 1 0), (1 0 1), (1 1 1), (2 1 1), (2

2 0), and (3 0 1), respectively. The $ZnTiO_3$-TiO_2 heterostructure nanomaterial obtained was indexed to an hexagonal phase with unit cell parameters *a* = *b* = 5.08 Å and *c* = 13.93 Å, and space group R-3(148) according to the standard JCPDS card No. 00-015-0591 for the $ZnTiO_3$ phase. The $TiO_{2\text{-}a}$ species was indexed to a tetragonal phase with unit cell parameters *a* = *b* = 3.79 Å and *c* = 9.51 Å, and space group I41/amd(141) according to the standard JCPDS card No. 01-073-1764, and the $TiO_{2\text{-}r}$ phase was assigned to a tetragonal phase with unit cell parameters *a* = *b* = 5.08 Å and *c* = 13.93 Å, and space group P42/mnm(136) according to the standard JCPDS card No. 03-065-0192.

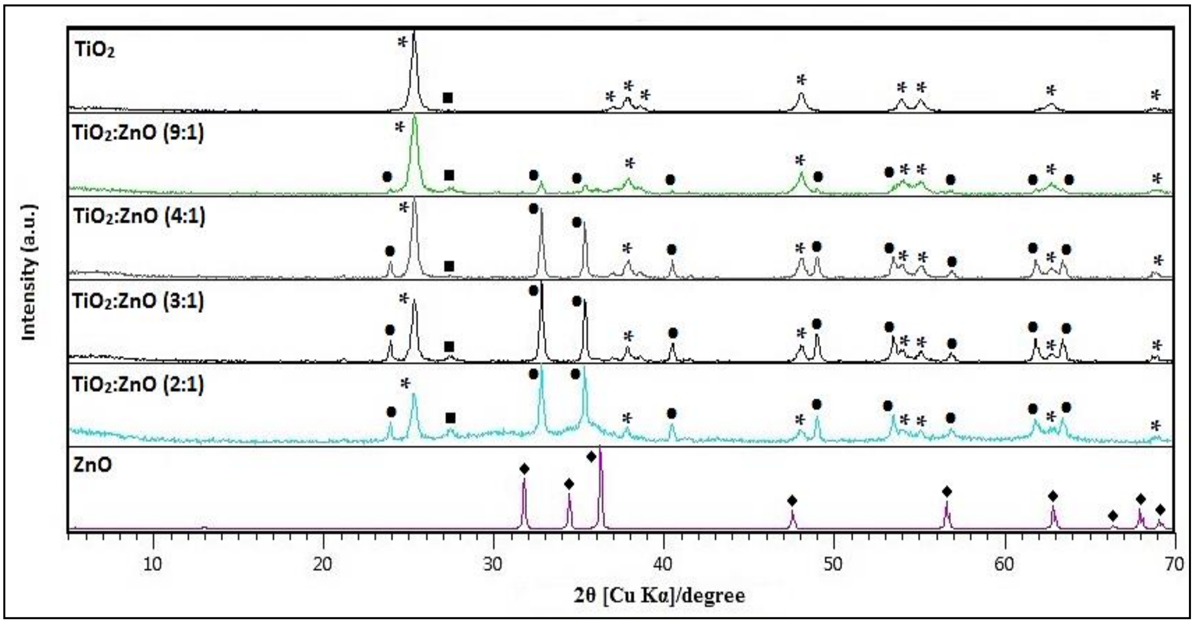

Figure 3. 1. X-Ray Diffractometry (XRD) of $ZnTiO_3/TiO_2$ synthesized at 500 °C with different TiO_2/ZnO molar ratios. *: $TiO_{2\text{-}a}$ (anatase), ■: $TiO_{2\text{-}r}$ (rutile), ●: $ZnTiO_3$ and ◆: ZnO.

Figure 3.2 demonstrates the effect of the calcination temperature on the formation of different crystallographic phases for the sample prepared with the molar ratio of TiO_2/ZnO (3:1).

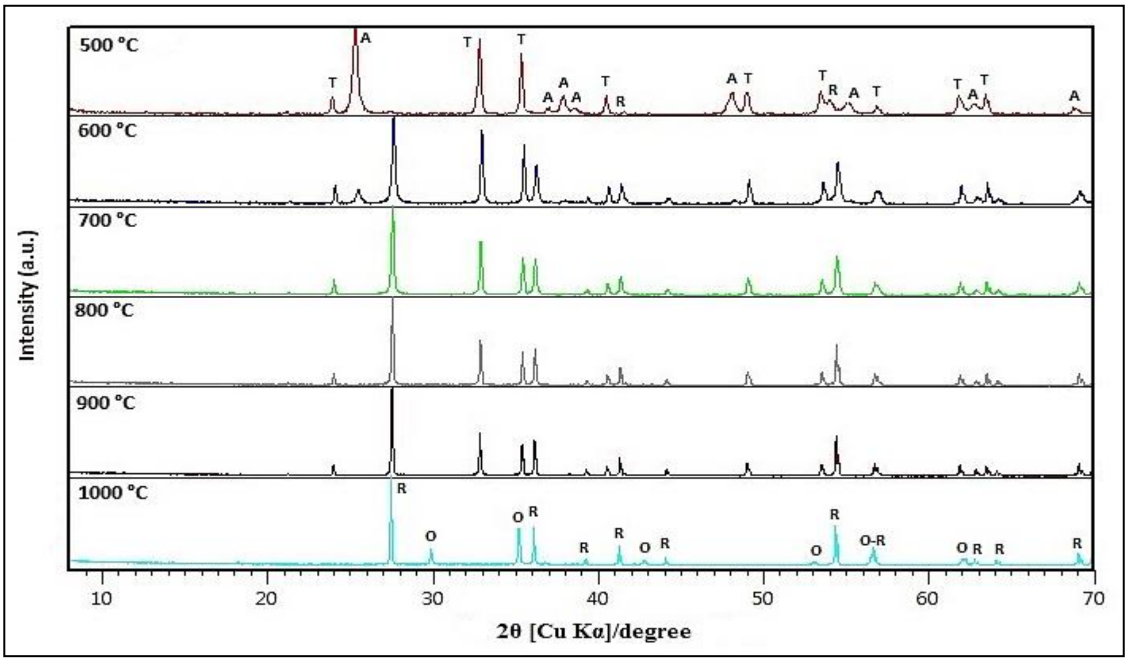

Figure 3. 2. XRD of Zn_xTiO_y-TiO_{2-a} synthesized to different temperatures. T: $ZnTiO_3$; A: TiO_{2-a}; R: TiO_{2-r}; O: Zn_2TiO_4.

The crystalline sizes of powder samples prepared at 500 °C with the molar ratio of TiO_2/ZnO (3:1) were calculated based on the main peak using the well-known Scherrer equation [41]:

$$A = \frac{K\lambda}{\beta \cos\theta} \tag{3.1}$$

where K is the shape factor (here, $K = 0.89$), λ is the wavelength of the X-ray beam used (here, $\lambda = 0.15406$ nm), θ is the Bragg angle, and β is the full width at half maximum (FWHM) of the X-ray diffraction peak, which was calculated using MDI JADE, version 6; Computer software, Materials Data Inc., Livermore, CA, USA, 2014. The average crystalline size of the phases present in the $ZnTiO_3/TiO_2$ composite were 33.79 (±3.67) and 21.47 (±3.91) nm for $ZnTiO_3$ and TiO_{2-a}, respectively.

3.3.1.2. SEM-EDS Analysis

Figure 3.3 shows the SEM image of the $ZnTiO_3/TiO_2$ heterostructure synthesized with a TiO_2:ZnO molar ratio of 3:1 and calcined at 500 °C. The image shows that the particles have an average particle size of 100 nm, are almost spherical and highly agglomerated.

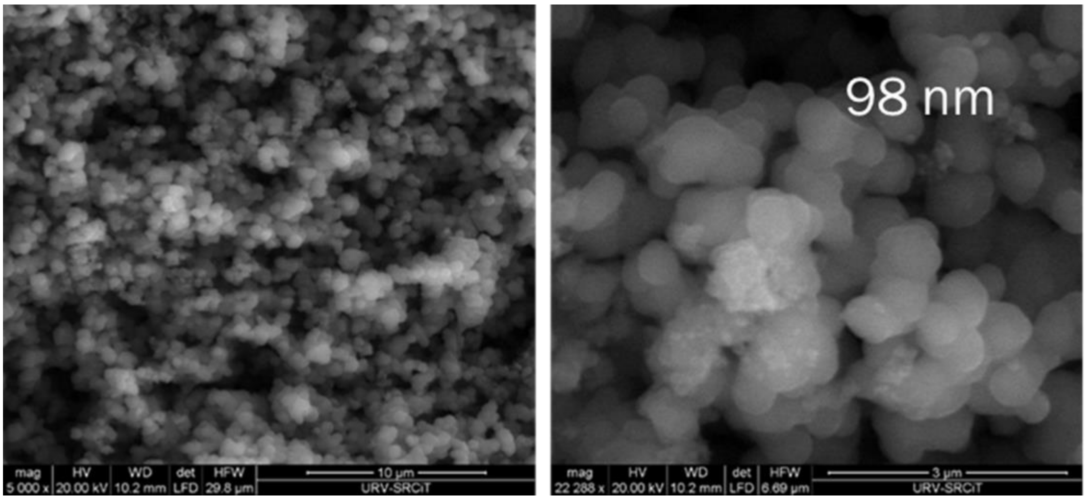

Figure 3. 3. Scanning Electron Microscopy (SEM) images of the $ZnTiO_3$-$TiO_{2\text{-}a}$ heterostructure material.

Figure 3.4 shows the Energy Dispersive X-ray (EDX) spectra of the $ZnTiO_3/TiO_2$ heterostructure, indicating the presence of O, Zn and Ti only in the $ZnTiO_3/TiO_2$ heterostructure material. The analyses showed that the heterostructure consisted of C (5.42%), O (33.6%), Ti (54.85%), and Zn (6.13%).

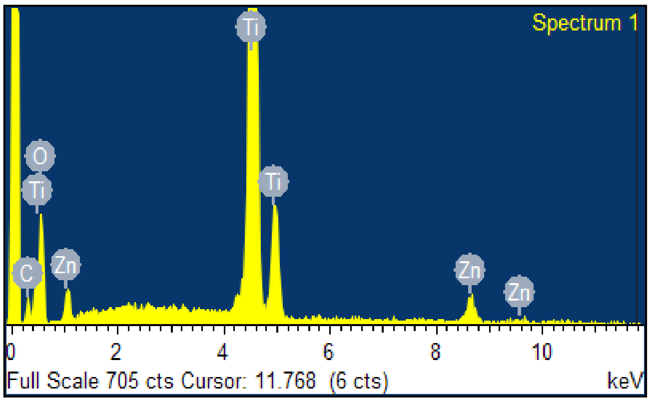

Figure 3. 4. Energy Dispersive X-ray (EDX) spectra of $ZnTiO_3/TiO_2$.

3.3.1.3. Optical and Photoelectric Properties

The optical absorption properties of photocatalysts can be characterized using the UV-visible (UV-vis) DRS in the range of 200–700 nm and at room temperature. Figure 3.5(a) shows the UV-vis XRD of $ZnTiO_3/TiO_2$ and TiO_2. Compared to TiO_2, the visible light absorption intensity of $ZnTiO_3/TiO_2$, at around 400 nm, was improved, suggesting that the $ZnTiO_3/TiO_2$ composite has a better response to visible light. The graphs of $(\alpha h v)^2$ versus hv for calculating the direct band-gap energy (E_g) are shown in Figure 3.5(b). According to Equation (2) [42], the direct E_g values were 3.07 and 3.12 eV for $ZnTiO_3/TiO_2$ and TiO_2, respectively. The direct E_g value calculated for $ZnTiO_3/TiO_2$ can be related to the direct band gap of hexagonal or cubic $ZnTiO_3$ compound [43].

$$E_g = \frac{1240}{\lambda} \tag{3.2}$$

where E_g is the band-gap energy in the electron volts (eV) and λ represents the lower cutoff wavelength in nanometers (nm).

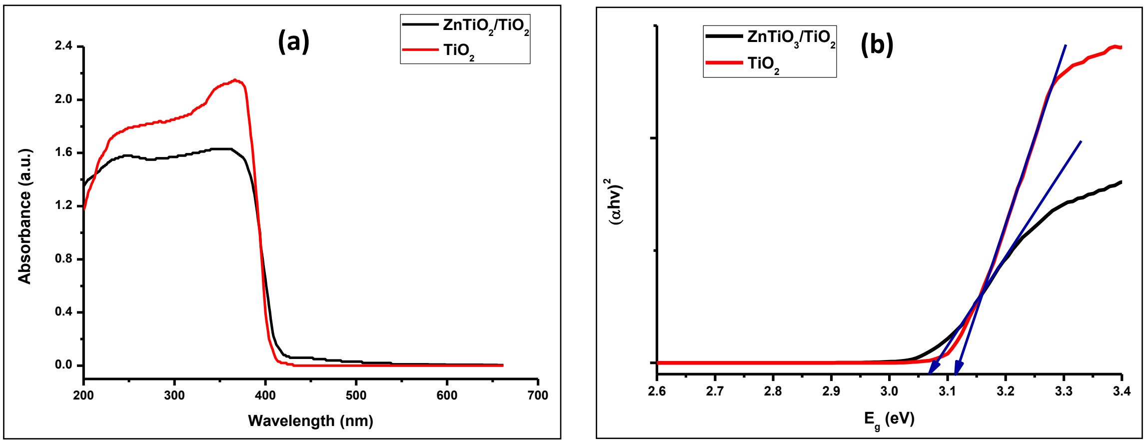

Figure 3. 5. (a) UV-vis XRD and (b) plots of $(\alpha h v)^2$ vs. E_g of $ZnTiO_3/TiO_2$ and TiO_2.

In order to analyze the photocatalytic mechanism of $ZnTiO_3/TiO_2$ heterojunction, the potentials of the Valencia Band (VB) and Conduction Band (CB) of TiO_2 and $ZnTiO_3$ were determined, which are important to estimate the flow diagram of pairs of photoexcited charge carriers in heterojunction. The Mulliken electronegativity theory was used to calculate the VB and CB potentials of TiO_2 and $ZnTiO_3$ [41]:

$$E_{\mathrm{CB}} = \chi - E_{\mathrm{c}} - 0.5E_{\mathrm{g}} \tag{3.3}$$

$$E_{\mathrm{VB}} = E_{\mathrm{CB}} + E_{\mathrm{g}} \tag{3.4}$$

where E_{CB} and E_{VB} are the CB edge potential and VB edge potential, respectively, E_g is the band gap energy of the semiconductor, E_c is the energy of free electrons on the hydrogen scale (approximately 4.5 eV), and χ is the electronegativity of the semiconductor. The values of $ZnTiO_3$ and TiO_2 were 4.0 and 5.8 respectively. According to the formula above, E_{CB} and E_{VB} for $ZnTiO_3$ and TiO_2 were (−0.22, +2.84) eV and (−2.06, +1.06) eV, respectively. Figure 3.6 describes the photocatalytic mechanism of the $ZnTiO_3/TiO_2$ heterojunction.

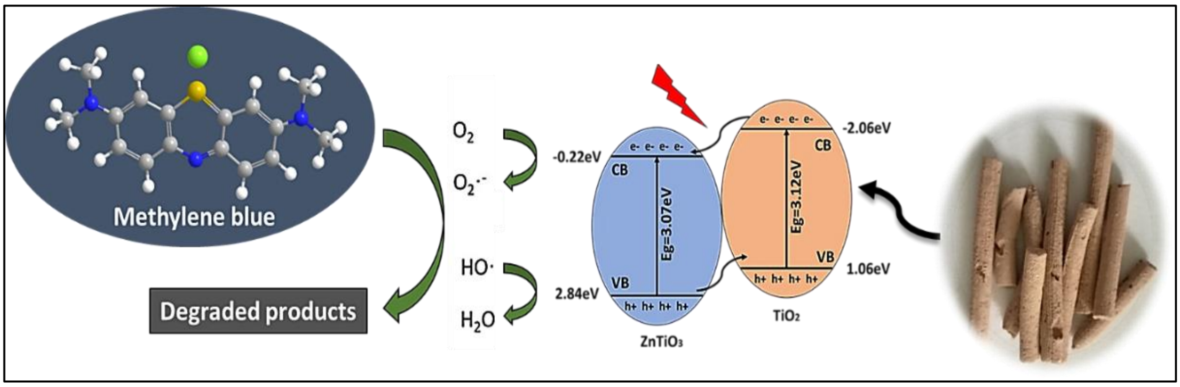

Figure 3. 6. Schematic of electron-hole separation and transportation on the interface $ZnTiO_3/TiO_2$ heterojunction.

It was clear that the CB edge of TiO_2 was more negative than the CB edge of $ZnTiO_3$; on the other hand, the VB edge of $ZnTiO_3$ was more positive than the VB edge of TiO_2. Consequently, the electrons excited from the CB of TiO_2 jumped to the CB of $ZnTiO_3$, and the holes generated from the VB of $ZnTiO_3$ transferred to the VB of TiO_2, which caused an efficient separation of e^- and h^+, and the photocatalytic activity improved due to the $ZnTiO_3/TiO_2$ heterojunction [27,44,45].

3.3.1.4. XRF Analysis

Clays are minerals that are widely distributed in nature, being produced by the erosion of rocks. The texture and chemical composition of the clays are greatly varied, depending on the presence of organic and inorganic impurities as well as the geological origin of the clays. Table 3.1 shows the composition of the clays used in the present work; all the clays contained TiO_2 and Fe_2O_3, but $Clay_{12}$ had the highest content of both oxides. Table 3.1 also shows the presence of other oxides, such as MgO, P_2O_4, K_2O, CaO, MnO, Co_3O_4, SnO_2, and CeO_2.

Table 3. 1. Composition (wt.%) of Ecuadorian clays.

CLAY	Al_2O_3	SiO_2	MgO	P_2O_5	K_2O	CaO	TiO_2	MnO	Fe_2O_3	Co_3O_4	SnO_2	CeO_2
CLAY 1	13.50	66.70	2.07	0.00	1.33	1.50	0.10	0.06	0.53	0.14	0.53	0.00
CLAY 2	12.10	61.00	0.00	0.26	1.19	0.53	0.29	0.06	1.63	0.42	0.16	0.04
CLAY 3	23.10	50.40	3.17	0.23	2.51	0.22	0.41	0.08	2.45	0.61	0.00	0.12
CLAY 4	18.50	52.90	0.69	0.00	1.49	0.33	0.45	0.08	2.14	0.54	0.03	0.11
CLAY 5	21.40	40.70	2.95	0.27	0.00	0.21	0.48	0.15	4.04	1.00	0.15	0.13
CLAY 6	21.20	45.60	2.05	0.29	1.63	1.22	0.39	0.06	1.94	0.48	0.00	0.10
CLAY 7	22.30	31.90	2.65	0.39	0.09	0.84	0.72	0.12	3.63	0.89	0.44	0.12
CLAY 8	19.90	30.20	0.00	0.30	0.03	0.28	1.01	0.35	7.81	0.00	0.05	0.18
CLAY 9	13.80	40.00	0.00	0.00	0.19	0.51	0.57	0.09	3.17	0.80	0.27	0.24
CLAY 10	22.50	35.47	0.00	0.05	0.18	0.87	1.81	0.38	17.27	0.00	0.07	0.00
CLAY 11	22.20	37.80	0.00	0.19	0.00	0.08	0.30	0.08	2.48	0.61	0.04	0.04
CLAY 12	27.10	39.40	0.00	0.26	0.78	0.12	2.16	0.10	22.40	0.07	0.17	0.08

3.3.2. Adsorption and Photocatalytic Degradation

Photocatalysts can degrade organics compounds due to strong oxidizing capacity they exhibit, especially when they are irradiated by light. In this work, the photocatalytic activity of the TiO_2 and $ZnTiO_3/TiO_2$ photocatalyst was first tested by the degradation of methylene blue (MB) in water, using irradiation with both a) solar light and b) UV-C light. Figure 3.7 shows the results obtained in the test.

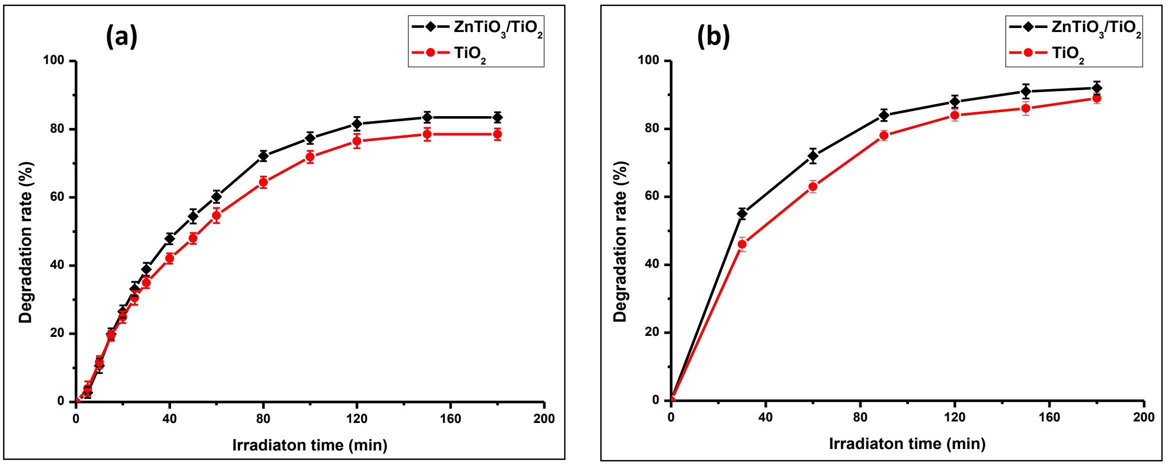

Figure 3. 7. (a) Photocatalytic degradation activity of Methylene Blue (MB) for $ZnTiO_3/TiO_2$ and TiO_2 under irradiation of solar light and (b) under UV-C light.

Figure 3.7 shows that the highest removal percentage was obtained with UV-C irradiation; therefore, it was used for photocatalytic degradation tests with photocatalysts supported on clays. Figure 3.8 shows the photocatalytic activity of the clays and the clay supported photocatalyst. In all tests, the clays improve their catalytic activity with the presence of photocatalysts. $ZnTiO_3/TiO_2$ have higher photocatalytic activity than TiO_2 in almost all the clays. In this Figure, it is observed that the composites TiO_2-Clay$_1$, TiO_2-Clay$_2$, TiO_2-Clay$_{12}$, and $ZnTiO_3/TiO_2$-Clay$_{12}$ had the highest photocatalytic activity and among the clays, Clay$_{12}$ was the most photocatalytic.

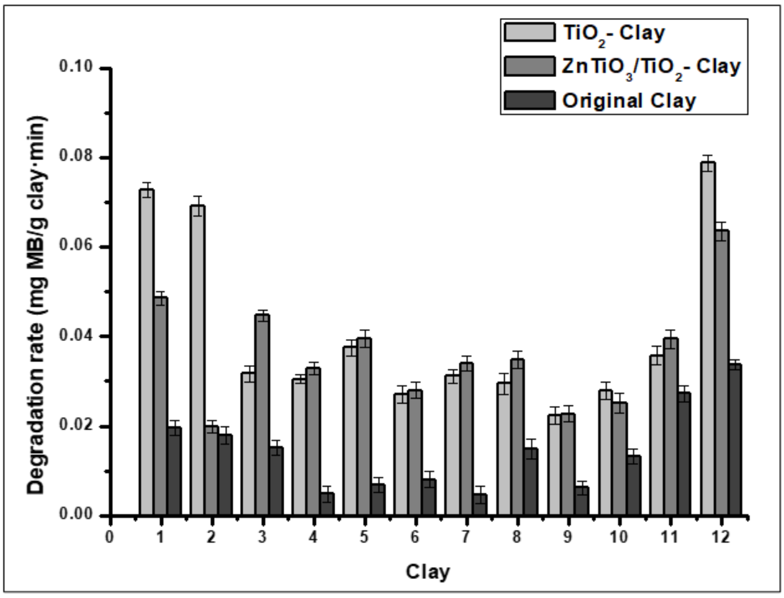

Figure 3. 8. Photocatalytic degradation activity of MB for clay and clay-supported photocatalysts.

Figure 3.9 presents XRD pattern of Clay12, which consists of Kaolinite (K), Quartz (Q), and Hematite (H). This clay has a specific surface area (BET) of 48.8 m²/g determined in the Chemisorb 2720 equipment coupled to TPx.

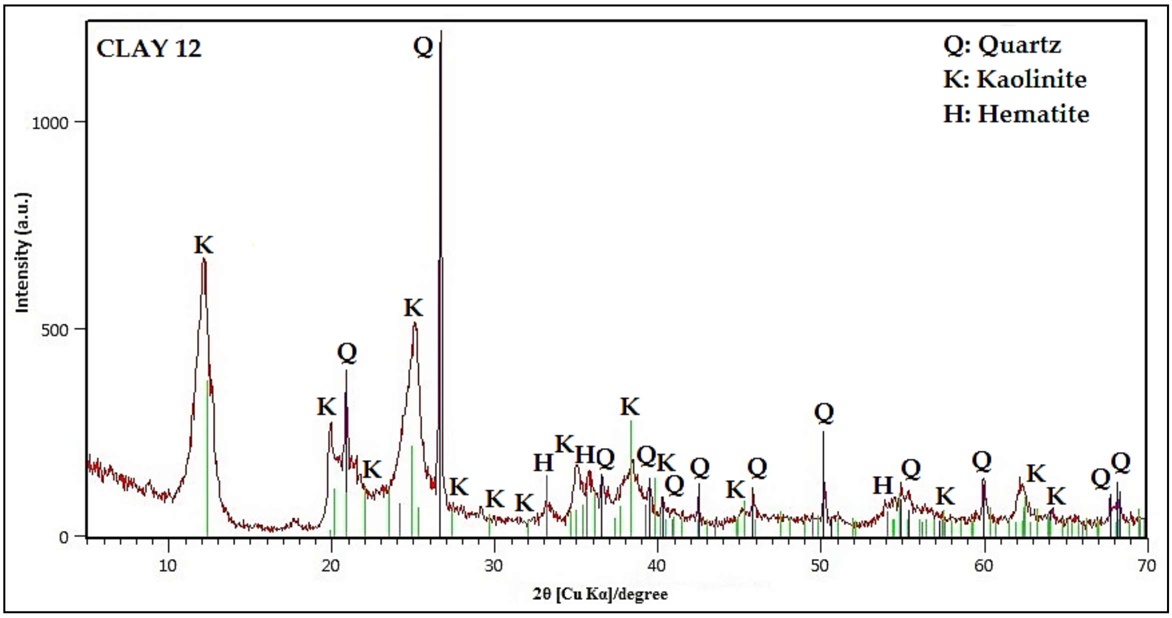

Figure 3. 9. XRD pattern Clay 12.

The surface morphology of Clay12 and of the composites (TiO2-Clay12 and ZnTiO3/TiO2-Clay12) was investigated by SEM, and the results are shown in Figure 3.10, from which it can be seen that Clay12 has a different surface morphology than composites of photocatalyst-Clay12. The surface morphology of $Clay_{12}$ seems as a smooth surface in some parts of the particle, while the composites of photocatalyst-$Clay_{12}$, has some catalysts particles incorporated into its surface (smaller TiO_2 and $ZnTiO_3/TiO_2$ grains on the outer face of $Clay_{12}$). The EDS spectra confirms that the composites contain an important amount of titanium and zinc, as shown in Figure 3.10.

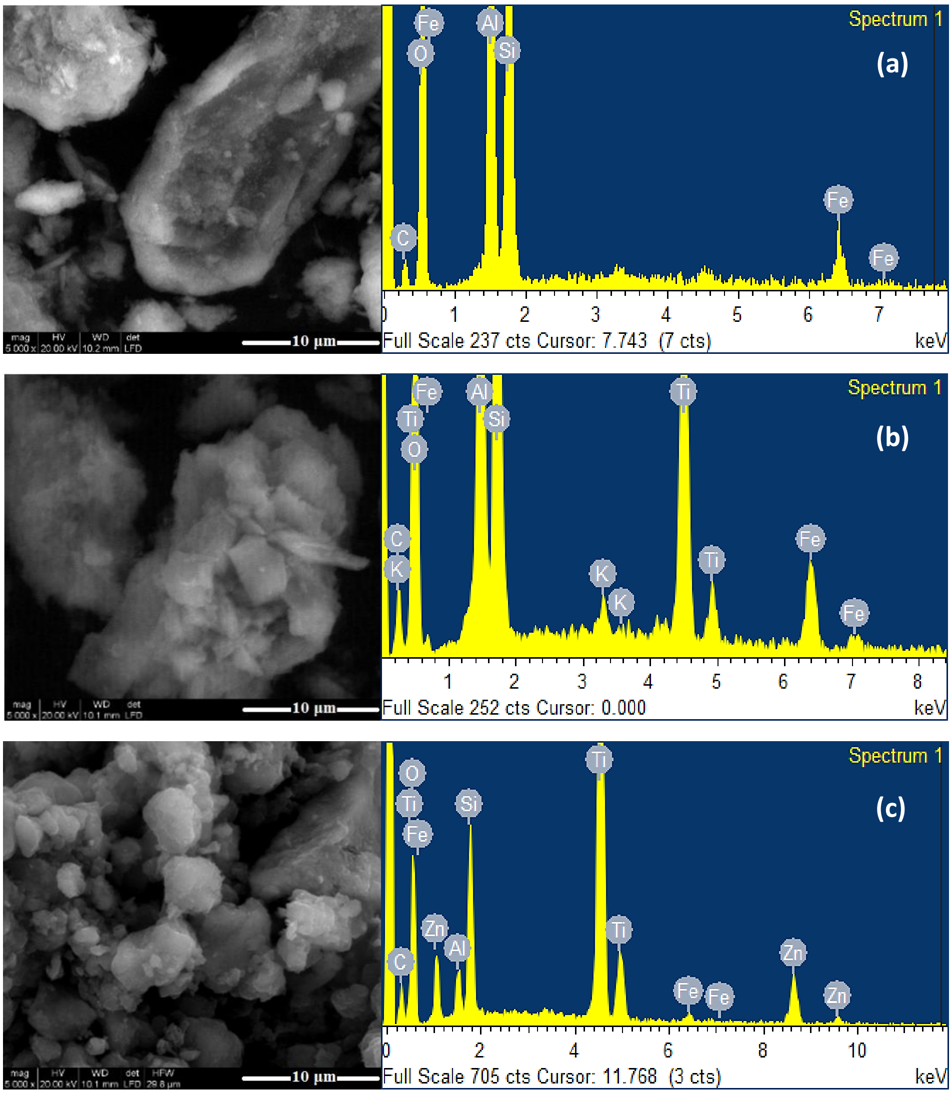

Figure 3. 10. SEM image and EDS spectra of: (a) $Clay_{12}$; (b) TiO_2-$Clay_{12}$; (c) $ZnTiO_3/TiO_2$-$Clay_{12}$.

Figure 3.11 shows the adsorption results of the clays and clay-supported photocatalysts. Most clays exceed the adsorption capacity of clay-supported photocatalysts. However, TiO_2 improves the adsorption capacity of $Clay_5$ while $ZnTiO_3$ slightly improves the adsorption capacity of $Clay_7$, $Clay_{11}$, and $Clay_{12}$. In $Clay_1$, the presence of photocatalysts did not affect the adsorption capacity of the clay.

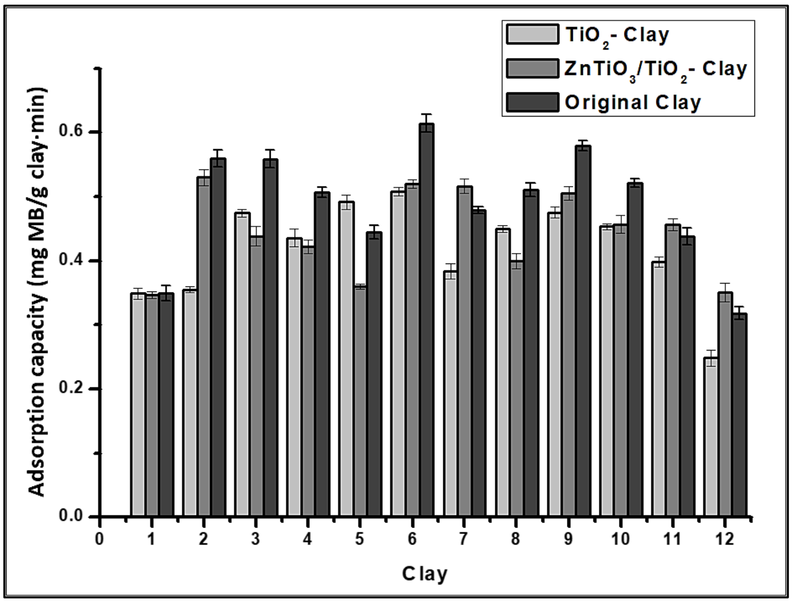

Figure 3. 11. Adsorption capacity for clay and clay-supported photocatalysts.

In Figure 3.11, $Clay_6$ shows the highest MB removal capacity. The XRD pattern in Figure 3.12 shows that $Clay_6$ consists mainly of Metahalloysite (M) and Quartz (Q), which could also contribute to the high adsorption capacity of the clay. This clay has a specific surface area of 42.8 m^2/g, which was calculated from N_2 gas adsorption using the Brunauer–Emmet–Teller (BET) isotherm in the Chemisorb 2720 equipment coupled to TPx.

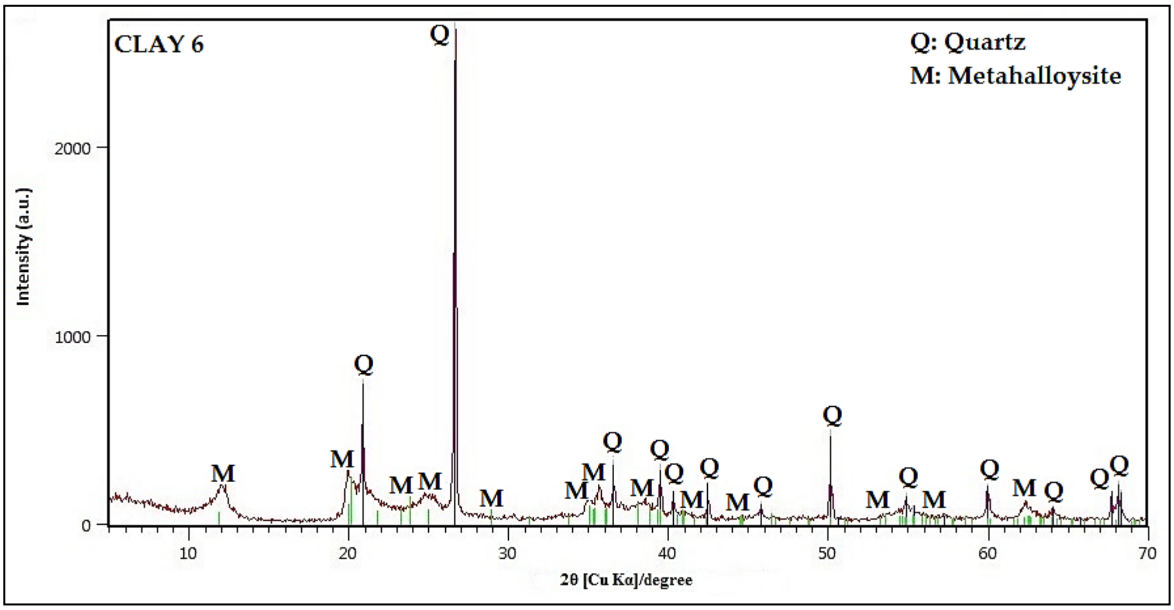

Figure 3. 12. XRD pattern of Clay 6.

Figure 3.13 show the surface morphology of $Clay_6$ and of the composites (TiO_2-$Clay_6$ and $ZnTiO_3/TiO_2$-$Clay_6$) examined by SEM. From this Figure, it can be seen that $Clay_6$ has a different surface morphology than composites of photocatalyst-$Clay_6$. The surface morphology of $Clay_6$ seems to be a flake-like structure, while in the composites of photocatalyst-$Clay_6$, the surface appears with less flake but with some catalyst particles incorporated (smaller TiO_2 and $ZnTiO_3/TiO_2$ grains) on the outer face of $Clay_6$. The changes in the morphology of $Clay_6$ is due to the thermal treatment to incorporate the photocatalysts. This treatment decreased the specific surface area of $Clay_6$ to 27.2 m^2/g and 25.8 m^2/g when impregnated with TiO_2 and $ZnTiO_3$, respectively. The EDS spectra confirms that the composites contain an important amount of titanium and zinc, as shown in Figure 3.13.

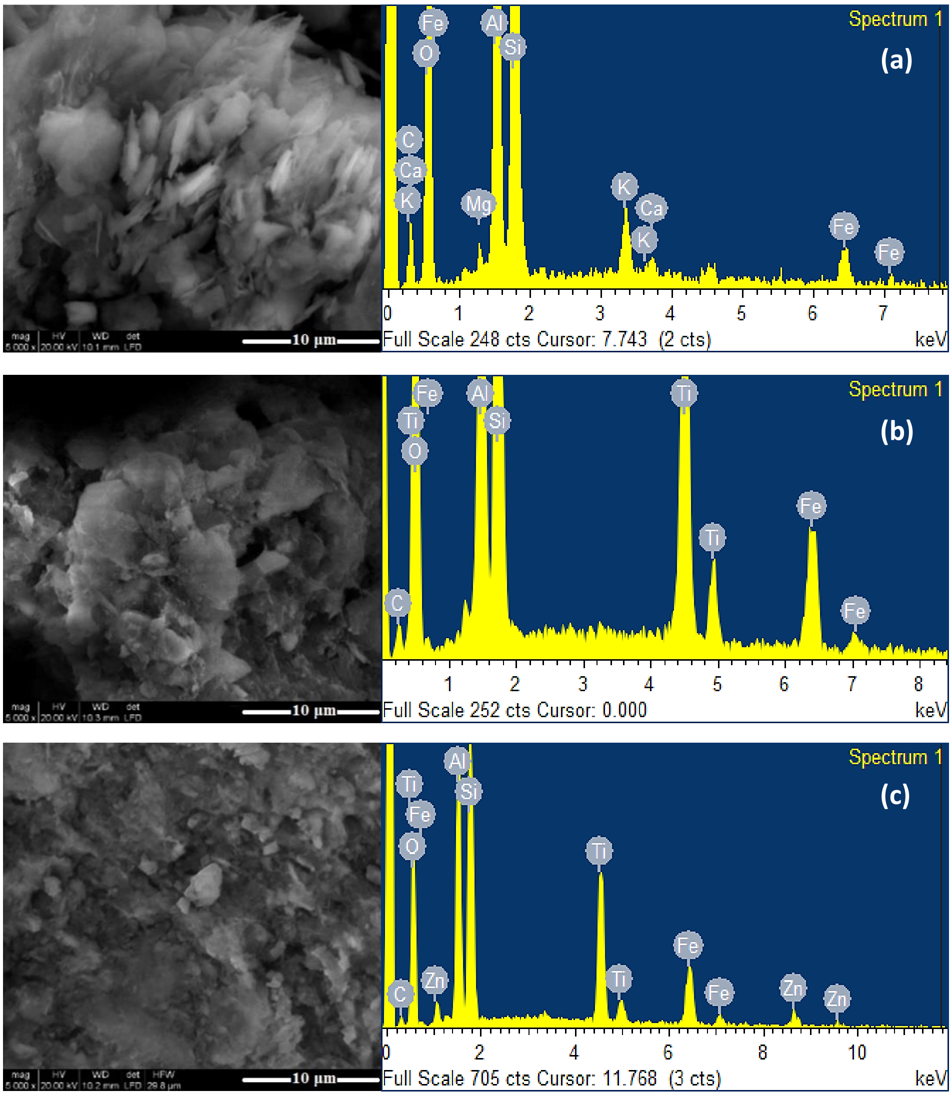

Figure 3. 13. SEM images and EDS spectra of: (a) $Clay_6$; (b) TiO_2-$Clay_6$; (c) $ZnTiO_3/TiO_2$-$Clay_6$.

3.3.3. Reuse of the Supported Photocatalysts

The recyclability and stability of the photocatalysts are important factors for their application in large scale; therefore, five consecutive photocatalytic experiments were carried out for the extrudates of $Clay_6$, photocatalyst-$Clay_6$, $Clay_{12}$, and photocatalyst-$Clay_{12}$. Figure 3.14 shows the degradation efficiency of these materials for five cycles.

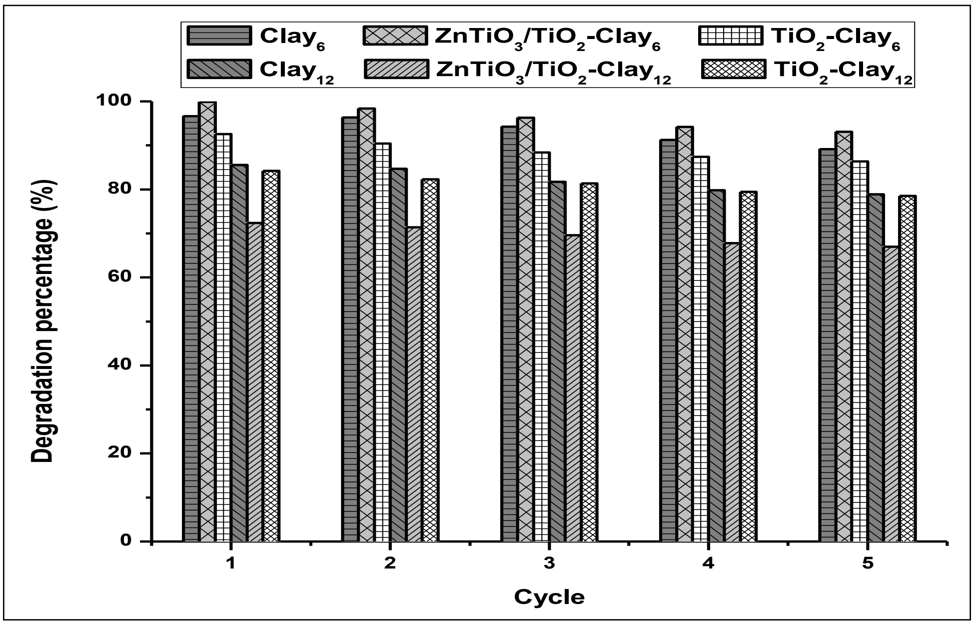

Figure 3. 14. Photodegradation percentage of MB for five successive photocatalytic cycles.

Figure 3.14 clearly shows that the percentage of MB removal decreases slightly with increasing cycle times. However, after five cycles, the synthesized materials still have high activity and can efficiently degrade MB in aqueous solution.

3.4. Discussion

3.4.1. Synthesis and Characterization of the $TiO_2/ZnTiO_3$-Clay Composite

In this work, $ZnTiO_3/TiO_2$ nanoparticles were successfully synthesized using the sol-gel method and supported on twelve raw clays of Ecuadorian origin. In the synthesis process when the TiO_2/ZnO molar ratio was decreased, the formation of TiO_2 also decreased, but the formation of $ZnTiO_3$ increased due to the greater availability to form the heterostructure. The obtained nanomaterial of $ZnTiO_3/TiO_2$ heterostructure had high purity and no other crystalline phases were observed for the sample. These results are consistent with those reported by Bhagwat et al., who synthesized $ZnTiO_3@TiO_2$ at 700 °C using TiO_2 (P-25) with zinc nitrate as a precursor [28].

Several calcination temperatures were tested for the synthesis of the $ZnTiO_3/TiO_2$ heterostructure. When the heat treatment temperature was increased to 500 °C, TiO_{2-a} (anatase phase) was the primary crystalline phase with TiO_{2-r} (rutile phase) traces. In addition, a hexagonal phase of $ZnTiO_3$ was also present in the sample prepared at 500 °C. With a temperature increment from 600 °C to 900 °C, TiO_{2-r} appeared, and TiO_{2-a} disappeared completely. However, the hexagonal phase of $ZnTiO_3$ still existed in the sample at 900 °C. This indicates that TiO_{2-r} was transformed from TiO_{2-a}, but not by decomposition of $ZnTiO_3$. This is in agreement with previous studies which revealed that the phase transition from TiO_{2-a} to TiO_{2-r} occur in a temperature range of 600–1100 °C [41]. In addition, the hexagonal $ZnTiO_3$ would decompose at about 1000 °C into the metastable form $Zn_2Ti_3O_8$ and finally to the stable cubic phase Zn_2TiO_4 with TiO_{2-r}. These results agree with the conclusions of several authors, who indicate the presence of a low percentage of zinc oxide formation from the metastable $ZnTiO_3$ which ultimately transforms (>90% conversion) to Zn_2TiO_4 (<900 °C) and to TiO_{2-r} from 700 °C [38,42–44]. The literature also indicates that obtaining either of these Ti-Zn mixed oxides as phase-pure at a low processing temperature is a challenge in materials chemistry [26,38]. On the other hand, SEM images were used to determine the shape, particle size, and morphology of the samples. The $ZnTiO_3/TiO_2$ heterostructure synthesized with a TiO_2:ZnO molar ratio of 3:1 and calcined at 500 °C was almost spherical with an average particle size of 100 nm and, highly agglomerated. These results agree with those reported by Mehrabi et al. [42].

According to Equation (2), the calculated band gaps of $ZnTiO_3/TiO_2$ and TiO_2 for the present study were 3.07 and 3.12 eV, respectively. These values are smaller than those reported by Li et al. [45], who synthesized a-$TiO_2/ZnTiO_3$ and a-TiO_2 nanoparticles with a particle size smaller than 100 nm and found band gap values of 3.14 and 3.23 eV for both photocatalysts, respectively. This band gap difference may be due to the difference in particle size also known as the quantum size effect [39]. To improve conversion efficiency, a good alternative is to reduce the band gap to shift the spectral range of light absorption into the visible-light region and even the near-infrared light region [46]. Therefore, the $ZnTiO_3/TiO_2$ composite synthesized in the present study could be a promising alternative for the photocatalytic degradation of colorants in aqueous systems due to its band gap.

3.4.2. Adsorption and Photocatalytic Degradation

The photocatalytic activity of the clay-supported $ZnTiO_3/TiO_2$ was determined by decomposition under UV-C light irradiation of Methylene Blue (MB) in water following the methodology described by Ke et al. [41], with some modifications. The literature reports that UV light excites photocatalysts to decompose the organic pollutant due to the generation of electron pairs and VB holes (e^-/h^+) produced. The e^- and h^+ can move in the catalyst. When they move to the surface of the catalyst, e^- reacts with O_2 in the solution to generate *OH and *O_2 radicals. These active species then react with MB to oxidize it and transform it into small molecules, thus achieving both purposes, decolorization and degradation of the organic matter [31,46–48].

The results obtained in the present study clearly indicate that $ZnTiO_3/TiO_2$ possesses excellent photocatalytic performance. These results are in line with the findings of several authors [49–53]. Furthermore, the $ZnTiO_3/TiO_2$ composite exhibited an important increase of the photocatalytic activity as compared with pure TiO_2. The composite probably had better photocatalytic activity because the coupling promotes an effective separation of photo-generated electron-hole pairs between TiO_2 and $ZnTiO_3$ [41].

Ke *et al*. [41] reported the photocatalytic activity of *a*-TiO_2, *a*-$TiO_2/ZnTiO_3$, and *r*-$TiO_2/ZnTiO_3$. These authors synthesized *a*-$TiO_2/ZnTiO_3$ at 800 °C and found that it had the highest photocatalytic activity, removing approximately 80% of the dye from a 5 mg/L MB solution and under UV-C light. In the present study, $ZnTiO_3/TiO_{2\text{-}a}$ was synthesized at 500 °C and approximately 90% of the dye was removed from an MB solution of the same concentration and under UV-C light. This improvement is probably due to the TiO_2:ZnO molar ratio used in the present study, which may improve the separation of the electron-hole pairs [41].

On the other hand, in agreement with other authors [54–61], the clay minerals and clay-derived materials have many diverse applications including catalysis and adsorption, which are based on their unique surface properties. The evidence of this work indicates that raw clays can be valuable supports for materials used for the removal of dyes.

The high photocatalytic activity of $Clay_{12}$ and its photocatalytic derivatives is probably caused by the presence of natural TiO_2 in its composition. This clay shows a deep-red color due to the presence of a high content of Fe_2O_3. The photocatalytic derivatives of TiO_2 and both $Clay_1$ and $Clay_2$ also show high photocatalytic activity, probably due to their mineralogical composition. Both clays are rich in SiO_2, and according to the literature, TiO_2/SiO_2 photocatalysts exhibit high photocatalytic activity toward pollutant molecule decomposition [62].

In the present study, $Clay_6$ shows the highest MB removal capacity. According to the literature, electrostatic interaction, complexation chemical reactions, or ionic exchange between the adsorbent and the adsorbate are some of the mechanisms that may be involved in the adsorption of MB on the surface of clay minerals [2,59]. $Clay_6$ has a zero-charge point (ZCP) of 3.0. The ZCP of both TiO_2 and $ZnTiO_3/TiO_2$ supported in $Clay_6$ was 7.0. The tests were carried out at pH = 8.0; therefore, the surface of $Clay_6$ was negatively charged, improving the MB cation adsorption. Moreover, according to Table 3.1, $Clay_6$ presents several oxides, such as MgO, K_2O, CaO, TiO_2, MnO, and others that could promote the cationic exchange capacity of the clay to improve its adsorption capacity [63,64]. Furthermore, $Clay_6$ contains Metahalloysite (M), which could also contribute to the high adsorption capacity of the clay since, according to the literature, metahalloysite has a potential application in the design and preparation of heterogeneous catalysts in procedures where the temperature did not exceed 450 °C [65].

It is important to mention that prior to illumination, MB was adsorbed onto the composites surface for 30 min in the dark and the average adsorption capacity was of 73%, 66%, 63%, 55%, and 46% approximately for Clay$_{X}$, $ZnTiO_3/TiO_2$-Clay$_{X}$, TiO_2-Clay$_{X}$, $ZnTiO_3/TiO_2$, and TiO_2, respectively. It is evident from these results that adsorption played a significant role in the degradation process of MB but is not sufficient to achieve complete degradation. Batch adsorption was therefore followed by 150 min of photocatalysis to further improve the degradation process. After 150 minutes of illumination, the average decolorization was improved to 89%, 82%, 85%, 92%, and 89% approximately for Clay$_{X}$, $ZnTiO_3/TiO_2$-Clay$_{X}$, TiO_2-Clay$_{X}$, $ZnTiO_3/TiO_2$, and TiO_2, respectively, which confirmed that adsorption combined with photocatalysis is an efficient process for dye degradation. These results agree with those obtained by other authors for the degradation of MB by adsorption and photocatalysis [66–71].

It is known that the separation, recovery, and reuse of the photocatalyst particles are important issues determining the future application of photocatalytic technology [72]. Therefore, in the present work, extrudates of photocatalyst-clay were prepared to facilitate the recovery of the synthesized composites. The extrudates preserved their structure during the process and no fine particles from attrition were observed; however, filters were used prior to spectrophotometer determination to avoid any interference. The use of clay extrudates with immobilized nanostructured semiconductors was an effective alternative to obtain porous photocatalysts with better active surface and adsorption capacity than isolated semiconductors, preserving their electronic and structural properties for their application in the degradation of MB under UV-C irradiation.

3.4.3. Reuse of the Supported Photocatalysts

Mechanical stability is an especially important property, which is directly related to the useful life of the supported photocatalyst. When the mechanical stability is poor, the photocatalyst will gradually flake away from the support into the reaction solution during the process; consequently, the supported photocatalyst loses its activity prematurely, and causes both secondary contamination and waste of the photocatalyst. Some investigations results showed that mechanical stability of the material is correlated with the calcination temperature [73]. Consequently, increasing the calcination temperature produces better mechanical stability, although there is an optimal calcination temperature to achieve maximum mechanical stability. In the present work, a maximum calcination temperature of the extrudates of 500 °C was used to avoid the change of crystalline phase of the synthesized photocatalysts. On average, the loss of activity of the materials did not exceed 10% at the end of the fifth cycle; thus, 500 °C is the optimum calcination temperature to achieve adequate photocatalytic activity and reuse property under the operating conditions used in this study.

Finally, the synthesized clay-supported composite reported in this paper could be an efficient alternative to remove dyes in aqueous effluents and the most probable reason is the combined effects of several factors, such as the specific surface area, the crystal size and crystallization phases, absorption capacity, photocatalytic activity, and mechanical stability. Table 3.2 shows the comparison of the MB degradation capacity of the main synthesized composites with other composites reported in the literature.

Table 3. 2. **MB adsorption capacity of synthesized composites and other composites reported in the literature.**

Material	MB Adsorption Capacity (mg/g)	References
$Clay_6$	19.33	This study
$ZnTiO_3/TiO_2$-$Clay_6$	19.98	This study
TiO_2-$Clay_6$	18.52	This study
$Clay_{12}$	17.11	This study
$ZnTiO_3/TiO_2$-$Clay_{12}$	14.47	This study
TiO_2-$Clay_{12}$	16.85	This study
$ZnTiO_3/TiO_2$	18.40	This study
TiO_2	17.80	This study
a-$TiO_2/ZnTiO_3$	16.00	[41]
a-TiO_2	15.00	[41]
Red-clay	18.83	[64]
Zeolite	16.37	[74]
Natural clay	15.40	[75]
Raw Coal fly ash	5.06	[76]
Activated carbon	6.43	[77]
AC-ZnO	32.22	[78]

3.5. Conclusions

In summary, according to the results obtained, it can be concluded that the sol-gel method is useful to synthesize other perovskite-type oxides based on titanium with various architectures and novel properties. Different operating conditions were evaluated to determine the best TiO_2/ZnO molar ratio and the optimum synthesis temperature to obtain $ZnTiO_3/TiO_2$. The results indicate that the best synthesis conditions were the following: a molar ratio of 3:1 and a calcination temperature of 500 °C. The photocatalytic materials were tested for the removal of methylene blue and, as a result, it was obtained that $ZnTiO_3/TiO_2$ had better activity than TiO_{2-a}. Twelve Ecuadorian clays were characterized, some of them with exploitation potential and utility in the preparation of new materials. The photocatalysts were impregnated into the clays and their photocatalytic activity and adsorption capacity were evaluated. $Clay_{12}$ impregnated with TiO_{2-a} showed the best photocatalytic activity. The X-ray fluorescence results showed that $Clay_{12}$ has TiO_2 and Fe_2O_3 in its composition, which could improve its activity. $Clay_6$ had the best methylene blue adsorption capacity. The results of the X-ray diffraction allowed concluding that the presence of metahalloysite phase improves the adsorption capacity. In addition, $Clay_6$ has various oxides with exchange cations that could improve its adsorption capacity. Thus, both clays can be used as inexpensive materials for the removal of cationic dyes from wastewater. Nevertheless, the adsorption mechanisms and adsorption reversibility should be further investigated to confirm the efficiency of these clays, as well as to elucidate which are the adequate active sites to prevent the release of cationic dyes depending on the physical-chemical conditions.

3.6. References

[1] Anandan: S.; Ponnusamy, V.K.; AshokKumar, M. A review on hybrid techniques for the degradation of organic pollutants in aqueous environment. *Ultrason. Sonochemistry* 2020, *67*, 105130.

[2] Shwan, D.M.S.; Aziz, B.K.; Kaufhold, S. High adsorption efficiency of topkhana natural clay for methylene blue from medical laboratory wastewater: A linear and nonlinear regression. *Silicon* 2019, *12*, 87–99.

[3] Omer, O.S.; Hussein, M.A.; Hussein, B.H.; Mgaidi, A. Adsorption thermodynamics of cationic dyes (methylene blue and crystal violet) to a natural clay mineral from aqueous solution between 293.15 and 323.15 K. *Arab. J. Chem.* 2018, *11*, 615–623.

[4] Kang, S.; Qin, L.; Zhao, Y.; Wang, W.; Zhang, T.; Yang, L.; Rao, F.; Song, S.; Lei, Q. Enhanced removal of methyl orange on exfoliated montmorillonite/chitosan gel in presence of methylene blue. *Chemosphere* 2019, *238*, 124693.

[5] Lu, F.; Astruc, D. Nanocatalysts and other nanomaterials for water remediation from organic pollutants. *Co-ord. Chem. Rev.* 2020, *408*, 213180.

[6] Ang, W.L.; Mohammad, A.W. State of the art and sustainability of natural coagulants in water and wastewater treatment. *J. Clean. Prod.* 2020, *262*, 121267.

[7] Jun, B.-M.; Al-Hamadani, Y.A.; Son, A.; Park, C.M.; Jang, M.; Jang, A.; Kim, N.C.; Yoon, Y. Applications of metal-organic framework based membranes in water purification: A review. *Sep. Purif. Technol.* 2020, *247*, 116947.

[8] Chen, M.; Jafvert, C.T.; Wu, Y.; Cao, X.; Hankins, N.P. Inorganic anion removal using micellar enhanced ultrafiltration (MEUF), modeling anion distribution and suggested improvements of MEUF: A review. *Chem. Eng. J.* 2020, *398*, 125413.

[9] Pan, L.; Ai, M.; Huang, C.; Yin, L.; Liu, X.; Zhang, R.; Wang, S.; Jiang, Z.; Zhang, X.; Zou, J.-J.; et al. Manipulating spin polarization of titanium dioxide for efficient photocatalysis. *Nat. Commun.* 2020, *11*, 1–9.

[10] Long, Z.; Li, Q.; Wei, T.; Zhang, G.; Ren, Z. Historical development and prospects of photocatalysts for pollutant removal in water. *J. Hazard. Mater.* 2020, *395*, 122599.

[11] Nguyen, D.T.; Tran, M.D.; Van Hoang, T.; Trinh, D.T.; Pham, D.T.; Nguyen, D.L. Experimental and numerical study on photocatalytic activity of the ZnO nanorods/CuO composite film. *Sci. Rep.* 2020, *10*, 7792.

[12] Karthikeyan, C.; Arunachalam, P.; Ramachandran, K.; Al-Mayouf, A.M.; Karuppuchamy, S. Recent advances in semiconductor metal oxides with enhanced methods for solar photocatalytic applications. *J. Alloy. Compd.* 2020, *828*, 154281.

[13] Sánchez-Tovar, R.; Blasco-Tamarit, E.; Fernández-Domene, R.; Villanueva-Pascual, M.; García-Antón, J.M. Electrochemical formation of novel TiO_2-ZnO hybrid nanostructures for photoelectrochemical water splitting applications. *Surf. Coatings Technol.* 2020, *388*, 125605.

[14] Al-Mamun, M.; Kader, S.; Islam, S.; Khan, M. Photocatalytic activity improvement and application of UV-TiO_2 photocatalysis in textile wastewater treatment: A review. *J. Environ. Chem. Eng.* 2019, *7*, 103248.

[15] Sharma, S.; Kumar, K.; Thakur, N.; Chauhan, S. The effect of shape and size of ZnO nanoparticles on their antimicrobial and photocatalytic activities: A green approach. *Bull. Mater. Sci.* 2019, *43*, 20.

[16] Ramgir, N.; Bhusari, R.; Rawat, N.S.; Patil, S.J.; Debnath, A.K.; Gadkari, S.C.; Muthe, K.P. TiO_2/ZnO heterostructure nanowire based NO_2 sensor. *Mater. Sci. Semicond. Process*. 2020, *106*, 104770.

[17] Gnanaseelan, N.; Latha, M.; Mantilla, A.; Sathish-Kumar, K.; Caballero-Briones, F. The role of redox states and junctions in photocatalytic hydrogen generation of MoS_2-TiO_2-rGO and CeO_2-$Ce_2Ti_3O_{8.7}$-TiO_2-rGO composites. *Mater. Sci. Semicond. Process.* 2020, *118*, 105185.

[18] Zalani, N.M.; Kaleji, B.K.; Mazinani, B. Synthesis and characterisation of the mesoporous ZnO-TiO_2 nanocomposite; Taguchi optimisation and photocatalytic methylene blue degradation under visible light. *Mater. Technol.* 2019, *35*, 281–289.

[19] Jose, M.; Elakiya, M.; Dhas, S.A.M.B. Structural and optical properties of nanosized ZnO/$ZnTiO_3$ composite materials synthesized by a facile hydrothermal technique. *J. Mater. Sci. Mater. Electron.* 2017, *28*, 13649–13658.

[20] Chen, F.; Yu, C.; Wei, L.; Fan, Q.; Ma, F.; Zeng, J.; Yi, J.; Yang, K.; Ji, H. Fabrication and characterization of $ZnTiO_3$/$Zn_2Ti_3O_8$/ZnO ternary photocatalyst for synergetic removal of aqueous organic pollutants and Cr(VI) ions. *Sci. Total Environ*. 2020, *706*, 136026.

[21] Al-Hajji, L. A comparative study on the zinc metatitanate microstructure by ball milling and solvothermal approaches. *J. Struct. Chem*. 2019, *60*, 830–837.

[22] Baamran, K.S.; Tahir, M. Ni-embedded TiO_2-$ZnTiO_3$ reducible perovskite composite with synergistic effect of metal/support towards enhanced H_2 production via phenol steam reforming. *Energy Convers. Manag.* 2019, *200*, 112064.

[23] Chuaicham, C.; Karthikeyan, S.; Song, J.T.; Ishihara, T.; Ohtani, B.; Sasaki, K. Importance of $ZnTiO_3$ phase in ZnTi-mixed metal oxide photocatalysts derived from layered double hydroxide. *ACS Appl. Mater. Interfaces* 2020, *12*, 9169–9180.

[24] Surynek, M.; Spanhel, L.; Lapčík, Ľ.; Mrazek, J. Tuning the photocatalytic properties of sol-gel-derived single, coupled, and alloyed ZnO-TiO_2 nanoparticles. *Res. Chem. Intermed.* 2019, *45*, 4193–4204.

[25] Müllerová, J.; Šutta, P.; Medlín, R.; Netrvalova, M.; Novak, P. Optical properties of zinc titanate perovskite prepared by reactive RF sputtering. *J. Electr. Eng.* 2017, *68*, 10–16.

[26] Surendar, T.; Kumar, S.; Shanker, V. Influence of La-doping on phase transformation and photocatalytic properties of $ZnTiO_3$ nanoparticles synthesized via modified sol-gel method. *Phys. Chem. Chem. Phys.* 2014, *16*, 728–735.

[27] Acosta-Silva, Y.; Castanedo-Perez, R.; Torres-Delgado, G.; Méndez-López, A.; Zelaya-Ángel, O. Analysis of the photocatalytic activity of CdS+$ZnTiO_3$ nanocomposite films prepared by sputtering process. *Superlattices Microstruct.* 2016, *100*, 148–157.

[28] Bhagwat, U.O.; Wu, J.J.; Asiri, A.M.; Anandan, S. Synthesis of $ZnTiO_3$@TiO_2 heterostructure nanomaterial as a visible light photocatalyst. *ChemistrySelect* 2019, *4*, 6106–6112.

[29] Sarkar, M.; Sarkar, S.; Biswas, A.; De, S.; Kumar, P.R.; Mothi, E.; Kathiravan, A. Zinc titanate nanomaterials—Photocatalytic studies and sensitization of hydantoin derivatized porphyrin dye. *Nano-Struct. Nano-Objects* 2020, *21*, 100412.

[30] Hadjltaief, H.B.; Ben Ameur, S.; Da Costa, P.; Ben Zina, M.; Galvez, M.E. Photocatalytic decolorization of cationic and anionic dyes over ZnO nanoparticle immobilized on natural Tunisian clay. *Appl. Clay Sci.* 2018, *152*, 148–157.

[31] Tobajas, M.; Belver, C.; Rodriguez, J.J. Degradation of emerging pollutants in water under solar irradiation using novel TiO_2-ZnO / clay nanoarchitectures. *Chem. Eng. J.* 2016, *309*, 596–606.

[32] Belver, C.; Bedia, J.; Rodriguez, J.J. Environmental Titania—Clay heterostructures with solar photocatalytic applications. *Appl. Catal. B Environ*. 2015, *176*, 278–287.

[33] Wadhwa, S.; Mathur, A.; Pendurthi, R.; Singhal, U.; Khanuja, M.; Roy, S.S. Titania-based porous nanocomposites for potential environmental applications. *Bull. Mater. Sci.* 2020, *43*, 47.

[34] Jing, G.; Sun, Z.; Ye, P.; Wei, S.; Liang, Y. Clays for heterogeneous photocatalytic decolorization of wastewaters contaminated with synthetic dyes: A review. *Water Pr. Technol.* 2017, *12*, 432–443.

[35] Akkari, M.; Aranda, P.; Ben Rhaiem, H.; Amara, A.B.H.; Ruiz-Hitzky, E. ZnO/clay nanoarchitectures: Synthesis, characterization and evaluation as photocatalysts. *Appl. Clay Sci.* 2016, *131*, 131–139.

[36] Wu, A.; Wang, D.; Wei, C.; Zhang, X.; Liu, Z.; Feng, P.; Ou, X.; Qiang, Y.; Garcia, H.; Niu, J.N. A comparative photocatalytic study of TiO_2 loaded on three natural clays with different morphologies. *Appl. Clay Sci.* 2019, *183*, 105352.

[37] Krupskaya, V.V.; Zakusin, S.; Tyupina, E.A.; Dorzhieva, O.; Zhukhlistov, A.P.; Belousov, P.; Timofeeva, M.N. Experimental study of montmorillonite structure and transformation of its properties under treatment with inorganic acid solutions. *Minerals* 2017, *7*, 49.

[38] Nolan, N.T.; Seery, M.K.; Pillai, S.C. Crystallization and phase-transition characteristics of sol-gel-synthesized zinc titanates. *Chem. Mater.* 2011, *23*, 1496–1504.

[39] Salavati-Niasari, M.; Soofivand, F.; Sobhani-Nasab, A.; Shakouri-Arani, M.; Faal, A.Y.; Bagheri, S. Synthesis, characterization, and morphological control of $ZnTiO_3$ nanoparticles through sol-gel processes and its photocatalyst application. *Adv. Powder Technol.* 2016, *27*, 2066–2075.

[40] Alkaykh, S.; Mbarek, A.; Ali-Shattle, E.E. Photocatalytic degradation of methylene blue dye in aqueous solution by $MnTiO_3$ nanoparticles under sunlight irradiation. *Heliyon* 2020, *6*, 4–9.

[41] Ke, S.; Cheng, X.; Wang, Q.; Wang, Y.; Pan, Z. Preparation of a photocatalytic $TiO_2/ZnTiO_3$ coating on glazed ceramic tiles. *Ceram. Int.* 2014, *40*, 8891–8895.

[42] Mehrabi, M.; Javanbakht, V. Photocatalytic degradation of cationic and anionic dyes by a novel nanophotocatalyst of $TiO_2/ZnTiO_3/\alpha Fe_2O_3$ by ultraviolet light irradiation. *J. Mater. Sci. Mater. Electron.* 2018, *29*, 9908–9919.

[43] García-Ramírez, E.; Mondragón, M.; Zelaya-Ángel, O. Band gap coupling in photocatalytic activity in ZnO-TiO_2 thin films. *Appl. Phys. A* 2012, *108*, 291–297.

[44] Lei, S.; Fan, H.; Ren, X.; Fang, J.; Ma, L.; Liu, Z. Novel sintering and band gap engineering of $ZnTiO_3$ ceramics with excellent microwave dielectric properties. *J. Mater. Chem. C* 2017, *5*, 4040–4047.

[45] Li, X.; Xiong, J.; Huang, J.; Feng, Z.; Luo, J. Novel g-C_3N_4/h′$ZnTiO_3$-a′TiO_2 direct Z-scheme heterojunction with significantly enhanced visible-light photocatalytic activity. *J. Alloys Compd*. 2019, *774*, 768–778.

[46] Wang, C.-L.; Hwang, W.-S.; Chang, K.-M.; Kuo, Y.-H.; Hsi, C.-S.; Huang, H.-H.; Wang, M.-C. Formation and morphology of $Zn_2Ti_3O_8$ powders using hydrothermal process without dispersant agent or mineralizer. *Int. J. Mol. Sci.* 2011, *12*, 935–945.

[47] Thein, M.T.; Pung, S.-Y.; Aziz, A.; Itoh, M. The role of ammonia hydroxide in the formation of ZnO hexagonal nanodisks using sol–gel technique and their photocatalytic study. *J. Exp. Nanosci.* 2014, *10*, 1068–1081.

[48] Budigi, L.; Nasina, M.R.; Shaik, K.; Amaravadi, S. Structural and optical properties of zinc titanates synthesized by precipitation method. *J. Chem. Sci.* 2015, *127*, 509–518.

[49] Li, J.; Wu, N. Catalysis Science & Technology. *Catal. Sci. Technol*. 2015, *5*, 1360–1384.

[50] Meshram, S.; Limaye, R.; Ghodke, S.; Nigam, S.; Sonawane, S.; Chikate, R. Continuous flow photocatalytic reactor using ZnO—Bentonite nanocomposite for degradation of phenol. *Chem. Eng. J.* 2011, *172*, 1008–1015.

[51] Kubacka, A.; Fernández-García, M.; Colón, G. Advanced nanoarchitectures for solar photocatalytic applications. *Chem. Rev.* 2011, *112*, 1555–1614.

[52] Pan, G.; Xu, M.; Zhou, K.; Meng, Y.; Chen, H.; Guo, Y.; Wu, T. Photocatalytic degradation of methylene blue over layered double hydroxides using various divalent metal ions. *Clays Clay Miner.* 2019, *67*, 340–347.

[53] Gayathri, S.; Jayabal, P.; Kottaisamy, M.; Ramakrishnan, V. Synthesis of the graphene-$ZnTiO_3$ nanocomposite for solar light assisted photodegradation of methylene blue. *J. Phys. D Appl. Phys.* 2015, *48*, 415305.

[54] Ozturk, B.; Pozan, G.S. Promoting role of transition metal oxide on $ZnTiO_3$-TiO_2 nanocomposites for the photocatalytic activity under solar light irradiation. *Ceram. Int.* 2016, *42*, 11184–11192.

[55] Wu, L.; Wu, P.; Zhu, Y.; Zhu, N.; Dang, Z. Preparation and characterization of $ZnTiO_3$-TiO_2/pillared montmorillonite composite catalyst for enhanced photocatalytic activity. *Res. Chem. Intermed*. 2016, *42*, 5253–5268.

[56] Wang, A.-M.; Bai, N.; Wang, J.-X.; Fan, X.-Y.; Kang, Y.-H.; Ma, X.-R. Preparation and photocatalytic property of $ZnTiO_3$/TiO_2 heterogeneous composite material. *Rengong Jingti Xuebao/J. Synth. Cryst*. 2018, *47*, 382–388.

[57] Zang, W.-H.; Ji, Q.-H.; Lan, H.-C.; Li, J. Preparation of $ZnTiO_3$/TiO_2 photocatalyst and its mechanism on photocatalytic degradation of organic pollutants. *Huanjing Kexue/Environ. Sci*. 2019, *40*, 693–700.

[58] El Mouzdahir, Y.; Elmchaouri, A.; Mahboub, R.; Gil, A.; Korili, S.A. Adsorption of methylene blue from aqueous solutions on a Moroccan clay. *J. Chem. Eng. Data* 2007, *52*, 1621–1625.

[59] Almeida, C.; Debacher, N.A.; Downs, A.; Cottet, L.; Mello, C. Removal of methylene blue from colored effluents by adsorption on montmorillonite clay. *J. Colloid Interface Sci.* 2009, *332*, 46–53.

[60] Aguiar, J.E.; Cecilia, J.A.; Tavares, P.A.S.; Azevedo, D.C.S.; Rodríguez Castellón, E.; Lucena, S.M.P.; Silva Junior, I.J. Applied clay science adsorption study of reactive dyes onto porous clay heterostructures. *Appl. Clay Sci.* 2017, *135*, 35–44.

[61] Ruiz-Hitzky, E.; Aranda, P.; Akkari, M.; Khaorapapong, N.; Ogawa, M. Photoactive nanoarchitectures based on clays incorporating TiO_2 and ZnO nanoparticles. *Beilstein J. Nanotechnol.* 2019, *10*, 1140–1156.

[62] Zhang, Z.; Hu, L.; Zhang, H.; Yu, L.; Liang, Y. Large-sized nano-TiO_2/SiO_2 mesoporous nanofilmconstructed macroporous photocatalysts with excellent photocatalytic performance. *Front. Mater. Sci*. 2020, *14*, 163–176.

[63] Susana, S.; Vercelone, Z.; Sham, E.L.; Mónica, E.; Torres, F. Caracterización superficial y textural de organoarcillas pilareadas con TiO_2 Surface and textural characterization of TiO_2 pillared organoclays. *RevistaMateria* 2015, *20*, 757–763.

[64] Bentahar, Y.; Draoui, K.; Hurel, C.; Ajouyed, O.; Khairoun, S.; Marmier, N. Physico-chemical characterization and valorization of swelling and non-swelling Moroccan clays in basic dye removal from aqueous solutions. *J. Afr. Earth Sci.* 2019, *154*, 80–88.

[65] Carrillo, A.M.; Urruchurto, C.M.; Carriazo, J.G.; Moreno, S.; Molina, R.A. Structural and textural characterization of a Colombian halloysite. *Rev. Mex. Ing. Quim*. 2014, *3*, 563–571.

[66] Laysandra, L.; Sari, M.W.M.K.; Soetaredjo, F.E.; Foe, K.; Putro, J.N.; Kurniawan, A.; Ju, Y.-H.; Ismadji, S. Adsorption and photocatalytic performance of bentonite-titanium dioxide composites for methylene blue and rhodamine B decoloration. *Heliyon* 2018, *3*, e00488.

[67] Chen, Y.; Xiang, Z.; Wang, D.; Kang, J.; Qi, H. Effective photocatalytic degradation and physical adsorption of methylene blue using cellulose/GO/TiO_2 hydrogels. *RSC Adv.* 2020, *10*, 23936–23943.

[68] Irani, M.; Mohammadi, T.; Mohebbi, S. Photocatalytic degradation of methylene blue with ZnO nanoparticles; a joint experimental and theoretical study. *J. Mex. Chem. Soc.* 2017, *60*, 218–225.

[69] Kurajica, S.; Minga, I.; Blazic, R.; Muzina, K.; Tominac, P. Adsorption and degradation kinetics of methylene blue on as-prepared and calcined titanate nanotubes. *Athens J. Sci.* 2018, *5*, 7–22.

[70] Makama, A.B.; Salmiaton, A.; Saion, E.B.; Choong, T.S.Y.; Abdullah, N. Synthesis of CdS sensitized TiO_2 photocatalysts: Methylene blue adsorption and enhanced photocatalytic activities. *Int. J. Photoenergy* 2016, *2016*, 1–14.

[71] Shahid, M.; El Saliby, I.; McDonagh, A.; Chekli, L.; Tijing, L.D.; Kim, J.-H.; Shon, H.K. Adsorption and photocatalytic degradation of methylene blue using potassium polytitanate and solar simulator. *J. Nanosci. Nanotechnol.* 2016, *16*, 4342–4349.

[72] Belver, C.; Hinojosa, M.; Bedia, J.; Tobajas, M.; Alvarez, M.A.; Rodríguez-González, V. Electronic supplementary information ag-coated heterostructures of ZnO-TiO_2/ delaminated montmorillonite as solar photocatalysts. *Materials*. 2017, *10*, 1–17.

[73] Shi, J.W.; Chen, S.H.; Wang, S.M.; Ye, Z.L.; Wu, P.; Xu, B. Favorable recycling photocatalyst TiO_2/CFA: Effects of calcination temperature on the structural property and photocatalytic activity. *J. Mol. Catal. A Chem.* 2010, *330*, 41–48.

[74] Han, R.; Zhang, J.; Han, P.; Wang, Y.; Zhao, Z.; Tang, M. Study of equilibrium, kinetic and thermodynamic parameters about methylene blue adsorption onto natural zeolite. *Chem. Eng. J.* 2009, *145*, 496–504.

[75] Sahoo, S.; Uma; Banerjee, S.; Sharma, Y.C. Application of natural clay as a potential adsorbent for the removal of a toxic dye from aqueous solutions. *Desalin. Water Treat.* 2013, *52*, 6703–6711.

[76] Li, H.; Dai, M.; Dai, S.; Dong, X.; Li, F. Methylene blue adsorption properties of mechanochemistry modified coal fly ash. *Hum. Ecol. Risk Assess. Int. J.* 2018, *24*, 2133–2141.

[77] Nayeri, D.; Mousavi, S.A.; Fatahi, M.; Almasi, A.; Khodadoost, F. Dataset on adsorption of methylene blue from aqueous solution onto activated carbon obtained from low cost wastes by chemical-thermal activation—Modelling using response surface methodology. *Data Br*. 2019, *25*, 104036.

[78] Nourmoradi, H.; Ghiasvand, A.; Noorimotlagh, Z. Removal of methylene blue and acid orange 7 from aqueous solutions by activated carbon coated with zinc oxide (ZnO) nanoparticles: Equilibrium, kinetic, and thermodynamic study. *Desalin. Water Treat.* 2014, *55*, 252–262.

CHAPTER 4

STRUCTURING OF $ZnTiO_3/TiO_2$ ADSORBENTS FOR THE REMOVAL OF METHYLENE BLUE, USING ZEOLITE PRECURSOR CLAYS AS NATURAL ADDITIVES

4.1. Introduction

Dyes are substances with an important application in various industries such as food, printing, plastics, textiles, paper, leather, and pharmaceutical products [1]. Methylene blue (MB) dye, which is widely used in the textile industry, is one of the most famous water pollutants [2]. MB is frequently discharged into the environment without restriction or control, having dangerous effects on living organisms [3]. MB also affects the environment and damages the ecosystem's balance since, even in low concentrations, the presence of this dye in water inhibits photosynthesis in the aquatic environment due to the reduction of solar irradiation [4,5]. Therefore, effluent treatment with MB dye prior to its discharge is of interest due to its harmful impacts on receiving water [6].

Numerous technologies, including biological degradation as well as chemical and physical methods, have been extensively studied to treat wastewater contaminated with dyes [7–12]. Adsorption is an attractive method for removing pollutants from effluents as it is a flexible process in terms of design and operation and produces pollutant-free effluents that are suitable for reuse [13,14]. The efficiency of the adsorption process depends on the characteristics of the solution medium, the adsorbate, and the adsorbent [15,16]. An ideal adsorbent should have a porous structure, a large specific surface area, good physical, mechanical and chemical stability, and high affinity for the adsorbate [17]; therefore, research on materials that are both efficient and economical should be encouraged.

In recent years, there has been a growing interest in the use of metallic and non-metallic oxides to adsorb organic and inorganic contaminants. $ZnTiO_3$ is a mixed oxide obtained by the sol-gel method during the synthesis of coupled ZnO-TiO_2 [18–20]. This oxide is usually synthesized with some impurity phases such as anatase and rutile [21–23]. This mixed oxide is interesting for its technological applications as an adsorbent and photocatalyst; it is also a low-cost and environmentally friendly material [24,25]. Previous studies show that $ZnTiO_3/TiO_2$ can eliminate methylene blue dye from aqueous systems, being of interest for effluent treatment [26].

Other interesting adsorbent materials are clays since they are abundant in nature, are low-cost, and have high absorption properties and ion exchange potential. Most clays are also suitable precursors for the synthesis of materials with improved properties, due to their mineralogical composition [27]. Several authors have reported the use of clays to obtain zeolites with greater structural regularity and greater porosity, as well as a particular surface chemistry that improves their adsorbent capacity [1]. In recent years, zeolite FAU and zeolite LTA have shown important applications as catalysts, ion exchange materials, and adsorbents. Both zeolites can be synthesized from natural solids using the hydrothermal method, making them suitable high value-added materials to efficiently remove pollutants from wastewater.

Although the literature indicates that various adsorbents can be widely used for wastewater treatment, their recovery at the end of the process limits their practical application. Structured materials offer an alternative to avoid the separation step at the end of the process [28–30]. The structured materials are prepared in the presence of a binder or matrix. The literature shows several types of binders for the preparation of structured materials, for instance: clays, titania, alumina, and/or silica or combinations of these materials [31,32]. Clays represent a very promising alternative because of their high mechanical and chemical stability [33,34]. Clays are attractive minerals for use in adsorption, catalysis processes, controlled release of active compounds and also offer an interesting route to revalue local natural resources [35–37].

Clays, being inexpensive and widely available, represent an attractive binder for the immobilization of a variety of active compounds that are in powder form [38]. The clays used as inorganic binders allow to achieve mechanically resistant structured bodies after the respective calcination process. This thermally induced increase in mechanical strength is probably related to the creation of new and stronger bonds between the constituent powders that also improve the wear resistance of the material during the process [39].

Clay minerals are an important source of raw material for obtaining, through physical and chemical modification, new supports with desired porosity, appropriate inorganic structure and adequate SiO_2/Al_2O_3 ratios, providing solids with unique characteristics [39]. Therefore, clays represent a promising material for cleaning natural resources and improving the quality of life of the population [40].

Several authors have studied the adsorption of methylene blue from aqueous systems using clays [41–46] and zeolites [47–52] as adsorbents. In addition, we previously reported the use of $ZnTiO_3/TiO_2$ to remove methylene blue. The results of this study showed that this mixed oxide can degrade the dye, especially by photocatalysis, although it also showed slight adsorbent activity [26]. However, no studies have been found in the literature in which $ZnTiO_3/TiO_2$, zeolites, and clays are combined to prepare composites that serve to adsorb colorants in general, and methylene blue in particular, from aqueous systems. Additionally, despite the great industrial importance of producing structured adsorbents from porous powders, few papers in the academic literature are devoted to reporting studies of the structuring [39].

In light of the above, this work reports the synthesis of $ZnTiO_3/TiO_2$ and zeolites from natural clays, as well as the preparation of extruded composites from these materials for the removal of methylene blue in aqueous effluents. The synthesized compounds were characterized by X-ray diffraction (XRD), X-ray fluorescence (XRF), scanning electron microscopy (SEM-EDX), and specific surface area (BET). In addition, the adsorption capacity of the synthesized extruded composites was measured in batch experiments, varying the pH of the solution, the concentration of the adsorbent, and the contact time.

4.2. Materials and Methods

4.2.1. Materials

All of the reagents used in this work were of analytical grade and used without additional purification: $Ti(OC_3H_7)_4$ (Sigma Aldrich, St. Louis, MO, USA,98%), CH_3COOH (Fisher Scientific, Waltham, MA, USA, 99.8%), CH_3OH (Sigma Aldrich, St. Louis, MO, USA, ≥99.8%), HCl (Fisher Scientific, Waltham, MA, USA, 37%), cetyl-trimethyl ammonium chloride

($C_{19}H_{42}NCl$) (Sigma Aldrich, St. Louis, MO, USA, 25%), H_2O_2 (Sigma Aldrich, St. Louis, MO, USA, 35%), $AgNO_3$ (Sigma Aldrich, St. Louis, MO, USA, >99.8%), HNO_3 (Sigma Aldrich, St. Louis, MO, USA, 69%), $Zn(CH_3COO)_2{\cdot}2H_2O$ (ACS, St. Louis, MO, USA, ≥98%), $C_{16}H_{18}ClN_3S{\cdot}xH_2O$ (Sigma Aldrich, St. Louis, MO, USA, ≥95%), NaOH (ACS, St. Louis, MO, USA, ≥97%).

4.2.2. Clay Purification

The raw clays were collected from southern Ecuador. The clays were labeled R-Clay and G-Clay due to their red and gray color, respectively. The clay samples were ground and sieved to 200-mesh (0.074 mm) size. Carbonates of calcium and magnesium were removed using hydrochloric acid (0.1 N) at a ratio of 10 mL g^{-1}. The organic matter present in the clay samples was oxidized by the addition of H_2O_2 (33%) at a ratio of 10 mL g^{-1} under agitation for 2 h at room temperature. After centrifugation, the purified clays were washed with distilled water for the removal of Cl^- ions; this was checked with a test with $AgNO_3$. The clay adsorption sites were activated with nitric acid (0.8 N) in a proportion of 10 mL g^{-1}. The activated clay samples were centrifuged, washed with distilled water, and dried at 60 °C for 24 h.

4.2.3. Synthesis of the $ZnTiO_3/TiO_2$ Semiconductor

The $ZnTiO_3/TiO_2$ compound was synthesized following a modified sol-gel method described by other authors [53,54]. A quantity of TiIPO in iPrOH (70 v/v%) was dissolved at room temperature. An aqueous solution formed by Zn(acet)/water/iPrOH was slowly added, using ZnO/TiO_2 at 1:3 molar ratio. The amount of water was stoichiometric for hydrolyzing the TiIPO molecules, adding a solution containing a 50 v/v% iPrOH/water ratio. The synthesis was performed at room temperature. The reaction system was additionally stirred for 30 min. The mixture was kept under stirring at room temperature for another 30 min after the formation of a precipitate. The precipitate was dried at 60 °C for 24 h and calcined at 500 °C for 4 h. Finally, the products were cooled at room temperature.

4.2.4. Synthesis of Zeolite from Ecuadorian Clays

The synthesis conditions were set based on previous work on zeolite synthesis from aluminosilicate gels [55,56]. The preliminary process consisted of the following steps: 20 g of each clay were mixed with 25 g of NaOH in 50 mL of water, to form a homogeneous mud. Each clay-NaOH mud was calcined at 800 °C for 5 h.

To synthesize zeolite from R-Clay, the necessary reagents were added until reaching the composition established for the synthesis mixture: SiO_2/Al_2O_3 = 2.47, Na_2O/SiO_2 = 3.0, H_2O/Na_2O = 20. The calcined product was crushed and suspended in 125 mL of water. The mixture was stirred and homogenized at room temperature for 1 h. Hydrothermal treatment of the mixture was carried out in covered containers and heated to 90 °C for 2 h. Finally, the solid product was filtered, washed with water to remove excess alkali, and dried at 90 °C overnight. The main product obtained with this procedure was labeled R-Zeolite and identified as Na-LTA type zeolite with small amounts of Na-FAU type zeolite. To synthesize zeolite from G-Clay, the necessary reagents were added to achieve the composition established for the synthesis mixture: SiO_2/Al_2O_3 = 4.0, Na_2O/SiO_2 = 1.65, H_2O/Na_2O = 40. The calcined product was crushed and suspended in 128 mL of water. The mixture was stirred at room temperature for 1 h, to homogenize. Subsequently, the solution was aged for 24 h at room temperature. After this, hydrothermal treatment of the mixture was carried out in covered containers and heated to 90 °C for 24 h. Finally, the solid product was filtered, washed with water to remove excess alkali, and dried at 90 °C overnight. The main product obtained with this procedure was labeled G-Zeolite and consisted of Na-FAU type zeolite with small amounts of Na-P1 type zeolite.

4.2.5. Preparation of Extruded Composites

For the evaluation of solid materials, cylindrical extrudates with approximate dimensions of 1.0 cm in length and 0.2 cm in diameter were prepared. The preparation of these solids was performed by mixing the $ZnTiO_3/TiO_2$ semiconductor with zeolite and the precursor clay at a ratio of 30:30:40, respectively. Extrudates were also prepared by mixing the $ZnTiO_3/TiO_2$

semiconductor with clay at a ratio of 60:40, respectively. Finally, clay extrudates were also prepared by the same process using only clay in the composition without adding any other components. An amount of water (approximately 35%) was added to each mixture to form a paste with good plasticity. These mixtures were extruded with a 2.5 mm diameter syringe. The extrudates were dried at 90 °C for 2 h and finally calcined at 500 °C for 8 h. The presence of clay is important for the formation of extrudates. In this study, extrudates prepared only with semiconductor and zeolite were not considered because they disintegrate easily. The extruded composites prepared were labeled as follows: R (R-Clay), RT (R-Clay and $ZnTiO_3/TiO_2$), RZT (R-Clay, R-Zeolite, and $ZnTiO_3/TiO_2$), G (G-Clay), GT (G-Clay and $ZnTiO_3/TiO_2$), GZT (G-Clay, G-Zeolite, and $ZnTiO_3/TiO_2$).

4.2.6. Characterization

The synthesized materials were characterized using a JEOL JSM 6400 scanning electron microscope (SEM-EDX) (JEOL, Peabody, MA, USA). X-Ray fluorescence (XRF) measurements were recorded in a Bruker S1 Turbo SDR portable spectrometer (Bruker Handheld LLC, Kennewick, WA, USA), using the Mining Light Elements measurement method. The X-ray diffraction (XRD) measurements were recorded in a Bruker AXS D8-Discover diffractometer (Bruker AXS, Karlsruhe, Germany) equipped with a vertical θ-θ goniometer, parallel incident beam (Göbel mirror), and a HI-STAR General AREA Diffraction Detection System (GADDS) (Bruker AXS, Karlsruhe, Germany). The X-ray diffractometer was operated at 40 kV and 40 mA to generate the Cu $K\alpha$ radiation (1.5406 Å). Data were recorded from 5 to 70° in the 2θ range. Identification of the crystal phases was achieved by comparison of the XRD profile with the ICDD (International Centre for Diffraction Data, release 2018) database. The determination of the specific surface area (SSA) of the solids (m^2/g) was carried out in the ChemiSorb 2720 equipment (Micromeritics, Norcross, GA, USA) coupled to temperature-programmed controller and software (TPx) by nitrogen adsorption at the temperature of liquid nitrogen (−196 °C) with a 30% gas mixture of N_2 diluted in He. The Chemisoft TPx System (version 1.03; Data analysis software; Micromeritics, Norcross, GA, USA, 2011) allowed calculating the specific surface area using the Brunauer-Emmet-Teller (BET) equation and the single point method. Finally, the adsorbents were also characterized by the point of zero charges (pH_{PZC})

at different pH values using a Jenway 7350 spectrophotometer (Cole-Parmer, Staffordshire, UK).

4.2.7. Adsorption Studies

The adsorption experiments were conducted using a batch method at room temperature. Typically, 25 mg of extruded adsorbents were magnetically stirred in a methylene blue aqueous solution (100 mL of water containing 20 mg mL^{-1} methylene blue). The remaining concentrations of methylene blue were determined at 623 nm using a Jenway 7350 spectrophotometer (Cole-Parmer, Staffordshire, UK). The adsorption rate of MB was calculated by the absorbance according to the Beer–Lambert law. Samples were drawn at 5 min intervals with a syringe and filtered through a 0.45 μm membrane filter to remove any solid particles interfering with the measurement. All tests were carried out in triplicate. The procedure was repeated using a methylene blue reference solution without extruded adsorbents to eliminate any photolysis effects causing discoloration of the solution due to natural light. The adsorbed quantity of methylene blue was calculated by Equation (4.1):

$$q_e = (C_0 - C_e) \times \frac{v}{w} \qquad \textbf{(4.1)}$$

where C_0 (mg L^{-1}) and C_e (mg L^{-1}) represent the initial and equilibrium concentration, respectively; v (L) is the volume of solution and w (g) is the mass of adsorbent.

4.2.7.1. Effect of pH

The effect of pH on MB adsorption onto the adsorbents was investigated under varying pH values from 3 to 10. The initial MB concentration used was 25 mg mL^{-1} for all extrudates. The contact time was fixed at 180 min and corresponded to the time necessary to reach adsorption equilibrium for all adsorbents. To evaluate the impact of pH on the solid surface, a point of zero charges pH_{PZC} measurement was also performed for all extrudates. The pH_{PZC} determinations were performed in aqueous suspensions of the extrudates at two concentrations (0.01 and 0.05 M) of the NaCl inert electrolyte. Potentiometric titrations were made over the entire pH range of 3–10.

4.2.7.2. Isotherm Models

The effect of the initial MB concentration was investigated from 0.25 to 30 mg L^{-1}. The experiments were performed without adjusting the pH of the solution. At the end of the experiments, the equilibrium pH was measured and found to be constant, around 7 for each adsorbent. The equilibrium sorption of MB was evaluated according to the Langmuir and Freundlich isotherm models, since these models can help to explain the adsorption mechanism and the heterogeneity of the adsorbent surface [15,48,57].

The expression of the Langmuir isotherm model can be expressed by Equation (4.2):

$$\frac{C_e}{q} = \frac{1}{K_L q_{max}} + \frac{C_e}{q_{max}} \tag{4.2}$$

where $q_{\max}$ is the maximum monolayer adsorption, K_L is the equilibrium Langmuir constant related to the adsorption energy, and C_e is the concentration of solute at equilibrium. Additionally, the R_L separation factor values, which provide an insight into the nature of adsorption, can be expressed by Equation (4.3):

$$R_L = \frac{1}{(1+K_L C_e)} \tag{4.3}$$

The expression of the Freundlich isotherm model can be represented by Equation (4.4):

$$q = K_F C_e^{1/n} \tag{4.4}$$

where K_F is the Freundlich constant, which indicates the adsorption affinity of the adsorbents and $1/n$ is another constant that represents the intensity of adsorption.

4.2.7.3. Kinetic Models

The solute absorption rate of the solute–solution interface was described in this study using reaction-based models, called pseudo-first-order and pseudo-second-order, as well as diffusion-based models, called intraparticle diffusion, external-film diffusion, and internal-pore diffusion [2].

The pseudo-first- and second-order models assume that the difference between the average solid-phase concentration (q_t) and the equilibrium concentration (q_e) is the driving force for adsorption and that the overall adsorption rate is proportional to this driving force. Both equations have been widely applied to explain the experimental results obtained for aqueous pollutants such as dyes and metal ions [15,48,57]

The pseudo-first-order kinetic model is expressed by Equation (4.5):

$$\ln(q_e - q_t) = \ln(q_e) - k_1 t \qquad \textbf{(4.5)}$$

where k_1 is the rate constant (min^{-1}), and q_e and q_t represent the MB adsorbed per unit weight (mg g^{-1}) at equilibrium and at any time t, respectively.

The pseudo-second-order kinetic is expressed by Equation (4.6):

$$\frac{t}{q_t} = \frac{1}{k_2 q_e^2} + \frac{1}{q_e} t \qquad \textbf{(4.6)}$$

where k_2 is the pseudo-second-order rate constant ($\text{g mg}^{-1}\ \text{min}^{-1}$).

The intraparticle diffusion model assumes that intraparticle diffusion is the rate control step, which is generally the case for well-mixed solutions [6]. The mathematical expression of the intraparticle diffusion model is described by Equation (4.7):

$$q_t = k_3 t^{1/2} + A \tag{4.7}$$

where k_3 (mg g^{-1} $min^{-1/2}$) is the intraparticle diffusion rate constant and A (mg g^{-1}) is a constant that indicates the thickness of the boundary layer, i.e., the higher the value of A, the greater the boundary layer effect. In some cases, the plot q_t versus square root time can show multi-linearity, which indicates that several steps occur in the process.

The internal-pore diffusion model was also used to describe the kinetic sorption data. If particle diffusion controls (D_p) the sorption rate is described using Equation (4.8):

$$-ln\left(1-\left(\frac{q_t}{q_e}\right)^2\right) = \frac{2\pi^2 D_p}{r^2}\, t \tag{4.8}$$

When the rate of sorption is controlled by external-film diffusion, it is expressed by Equation (9):

$$-ln\left(1-\left(\frac{q_t}{q_e}\right)\right) = \frac{D_f C_s}{h\, r\, C_z}\, t \tag{4.9}$$

where q_t and q_e are the solute loadings on the adsorbent phase at time t and at equilibrium (mg g^{-1}), respectively, t is the contact time (min), C_s (mg L^{-1}) and C_z (mg kg^{-1}) are the ion concentrations in the solution and in the adsorbent, respectively, r is the average radius of the adsorbent particles (1×10^{-7} m), and h is the film thickness around the adsorbent particles, accepted as 10^{-6} m for poorly stirred solutions [58]. D_p is the diffusion coefficient in the adsorbent phase (m^2 min^{-1}) and D_f (m^2 min^{-1}) is the diffusion in the film phase surrounding the adsorbent particles.

4.2.7.4. Reuse of the Adsorbents

In this study, composites were desorbed after completing one treatment cycle and reused to determine their recycling property. MB desorption from composites loaded with this dye was verified using pure methanol and methanol solutions containing 6% (v/v) acetic acid as eluent.

After desorption, the composites were dried and used in a new cycle under the same conditions as the previous cycle. The recycling experiments were carried out in three cycles.

4.3. Results

4.3.1. Characterization of the Compounds

4.3.1.1. XRD Analysis

Figure 4.1 presents the XRD patterns of red clay (R-Clay), zeolites synthesized from this clay (R-Zeolite), gray clay (G-Clay), zeolites synthesized from this clay (G-Zeolite), and the $ZnTiO_3/TiO_2$ semiconductor. These compounds were used as precursors to prepare extruded composites.

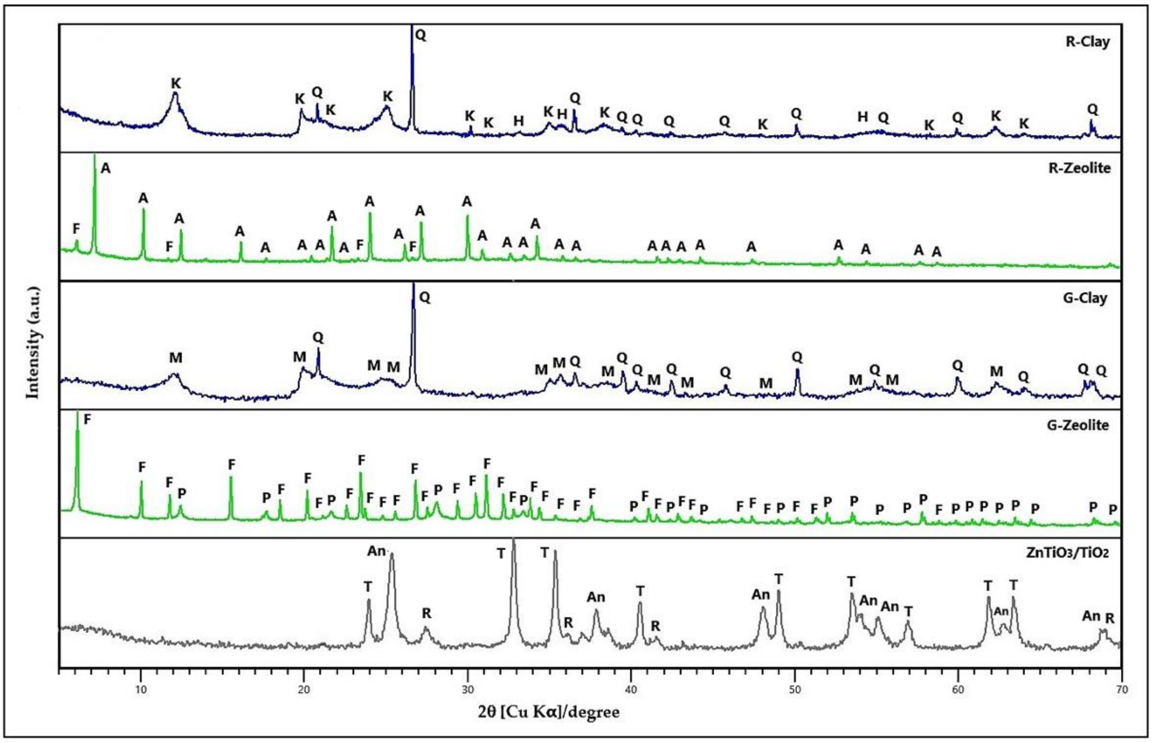

Figure 4. 1. X-ray diffraction (XRD) pattern of R-Clay, R-Zeolite, G-Clay, G-Zeolite, and $ZnTiO_3/TiO_2$. K: Kaolinite, Q: Quartz, H: Hematite, M: Metahalloysite, Q: Quartz, F: FAU zeolite, A: LTA zeolite, P: Na-P1 zeolite, T: Titanate, An: Anatase, R: Rutile.

R-Clay consists of quartz (Q), kaolinite (K) and hematite (H). R-Zeolite consists of LTA, and FAU zeolites. Figure 4.1 shows the main diffraction peaks of LTA zeolite of the sodium form (see Appendices, Table B1). The LTA zeolite was indexed to cubic phase with unit cell parameters a = b = c = 24.61 Å and space group Fm3c(226) according to the standard ICDD card No: 39-0222. Figure 4.1 also shows the main diffraction peaks of the FAU zeolite of the sodium form (see Appendices, Table B1). The FAU zeolite was indexed to cubic phase with unit cell parameters a = b = c = 25.028 Å and space group Fd-3(203) according to the standard ICDD card No: 39-0218. The zeolites presented a percentage of crystallinity of 67% compared to the standards.

On the other hand, G-Clay consists of quartz (Q) and metahalloysite (M). G-Zeolite consists of FAU and Na-P1 zeolites. Figure 4.1 shows the main diffraction peaks of the FAU zeolite of the sodium form (see Appendices, Table B1). The FAU zeolite was indexed to cubic phase with unit cell parameters a = b = c = 25.028 Å and space group Fd-3(203) according to the standard ICDD card No: 39-0218. The number of structural Al atoms in the FAU and the structural Si/Al ratio of this zeolite were calculated using the Breck–Flanigen equation [59]. The results obtained (N_{Al} = 89 and Si/Al = 1.2) classify the synthesized FAU zeolite as type X [27].

Figure 4.1 also shows the main diffraction peaks of the Na-P1 zeolite (see Appendices, Table B1). The Na-P1 zeolite was indexed to tetragonal phase with unit cell parameters a = b = 9.999 Å and c = 10.069 Å and space group $I4_1$/amd(141) according to the standard ICDD card No: 44-0052. The zeolites presented a percentage of crystallinity of 63% compared to the standards.

Finally, Figure 4.1 shows the main diffraction peaks of the $ZnTiO_3/TiO_2$ heterostructure (see Appendices, Table B1). The $ZnTiO_3/TiO_2$ heterostructure nanomaterial obtained was indexed to hexagonal phase with unit cell parameters a = b = 5.08 Å and c =13.93 Å and space group R-3(148) according to the standard JCPDS card No. 00-015-0591 for the $ZnTiO_3$ phase. The TiO_{2-a} species was indexed to tetragonal phase with unit cell parameters a = b = 3.79 Å and c = 9.51 Å and space group $I4_1$/amd(141) according to the standard JCPDS card No. 01-073-1764. The

TiO_{2-r} phase was assigned to tetragonal phase with unit cell parameters a = b = 5.08 Å and c = 13.93 Å and space group P42/mnm(136) according to the standard JCPDS card No. 03-065-0192.

When comparing the diffraction patterns of the extruded composites with their respective constituent compounds (see Appendices, Figures B1 and B2), no alteration of the diffraction peaks of the zeolites or the mixed oxide $ZnTiO_3/TiO_2$ was observed, probably due to the calcination temperature of the extruded composites being lower than the thermal stability of the zeolites [60] and mixed oxide [26] used. Therefore, the calcination temperature of 500 °C made it possible to achieve a mechanically strong adsorbent while keeping the crystalline structure of the zeolites and the photocatalyst intact.

4.3.1.2. SEM-EDX Analysis

Figure 4.2 presents the EDX (energy dispersive X-ray) spectra of clays and zeolites obtained from these clays, indicating the presence of several elements such as C, Al, Si, Fe, Ca, Na, K, Mg, and O. G-Clay and G-Zeolite had more exchange cations than R-Clay and R-Zeolite; however, R-Clay and R-Zeolite had a larger amount of Fe than G-Clay and G-Zeolite. In R-Clay the Fe was in the form of hematite, according to the diffraction pattern shown in Figure 1. Zeolites had a higher amount of sodium than their respective clays due to the calcination treatment carried out before synthesis. Figure 4.2 also shows the EDX spectra of the $ZnTiO_3/TiO_2$ heterostructure, indicating the presence of O, Zn and Ti.

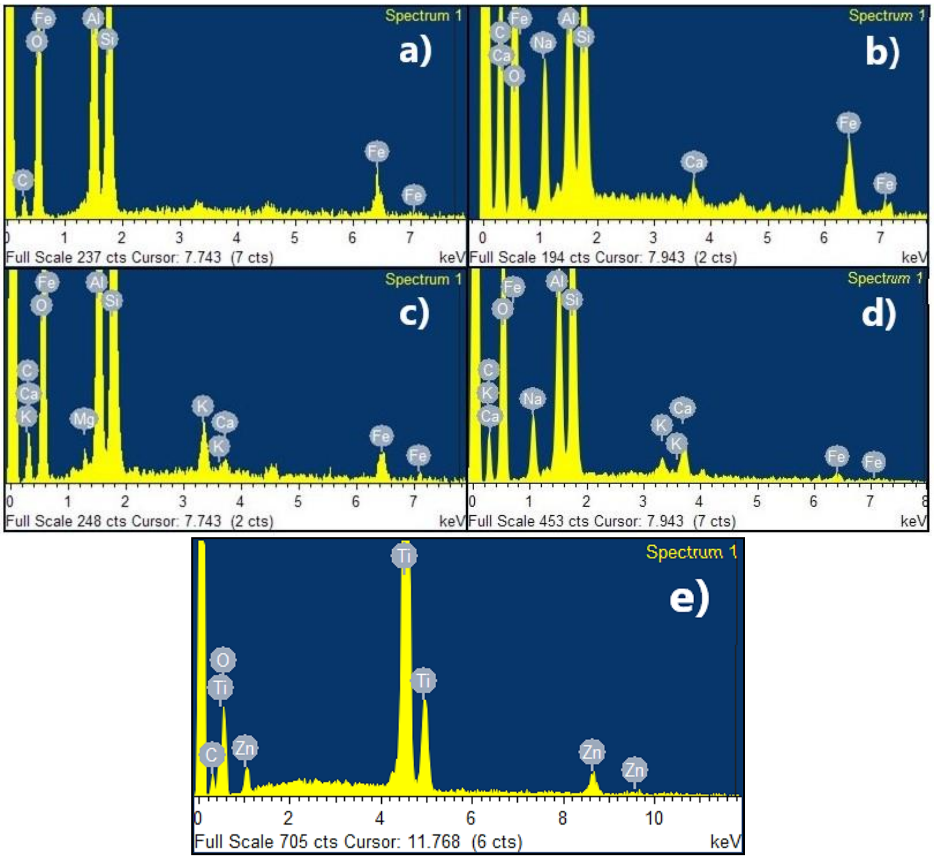

Figure 4. 2. Energy dispersive X-ray (EDX) spectra of (a) R-Clay, (b) R-Zeolite, (c) G-Clay, (d) G-Zeolite and (e) $ZnTiO_3/TiO_2$.

Table 4.1 shows the elemental composition (%) analyzed by EDX for the clays and zeolites obtained from these clays and $ZnTiO_3/TiO_2$.

Table 4. 1. Elemental analysis (wt%) for clays and zeolites.

	C	O	Si	Al	Fe	Na	Ca	K	Mg	Ti	Zn	O
R-Clay	12.10	47.71	19.08	15.40	5.72	-	-	-	-	-	-	-
R-Zeolite	32.43	47.89	6.49	5.01	3.91	3.79	0.48	-	-	-	-	-
G-Clay	16.99	46.46	18.17	12.22	3.27	-	0.54	1.84	0.53	-	-	-
G-Zeolite	20.77	50.91	14.44	6.77	1.88	2.70	1.88	0.65	-	-	-	-
$ZnTiO_3/TiO_2$	5.42	-	-	-	-	-	-	-	-	54.85	6.13	33.60

Figure 4.3 shows the SEM photomicrograph of clays and zeolites obtained from these clays. Figure 4.3(a) shows intertwined hematite crystals with a "cauliflower" habit coating kaolinite of the R-Clay, while in (b) and (c) uniformly distributed granules are observed with a perfect morphology, typical of the LTA phase, and non-uniform agglomerates of nanocrystals are

also observed on the well-formed LTA zeolite crystals, which can be attributed to the growth of the FAU phase during the synthesis of the zeolite. Additionally, the SEM photomicrograph in Figure 4.3(d) shows aggregates of G-Clay with varied morphology and sizes and with a very rough-appearing surface due to the conformation similar to “stacked fibers” that are a consequence of the possible grouping of halloysite nanotubes. In Figure 4.3(e), 4.3(f), the presence of uniformly distributed cubic spheroidal granules is observed, which correspond to the FAU zeolite. The particle sizes determined by SEM for both LTA and FAU zeolites were 1.6 and 3.9 μm, respectively. The sizes were determined using ImageJ, which is a powerful, oft-referenced program for image processing [61]. Finally, Figure 4.3(g) shows the SEM image of the $ZnTiO_3/TiO_2$ heterostructure. The image shows that the particles have a particle size less than 100 nm, are almost spherical and are highly agglomerated.

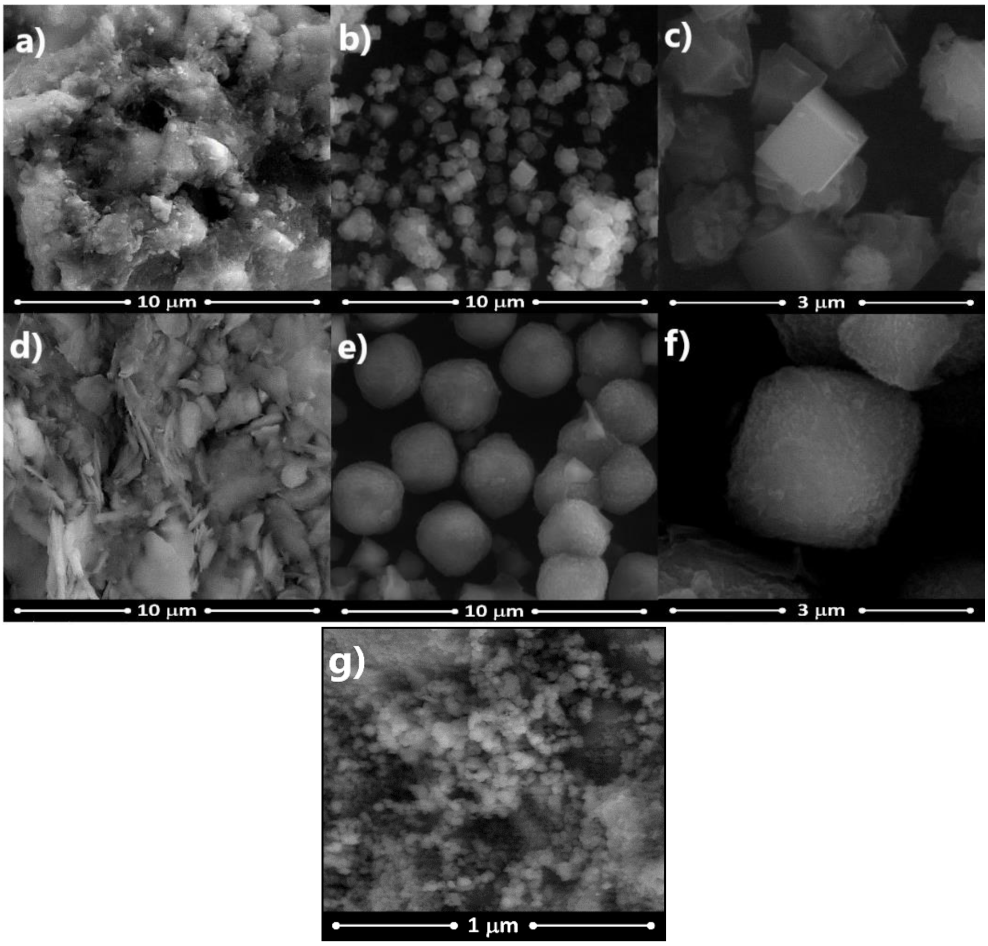

Figure 4. 3. Scanning electron microscopy (SEM) images of (a) R-Clay, (b) and (c) R-Zeolite, (d) G-Clay, (e) and (f) G-Zeolite, (g) $ZnTiO_3/TiO_2$.

4.3.1.3. XRF Analysis

Table 4.2 shows the main oxides present in the clays, zeolites, and compounds investigated in this study. In Table 4.2, the XRF analysis showed the majority presence of the cations Al, Si, Fe, Ca, K, Mg, and O in all the compounds, in addition to Ti and Zn, which were mainly incorporated as a mixed oxide of $ZnTiO_3/TiO_2$ in extrudates.

Table 4. 2. Composition (%) of clays, zeolites, and composites.

Compound	Al_2O_3	SiO_2	K_2O	CaO	TiO_2	MgO	Fe_2O_3	ZnO
G-Clay	21.20 (±0.85)	45.60 (±0.68)	1.63 (±0.03)	0.22 (±0.01)	0.39 (±0.01)	0.16 (±0.00)	1.94 (±0.01)	0.01 (±0.00)
G-Zeolite	19.60 (±0.79)	41.30 (±0.63)	0.49 (±0.02)	4.11 (±0.02)	0.19 (±0.01)	0.07 (±0.00)	0.70 (±0.01)	0.06 (±0.00)
GT	11.60 (±1.56)	12.20 (±0.53)	0.32 (±0.03)	1.59 (±0.02)	51.30 (±0.13)	0.04 (±0.01)	3.64 (±0.03)	18.95 (±0.05)
GZT	18.00 (±1.20)	34.60 (±0.68)	1.58 (±0.04)	2.67 (±0.03)	28.10 (±0.08)	0.07 (±0.01)	2.38 (±0.02)	12.29 (±0.03)
R-Clay	27.10 (±0.98)	39.40 (±0.65)	0.78 (±0.02)	0.12 (±0.01)	1.01 (±0.01)	0.09 (±0.00)	7.81 (±0.02)	0.01 (±0.00)
R-Zeolite	18.60 (±0.99)	27.60 (±0.59)	-	1.52 (±0.02)	1.09 (±0.01)	0.08 (±0.00)	6.72 (±0.02)	0.08 (±0.00)
RT	8.88 (±1.62)	13.90 (±0.58)	1.19 (±0.04)	1.69 (±0.02)	51.40 (±0.14)	-	2.09 (±0.03)	20.66 (±0.06)
RZT	10.10 (±1.31)	15.60 (±0.58)	0.38 (±0.59)	2.20 (±0.50)	31.30 (±1.82)	0.06 (±0.16)	7.87 (±0.69)	16.30 (±0.07)

4.3.1.4. Specific Surface Area (SSA) Analysis

The specific surface area of the adsorbents in both powder and extrudate form are summarized in Table 4.3. The prepared extruded composites had a smaller surface area compared to that of adsorbents in powder form due to the heat treatment required for their preparation. Despite the reduction in the specific surface area in the extrudates, the presence of exchange cations in their structure could contribute to the elimination of the dye from the solution since different mechanisms participate in the adsorption process.

Table 4. 3. Specific surface area (SSA) (m^2/g) of clays, zeolites, and composites.

Adsorbent	Composition	Form	SSA (m^2/g)
R-Clay	Red clay	Powder	48.8
R-Clay (R)	Red clay	Extrudate	29.3
R-Zeolite	LTA/FAU zeolites	Powder	104
R-Composite	Red clay + $ZnTiO_3/TiO_2$	Powder	82.5
R-Composite (RT)	Red clay + $ZnTiO_3/TiO_2$	Extrudate	29.5
R-Composite	Red clay + LTA/FAU zeolites + $ZnTiO_3/TiO_2$	Powder	84.1
R-Composite (RZT)	Red clay + LTA/FAU zeolites + $ZnTiO_3/TiO_2$	Extrudate	31.1
G-Clay	Gray clay	Powder	42.8
G-Clay (G)	Gray clay	Extrudate	25.5
G-Zeolite	FAU/Na-P1 zeolites	Powder	349
G-Composite	Gray clay + $ZnTiO_3/TiO_2$	Powder	184
G-Composite (GT)	Gray clay + $ZnTiO_3/TiO_2$	Extrudate	25.8
G-Composite	Gray clay + FAU/Na-P1 zeolites + $ZnTiO_3/TiO_2$	Powder	188
G-Composite (GZT)	Gray clay + FAU/Na-P1 zeolites + $ZnTiO_3/TiO_2$	Extrudate	26.4

4.3.2. Adsorption of MB

Figure 4.4 shows that G-Zeolite and G-Clay had a higher adsorption capacity of the MB dye than R-Zeolite, R-Clay, and the $ZnTiO_3/TiO_2$ semiconductor. The results of the evaluation of powder samples. As expected, zeolites had better adsorption capacity than clays and mixed oxide of Zn and Ti. Additionally, G-Zeolite had better MB adsorption capacity than R-Zeolite and, similarly, G-Clay had better MB adsorption capacity than R-Clay. In addition, the higher adsorption capacity of G-Zeolite compared to R-Zeolite may be due to the much larger pore of FAU zeolite compared to LTA zeolite.

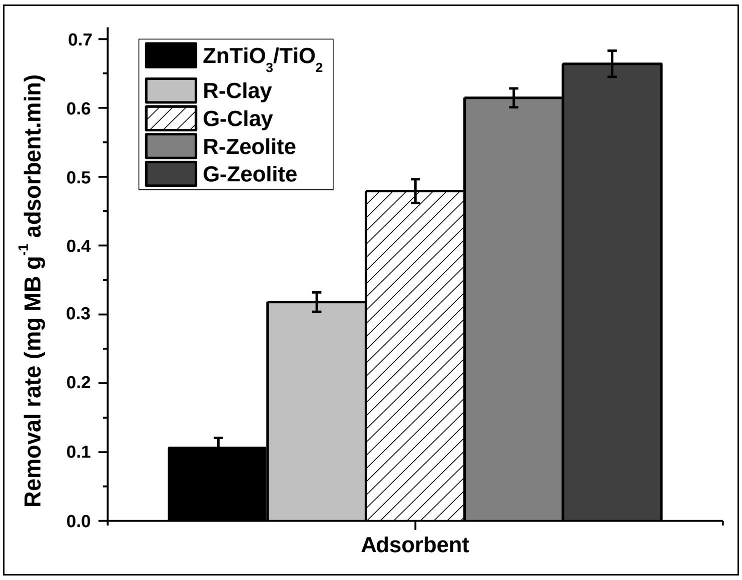

Figure 4. 4. Methylene blue (MB) removal capacity of the $ZnTiO_3/TiO_2$ semiconductor, R-Clay, R-Zeolite, G-Clay, and G-Zeolite.

4.3.2.1. Effect of pH

The R and G extrudates showed pH_{PZC} values around 4.0, while the GT, GZT, RT, and RZT extrudates showed pH_{PZC} values around 6.0. At a pH higher than pH_{PZC}, the surface had a net negative charge and the adsorption of the cationic dye molecule was promoted. However, MB adsorption was reduced at a pH lower than pH_{PZC} due to the net positive charge on the surface, which causes electrostatic repulsion. Figure 4.5 shows this effect of pH on (G) G-Clay, (GT) G-Clay-$ZnTiO_3/TiO_2$, (GZT) G-Clay-Zeolite-$ZnTiO_3/TiO_2$, (R) R-Clay, (RZ) R-Clay-$ZnTiO_3/TiO_2$ and (RZT) R-Clay-Zeolite-$ZnTiO_3/TiO_2$.

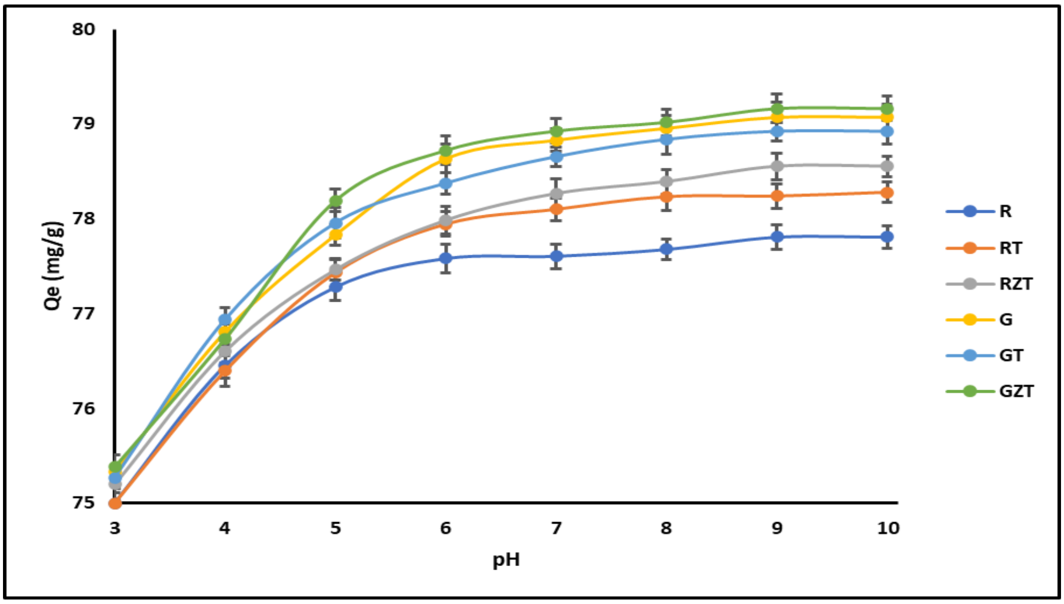

Figure 4. 5. Effect of pH on the adsorption of MB onto composites.

From the minimal increment in adsorption of MB in the solution at pH values above 8, it was decided that adsorption at pH 7 was the optimum operating condition for adsorption experiments.

4.3.2.2. Adsorption Isotherm

Figure 4.6 shows the adsorption isotherms of the extruded composites: (G) G-Clay, (GT) G-Clay-$ZnTiO_3/TiO_2$, (GZT) G-Clay-Zeolite-$ZnTiO_3/TiO_2$, (R) R-Clay, (RZ) R-Clay-$ZnTiO_3/TiO_2$, and (RZT) R-Clay-Zeolite-$ZnTiO_3/TiO_2$. In this figure, it is evident that the Langmuir model is better than the Freundlich model to describe the behavior of all composites.

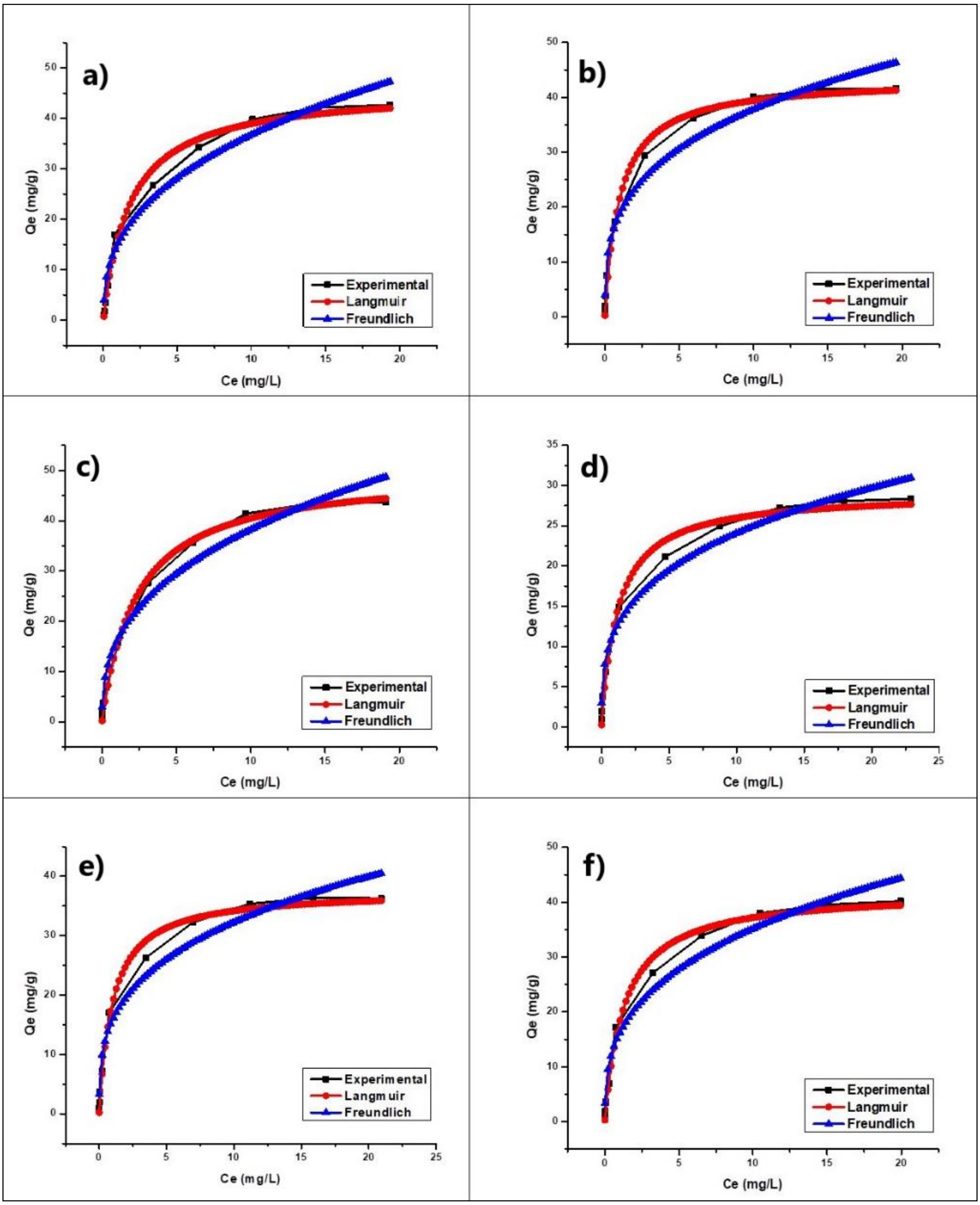

Figure 4. 6. Adsorption isotherm of (a) G, (b) GT, (c) GZT, (d) R, (e) RT and (f) RZT.

Table 4.4 shows the equilibrium data of MB sorption by extruded composites (G) G-Clay, (GT) G-Clay-$ZnTiO_3/TiO_2$, (GZT) G-Clay-Zeolite-$ZnTiO_3/TiO_2$, (R) R-Clay, (RZ) R-Clay-$ZnTiO_3/TiO_2$ and (RZT) R-Clay-Zeolite-$ZnTiO_3/TiO_2$. Furthermore, the R_L separation factor or equilibrium parameter was calculated using Equation (3), obtaining low R_L values for all the adsorbents. When $0 < R_L < 1$, favorable adsorption was indicated, and $R_L > 1$ meant unfavorable adsorption; $R_L = 0$ indicated irreversible adsorption [11].

Table 4. 4. Isotherm parameters for MB adsorption on composites.

Isotherm	Parameters	R	RT	RZT	G	GT	GZT
Langmuir	q_{max}	29.14	37.59	42.00	45.88	43.40	49.81
	(mg g^{-1})	(±0.97)	(±0.98)	(±1.16)	(±1.65)	(±1.33)	(±1.33)
	K_L	0.82	1.00	0.77	0.56	0.99	0.43
	(L mg^{-1})	(±0.15)	(±0.14)	(±0.11)	(±0.09)	(±0.17)	(±0.05)
	R_L	0.06	0.05	0.06	0.08	0.05	0.10
	χ^2	2.00	2.11	2.34	3.36	3.38	1.60
	R^2	0.98	0.99	0.99	0.99	0.99	0.99
Freundlich	K_F	11.98	15.88	16.16	15.26	18.80	16.12
	(L mg^{-1})	(±0.92)	(±1.46)	(±1.55)	(±1.62)	(±1.58)	(±1.59)
	N	3.30	3.25	2.96	2.62	3.30	2.66
		(±0.32)	(±0.39)	(±0.34)	(±0.30)	(±0.37)	(±0.29)
	$1/n$	0.30	0.31	0.34	0.38	0.30	0.38
	χ^2	3.81	9.84	11.10	12.40	11.50	11.10
	R^2	0.97	0.96	0.96	0.96	0.96	0.97

4.3.2.3. Adsorption Kinetics

Figure 4.7 shows the time-course variation of concentration C_t (mg L^{-1}) curves of the extruded composites (G) G-Clay, (GT) G-Clay-$ZnTiO_3/TiO_2$, (GZT) G-Clay-Zeolite-$ZnTiO_3/TiO_2$, (R) R-Clay, (RZ) R-Clay-$ZnTiO_3/TiO_2$ and (RZT) R-Clay-Zeolite-$ZnTiO_3/TiO_2$. The figure shows that the MB concentration in the solution decreased rapidly around the first 60 min, after which removal tended to become constant.

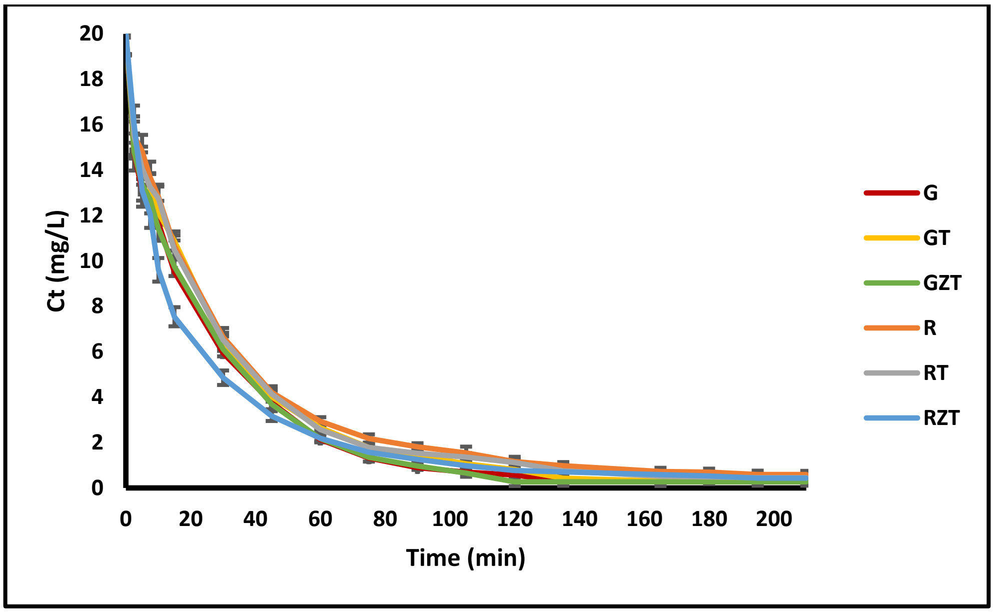

Figure 4. 7. Time-course variation of the composites' C_t (mg L^{-1}) curves.

The intra-particle diffusion model fitted well the experimental data, as can be seen in Figure 4.8, indicating that the entire sorption process was divided into two linear regions. Hence, the MB sorption process might be described by film diffusion followed by a particle diffusion process [6].

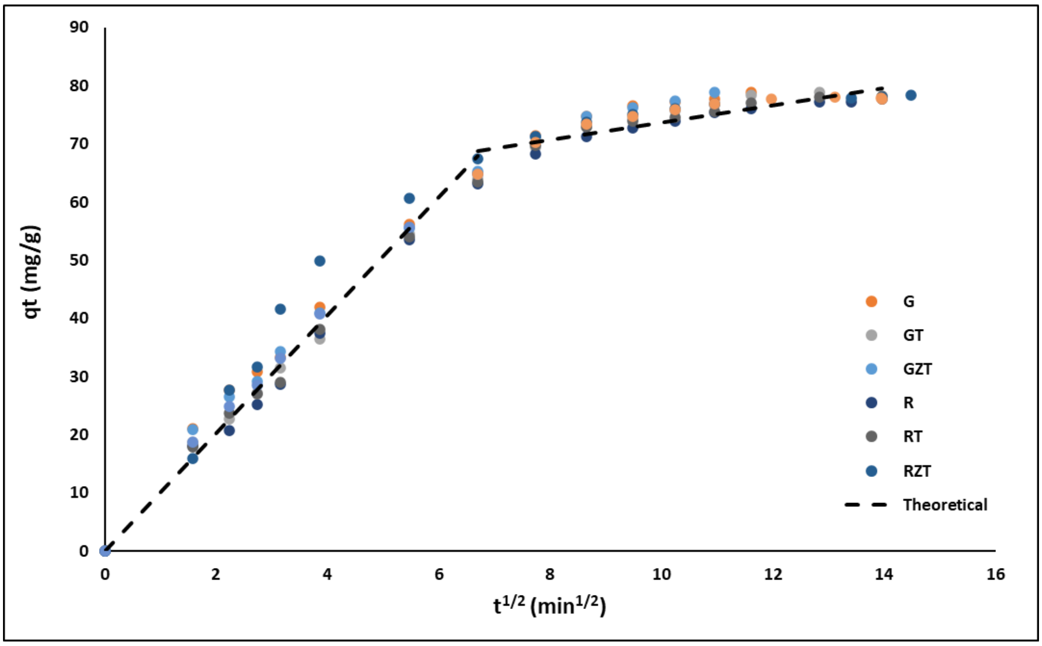

Figure 4. 8. Intra-particle diffusion plots for MB removal by the extrudates.

Table 4.5 shows the equilibrium data of MB sorption by the extruded composites (G) G-Clay, (GT) G-Clay-$ZnTiO_3/TiO_2$, (GZT) G-Clay-Zeolite-$ZnTiO_3/TiO_2$, (R) R-Clay, (RZ) R-Clay-$ZnTiO_3/TiO_2$ and (RZT) R-Clay-Zeolite-$ZnTiO_3/TiO_2$.

Table 4. 5. Kinetic parameters for MB removal on composites.

Kinetic Parameters		**R**	**RT**	**RZT**	**G**	**GT**	**GZT**
Pseudo-first-order	q_{max}	75.47	75.84	75.50	76.43	76.57	76.37
	(mg g^{-1})	(±1.15)	(±1.35)	(±1.04)	(±1.73)	(±1.42)	(±1.87)
	k_1	0.05	0.05	0.07	0.06	0.05	0.06
	(L mg^{-1})	(±3.28 x 10^{-3})	(±3.90 x 10^{-3})	(±4.73 x 10^{-3})	(±5.75 x 10^{-3})	(±3.99 x 10^{-3})	(±5.75 x 10^{-3})
	χ^2	11.20	14.30	10.10	22.60	15.50	22.60
	R^2	0.98	0.98	0.98	0.97	0.98	0.97
Pseudo-second-order	q_{max}	85.45	85.90	82.92	85.99	87.01	87.16
	(mg g^{-1})	(±1.20)	(±1.41)	(±0.48)	(±1.64)	(±1.44)	(±1.84)
	k_2	6.89 x 10^{-4}	7.19 x 10^{-4}	1.16 x 10^{-3}	8.66 x 10^{-4}	6.97 x 10^{-4}	8.02 x 10^{-4}
	(L mg^{-1})	(±5.29 x 10^{-5})	(±6.31 x 10^{-5})	(±3.97 x 10^{-5})	(±8.82 x 10^{-5})	(±6.09 x 10^{-5})	(±8.57 x 10^{-5})
	χ^2	5.04	6.45	1.14	8.78	6.40	8.74
	R^2	0.99	0.99	1.00	0.99	0.99	0.99
Intraparticle diffusion	k_3	5.50	5.72	4.92	6.61	6.28	7.10
	(mg g^{-1} min$^{-1/2}$)	(±0.40)	(±0.28)	(±0.36)	(±0.29)	(±0.26)	(±0.79)
	A	13.58	13.55	21.13	12.47	11.35	10.34
		(±1.75)	(±1.25)	(±1.57)	(±1.27)	(±1.16)	(±3.49)
	R^2	0.90	0.90	0.81	0.94	0.93	0.95
External-film diffusion	D_f (m^2 min^{-1})	1.10 x 10^{-11}	1.21 x 10^{-11}	1.13 x 10^{-11}	1.38 x 10^{-11}	1.25 x 10^{-11}	1.42 x 10^{-11}
	R^2	0.99	0.98	0.99	0.99	0.98	0.99
Internal-pore diffusion	D_p (m^2 min^{-1})	1.3 x 10^{-17}	1.4 x 10^{-17}	1.3 x 10^{-17}	1.6 x 10^{-17}	1.4 x 10^{-17}	1.6 x 10^{-17}
	R^2	0.98	0.97	0.98	0.98	0.97	0.98

4.3.3. Reuse of the Adsorbents

Figure 4.9 shows the MB adsorption capacity for three cycles of the extruded composites (G) G-Clay, (GT) G-Clay-$ZnTiO_3/TiO_2$, (GZT) G-Clay-Zeolite-$ZnTiO_3/TiO_2$, (R) R-Clay, (RZ) R-Clay-$ZnTiO_3/TiO_2$, and (RZT) R-Clay-Zeolite-$ZnTiO_3/TiO_2$. The figure shows that the adsorption capacity of composites containing zeolite decreased more than in extrudates without zeolite after the first and second regeneration cycles when an acid solution was used for desorption.

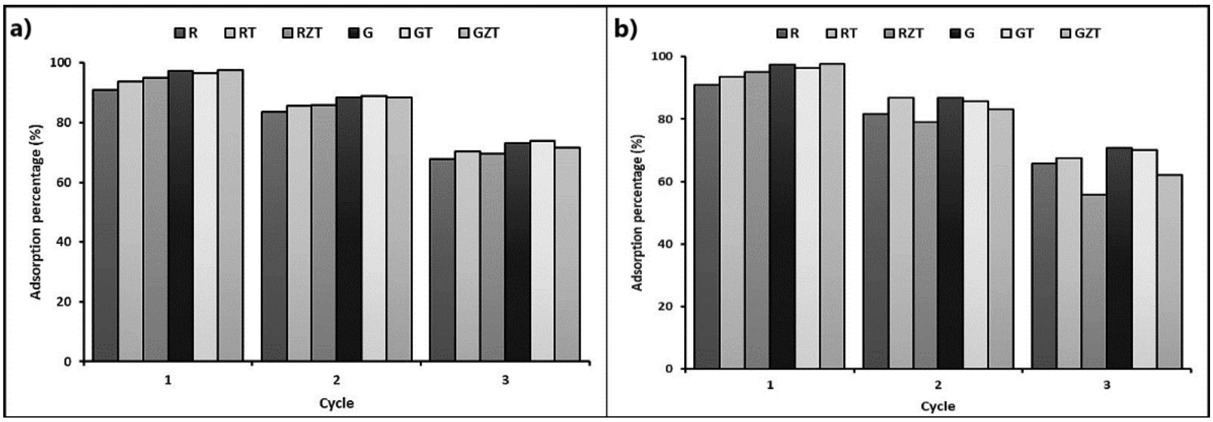

Figure 4. 9. Adsorption percentage of MB for three successive adsorption cycles. (a) Composites desorbed with methanol; (b) composites desorbed with an acid solution.

4.4. Discussion

4.4.1. Synthesis and Characterization of Compounds

Firstly, the structural identification of the clays, zeolites, and mixed oxide of Zn and Ti was performed using XRD. When comparing in Figure 4.1 the diffraction patterns of the zeolites with the respective clays, disappearance of the quartz reflections and the other mineralogical phases present in the clays was observed. Next, the diffraction patterns of the zeolites evidenced the appearance of peaks corresponding to the LTA-FAU and FAU-NaP$_1$ phases. The presence of these phases revealed the transformation of the clays, which could begin with the formation of an amorphous material followed by the subsequent co-crystallization of the LTA-FAU and FAU-NaP$_1$ zeolitic phases. On the one hand, these results are consistent with the metastable character of the zeolitic phases obtained; in agreement with the literature, the mix of stable metaphases was favored by the differences in the Si/Al ratio and the effect of the cations present in the original clays [62–64]. On the other hand, the percentages of the crystalline phase of R-Zeolite and G-Zeolite were determined using XRD, being 67% and 63%, respectively. In general, the amorphous phase formation can be related to the presence of geopolymers [65,66]. Specifically, geopolymers can be identified as the amorphous equivalent of crystalline structures of aluminosilicates with an equal chemical composition of the zeolites, but those presented a disordered structure unlike the ordered structure of zeolites [67–69]. Regarding the results, the diffraction pattern showed that R-Clay was formed from kaolinite (K), quartz (Q), and hematite (H), while G-Clay consisted mainly of metahalloysite (M) and quartz (Q). Furthermore, Figure 4.1 shows the diffraction pattern of the $ZnTiO_3/TiO_2$ heterostructure, which was obtained without impurities, as we reported in previous works [26].

In this study, clays and zeolites were also characterized by EDX to determine their chemical composition. In previous works, the characterization by EDX of the mixed oxide of Zn and Ti was presented. From the EDX results shown in Figure 4.2, the change in the weight percentage of the synthesized materials was observed after the treatment carried out to obtain zeolites. In general, the impurities of the starting clays decreased either by the action of the thermal and hydrothermal treatments and/or by dilution effects after the addition of new components in the synthesis gel, such as alumina and NaOH [70]. However, the percentages of Na^+ increased significantly due to the incorporation of NaOH as a mineralizing agent in the synthesis of the zeolites [71,72]. This specific fact is due to the capture of Na^+ ions by the zeolitic structure, to neutralize the negative charge of aluminum in the zeolite and/or geopolymer when they have been formed [73]. On the other hand, from the XRF analysis, the presence of various oxides in the sorbents studied was determined. Table 4.2 shows that the sorbents were mainly made up of SiO_2, Al_2O_3, TiO_2, ZnO, as well as lower percentages of Fe_2O_3, K_2O, CaO, and MgO. These oxides provided qualities to the sorbents to improve the adsorption of methylene blue by cation exchange.

The morphological and textural characterization of the clays and zeolites was performed to have a more complete characterization map of these solids. The morphology of the clays and zeolites was identified by scanning electron microscopy (SEM). The SEM photomicrographs obtained and presented in Figure 4.3 show the morphology of the clays according to their mineralogical composition. Likewise, Figure 4.3 shows the typical morphology of the LTA and FAU phases, which are similar to those described by various authors for these phases [74–76].

To characterize the textural properties of the materials, the specific surface area of the synthesized materials was determined by the physisorption of N_2. The results listed in Table 4.2 show that the extrudate materials had a lower specific surface area than the powdered ones. Probably, the thermal conditions used in the calcination of the extrudates reduced their surface area [77,78].

The decrease in the surface area of the extruded adsorbents is essentially attributed to the elimination of some of the constituents from the internal surface of the clay (e.g., adsorbed species) after the calcination process. The removal of these constituents created additional spaces within the wide pores of the clay structure and also resulted in a reduction of the internal surface area probably due to shrinkage. It is believed that this behavior, due to the increase in temperature, occurred due to the elimination of the physisorbed water as well as the superficial hydroxyl groups weakly attached to the clay structure [79]. In the present study, the addition of zeolites as a porous material to the extruded adsorbents did not improve their MB adsorption capacity from the aqueous solution. Although clay used as an inorganic binder provided strength and wear resistance in extruded adsorbents, the incorporation of clay can dilute the active porous component (i.e., the zeolite), resulting in a reduced specific surface area. Also, the clay could coat the surface of the zeolite and cause the pores to become blocked. Consequently, the MB removal capacity in aqueous systems of extrudates having zeolite did not improve compared to extrudates free of zeolite. These results are in agreement with that reported by Akhtar et al. [39]

Although usually the powdered materials have a higher specific surface area, in this study the extrudates were chosen to adsorb MB due to their appropriate mechanical and chemical stability, which facilitated their recovery at the end of the process and their reuse after several cycles.

4.4.2. Adsorption of MB

Preliminary batch adsorption of MB was performed from an aqueous solution to investigate the adsorption properties of clays, zeolites, and $ZnTiO_3/TiO_2$, which were used in powder form. Figure 4.4 shows that zeolites had the highest adsorption capacity. This great adsorption capacity was because zeolites have a porous structure and therefore a higher specific surface than clays, so they can easily host large molecules on their surface [80,81]. On the other hand, the extrudates showed a lower specific surface area, but were also effective in removing MB from the aqueous solution, probably through other mechanisms, including electrostatic interaction, chemical reactions such as complexation, or ion exchange between sorbent and MB [82]. Consequently, despite the reduction in specific surface area in the extrudates, the surface chemistry of these materials was also an important factor controlling MB adsorption. The extruded clays showed a pH_{PZC} value around 4, and the adsorption tests were carried out at pH = 7.0, so the surface of these materials was negatively charged, improving the adsorption of cationic dye. Also, according to Tables 4.1 and 4.2, clays and zeolites contained various cations, such as Mg, K, Ca, Na, and Fe, that could promote the cation exchange capacity of prepared extruded composites to improve their MB adsorption capacity [83]. In addition to that, G-Clay contains metahalloysite (M), a mineralogical phase with applications in the design and preparation of materials with adsorbent properties [84].

Since the absorption process occurs by different mechanisms, several batch adsorption experiments of MB from an aqueous solution were developed to investigate the performance of the G, GT, GT, R, RT, and RZT extrudates. The experiments were developed varying the following parameters: the initial pH of the MB solution, the initial MB concentration, and the contact time.

4.4.2.1. Effect of pH

A factor affecting the adsorption of dyes is the pH of the solution. pH affects the adsorbent surface charge, the electrical charge of the dye, and the degree of ionization, which control the adsorption process. It is expected that adsorption will increase with pH, particularly for an adsorbate with a cationic nature [71]. At pH values above pH_{PZC}, the surface has a net negative charge and tends to accumulate cationic dye molecules due to the electrostatic attraction between the cationic dye molecule and the negatively charged extrudate surface, as suggested by other authors [85]. However, MB adsorption is reduced at a pH lower than pH_{PZC} due to the net positive charge on the surface, which causes electrostatic repulsion. As shown in Figure 4.5, the amount of MB adsorbed increased when the pH increased from 3.0 to 9.0. However, an increase in adsorption at pH values between 7.0 and 9.0 was relatively lower than the increase in adsorption at pH values between 3.0 and 7.0. The high adsorption capacity observed at alkaline pH values was due to the increase in hydroxyl ions and, therefore, to the increased electrostatic attraction between the positive and negative charges of the adsorption sites [11]. However, at very alkaline pH levels, it appears that OH ions formed a complex with other ions within alkaline pH ranges, affecting the adsorption of the dye by the adsorbent [3]. This could lead to precipitation of MB on the adsorbent surface, since the adsorption process was probably a combination of electrostatic attraction, sorption, and precipitation [82].

4.4.2.2. Adsorption Isotherm

The results of the adsorption isotherm studies showed that using the extrudates, the MB removal rate first increased from 0.25 to 20 mg L^{-1}, and that it then was reduced when the initial MB concentration (20–30 mg L^{-1}) was increased. This can be explained by the fact that, at higher concentrations, more MB molecules were competing for the active sites available on the surface of the adsorbent material. These active sites, which were in limited quantity, were quickly saturated when the concentration of MB increased. Therefore, the initial concentration of dye provided a significant driving force to overcome the mass transfer resistance of the dye between the aqueous solution and the surface of the extrudates [2].

The parameters corresponding to the fitting of these results to the Langmuir and Freundlich isotherm models are summarized in Table 4.3. The experimental data of the adsorption seemed fit to Langmuir and Freundlich isotherm models. The correlation coefficients in both isotherm models were near 1, indicating that the two models fit the experimental data well [86]. However, as shown in Figure 4.6, Langmuir isotherm models gave better fitting than Freundlich isotherm models. It can be concluded that adsorption of MB onto these adsorbents is considered as monolayer adsorption rather than as multi-layer adsorption. This fact supposes that the adsorption of MB on the extrudates occurs as a phenomenon of electrostatic attraction where the adsorption energy is uniform [87]. During this adsorption process, the cationic dye tends to move through the pores and channels of the extrudates, replacing the exchangeable cations present in the synthesized materials, which are shown in Table 4.1.

4.4.2.3. Adsorption Kinetics

Although the adsorption models help to establish the efficiency in the process, it is also important to determine the kinetic mechanism. The adsorption kinetic models express the contact time required for the complete adsorption of the chemical species. From them, we can establish the optimal conditions for a process of continuous dye removal and/or scaling at an industrial level. Figure 4.7 illustrates the concentration of MB in an aqueous solution at different contact times. It was observed that MB concentration decreased rapidly at the initial adsorption process, and then was followed by a slow reduction beyond 60 min for all adsorbents. From this trend, we can conclude that the equilibrium was reached at the contact time of around 180 min. The rapid initial stage of adsorption resulted from the presence of the vacant adsorption sites as well as the presence of a high concentration gradient. On the one hand, the adsorption by all extrudates can be attributed to the negative surface charge of these materials, leading to a high electrostatic attraction between the negatively charged sorbents and the positively charged cationic MB [88]. On the other hand, the efficiency of extrudates GT, GZT, RT, and RZT to adsorb dissolved MB dye molecules is also attributed to the presence of mixed oxide $ZnTiO_3/TiO_2$ nanoparticles, which provided additional active sites for the chemical adsorption of the dye.

The adsorption kinetic parameters are summarized in Table 4.4. The highest correlation coefficient (R^2) was obtained for the pseudo-second-order model; this kinetic model was the one that best fits in this study. The mechanism described by the pseudo-second-order model indicated a chemical adsorption of the cationic dye in the extrudates [89]. On the other hand, in Figure 4.8 two linear regions were identified when the experimental data were fitted to the intraparticle diffusion model, suggesting that the MB sorption process could be described by external-film diffusion followed by internal-pore diffusion. Table 4.4 also summarizes the linear regression analysis for the diffusion kinetic models. The highest values of the regression coefficient (R^2) were found for the external-film diffusion; furthermore, the values of A were relatively high, therefore, the surface adsorption was the rate-limiting step [5].

4.4.3. Reuse of the Adsorbents

The mechanical stability of structured materials is directly related to their useful life. If the mechanical stability is poor, the material will gradually disintegrate in the reaction solution, causing loss of activity and contamination of the medium. Mechanical stability correlates with calcination temperature [90]. The higher the calcination temperature, the better the mechanical stability, but there is an optimal calcination temperature for maximum mechanical stability. In this work, a maximum calcination temperature of the extrudates of 500 °C was used to avoid the change of crystalline phase of the synthesized compounds. The extruded materials thus prepared were subjected to desorption and regeneration studies to determine their economic viability in the MB adsorption process. The maximum desorption of cationic dye was obtained in acid solution, which indicates that the adsorption was performed through an ion exchange process. Regeneration studies were carried out for three regeneration cycles. However, as shown in Figure 4.9, the adsorption capacity of extrudates containing zeolite decreased more than in extrudates without zeolite after the first and second regeneration cycles when an acidic solution was used for desorption. This reduction in adsorption capacity could be due to decomposition or damage caused by the acid solution to certain adsorption sites or functional groups present on the surface of the extruded composites.

4.4.4. MB Adsorption Capacity of the Synthesized Compounds Compared to Other Compounds Described in the Literature

Table 4.6 shows that the compounds synthesized in this article were effective in removing dyes in aqueous effluents, and the reasons were probably due to the combined effects of several factors.

Table 4. 6. MB adsorption capacity of synthesized composites and of other composites reported in the literature.

Material	q_e (mg g^{-1})	References
R	85.45	This study
RT	85.90	This study
RZT	82.92	This study
G	85.99	This study
GT	87.01	This study
GZT	87.16	This study
Magnetic graphene oxide modified zeolite	97.35	[91]
Raw zeolite	6.10	[92]
Activated lignin-chitosan composite extrudates	36.25	[93]
Poly (dopamine hydrochloride) (PDA) microspheres	90.70	[94]
TiO_2/montmorillonite-albumin nanocomposite	18.18	[95]
Carboxymethyl cellulose/ZSM-5/ZIF-8	10.49	[96]
TiO_2 nanoparticles	88.10	[97]
ZSM-5 zeolite	105.82	[48]
NaX zeolite	127.13	[98]
Chitosan-epichlorohydrin/zeolite	156.10	[99]
Chitin/clay microspheres	152.20	[100]
Magnetic chitosan/clay beads	82.00	[101]
Activated carbon-clay composite	178.64	[102]
$KMgFe(PO_4)_2$	22.83	[103]
Hydroxysodalite	10.82	[104]
Kaolin	21.41	[105]
Nonporous silica	91.10	[106]

Table 4.6 shows that the presence of the mixed oxide $ZnTiO_3/TiO_2$ did not significantly improve the MB adsorption capacity of the extrudates compared to the extrudates free of $ZnTiO_3/TiO_2$. However, this mixed oxide can act as a photocatalyst to improve MB removal in aqueous systems when the process is carried out under UV or solar light, as we reported in a previous study [26]. The efficiency of $ZnTiO_3/TiO_2$ in the photocatalytic removal of MB in aqueous systems depends on the appropriate contact between the photocatalyst and the dye. Consequently, the extruded adsorbents reported in this study not only acted as supports for

the photocatalyst, but also efficiently captured the contaminant on its surface to initiate the oxidative process. Therefore, the addition of $ZnTiO_3/TiO_2$ in the extruded adsorbents will allow in the future combining both processes, adsorption and photocatalysis, to improve the removal of MB from aqueous systems.

Similarly, Table 4.6 shows that the zeolites did not improve the MB removal capacity of the extruded composites, despite the fact that the zeolites in powder form showed greater dye removal capacity than the precursor clays and the mixed oxide $ZnTiO_3/TiO_2$. This is because extruded zeolites have a lower specific surface area than powdered zeolites, significantly affecting their ability to remove dye. In the present study, the zeolites were obtained from two Ecuadorian clays. These clays by themselves were able to remove MB through different mechanisms, so from an economic and environmental point of view, clays are ideal for wastewater treatment. Clays were also used as inorganic binders to prepare structured materials with adequate mechanical strength and wear resistance. Consequently, clays proved to be materials that can offer universal and commercial opportunities to prepare sustainable materials with improved properties for various applications.

4.5. Conclusions

From hydrothermal synthesis and alkaline fusion methods, zeolites were successfully synthesized from ecuadorian clays, obtaining combinations of zeolites: LTA-FAU and FAU-NaP1, which showed good textural and morphological characteristics suitable for adsorption processes. The zeolites were combined with their precursor clays and the mixed oxide of Zn and Ti to prepare extrudates that were successfully used as adsorbents in methylene blue removal tests, determining the adsorption capacity and the kinetic model for the removal of MB of each synthesized material. In general, the experimental isotherms were fitted to the Langmuir model, which describes a monolayer adsorption on a surface containing an infinite number of identical sites. This model has correlated with the pseudo-second-order kinetic model found, which indicates a chemisorption process on the adsorbent. Evidently, the adsorption of the cationic dye increases rapidly until reaching a surface saturation in the structure due to two phenomena in particular. In the first of them, it is suggested that there is a comparable concentration of cationic species in the active centers of the extrudates that can be exchanged with the dye in question. On the other hand, the presence of MB complexes increases the adsorption of the cationic dye on the surface of the extrudates.

In particular, it was evidenced that extrudates derived from gray clay were the materials that showed the highest performance in the MB removal process. This fact was evidenced by the high adsorption capacity (q_m) determined in the Langmuir model. In the same way, as shown by the adsorption rate constant in the pseudo-second-order model, the removal percentages of the MB decreased due to the surface saturation of the extrudates. In this way, the usefulness of a natural resource such as clays and their transformation into higher value-added products such as zeolites was corroborated. The adsorption capacity and efficiency of these materials combined with $ZnTiO_3/TiO_2$ was demonstrated in the process of MB removal from aqueous solutions, which leaves a door open to the potential generation of clean technologies at an industrial scale from available natural resources.

4.6. References

[1] H. Ullah, K. A. Khan, and W. U. Khan, "ZnO/TiO2 nanocomposite synthesized by sol gel from highly soluble single source molecular precursor," *Chinese J. Chem. Phys.*, vol. 27, no. 5, pp. 548-554+i, 2014, doi: 10.1063/1674-0068/27/05/548-554.

[2] F. Chen *et al.*, "Fabrication and characterization of ZnTiO3/Zn2Ti3O8/ZnO ternary photocatalyst for synergetic removal of aqueous organic pollutants and Cr(VI) ions," *Sci. Total Environ.*, vol. 706, p. 136026, 2020, doi: 10.1016/j.scitotenv.2019.136026.

[3] M. Tobajas, C. Belver, and J. J. Rodriguez, "Degradation of emerging pollutants in water under solar irradiation using novel TiO 2 -ZnO / clay nanoarchitectures," *Chem. Eng. J.*, no. June, 2016, doi: 10.1016/j.cej.2016.10.002.

[4] C. Boon, L. Yong, and A. Wahab, "A review of ZnO nanoparticles as solar photocatalysts : Synthesis , mechanisms and applications," *Renew. Sustain. Energy Rev.*, vol. 81, no. August 2017, pp. 536–551, 2018, doi: 10.1016/j.rser.2017.08.020.

[5] Q. Zhao *et al.*, "Simultaneous efficient adsorption and photocatalytic degradation of methylene blue over iron(III)-based metal–organic frameworks: a comparative

study," *Transit. Met. Chem.*, vol. 44, no. 8, pp. 789–797, 2019, doi: 10.1007/s11243-019-00349-9.

[6] X. Zou, X. Dong, L. Wang, H. Ma, X. Zhang, and X. Zhang, "Preparation of ni doped ZnO-TiO2 composites and their enhanced photocatalytic activity," *Int. J. Photoenergy*, vol. 2014, 2014, doi: 10.1155/2014/893158.

[7] O. Sakin Omer, M. A. Hussein, B. H. M. Hussein, and A. Mgaidi, "Adsorption thermodynamics of cationic dyes (methylene blue and crystal violet) to a natural clay mineral from aqueous solution between 293.15 and 323.15 K," *Arab. J. Chem.*, vol. 11, no. 5, pp. 615–623, Jul. 2018, doi: 10.1016/j.arabjc.2017.10.007.

[8] Y. Chen, Z. Xiang, D. Wang, J. Kang, and H. Qi, "Effective photocatalytic degradation and physical adsorption of methylene blue using cellulose/GO/TiO2hydrogels," *RSC Adv.*, vol. 10, no. 40, pp. 23936–23943, 2020, doi: 10.1039/d0ra04509h.

[9] T. Tavakoli-Azar, A. R. Mahjoub, M. S. Sadjadi, N. Farhadyar, and M. H. Sadr, "Improving the photocatalytic performance of a perovskite ZnTiO3 through ZnTiO3@S nanocomposites for degradation of Crystal violet and Rhodamine B pollutants under sunlight," *Inorg. Chem. Commun.*, vol. 119, no. July, p. 108091, 2020, doi: 10.1016/j.inoche.2020.108091.

[10] H. Nourmoradi, A. R. Ghiasvand, and Z. Noorimotlagh, "Removal of methylene blue and acid orange 7 from aqueous solutions by activated carbon coated with zinc oxide (ZnO) nanoparticles: equilibrium, kinetic, and thermodynamic study," *Desalin. Water Treat.*, vol. 55, no. 1, pp. 252–262, 2015, doi: 10.1080/19443994.2014.914449.

[11] G. Cavallaro *et al.*, "Organic-nanoclay composite materials as removal agents for environmental decontamination," *RSC Adv.*, vol. 9, no. 69, pp. 40553–40564, 2019, doi: 10.1039/c9ra08230a.

[12] H. B. Hadjltaief *et al.*, "Photocatalytic degradation of methyl green dye in aqueous solution over natural clay-supported ZnO – TiO2 catalysts," *J. Photochem. Photobiol. A Chem.*, vol. 315, pp. 25–33, 2016, doi: 10.1016/j.jphotochem.2015.09.008.

[13] S. Sahoo, Uma, S. Banerjee, and Y. C. Sharma, "Application of natural clay as a potential adsorbent for the removal of a toxic dye from aqueous solutions," *Desalin. Water Treat.*, vol. 52, no. 34–36, pp. 6703–6711, 2014, doi: 10.1080/19443994.2013.816872.

[14] L. Lin *et al.*, “A highly efficient TiO2@ZnO n-p-n heterojunction nanorod photocatalyst,” *Nanoscale*, vol. 5, no. 2, pp. 588–593, 2013, doi: 10.1039/c2nr33109h.

[15] S. Kang *et al.*, “Enhanced removal of methyl orange on exfoliated montmorillonite/chitosan gel in presence of methylene blue,” *Chemosphere*, vol. 238, Jan. 2020, doi: 10.1016/j.chemosphere.2019.124693.

[16] M. A. Ahmed, E. E. El-Katori, and Z. H. Gharni, “Photocatalytic degradation of methylene blue dye using Fe2O 3/TiO2 nanoparticles prepared by sol-gel method,” *J. Alloys Compd.*, vol. 553, pp. 19–29, 2013, doi: 10.1016/j.jallcom.2012.10.038.

[17] J. Ma, S.-Y. Tian, S.-L. Mu, S.-L. Xie, and R.-J. Ying, “Adsorption Properties of Methylene Blue on ODA-Hectorite: Equilibrium, Kinetic Studies,” vol. 104, no. Icmcm, pp. 441–446, 2016, doi: 10.2991/icmse-16.2016.11.

[18] J. J. Salazar-Rabago, R. Leyva-Ramos, J. Rivera-Utrilla, R. Ocampo-Perez, and F. J. Cerino-Cordova, “Biosorption mechanism of Methylene Blue from aqueous solution onto White Pine (Pinus durangensis) sawdust: Effect of operating conditions,” *Sustain. Environ. Res.*, vol. 27, no. 1, pp. 32–40, 2017, doi: 10.1016/j.serj.2016.11.009.

[19] R. S. Raveendra *et al.*, “Synthesis, structural characterization of nano ZnTiO 3 ceramic: An effective azo dye adsorbent and antibacterial agent,” *J. Asian Ceram. Soc.*, vol. 2, no. 4, pp. 357–365, 2014, doi: 10.1016/j.jascer.2014.07.008.

[20] Y. Hanifehpour, N. Hamnabard, B. Khomami, S. W. Joo, B. K. Min, and J. H. Jung, “A novel visible-light Nd-doped CdTe photocatalyst for degradation of Reactive Red 43: Synthesis, characterization, and photocatalytic properties,” *J. Rare Earths*, vol. 34, no. 1, pp. 45–54, 2016, doi: 10.1016/S1002-0721(14)60576-7.

[21] S. O. Cigdem, “Adsorption and desorption kinetics behaviour of methylene blue onto activated carbon,” *Physicochem. Probl. Miner. Process.*, vol. 48, no. 2, pp. 441–454, 2012, doi: 10.5277/ppmp120210.

[22] L. Laysandra *et al.*, “Adsorption and photocatalytic performance of bentonite-titanium dioxide composites for methylene blue and rhodamine B decoloration,” *Heliyon*, vol. 3, no. 12, p. e00488, 2017, doi: 10.1016/j.heliyon.2017.e00488.

[23] Y. Kuang, X. Zhang, and S. Zhou, “Adsorption of Methylene Blue in Water onto Activated Carbon by Surfactant Modification,” *Water 2020, Vol. 12, Page 587*, vol. 12, no. 2, p. 587, Feb. 2020, doi: 10.3390/W12020587.

[24] S. Kurajica, I. Minga, R. Blazic, K. Muzina, and P. Tominac, "Adsorption and Degradation Kinetics of Methylene Blue on As-prepared and Calcined Titanate Nanotubes," *Athens J. Sci.*, vol. 5, no. 1, pp. 7–22, 2018, doi: 10.30958/ajs.5-1-1.

[25] B. Purevsuren *et al.*, "Investigation of adsorption of methylene blue from aqueous phase onto coal-based activated carbons," *J. Chinese Inst. Eng. Trans. Chinese Inst. Eng. A*, vol. 40, no. 4, pp. 355–360, 2017, doi: 10.1080/02533839.2017.1308273.

[26] H. Li, M. Dai, S. Dai, X. Dong, and F. Li, "Methylene blue adsorption properties of mechanochemistry modified coal fly ash," *Hum. Ecol. Risk Assess.*, vol. 24, no. 8, pp. 2133–2141, 2018, doi: 10.1080/10807039.2018.1440527.

[27] M. Shahid *et al.*, "Adsorption and photocatalytic degradation of methylene blue using potassium polytitanate and solar simulator," *J. Nanosci. Nanotechnol.*, vol. 16, no. 5, pp. 4342–4349, 2016, doi: 10.1166/jnn.2016.10998.

[28] T. Shindhal *et al.*, "A critical review on advances in the practices and perspectives for the treatment of dye industry wastewater," *https://doi.org/10.1080/21655979.2020.1863034*, vol. 12, no. 1, pp. 70–87, 2020, doi: 10.1080/21655979.2020.1863034.

[29] M. Faisal, M. Jalalah, F. A. Harraz, A. M. El-Toni, J. P. Labis, and M. S. Al-Assiri, "A novel Ag/PANI/ZnTiO3 ternary nanocomposite as a highly efficient visible-light-driven photocatalyst," *Sep. Purif. Technol.*, vol. 256, no. September 2020, p. 117847, 2021, doi: 10.1016/j.seppur.2020.117847.

[30] A. B. Makama, A. Salmiaton, E. B. Saion, T. S. Y. Choong, and N. Abdullah, "Synthesis of CdS Sensitized TiO2 Photocatalysts: Methylene Blue Adsorption and Enhanced Photocatalytic Activities," *Int. J. Photoenergy*, vol. 2016, 2016, doi: 10.1155/2016/2947510.

[31] S. Perween and A. Ranjan, "Improved visible-light photocatalytic activity in ZnTiO3 nanopowder prepared by sol-electrospinning," *Sol. Energy Mater. Sol. Cells*, vol. 163, no. August 2016, pp. 148–156, 2017, doi: 10.1016/j.solmat.2017.01.020.

[32] R. Abirami, C. R. Kalaiselvi, L. Kungumadevi, T. S. Senthil, and M. Kang, "Synthesis and characterization of ZnTiO3 and Ag doped ZnTiO3 perovskite nanoparticles and their enhanced photocatalytic and antibacterial activity," *J. Solid State Chem.*, vol. 281, no. October 2019, p. 121019, 2020, doi: 10.1016/j.jssc.2019.121019.

[33] E. A. El-Sharkawy, A. Y. Soliman, and K. M. Al-Amer, "Comparative study for the removal of methylene blue via adsorption and photocatalytic degradation," *J. Colloid Interface Sci.*, vol. 310, no. 2, pp. 498–508, 2007, doi: 10.1016/j.jcis.2007.02.013.

[34] A. Gil, F. C. C. Assis, S. Albeniz, and S. A. Korili, "Removal of dyes from wastewaters by adsorption on pillared clays," *Chem. Eng. J.*, vol. 168, no. 3, pp. 1032–1040, 2011, doi: 10.1016/j.cej.2011.01.078.

[35] C. Mahamadi and E. Mawere, "Kinetic Modeling of Methylene Blue and Crystal Violet Dyes Adsorption on Alginate-Fixed Water Hyacinth in Single and Binary Systems," *Am. J. Anal. Chem.*, vol. 04, no. 10, pp. 17–24, 2013, doi: 10.4236/ajac.2013.410a3003.

[36] M. N. Subramaniam, P. S. Goh, N. Abdullah, W. J. Lau, B. C. Ng, and A. F. Ismail, "Adsorption and photocatalytic degradation of methylene blue using high surface area titanate nanotubes (TNT) synthesized via hydrothermal method," *J. Nanoparticle Res.*, vol. 19, no. 6, 2017, doi: 10.1007/s11051-017-3920-9.

[37] M. F. Brigatti, E. Galán, and B. K. G. Theng, "Structure and Mineralogy of Clay Minerals," *Dev. Clay Sci.*, vol. 5, pp. 21–81, Jan. 2013, doi: 10.1016/B978-0-08-098258-8.00002-X.

[38] L. Lisuzzo, G. Cavallaro, S. Milioto, and G. Lazzara, "Layered composite based on halloysite and natural polymers: A carrier for the pH controlled release of drugs," *New J. Chem.*, vol. 43, no. 27, pp. 10887–10893, 2019, doi: 10.1039/c9nj02565k.

[39] R. Bingre, B. Louis, and P. Nguyen, "An overview on zeolite shaping technology and solutions to overcome diffusion limitations," *Catalysts*, vol. 8, no. 4. 2018, doi: 10.3390/catal8040163.

[40] A. L. Velosa, A. S. Silva, F. Rocha, E. Ferraz, and S. Andrejkovic, "Synthetic zeolite pellets incorporated to air lime – metakaolin mortars : Mechanical properties," vol. 69, pp. 243–252, 2014, doi: 10.1016/j.conbuildmat.2014.07.030.

[41] V. Ramamurthy, "Controlling photochemical reactions via confinement: Zeolites," *J. Photochem. Photobiol. C Photochem. Rev.*, vol. 1, no. 2, pp. 145–166, 2000, doi: 10.1016/S1389-5567(00)00010-1.

[42] M. Gougazeh and J.-C. Buhl, "Synthesis and characterization of zeolite A by hydrothermal transformation of natural Jordanian kaolin," *J. Assoc. Arab Univ. Basic*

Appl. Sci., vol. 15, pp. 35–42, Apr. 2014, doi: 10.1016/J.JAUBAS.2013.03.007.

[43] S. K. Masoudian, S. Sadighi, and A. Abbasi, "Synthesis and Characterization of High Aluminum Zeolite X from Technical Grade Materials," *Bull. Chem. React. Eng. Catal.*, vol. 8, no. 1, pp. 54–60, Jun. 2013, doi: 10.9767/bcrec.8.1.4321.54-60.

[44] R. Belaabed, S. Elabed, A. Addaou, A. Laajab, M. A. Rodríguez, and A. Lahsini, "Synthesis of LTA zeolite for bacterial adhesion," *Bol. la Soc. Esp. Ceram. y Vidr.*, vol. 55, no. 4, pp. 152–158, 2016, doi: 10.1016/j.bsecv.2016.05.001.

[45] K. Muraoka, Y. Sada, D. Miyazaki, W. Chaikittisilp, and T. Okubo, "Linking synthesis and structure descriptors from a large collection of synthetic records of zeolite materials," *Nat. Commun.*, vol. 10, no. 1, pp. 1–11, Dec. 2019, doi: 10.1038/s41467-019-12394-0.

[46] G. Giannetto, "Zeolitas - Caracteristicas, Propiedades Y Aplicaciones Industriales," *Editor. Innovación Tecnológica*, pp. 3–163, 2000, Accessed: Jul. 11, 2021. [Online]. Available: https://books.google.com/books/about/Zeolitas.html?hl=es&id=xArCPAAACAAJ.

[47] "LTA: 3D Drawing." https://asia.iza-structure.org/IZA-SC/framework_3d.php?STC=LTA (accessed Jul. 04, 2021).

[48] "FAU: 3D Drawing." https://asia.iza-structure.org/IZA-SC/framework_3d.php?STC=FAU (accessed Jul. 04, 2021).

[49] R. K. Parsapur and P. Selvam, "Rational design, synthesis, characterization and catalytic properties of high-quality low-silica hierarchical FAU- and LTA-type zeolites," *Sci. Rep.*, vol. 8, no. 1, pp. 1–13, Dec. 2018, doi: 10.1038/s41598-018-34479-4.

[50] A. B. Djurišić, Y. H. Leung, and A. M. C. Ng, "Strategies for improving the efficiency of semiconductor metal oxide photocatalysis," *Mater. Horizons*, vol. 1, no. 4, pp. 400–410, Jun. 2014, doi: 10.1039/C4MH00031E.

[51] G. K. Upadhyay, J. K. Rajput, T. K. Pathak, V. Kumar, and L. P. Purohit, "Synthesis of ZnO:TiO2 nanocomposites for photocatalyst application in visible light," *Vacuum*, vol. 160, pp. 154–163, 2019, doi: 10.1016/j.vacuum.2018.11.026.

[52] K. Pengkalsinan, Z. Tio, and F. Melalui, "EFFECT OF CALCINATION TEMPERATURE ON ZnO / TIO 2 COMPOSITE IN PHOTOCATALYTIC TREATMENT OF PHENOL UNDER VISIBLE LIGHT," vol. 21, no. 1, pp. 173–181,

2017.

[53] M. Irani, T. Mohammadi, and S. Mohebbi, “Photocatalytic degradation of methylene blue with zno nanoparticles; a joint experimental and theoretical study,” *J. Mex. Chem. Soc.*, vol. 60, no. 4, pp. 218–225, 2016, doi: 10.29356/jmcs.v60i4.115.

[54] B. Ozturk and G. S. P. Soylu, “Promoting role of transition metal oxide on ZnTiO3-TiO2 nanocomposites for the photocatalytic activity under solar light irradiation,” *Ceram. Int.*, vol. 42, no. 9, pp. 11184–11192, 2016, doi: 10.1016/j.ceramint.2016.04.027.

[55] K. S. Stefańska *et al.*, “TiO 2 -ZnO Binary Oxide Systems : Comprehensive Characterization and Tests of Photocatalytic Activity,” pp. 1–19, 2018, doi: 10.3390/ma11050841.

[56] C. Belver *et al.*, “Ag-Coated heterostructures of ZnO-TiO2/delaminated montmorillonite as solar photocatalysts,” *Materials (Basel).*, vol. 10, no. 8, 2017, doi: 10.3390/ma10080960.

[57] I. Daou, O. Zegaoui, and A. Elghazouani, “Physicochemical and photocatalytic properties of the ZnO particles synthesized by two different methods using three different precursors,” *Comptes Rendus Chim.*, vol. 20, no. 1, pp. 47–54, 2017, doi: 10.1016/j.crci.2016.04.003.

[58] M. R. Delsouz Khaki, M. S. Shafeeyan, A. A. A. Raman, and W. M. A. W. Daud, “Enhanced UV–Visible photocatalytic activity of Cu-doped ZnO/TiO2 nanoparticles,” *J. Mater. Sci. Mater. Electron.*, vol. 29, no. 7, pp. 5480–5495, 2018, doi: 10.1007/s10854-017-8515-9.

[59] H. Mohammadi and M. Ghorbani, “Synthesis photocatalytic TiO2/ZnO nanocomposite and investigation through anatase, wurtzite and ZnTiO3 phases antibacterial behaviors,” *J. Nano Res.*, vol. 51, pp. 69–77, 2018, doi: 10.4028/www.scientific.net/JNanoR.51.69.

[60] H. Wang *et al.*, “Semiconductor heterojunction photocatalysts: Design, construction, and photocatalytic performances,” *Chemical Society Reviews*, vol. 43, no. 15. Royal Society of Chemistry, pp. 5234–5244, Aug. 07, 2014, doi: 10.1039/c4cs00126e.

[61] S. J. Mofokeng, L. L. Noto, R. E. Kroon, O. M. Ntwaeaborwa, and M. S. Dhlamini, “Up-conversion luminescence and energy transfer mechanism in ZnTiO3: Er3+,Yb3+ phosphor,” *J. Lumin.*, vol. 223, no. March, p. 117192, 2020, doi:

10.1016/j.jlumin.2020.117192.

[62] A. D. Bachvarova-Nedelcheva, R. S. Iordanova, A. M. Stoyanova, R. D. Gegova, Y. B. Dimitriev, and A. R. Loukanov, "Photocatalytic properties of ZnO/TiO2 powders obtained via combustion gel method," *Cent. Eur. J. Chem.*, vol. 11, no. 3, pp. 364–370, 2013, doi: 10.2478/s11532-012-0167-2.

[63] R. Liu, H. Ye, X. Xiong, and H. Liu, "Fabrication of TiO2/ZnO composite nanofibers by electrospinning and their photocatalytic property," *Mater. Chem. Phys.*, vol. 121, no. 3, pp. 432–439, Jun. 2010, doi: 10.1016/j.matchemphys.2010.02.002.

[64] K. S. Ranjith and T. Uyar, "ZnO-TiO2 composites and ternary ZnTiO3 electrospun nanofibers: the influence of annealing on the photocatalytic response and reusable functionality," *CrystEngComm*, vol. 20, no. 38, pp. 5801–5813, 2018, doi: 10.1039/c8ce00920a.

[65] A. Stoyanova, H. Hitkova, R. Iordanova, N. Ivanova, and M. Sredkova, "SYNTHESIS AND ANTIBACTERIAL ACTIVITY OF TiO 2 / ZnO NANOCOMPOSITES PREPARED VIA NONHYDROLYTIC ROUTE a) b)," pp. 154–161, 2013.

[66] C. Wattanawikkam, T. Kansa-ard, and W. Pecharapa, "X-ray absorption spectroscopy analysis and photocatalytic behavior of ZnTiO 3 nanoparticles doped with Co and Mn synthesized by sonochemical method," *Appl. Surf. Sci.*, vol. 474, pp. 169–176, 2019, doi: 10.1016/j.apsusc.2018.03.175.

[67] K. Saeed Baamran and M. Tahir, "Thermodynamic investigation and experimental analysis on phenol steam reforming towards enhanced H2 production over structured Ni/ZnTiO3 nanocatalyst," *Energy Convers. Manag.*, vol. 180, no. October 2018, pp. 796–810, 2019, doi: 10.1016/j.enconman.2018.10.099.

[68] M. Vishnu Chittan, C. Mani Kumar, and B. Rajesh Kumar, "X-ray Peak Profile Analysis and Microstructural Characterization of Solid State Sintered TiO2 doped ZnO Ceramics," *Mater. Today Proc.*, vol. 4, no. 2, pp. 2879–2886, 2017, doi: 10.1016/j.matpr.2017.02.168.

[69] R. Fu *et al.*, "Effect of different processes and Ti/Zn molar ratios on the structure, morphology, and enhanced photoelectrochemical and photocatalytic performance of Ti3+ self-doped titanium-zinc hybrid oxides," *J. Power Sources*, vol. 285, pp. 449–459, 2015, doi: 10.1016/j.jpowsour.2015.03.070.

[70] Y. Chi, Q. Yuan, S. Hou, and Z. Zhao, "Synthesis and characterization of mesoporous ZnTiO3 rods via a polyvinylpyrrolidone assisted sol-gel method," *Ceram. Int.*, vol. 42, no. 4, pp. 5094–5099, 2016, doi: 10.1016/j.ceramint.2015.12.024.

[71] R. S. Koster, C. M. Fang, M. Dijkstra, A. van Blaaderen, and M. A. van Huis, "Stabilization of Rock Salt ZnO Nanocrystals by Low-Energy Surfaces and Mg Additions: A First-Principles Study," *J. Phys. Chem. C*, vol. 119, no. 10, pp. 5648–5656, Mar. 2015, doi: 10.1021/JP511503B.

[72] Y. C. Cheng, X. L. Wu, J. Zhu, L. L. Xu, S. H. Li, and P. K. Chu, "Optical properties of rocksalt and zinc blende AlN phases: First-principles calculations," *J. Appl. Phys.*, vol. 103, no. 7, p. 073707, Apr. 2008, doi: 10.1063/1.2903138.

[73] K. C. . L. Khang, M. H. M. Hatta, S. L. Lee, and L. Yuliati, "Photocatalytic removal of phenol over mesoporous ZnO/TiO2 composites," *J. Teknol.*, vol. 2, no. 80, pp. 153–160, 2018, doi: 10.11113/jt.v80.11209.

[74] I. Daou, R. Chfaira, O. Zegaoui, Z. Aouni, and H. Ahlafi, "Physico-Chemical Characterization and Interfacial Electrochemical Properties of Nanoparticles of Anatase-TiO2 Prepared by the Sol-Gel Method," *Mediterr. J. Chem.*, vol. 2, no. 4, pp. 569–582, 2013.

[75] J. Moellmann, S. Ehrlich, R. Tonner, and S. Grimme, "A DFT-D study of structural and energetic properties of TiO2 modifications," *J. Phys. Condens. Matter*, vol. 24, no. 42, p. 424206, Oct. 2012, doi: 10.1088/0953-8984/24/42/424206.

[76] L. E. Oi, M.-Y. Choo, H. V. Lee, H. C. Ong, S. B. A. Hamid, and J. C. Juan, "Recent advances of titanium dioxide (TiO2) for green organic synthesis," *RSC Adv.*, vol. 6, no. 110, pp. 108741–108754, Nov. 2016, doi: 10.1039/C6RA22894A.

[77] J. Wang, W. Mi, J. Tian, J. Dai, X. Wang, and X. Liu, "Effect of calcinations of TiO2/ZnO composite powder at high temperature on photodegradation of methyl orange," *Compos. Part B Eng.*, vol. 45, no. 1, pp. 758–767, 2013, doi: 10.1016/j.compositesb.2012.09.053.

[78] J. Lee, H. Ahn, J. Youn, Y. Kim, S. Suh, and H. Oh, "Synthesis and Characterization of ZnO / TiO 2 Photocatalyst Decorated with PbS QDs for the Degradation of Aniline Blue Solution," vol. 56, no. 12, pp. 900–909, 2018, doi: 10.3365/KJMM.2018.56.12.900.

[79] Y. Du and J. Rabani, "The Measure of TiO2 Photocatalytic Efficiency and the

Comparison of Different Photocatalytic Titania," *J. Phys. Chem. B*, vol. 107, no. 43, pp. 11970–11978, Oct. 2003, doi: 10.1021/jp035491z.

[80] J. Ryu and W. Choi, "Substrate-specific photocatalytic activities of TiO2 and multiactivity test for water treatment application," *Environ. Sci. Technol.*, vol. 42, no. 1, pp. 294–300, Jan. 2008, doi: 10.1021/es071470x.

[81] C. Karunakaran, G. Abiramasundari, P. Gomathisankar, G. Manikandan, and V. Anandi, "Preparation and characterization of ZnO–TiO2 nanocomposite for photocatalytic disinfection of bacteria and detoxification of cyanide under visible light," *Mater. Res. Bull.*, vol. 46, no. 10, pp. 1586–1592, Oct. 2011, doi: 10.1016/J.MATERRESBULL.2011.06.019.

[82] H. Chorf, M. Saadoun, L. Bousselmi, and B. Bessais, "TiO2-ITO and TiO2-ZnO nanocomposites: Application on water treatment," in *EPJ Web of Conferences*, 2012, vol. 29, doi: 10.1051/epjconf/20122900015.

[83] G. Lakshminarayana, J. Qiu, M. G. Brik, G. A. Kumar, and I. V. Kityk, "Spectral analysis of Er3+-, Er3+/Yb3+- and Er3+/Tm3+/Yb3+-doped TeO2-ZnO- WO3-TiO2-Na2O glasses," *J. Phys. Condens. Matter*, vol. 20, no. 37, Sep. 2008, doi: 10.1088/0953-8984/20/37/375101.

[84] C. Yu, W. Zhou, H. Liu, Y. Liu, and D. D. Dionysiou, "Design and fabrication of microsphere photocatalysts for environmental purification and energy conversion," *Chemical Engineering Journal*, vol. 287. Elsevier, pp. 117–129, Mar. 01, 2016, doi: 10.1016/j.cej.2015.10.112.

[85] M. Pérez-González, S. A. Tomás, M. Morales-Luna, M. A. Arvizu, and M. M. Tellez-Cruz, "Optical, structural, and morphological properties of photocatalytic TiO2-ZnO thin films synthesized by the sol-gel process," in *Thin Solid Films*, Nov. 2015, vol. 594, pp. 304–309, doi: 10.1016/j.tsf.2015.04.073.

[86] X. Zheng *et al.*, "Construction of ZnO/TiO2 photonic crystal heterostructures for enhanced photocatalytic properties," *Appl. Catal. B Environ.*, vol. 168–169, pp. 408–415, Jun. 2015, doi: 10.1016/J.APCATB.2015.01.001.

[87] E. Koufakis, G. N. Mathioudakis, A. C. Patsidis, and G. C. Psarras, "ZnTiO3/epoxy resin nanocomposites: Development, dielectric behaviour and functionality," *Polym. Test.*, vol. 77, no. April, 2019, doi: 10.1016/j.polymertesting.2019.04.017.

[88] Y. C. Lee and P. S. Chen, "Effect of Cu dopant on microstructure and phase transformation of ZnTiO 3 thin films prepared by radio frequency magnetron sputtering," *Thin Solid Films*, vol. 520, no. 7, pp. 2672–2678, 2012, doi: 10.1016/j.tsf.2011.11.035.

[89] M. Lee, A. Y. Mohamed, D. Kim, D. H. Kim, T. J. Park, and D. Y. Cho, "Identification of ZnTiO3 nanostructures in oxidized TiN/ZnS thin films using X-ray absorption spectroscopy," *Appl. Surf. Sci.*, vol. 494, no. December 2018, pp. 63–71, 2019, doi: 10.1016/j.apsusc.2019.07.188.

[90] M. T. Thein, S.-Y. Pung, A. Aziz, and M. Itoh, "The role of ammonia hydroxide in the formation of ZnO hexagonal nanodisks using sol–gel technique and their photocatalytic study," *J. Exp. Nanosci.*, vol. 10, no. 14, pp. 1068–1081, Sep. 2015, doi: 10.1080/17458080.2014.953609.

[91] M. Jose, M. Elakiya, and S. A. M. B. Dhas, "Structural and optical properties of nanosized ZnO/ZnTiO3 composite materials synthesized by a facile hydrothermal technique," *J. Mater. Sci. Mater. Electron.*, vol. 28, no. 18, pp. 13649–13658, 2017, doi: 10.1007/s10854-017-7207-9.

[92] L. Al-Hajji, "A Comparative Study on the Zinc Metatitanate Microstructure by Ball Milling and Solvothermal Approaches," *J. Struct. Chem.*, vol. 60, no. 5, pp. 830–837, May 2019, doi: 10.1134/S0022476619050172.

[93] M. Salavati-Niasari, F. Soofivand, A. Sobhani-Nasab, M. Shakouri-Arani, A. Yeganeh Faal, and S. Bagheri, "Synthesis, characterization, and morphological control of ZnTiO3 nanoparticles through sol-gel processes and its photocatalyst application," *Adv. Powder Technol.*, vol. 27, no. 5, pp. 2066–2075, 2016, doi: 10.1016/j.apt.2016.07.018.

[94] J. Lu *et al.*, "Rational design and preparation of nanoheterostructures based on zinc titanate for solar-driven photocatalytic conversion of CO2 to valuable fuels," *Appl. Catal. B Environ.*, vol. 256, no. May, pp. 2–11, 2019, doi: 10.1016/j.apcatb.2019.117800.

[95] Y. H. Yu and M. Xia, "Preparation and characterization of ZnTiO 3 powders by sol-gel process," *Mater. Lett.*, vol. 77, pp. 10–12, 2012, doi: 10.1016/j.matlet.2012.02.113.

[96] P. K. Jain, M. Salim, and D. Kaur, "Effect of phase transformation on optical and dielectric properties of pulsed laser deposited ZnTiO3 thin films," *Superlattices Microstruct.*, vol. 92, pp. 308–315, 2016, doi: 10.1016/j.spmi.2016.02.018.

[97] L. Budigi, M. R. Nasina, K. Shaik, and S. Amaravadi, “Structural and optical properties of zinc titanates synthesized by precipitation method,” *J. Chem. Sci.*, vol. 127, no. 3, pp. 509–518, 2015, doi: 10.1007/s12039-015-0802-5.

[98] E. Li, P. Zhang, S. Duan, J. Wang, Y. Yuan, and B. Tang, “Low temperature sintering of low-loss ZnTiO3 microwave dielectric ceramics with Zn-B-Si glass,” *J. Alloys Compd.*, vol. 647, pp. 866–872, 2015, doi: 10.1016/j.jallcom.2015.06.172.

[99] N. T. Nolan, M. K. Seery, and S. C. Pillai, “Crystallization and phase-transition characteristics of sol-gel-synthesized zinc titanates,” *Chem. Mater.*, vol. 23, no. 6, pp. 1496–1504, 2011, doi: 10.1021/cm1031688.

[100] I. Bobowska, A. Opasińska, A. Wypych, and P. Wojciechowski, “Synthesis and dielectric investigations of ZnTiO 3 obtained by a soft chemistry route,” *Mater. Chem. Phys.*, vol. 134, no. 1, pp. 87–92, 2012, doi: 10.1016/j.matchemphys.2012.02.033.

[101] Y. Inaguma *et al.*, “High-pressure synthesis, crystal structure, and phase stability relations of a LiNbO3-type polar titanate ZnTiO3 and its reinforced polarity by the second-order Jahn-Teller effect,” *J. Am. Chem. Soc.*, vol. 136, no. 7, pp. 2748–2756, Feb. 2014, doi: 10.1021/ja408931v.

[102] H. JIANG and Y. ZHANG, “Ethanol sensing properties of Bi3.15Nd0.85Ti3O12 films at low operating temperatures,” *Trans. Nonferrous Met. Soc. China (English Ed.*, vol. 26, no. 12, pp. 3189–3195, 2016, doi: 10.1016/S1003-6326(16)64451-5.

[103] T. Farahmand, S. Hashemian, and A. Sheibani, “Efficient one-pot synthesis of pyrano[2,3-d]pyrimidinone and pyrido [2,3-d] pyrimidine derivatives by using of Mn-ZIF-8@ZnTiO3 nanocatalyst,” *J. Mol. Struct.*, vol. 1206, p. 127667, 2020, doi: 10.1016/j.molstruc.2019.127667.

[104] H. Eskandarloo, A. Badiei, M. A. Behnajady, A. Tavakoli, and G. M. Ziarani, “Ultrasonic-assisted synthesis of Ce doped cubic-hexagonal ZnTiO3 with highly efficient sonocatalytic activity,” *Ultrason. Sonochem.*, vol. 29, pp. 258–269, 2016, doi: 10.1016/j.ultsonch.2015.10.004.

[105] P. Zhang *et al.*, “Bi 2MoO 6 ultrathin nanosheets on ZnTiO 3 nanofibers: A 3D open hierarchical heterostructures synergistic system with enhanced visible-light-driven photocatalytic activity,” *J. Hazard. Mater.*, vol. 217–218, pp. 422–428, 2012, doi: 10.1016/j.jhazmat.2012.03.046.

[106] M. C. Han, J. H. Zhang, P. Cui, Y. R. Zhu, and T. F. Yi, "Construction of spherical ZnTiO3/MWCNTs composites as anode material for high-performance Li-ion batteries," *Sustain. Mater. Technol.*, vol. 25, p. e00207, 2020, doi: 10.1016/j.susmat.2020.e00207.

[107] T. Zhong, W. Zhao, F. Jiang, and X. Liang, "Toluene sensor combining NASICON with ZnTiO3 electrode," *Sensors Actuators, B Chem.*, vol. 202, pp. 1103–1108, 2014, doi: 10.1016/j.snb.2014.06.073.

[108] X. Liu, "Molten salt synthesis of ZnTiO 3 powders with around 100 nm grain size crystalline morphology," *Mater. Lett.*, vol. 80, pp. 69–71, 2012, doi: 10.1016/j.matlet.2012.04.048.

[109] Y. L. Chai, Y. S. Chang, K. T. Liu, and L. G. Teoh, "The structure and PTCR effects of Mg-doped ZnTiO 3 ceramics," *Ceram. Int.*, vol. 38, no. 5, pp. 3613–3618, 2012, doi: 10.1016/j.ceramint.2011.12.078.

[110] T. Bernert, J. Ruiz-Fuertes, L. Bayarjargal, and B. Winkler, "Synthesis and high (pressure, temperature) stability of ZnTiO3 polymorphs studied by Raman spectroscopy," *Solid State Sci.*, vol. 43, pp. 53–58, 2015, doi: 10.1016/j.solidstatesciences.2015.03.014.

[111] Y. Yan, H. Gao, J. Tian, F. Tan, H. Zheng, and W. Zhang, "Ferromagnetic Enhancement in ZnTiO 3 films induced by Co doping," *Ceram. Int.*, vol. 45, no. 9, pp. 11309–11315, 2019, doi: 10.1016/j.ceramint.2019.02.208.

[112] S. J. Mofokeng, L. L. Noto, and M. S. Dhlamini, "Photoluminescence properties of ZnTiO3:Eu3+ phosphor with enhanced red emission by Al3+ charge compensation," *J. Lumin.*, vol. 228, no. July, p. 117569, 2020, doi: 10.1016/j.jlumin.2020.117569.

[113] J. Zhang, B. Xu, Y. S. Wang, Z. Qin, and S. H. Ke, "First-principles investigation of the ferroelectric, piezoelectric and nonlinear optical properties of LiNbO3-type ZnTiO3," *Sci. Rep.*, vol. 9, no. 1, pp. 1–14, 2019, doi: 10.1038/s41598-019-53986-6.

[114] J. Ruiz-Fuertes *et al.*, "Ferroelectric soft mode of polar ZnTiO3 investigated by Raman spectroscopy at high pressure," *Phys. Rev. B - Condens. Matter Mater. Phys.*, vol. 91, no. 21, 2015, doi: 10.1103/PhysRevB.91.214110.

[115] C. Bao *et al.*, "A signal-off type photoelectrochemical immunosensor for the ultrasensitive detection of procalcitonin: Ru(bpy)32+ and Bi2S3 co-sensitized

ZnTiO3/TiO2 polyhedra as matrix and dual inhibition by SiO2/PDA-Au," *Biosens. Bioelectron.*, vol. 142, no. May, 2019, doi: 10.1016/j.bios.2019.111513.

[116] I. Udom *et al.*, "Optimization of Photocatalytic Degradation of Phenol Using Simple Photocatalytic Reactor," *Am. J. Anal. Chem.*, vol. 05, no. 11, pp. 743–750, Aug. 2014, doi: 10.4236/ajac.2014.511083.

[117] Y.-L. Chai, Y.-S. Chang, G.-J. Chen, and Y.-J. Hsiao, "The effects of heat-treatment on the structure evolution and crystallinity of ZnTiO3 nano-crystals prepared by Pechini process," *Mater. Res. Bull.*, vol. 43, no. 5, pp. 1066–1073, May 2008, doi: 10.1016/J.MATERRESBULL.2007.06.002.

[118] X. Chen and S. S. Mao, "Titanium Dioxide Nanomaterials : Synthesis , Properties , Modifications , and Applications," 2007, doi: 10.1021/cr0500535.

[119] K. R. M. Macedo, G. A. C. Oliveira, K. A. B. Pereira, L. C. Mendes, A. S. Araújo, and R. J. Cassella, "Titanium-zinc polycitrate precursor: Influence of thermal treatment on structural, thermal, optical characteristics of zinc titanates," *Mater. Chem. Phys.*, vol. 236, no. May, p. 121768, 2019, doi: 10.1016/j.matchemphys.2019.121768.

[120] Z. Zhang, L. Hu, H. Zhang, L. Yu, and Y. Liang, "Large-sized nano-TiO2/SiO2 mesoporous nanofilmconstructed macroporous photocatalysts with excellent photocatalytic performance," *Front. Mater. Sci.*, vol. 14, no. 2, pp. 163–176, Jun. 2020, doi: 10.1007/s11706-020-0506-8.

[121] K. Sahel *et al.*, "Photocatalytic degradation of anionic and cationic dyes over TiO2 P25, and Ti-pillared clays and Ag-doped Ti-pillared clays," *Appl. Clay Sci.*, vol. 95, pp. 205–210, Jun. 2014, doi: 10.1016/j.clay.2014.04.014.

[122] F. Akhtar, L. Andersson, S. Ogunwumi, N. Hedin, and L. Bergström, "Structuring adsorbents and catalysts by processing of porous powders," *J. Eur. Ceram. Soc.*, vol. 34, no. 7, pp. 1643–1666, 2014, doi: 10.1016/j.jeurceramsoc.2014.01.008.

[123] C. Belver, J. Bedia, and J. J. Rodriguez, "Applied Catalysis B : Environmental Titania – clay heterostructures with solar photocatalytic applications," *"Applied Catal. B, Environ.*, vol. 176–177, pp. 278–287, 2015, doi: 10.1016/j.apcatb.2015.04.004.

[124] M. Akkari, P. Aranda, H. Ben Rhaiem, A. Ben Haj, and E. Ruiz-Hitzky, "ZnO/clay nanoarchitectures: Synthesis , characterization and evaluation as photocatalysts," *Appl. Clay Sci.*, pp. 1–9, 2015, doi: doi.org/10.1016/j.tsf.2011.08.095.

[125] K. Rajeshwar and W. Chanmanee, “Bioinspired photocatalyst assemblies for environmental remediation,” *Electrochim. Acta*, vol. 84, pp. 96–102, Dec. 2012, doi: 10.1016/j.electacta.2012.04.072.

[126] J. Liu and G. Zhang, “Recent advances in synthesis and applications of clay-based photocatalysts: A review,” *Physical Chemistry Chemical Physics*, vol. 16, no. 18. Royal Society of Chemistry, pp. 8178–8192, May 14, 2014, doi: 10.1039/c3cp54146k.

[127] G. T. Whiting, A. D. Chowdhury, R. Oord, P. Paalanen, and B. M. Weckhuysen, “The curious case of zeolite–clay/binder interactions and their consequences for catalyst preparation,” *Faraday Discuss.*, vol. 188, no. 0, pp. 369–386, Jul. 2016, doi: 10.1039/C5FD00200A.

[128] E. G. Lewars, *Computational chemistry: Introduction to the theory and applications of molecular and quantum mechanics*. Springer Netherlands, 2011.

[129] R. J. Boyd, “Theoretical and Computational Chemistry,” in *Reference Module in Chemistry, Molecular Sciences and Chemical Engineering*, Elsevier, 2019.

[130] I. B. Djordjevic, “Quantum Mechanics Fundamentals,” in *Quantum Information Processing, Quantum Computing, and Quantum Error Correction*, Elsevier, 2021, pp. 31–95.

[131] J. Morrison, “The Schrödinger wave equation,” in *Modern Physics with Modern Computational Methods*, Elsevier, 2021, pp. 19–36.

[132] A. Popa, “Connection Between Schrődinger and Hamilton–Jacobi Equations in the Case of Stationary Atomic and Molecular Systems,” in *Theory of Quantum and Classical Connections in Modeling Atomic, Molecular and Electrodynamical Systems*, Elsevier, 2014, pp. 1–21.

[133] C. Yu, N. Fu, C. Dai, H. Wang, G. Zhang, and J. Yao, “Time-dependent Born-Oppenheimer approximation approach for Schrödinger equation: Application to H2+,” *Opt. Commun.*, vol. 300, pp. 199–203, Jul. 2013, doi: 10.1016/j.optcom.2013.02.056.

[134] S. M. Blinder, “Introduction to the hartree-fock method,” in *Mathematical Physics in Theoretical Chemistry*, Elsevier, 2018, pp. 1–30.

[135] J. B. Condon, “Density functional theory (DFT),” in *Surface Area and Porosity Determinations by Physisorption*, Elsevier, 2020, pp. 335–360.

[136] Y. A. Wang and P. Xiang, "From the Hohenberg-Kohn Theory to the Kohn-Sham Equations," 2013, pp. 3–12.

[137] S. Śmiga, A. Buksztel, and I. Grabowski, "Density-Dependent Exchange-Correlation potentials derived from highly accurate Ab initio calculations," in *Advances in Quantum Chemistry*, vol. 68, Academic Press Inc., 2014, pp. 125–151.

[138] V. N. Staroverov and E. Ospadov, "Unified construction of Fermi, Pauli and exchange-correlation potentials," in *Advances in Quantum Chemistry*, vol. 79, Academic Press Inc., 2019, pp. 201–219.

[139] J. Andrés Bort and J. Beltrán Comulada, *Química teórica y computacional*, 1st ed. Universitat Jaume I. Servei de Comunicació i Publicacions, 2001.

[140] J. P. Perdew, K. Burke, and M. Ernzerhof, "Generalized gradient approximation made simple," *Phys. Rev. Lett.*, vol. 77, no. 18, pp. 3865–3868, Oct. 1996, doi: 10.1103/PhysRevLett.77.3865.

[141] I. Levine, *Physical Chemistry*. Brooklyn, New York: McGraw-Hill, 2001.

[142] A. R. Tackett, N. A. W. Holzwarth, and G. E. Matthews, "A Projector Augmented Wave (PAW) code for electronic structure calculations, Part II: pwpaw for periodic solids in a plane wave basis," *Comput. Phys. Commun.*, vol. 135, no. 3, pp. 348–376, Apr. 2001, doi: 10.1016/S0010-4655(00)00241-1.

CHAPTER 5

La-DOPED $ZnTiO_3/TiO_2$ NANOCOMPOSITE SUPPORTED ON ECUADORIAN DIATOMACEOUS EARTH AS A HIGHLY EFFICIENT PHOTOCATALYST DRIVEN BY SOLAR LIGHT

5.1. Introduction

In recent years, water contamination by dyes has become one of the most important global concerns [1,2]. Currently, there are more than 10,000 types of commercial dyes available with an annual production of over 7×10^5 tons [3], and with a considerable fraction discharged from industries such as textile, paper, plastic, leather, ceramics, cosmetics, pharmaceuticals, and food processing [4–6]. In particular, effluents from these industries are considered an important source of pollution that generates by-products that are dangerous to health, in addition to preventing the penetration of sunlight and delaying photosynthesis in aquatic systems [7].

Recently, various chemical, physical, and biological treatment methods have been developed for the removal of dyes from aqueous solutions. These treatments include adsorption; precipitation; coagulation–flocculation; reverse osmosis; photocatalysis; oxidation with ozone, chlorine, or hydrogen peroxide; electrolysis, the use of anion exchange membranes; biological treatment; and other processes [8–10]. Among these, adsorption of the dye using porous materials and photocatalytic degradation of the dye through the use of semiconductors have attracted extraordinary attention in the last two decades [11–15]. Compared to other processes, adsorption and photocatalysis allow some flexibility in terms of simplicity of design, ease of operation, and low cost, as well as producing contaminant-free effluents that can be suitable for reuse [16].

Adsorption is a process that can be performed by different mechanisms, including electrostatic interaction, a chemical reaction such as complexation, or an ion exchange between the adsorbate and the adsorbent. Furthermore, pore structure and adsorbent surface chemistry exert the greatest influence on the adsorption process, whereas pore size distribution affects the efficiency and selectivity of the process [17]. For the adsorption process to be efficient, the adsorbent materials must have large specific surface area, high adsorption capacity, and active sites on their surfaces. In addition, they must be environmentally friendly, highly efficient, inexpensive, regenerable, and available in large quantities [18]. Therefore, mineral species such as clays, zeolites, and diatomaceous earth, among others [19–21], are the most promising materials for this purpose.

Diatomaceous earth (DE) or diatomite are natural fossilized remains of unicellular aquatic algae called diatoms. DE belongs to the group of almost pure sedimentary silica rocks that is typically composed by 87%–91% silicon dioxide (SiO_2), with significant amounts of alumina (Al_2O_3) and ferric oxide (Fe_2O_3) [22]. DE can also present variable amounts of impurities such as mineral clays, salts (mainly carbonates), and organic matter [23]. Other properties that allow DE to be industrially valuable include a low conductivity coefficient, low density, high porosity, large surface area, high adsorption capacity, and excellent thermal resistance [24]. Diatomite has been widely used in acoustic and thermal insulation, and as a filter aid, pharmaceutical carrier, and adsorbent. Recently, the use of diatomite has also been reported to be an excellent support material in the preparation of solid catalysts [25], because it presents siloxane bridges and silanol groups, which are key reactive sites for various surface reactions [26]. Thus, diatomite is a promising candidate for industrial production due to its great versatility, easy physical separation, and low cost [24].

On the other hand, heterogeneous photocatalysis is a promising advanced oxidation process (AOP) for the treatment of contaminated wastewater because it allows for complete mineralization of different organic and inorganic compounds using semiconductor catalysts that are activated by natural or artificial light [27–34]. The photocatalytic activity of semiconductors is influenced by a wide variety of factors such as morphology, specific surface area, affinity and adsorption capacity of organic pollutants, intensity and spectral distribution of the illuminating light, and pH of the solutions, among others [35]. Among the many semiconductors, TiO_2 nanostructures have drawn increasing interest in wastewater treatment [36,37] due to several attractive properties including high reactivity, chemical stability, high oxidative capacity, non-toxicity, and low cost [38–41]. However, TiO_2 has some disadvantages that hinder its cost-effectiveness and applicability, such as a wide bandgap (~3.2 eV), which limits its activity to a small proportion of the solar spectrum in the ultraviolet region. Furthermore, TiO_2 has low quantum efficiency due to the rapid recombination rate of photogenerated electron-hole pairs, and shows a high particle agglomeration effect that reduces the number of active sites [42,43]. Many promising methods have been applied to address these characteristic disadvantages. For example, immobilization of the semiconductor in porous supports (e.g., diatomite) has proved to be an effective method to prevent agglomeration. At the same time, it increases the surface area and facilitates recovery of the photocatalyst at the end of the process. Likewise, intensive research has been conducted to improve the photocatalytic efficiency of TiO_2 through common pathways such as doping with metallic and non-metallic ions, noble metal deposition, sensitization by inorganic complexes or organic dyes, coupling of semiconductors, and doping with rare earth (RE) elements [44–48].

Doping has long been known as one of the most effective approaches for altering the intrinsic electron structure of TiO_2, lowering its bandgap energy, and consequently enhancing its sensitivity to visible light by improving electron-hole separation or extending the optical absorption span [49,50]. Among various dopants, rare earth elements have received much attention for the preparation of versatile photocatalysts [51–55]. Lanthanum is a widely investigated rare earth metal element, and the efficacy of using La ≤ 1–2 wt.% to dope TiO_2 enhances its photocatalytic activity in both the UV and visible-light region [56–60]. Since the ionic radius of the La^{3+} ion (1.03 Å) is much higher than that of Ti^{4+} (0.64 Å), La^{3+} would disperse on the surface of TiO_2 particles, forming Ti-O-La bonds rather than replacing the lattice site of Ti^{4+}, according to several studies [61–64]. Lanthanum-doped compounds are generally used as efficient catalysts and light-conversion devices due to their electronic, optical, and chemical characteristics arising from their 4f electrons transition [65,66]. In particular, doping TiO_2 with La can inhibit phase transition from anatase to rutile and restrain crystal growth [67], increase the surface area and the concentration of surface hydroxyl (-OH) groups, improve the optical properties due to the increase in the concentration of oxygen vacancies, and promote chemical adsorption of the organic substrates on the semiconductor's surface, which also benefits the improvement of its photocatalytic efficiency for diverse applications [68–75].

Like the doping process, the coupling or heterojunction of two semiconductors that possess different levels of redox energy for their corresponding conduction (CB) and valence (VB) band has been extensively studied. This coupling has proven to be an attractive approach to compensate for the disadvantages of individual components and lead to more efficient charge separation, longer life of charge carriers, and improved interfacial charge transfer to adsorbed substrates [76,77]. Several semiconductors have been reported for the potential coupling of TiO_2, including SiO_2, MoO_3, CdS, MgO, WO_3, SnO_2, ZrO_2, CuO, Fe_2O_3, and ZnO [78–81]. The characteristics and compatibility of the coupling semiconductor are important for the physicochemical properties and stability of the hybrid semiconductor. Each semiconductor substantially affects the surface charge of the material and therefore increases or weakens its photocatalytic capacity [30]. Among the numerous semiconductor combinations, the integration of $ZnTiO_3$ with TiO_2 has previously been reported as a promising alternative for the adsorption and photocatalytic degradation of MB in wastewater [82,83]. Although $ZnTiO_3$ has proven to be the most versatile perovskite-type oxide for various applications [84], the physical and chemical properties of the $ZnTiO_3/TiO_2$ heterojunction have been shown to be greater than those of the individual components, evidently resulting from the modification of their electronic states [85].

This paper reports on the doping of the $ZnTiO_3/TiO_2$ nano-heterojunction with lanthanum that was synthesized using the sol-gel method. Nanocomposites of $ZnTiO_3/TiO_2$ (ZTO) and $ZnTiO_3/TiO_2/La$ (ZTO/La) were immobilized on diatomaceous earth (DE) to achieve innovative and eco-friendly nanomaterials, with adsorbent and photocatalytic properties for the effective removal of methylene blue (MB) in wastewater. The adsorption and photocatalytic degradation of MB were determined in batch experiments. The dye amount was determined by UV-visible spectrophotometry. The adsorption capacity of the synthesized composites was measured by varying the pH of the solutions, the concentration of the adsorbent, and the contact time, whereas the photocatalytic activity was determined under solar irradiation. The synthesized composites were characterized using X-ray diffractometry (XRD), X-ray fluorescence (XRF), diffuse reflectance spectroscopy (DRS), scanning electron microscopy (SEM-EDX), and specific surface area (SSA).

5.2. Materials and Methods

5.2.1. Materials

All of the reagents used in this study were of analytical grade and used without additional purification: C_3H_8O (Sigma Aldrich, St. Louis, MO, USA, ≥99.5%), $Ti(OC_3H_7)_4$ (Sigma Aldrich, St. Louis, MO, 98.0%), CH_3COOH (Sigma Aldrich, St. Louis, MO, 99.8%), H_2O_2 (Sigma Aldrich, St. Louis, MO, 35.0%), $Zn(CH_3COO)_2{\cdot}2H_2O$ (ACS, St. Louis, MO, USA, ≥98.0%), $C_{16}H_{18}ClN_3S \cdot nH_2O$ (Sigma Aldrich, St. Louis, MO, ≥95.0%), $La(NO_3)_3{\cdot}6H_2O$ (Sigma Aldrich, St. Louis, MO, 99.9%), HCl (Fisher Scientific, Waltham, MA, USA, 37%), cetyl-trimethyl ammonium chloride ($C_{19}H_{42}NCl$) (Sigma Aldrich, St. Louis, MO, 25%), $AgNO_3$ (Sigma Aldrich, St. Louis, MO, >99.8%), and HNO_3 (Sigma Aldrich, St. Louis, MO, 69%).

5.2.2. Diatomaceous Earth Purification

The raw diatomaceous earth (DE) was collected from southern Ecuador. The DE sample was ground and sieved to 200-mesh (0.074 mm) size. Calcium and magnesium carbonates were removed using hydrochloric acid (0.1 N) at a ratio of 10 mL g^{-1}. The organic matter present in the DE sample was oxidized by adding H_2O_2 (33%) at a ratio of 10 mL g^{-1} under agitation for 2 h at room temperature. After centrifugation, the purified DE was washed with distilled water for the removal of Cl^- ions; this was checked with a test with $AgNO_3$. The DE adsorption sites were activated with nitric acid (0.8 N) in a proportion of 10 mL g^{-1}. Activation is a process through which a partially dissolved material is obtained, which has greater surface acidity, porosity, specific surface area, and adsorption capacity [22,23,139,140]. The activated DE samples were centrifuged, washed with distilled water, and dried at 60 °C for 24 h.

5.2.3. Synthesis of the DE-Supported Nanocomposites

The $ZnTiO_3/TiO_2$ (ZTO) and $ZnTiO_3/TiO_2/La$ (ZTO/La) nanocomposites were synthesized following a modified sol-gel method described in previous studies [83,90]. To obtain the ZTO nanocomposite, a quantity of titanium (IV) isopropoxide (TiPO) in isopropyl alcohol (iPrOH)

(70 *v*/*v*%) was dispersed at room temperature. An aqueous solution formed by Zn(acet), water, and iPrOH was slowly added, using ZnO/TiO_2 in a 1:3 molar ratio. The amount of water had a 50 *v*/*v*% iPrOH/water ratio and was determined by stoichiometry, being the amount necessary to hydrolyze the TiPO molecules. The synthesis was performed at room temperature. The reaction system was additionally stirred for 30 min. The mixture was kept under stirring at room temperature for another 30 min after formation of a precipitate. The precipitate was dried at 60 °C for 24 h and then calcined at 500 °C for 4 h. Finally, the solids were cooled at room temperature. To obtain the ZTO/La nanocomposite, the procedure described above was repeated, adding $La(NO_3)_3{\cdot}6H_2O$ to the aqueous Zn solution to obtain a final lanthanum concentration of 1% per gram of ZTO. The previous synthesis process was repeated for each photocatalyst using, at the beginning of the process, a solution (10 *w*/*w*%) of diatomaceous earth in isopropyl alcohol (iPrOH).

5.2.4. Structuring of the DE-Supported Nanocomposites

For the evaluation of the solid materials, cylindrical extrudates with approximate dimensions of 0.2 cm in diameter and 1.0 cm in length were prepared. The preparation of these solids was carried out by mixing each DE-supported nanocomposite with an amount of water (approximately 35%) to form a mixture with good plasticity. This mixture was extruded with a 2.5 mm-diameter syringe. The extrudates were dried at 90 °C for 2 h and finally calcined at 500 °C for 8 h.

5.2.5. Characterization

The synthetized materials were characterized using a JEOL JSM 6400 scanning electron microscope (SEM) (JEOL, Peabody, MA, USA). The X-ray fluorescence (XRF) measurements were recorded in a Bruker S1 Turbo SDR portable spectrometer (Bruker Handheld LLC, Kennewick, WA, USA), using the mining light elements measurement method. The X-ray diffraction (XRD) measurements were recorded in a Bruker-AXS D8-Discover diffractometer (Bruker AXS, Karlsruhe, Germany) equipped with a vertical θ-θ goniometer, a parallel incident beam (Göbel mirror), and a HI-STAR general area diffraction detection system

(GADDS) (Bruker AXS, Karlsruhe, Germany). The X-ray diffractometer was operated at 40 kV and 40 mA to produce Cu Kα radiation (1.5406 Å). The data were recorded from 5 to 70° in the 2θ range. Identification of the crystal phases was obtained by comparison of the XRD profile with the ICDD (International Centre for Diffraction Data, release 2018) database. Determination of the specific surface area of the solids (m^2/g) was carried out in the ChemiSorb 2720 equipment (Micromeritics, Norcross, GA, USA) by nitrogen adsorption at the temperature of liquid nitrogen (−196 °C) with a 30% gas mixture of N_2 diluted in He. The Chemisoft TPx system (version 1.03; data analysis software; Micromeritics, Norcross, GA, USA, 2011) allowed the specific surface area to be calculated using the Brunauer–Emmet–Teller (BET) equation and the single-point method. The UV-Vis diffuse reflectance spectrum (DRS) of the photocatalysts was obtained by a UV-Vis Thermo spectrophotometer model: Nicolet Evolution 201/220 (ThermoFisher, Waltham, MA, USA), equipped with an integration sphere unit using $BaSO_4$ as reference. Finally, the adsorbents were also characterized by the point of zero charges (pH_{PZC}) at different pH values using a Jenway 7350 spectrophotometer (Cole-Parmer, Staffordshire, UK).

5.2.6. Adsorption Studies

The adsorption experiments were conducted using a batch method at room temperature. Typically, 25 mg of extruded adsorbents were magnetically stirred in a methylene blue aqueous solution (100 mL of water containing 20 mg mL^{-1} methylene blue). The remaining concentrations of methylene blue were determined at 623 nm using a Jenway 7350 spectrophotometer (Cole-Parmer, Staffordshire, UK). The adsorption rate of MB was calculated by the absorbance according to the Beer–Lambert law. Samples were drawn at 5 min intervals with a syringe and filtered through a 0.45 μm membrane filter to remove any solid particles interfering with the measurement. All tests were carried out in triplicate. The procedure was repeated using a methylene blue reference solution without extruded adsorbents to eliminate any photolysis effects causing discoloration of the solution due to natural light. The adsorbed quantity q_e of methylene blue was calculated by means of Equation (5.1):

$$q_e = (C_0 - C_e) \times \frac{v}{w} \quad \textbf{(5.1)}$$

where C_0 (mg L^{-1}) and C_e (mg L^{-1}) represent the initial and equilibrium concentration, respectively; v (L) is the volume of the solution; and w (g) is the mass of the adsorbent [83].

5.2.6.1. Effect of pH

The effect of pH on MB adsorption onto the adsorbents was investigated under pH values varying from 3 to 10. The initial MB concentration used was 25 mg mL^{-1} for all extrudates. Contact time was fixed at 180 min and corresponded to the time necessary to reach adsorption equilibrium for all adsorbents. To evaluate the impact of pH on the solid surface, a point of zero charges pH_{PZC} measurement was also performed for all extrudates. The pH_{PZC} determinations were performed in aqueous suspensions of the extrudates at two concentrations (0.01 and 0.05 M) of the NaCl inert electrolyte. Potentiometric titrations were made over the entire pH range of 3 to 10.

5.2.6.2. Isotherm Models

The effect of the initial MB concentration was investigated from 0.25 to 30 mg L^{-1}. The experiments were performed without adjusting the pH of the solution. At the end of the experiments, the equilibrium pH was measured and found to be constant, around 7 for each adsorbent. The equilibrium MB adsorption was evaluated according to the Langmuir and Freundlich isotherm models, since these models can help to explain the adsorption mechanism and the heterogeneity of the adsorbent surface [83,117,141,142].

The expression of the Langmuir isotherm model can be represented by Equation (5.2):

$$\boldsymbol{\frac{C_e}{q} = \frac{1}{K_L q_{max}} + \frac{C_e}{q_{max}}} \quad \textbf{(5.2)}$$

where $q_{\max}$ is the maximum monolayer adsorption, K_L is the equilibrium Langmuir constant related to the adsorption energy, and C_e is the concentration of solute at equilibrium. Additionally, the R_L separation factor values, which provide an insight into the adsorption nature, can be expressed by means of Equation (5.3):

$$\boldsymbol{R_L = \frac{1}{(1 + K_L C_e)}} \quad \textbf{(5.3)}$$

The expression of the Freundlich isotherm model can be represented by Equation (5.4):

$$\boldsymbol{q = K_F C_e^{1/n}} \quad \textbf{(5.4)}$$

where K_F is the Freundlich constant, which indicates the adsorption affinity of the adsorbents, and $1/n$ is another constant that represents the adsorption intensity.

5.2.6.3. Kinetic Models

The solute absorption rate of the solute–solution interface was described in this study using reaction-based models, called pseudo-first-order and pseudo-second-order, as well as diffusion-based models, called intraparticle diffusion, external-film diffusion, and internal-pore diffusion [107]. The pseudo-first-order and pseudo-second-order models assume that the difference between the average solid-phase concentration (q_t) and the equilibrium concentration (q_e) is the driving force for adsorption and that the overall adsorption rate is proportional to this driving force. Both equations have been widely applied to explain the experimental results obtained for aqueous pollutants such as dyes and metal ions [83,117,141,142].

The pseudo-first-order kinetic model is expressed by means of Equation (5.5):

$$\boldsymbol{\ln(q_e - q_t) = \ln(q_e) - k_1 t} \quad \textbf{(5.5)}$$

where k_1 is the rate constant (min^{-1}) and q_e and q_t represent the MB adsorbed per unit weight (mg g^{-1}) at equilibrium and at any time t, respectively [59].

The pseudo-second-order kinetic is expressed by means of Equation (5.6):

$$\frac{t}{q_t} = \frac{1}{k_2 q_e^2} + \frac{1}{q_e} t \tag{5.6}$$

where k_2 is the pseudo-second-order rate constant (g mg^{-1} min^{-1}) [143].

In order to gain good insight into the adsorption mechanism, determination of the rate-limiting step is necessary in the adsorption process. The intraparticle diffusion model, based on the theory proposed by Weber and Morris, assumes that intraparticle diffusion is the rate-control step, which is generally the case for well-mixed solutions [92]. The mathematical expression of the intraparticle diffusion model is described by Equation (5.7):

$$q_t = k_3 t^{1/2} + A \tag{5.7}$$

where k_3 (mg g^{-1} min$^{-1/2}$) is the intraparticle diffusion rate constant and A (mg g^{-1}) is a constant that indicates the thickness of the boundary layer, i.e., the higher the value of A, the greater the boundary-layer effect. In some cases, the plot q_t versus square root time can show multi-linearity, which indicates that several steps occur in the process.

The internal-pore diffusion model was also used to describe the kinetic adsorption data. If particle diffusion controls (D_p), the adsorption rate is described using Equation (5.8):

$$-\ln\left(1 - \left(\frac{q_t}{q_e}\right)^2\right) = \frac{2\pi^2 D_p}{r^2} t \tag{5.8}$$

When the adsorption rate is controlled by external-film diffusion, it is expressed by means of Equation (5.9):

$$-ln\left(1-\left(\frac{q_t}{q_e}\right)\right)=\frac{D_f C_s}{h\, r\, C_z}\, t \qquad (5.9)$$

where q_t and q_e are the solute loadings on the adsorbent phase at time t and at equilibrium (mg g^{-1}), respectively; t is the contact time (min); C_s (mg L^{-1}) and C_z (mg kg^{-1}) are the ion concentrations in the solution and in the adsorbent, respectively; r is the average radius of the adsorbent particles (1×10^{-7} m); and h is the film thickness around the adsorbent particles, accepted as 10^{-6} m for poorly stirred solutions [58]. D_p is the diffusion coefficient in the adsorbent phase (m^2 min^{-1}) and D_f (m^2 min^{-1}) is the diffusion in the film phase surrounding the adsorbent particles

5.2.7. Photocatalytic Degradation

Heterogeneous photocatalysis experiments were carried out, without adjusting pH = 7.0, for 150 min. Typically, 25 mg of composites were magnetically stirred in a methylene blue (MB) aqueous solution (100 mL of water containing 20 mg L^{-1} methylene blue). The solution was maintained in dark conditions for 30 min to attain the adsorption–desorption equilibrium. The photocatalytic activity of the composites was evaluated by the photocatalytic degradation of methylene blue under solar light radiation. Solar light was simulated by a solar box equipped with an air-cooled 1500 W Xenon lamp (Atlas Material Testing Technology, Mount Prospect, IL, USA), which allows 300–800 nm wavelengths to pass through (ATLAS, SUNTEST CPS+). Irradiance was set to 250 W/m^2.

The remaining methylene blue concentrations were determined at 623 nm using a Jenway 7350 spectrophotometer (Cole-Parmer, Staffordshire, UK). The MB removal rate was calculated by absorbance according to the Beer–Lambert law. Samples were drawn at 5 min intervals with a syringe and filtered through a 0.45 μm membrane filter to remove any solid particles interfering with the measurement. All tests were carried out in triplicate using a blank methylene blue solution irradiated with solar light to eliminate any photolysis effect due to the light.

5.2.8. Reuse of the Supported Photocatalysts

A recycling experiment on photocatalytic degradation of MB by ZTO-DE and ZTO/La-DE was designed to determine the recycling property of these composites. After completing a treatment cycle, the catalyst extrudates were left in quiescent conditions for 60 min to achieve their precipitate. Then, the clear solution was removed from the reaction system and 100 mL of fresh MB solution (5 mg/L) were injected into the reaction system, initiating the next cycle. The recycling experiment was carried out for five cycles. Each cycle lasted 150 min under solar irradiation.

5.3. Results

5.3.1. Characterization of the Samples

5.3.1.1. XRD and XRF Analysis

Figure 5.1 displays the XRD pattern of diatomaceous earth (DE), (a) raw and (b) purified, which consists of quartz (Q), jarosite (J), albite (A), muscovite (W), and montmorillonite (M). By comparing Figures 6.1(a) and 6.1(b), it can be noticed that the main peak related to montmorillonite at d-spacing = 15.0 (2θ = 6°) disappeared, probably due to the purification process.

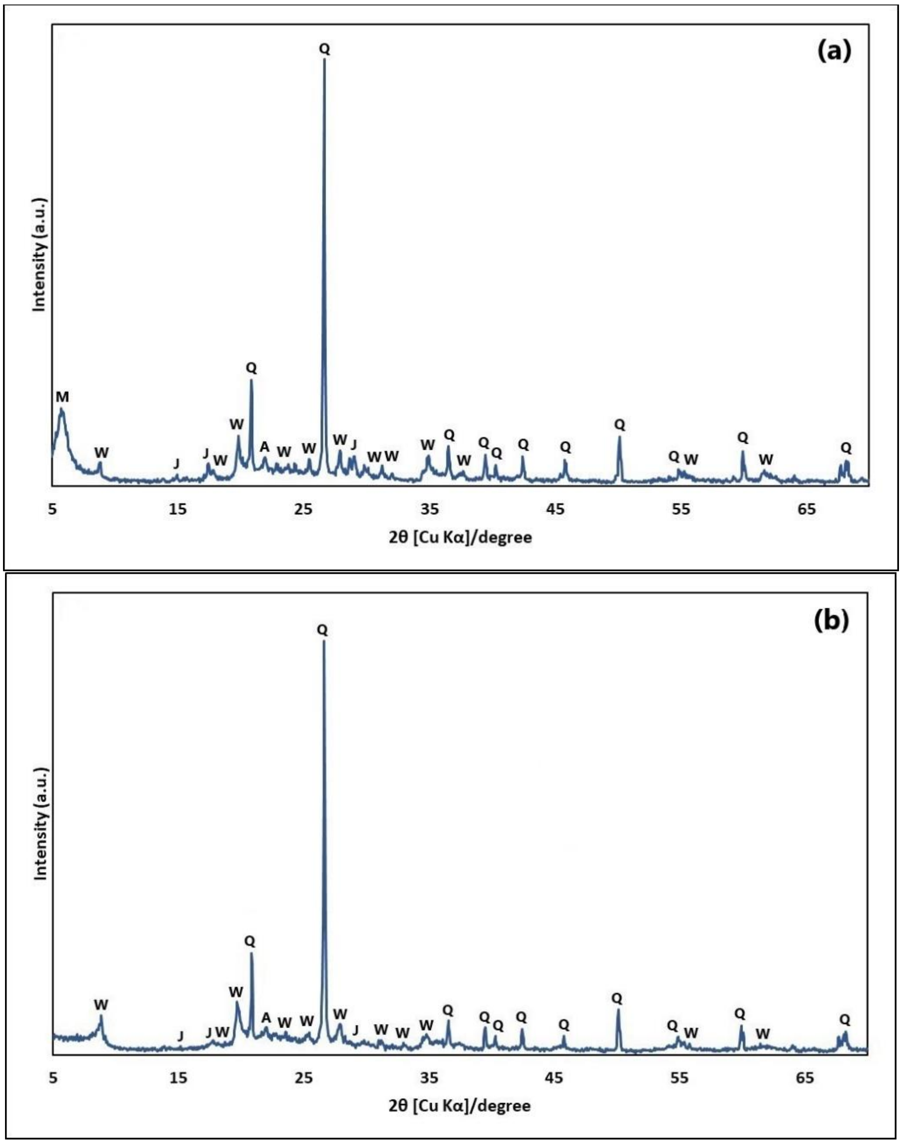

Figure 5. 1. X-ray diffraction (XRD) pattern of diatomaceous earth (DE): (a) raw and (b) purified. Q: quartz, J: jarosite, A: albite, W: muscovite, M: montmorillonite.

In addition, the XRF analysis demonstrated that raw DE contains mainly SiO_2 and Al_2O_3 as well as other oxides, which are shown in Table 5.1.

Table 5. 1. Composition ($wt\%$) of diatomaceous earth

Al_2O_3	SiO_2	S	P_2O_5	K_2O	CaO	TiO_2	MgO	Fe_2O_3	Co_3O_4	SnO_2	CeO_2	WO_3
12.10 (±0.72)	61.00 (±0.80)	0.71 (±0.03)	0.26 (±0.09)	1.19 (±0.02)	0.53 (±0.01)	0.29 (±0.01)	0.06 (±0.00)	1.63 (±0.01)	0.42 (±0.01)	0.16 (±0.04)	0.04 (±0.01)	0.01 (±0.00)

On the other hand, Figure 5.2 shows the XRD pattern of the $ZnTiO_3/TiO_2$ (ZTO) and $ZnTiO_3/TiO_2/La$ (ZTO/La) nanocomposites. The characteristic peaks of $ZnTiO_3$ were shown at 2θ~32.79° and 35.31°. The nanocomposite, in addition to the $ZnTiO_3$ phase, consisted mainly of the anatase phase, whose characteristic peak appeared at 25.28° and, to a lesser extent, the rutile phase, whose characteristic peak appeared at 27.40° only for ZTO. This demonstrates that La-doping inhibited the transition of anatase to the rutile phase at the temperature–time conditions applied [2]. Furthermore, due to its low concentration, there were no diffraction peaks (50° and 60°) corresponding to the presence of La_2O_3 oxide [59].

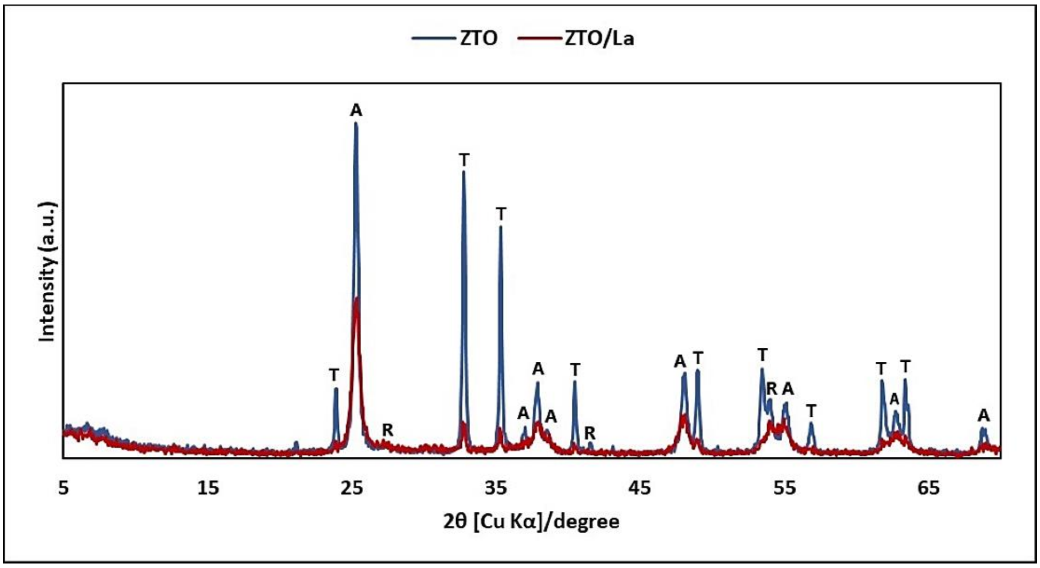

Figure 5. 2. X-ray diffraction (XRD) pattern of $ZnTiO_3/TiO_2$ (ZTO) and $ZnTiO_3/TiO_2/La$ (ZTO/La). T: titanate, A: anatase, R: rutile

The crystalline sizes of $ZnTiO_3/TiO_2$ doped with La (ZTO/La) were calculated based on the main peak using the well-known Scherrer equation (Equation (5.10)) [86,87].

$$A = \frac{K\lambda}{\beta\ cos\theta} \tag{5.10}$$

where K is the shape factor (here, $K = 0.89$) and λ is the wavelength of the X-ray beam used (here, $\lambda = 0.15406$ nm, θ is the Bragg angle, and β is the full width at half maximum (FWHM) of the X-ray diffraction peak, which was calculated using the MDI JADE computer software, version 6 (Materials Data Inc., Livermore, CA, USA, 014)). The average crystalline sizes of the main phases present in the ZTO/La nanocomposite were 29.09 (±0.92) and 16.33 (±1.03) nm for $ZnTiO_3$ and TiO_2 (anatase phase), respectively. These values were lower than those calculated for the $ZnTiO_3/TiO_2$ nanocomposite: 41.35 (±1.27) and 26.76 (±1.31) nm for $ZnTiO_3$ and TiO_2 (anatase phase), respectively. From these results, the specific effect of lanthanum on the inhibition of crystallite growth and the stabilization of the $ZnTiO_3$ and TiO_2 phases was observed.

5.3.1.2. Optical and Photoelectric Properties

The optical absorption properties of photocatalysts can be characterized by the UV-visible (UV-vis) DRS in the range of 200–600 nm at room temperature. Figure 5.3(a) shows the UV-vis DRS of $ZnTiO_3/TiO_2$ (ZTO) and $ZnTiO_3/TiO_2$/La (ZTO/La). Comparatively, the visible light absorption intensity of the ZTO/La spectrum, at around 400 nm, was slightly improved, suggesting that the ZTO/La composite has better response to visible light. The graphs of $(\alpha \boldsymbol{hv})^2$ versus $\boldsymbol{hv}$ to calculate the direct band-gap energy (E_g) are shown in Figure 5.3(b). According to this figure, the direct E_g values obtained from the intersections of the straight line with the energy axis [88] were 3.07 and 3.04 eV for ZTO and ZTO/La, respectively. The direct E_g values, represented in Figure 5.3(b), were calculated for ZTO and ZTO/La using the Equation (5.11) [89].

$$E_g = \frac{1240}{\lambda} \tag{5.11}$$

where E_g is the band-gap energy in electron volts (eV) and λ represents the lower cutoff wavelength in nanometers (nm).

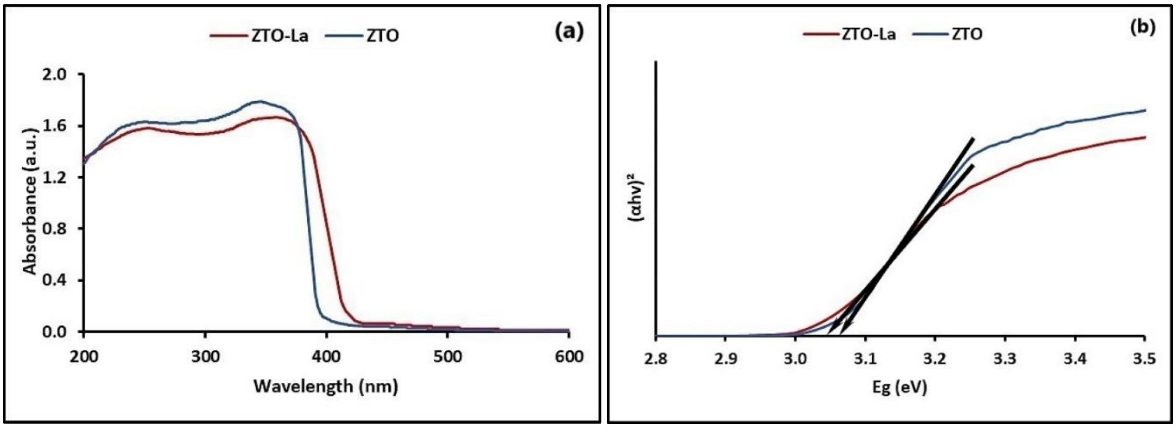

Figure 5. 3. (a) UV-vis DRS and (b) plots of $(\alpha h\nu)^2$ vs. E_g of $ZnTiO_3/TiO_2/La$ and $ZnTiO_2/TiO_2$.

5.3.1.3. SEM and EDS Analysis

Figure 5.4(a) shows the SEM micrographs of ZTO/La, which consisted of nearly spherical particles that had a strong tendency to form agglomerates. These particles were smaller in size than the non-doped nanocomposite that we reported in previous studies [90]. The mean particle size of the ZTO compound without the addition of La^{3+} was 98 nm, in contrast to the ZTO/La compound with La^{3+} ions, where the mean particle size was 78 nm. The results presented indicate that, as a dopant, La^{3+} is effective at hindering the growth of crystallites and stabilizing the ZTO compound. Additionally, the surface morphology of Ecuadorian diatomaceous earth (DE) was also investigated by SEM, and the results are shown in Figure 5.4(b), from which it can be seen that the initial DE showed a cylindrical structure with a length of approximately 14–36 μm, an external pore diameter of around 16 μm, and an internal pore diameter in the higher cylinder of around 6 μm. There was a nearly regular array of submicron pores in an average diameter of 286 nm in the wall. Because of the macroporosity and the micron scales, reactants diffusion and physical separation are very facile [24]. The SEM micrographs of both $ZnTiO_3/TiO_2$-DE (ZTO-DE) and $ZnTiO_3/TiO_2/La$-DE (ZTO/La-DE) are presented in Figures 5.4(c) and 5.4(d), respectively. In these figures, the supported composites appear with fewer cylindrical structures but with some catalyst particles incorporated (smaller ZTO and ZTO-La grains) on the outer face of DE.

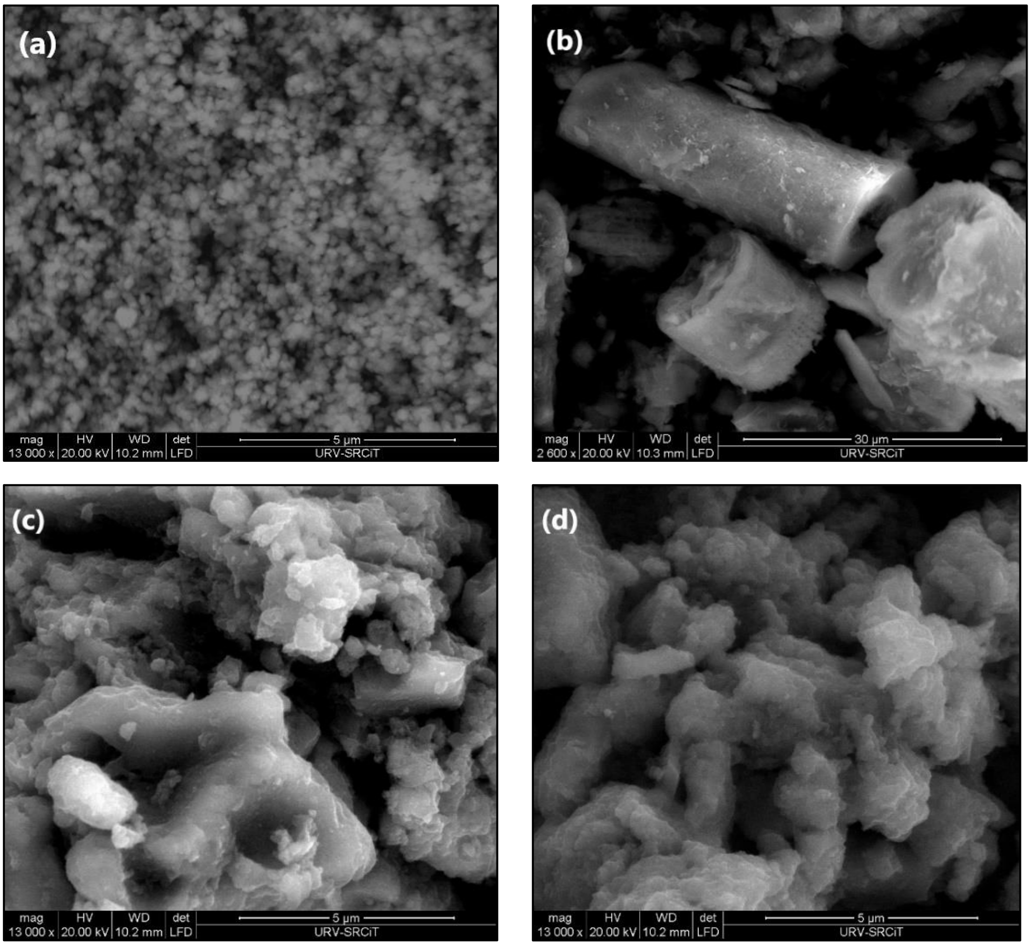

Figure 5. 4. Scanning electron microscopy (SEM) images of (a) $ZnTiO_3/TiO_2/La$ (ZTO/La), (b) diatomaceous earth (DE), (c) $ZnTiO_3/TiO_2$-DE (ZTO-DE), and (d) $ZnTiO_3/TiO_2/La$-DE (ZTO/La-DE)

The presence of La in the ZTO/La synthesized composite was confirmed by energy dispersive X-ray spectroscopy (EDS) (Figure 5.4(a)). According to the EDS analysis of the pure and La-doped composite, lanthanum was incorporated into ZTO nanoparticles. According to the EDS analysis, ZTO/La consisted of C (8.02%), O (59.29%), Ti (28.79%), Zn (2.47%), and La (1.43%). On the other hand, according to the EDS analysis in Figure 5.5(b), DE consisted of C (11.62%), Ca (0.52%), K (2.19%), Fe (2.79%), O (50.41%), Mg (0.61%), Al (6.32%), Si (24.86%), and S (0.68%). The EDS analysis of Figures 5.5(c) and 5.5(d) confirmed that ZTO-DE- and ZTO/La-DE-supported composites contained an important amount of titanium and zinc, respectively, whereas lanthanum was present only in ZTO/La-DE.

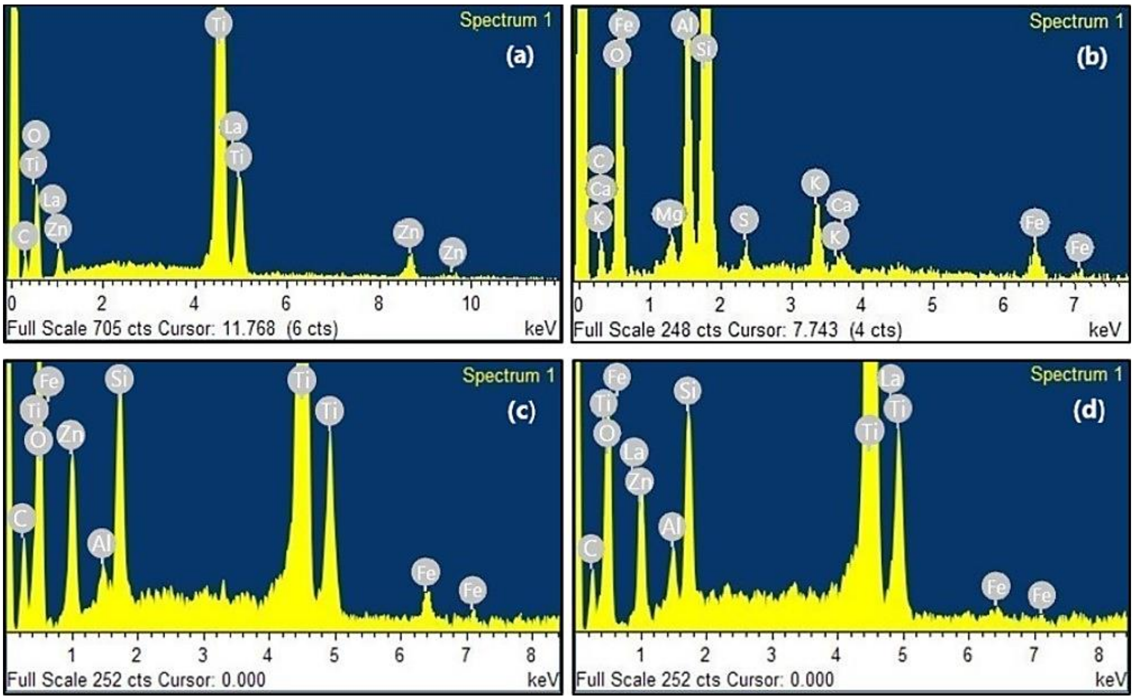

Figure 5. 5. Energy dispersive X-ray (EDX) spectrum of (a) $ZnTiO_3/TiO_2/La$ (ZTO/La), (b) diatomaceous earth (DE), (c) $ZnTiO_3/TiO_2$-DE (ZTO-DE), and (d) $ZnTiO_3/TiO_2/La$-DE

5.3.1.4. Specific Surface Area (SSA) Analysis

The specific surface area of the adsorbents, both in their powder and extrudate forms, are summarized in Table 5.2. The extruded adsorbents prepared had a smaller surface area compared to that of adsorbents in powder form probably due to the heat treatment required for their preparation and to the lower surface area of DE. Despite the reduction in the specific surface area of the extrudates, the presence of exchange cations in their structure can contribute to elimination of the dye from the solution, since different mechanisms participate in the adsorption process.

Table 5. 2. SSA (m^2/g) of ZTO/La, ZTO, DE, and composites

Adsorbent	Form	SSA (m^2/g)
ZTO/La	Powder	126.45
ZTO	Powder	105.84
DE	Powder	89.84
DE	Extrudate	48.89

ZTO/La-DE	Powder	93.24
ZTO/La-DE	Extrudate	67.38
ZTO-DE	Powder	72.21
ZTO-DE	Extrudate	40.36

5.3.2. MB Adsorption

5.3.2.1. Effect of pH

DE showed a pH_{PZC} value of around 4.4, whereas the ZTO-DE and ZTO/La-DE extrudates showed pH_{PZC} values of around 6.2. At a pH higher than pH_{PZC}, the surface had a net negative charge and adsorption of the cationic dye molecule was promoted. However, MB adsorption was reduced at a pH lower than pH_{PZC} due to the net positive charge on the surface, which caused electrostatic repulsion. Figure 5.6 shows this effect of pH on DE, ZTO-DE, and ZTO/La-DE extrudates.

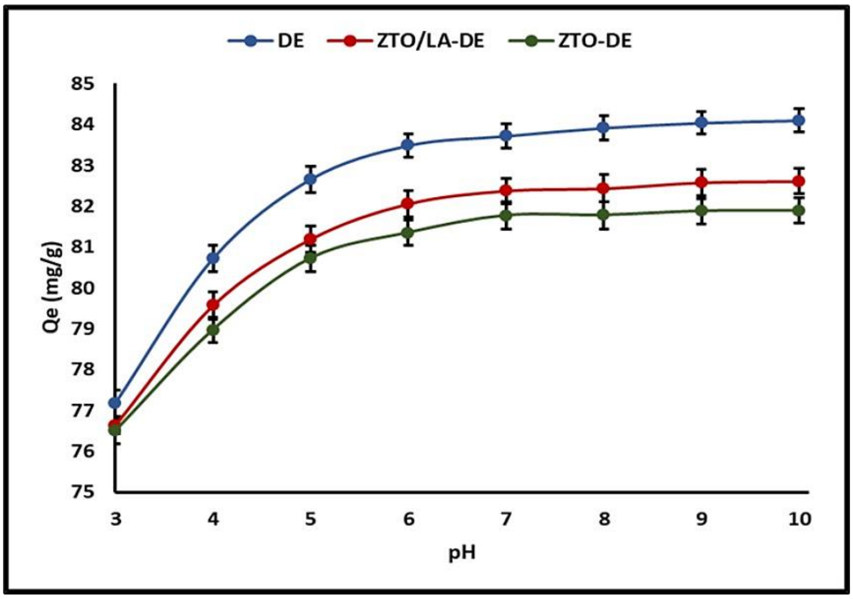

Figure 5. 6. Effect of pH on MB adsorption onto composites

From the minimal increment in MB adsorption in the solution at pH values above 8, it was decided that adsorption at pH = 7 was the optimum operating condition for adsorption experiments.

5.3.2.2. Adsorption Isotherm

Figure 5.7 shows the adsorption isotherms of the extruded composites: DE, ZTO-DE, and ZTO/La-DE. This figure shows that the behavior of all composites fit the Langmuir model better than the Freundlich model.

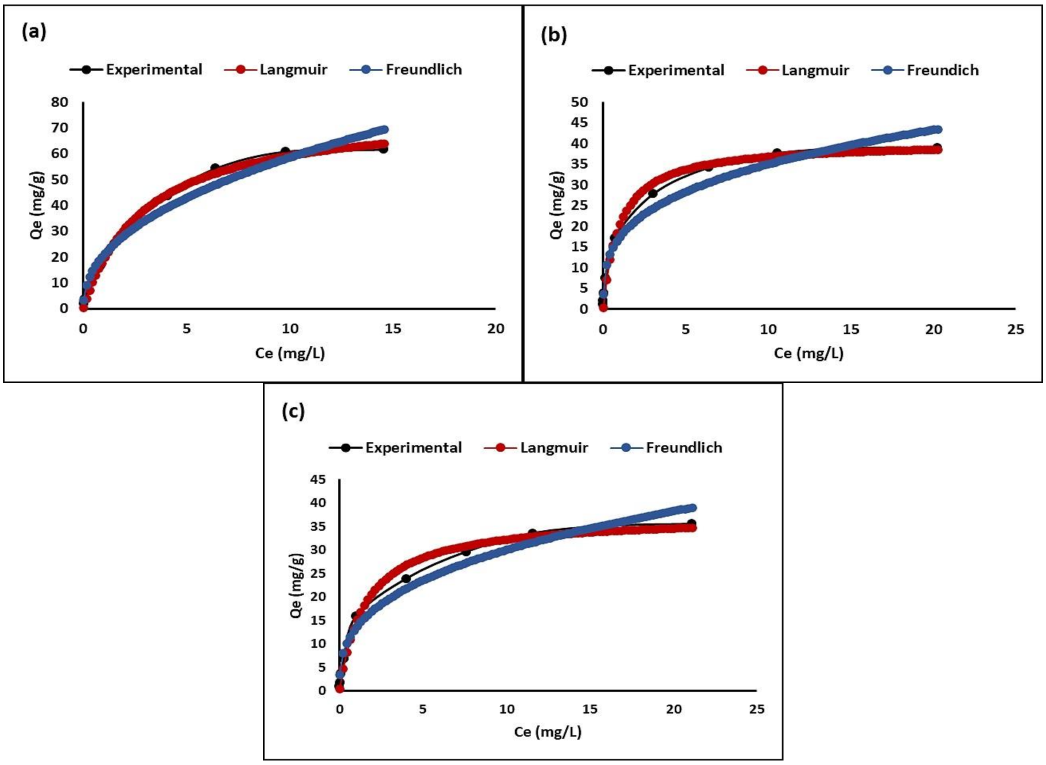

Figure 5. 7. Adsorption isotherm of (a) DE, (b) ZTO/La-DE, and (c) ZTO-DE

Table 5.3 shows the equilibrium data of MB adsorption by extruded composites DE, ZTO-DE, and ZTO/La-DE. Furthermore, the R_L separation factor or equilibrium parameter was calculated using Equation (3), obtaining low R_L values for all the adsorbents. When $0 < R_L < 1$, favorable adsorption was indicated, and $R_L > 1$ meant unfavorable adsorption; $R_L = 0$ indicated irreversible adsorption, and $R_L = 1$ meant energy dispersive X-ray linear adsorption [91].

Table 5. 3. Isotherm parameters for MB adsorption on composites

Isotherm Parameters		ZTO-DE	ZTO/La-DE	DE
Langmuir	q_{max} (mg g^{-1})	37.32 (±1.21)	40.44 (±1.06)	77.05 (±2.33)
	K_L (L mg^{-1})	0.63 (±0.10)	0.99 (±0.14)	0.56 (±0.06)

	R_L	0.03	0.02	0.06
	χ^2	2.27	2.31	2.30
	R^2	0.99	0.99	0.99
Freundlich	K_F (L mg^{-1})	13.38 (±1.21)	17.24 (±1.51)	20.82 (±2.22)
	n	2.85 (±0.90)	3.26 (±0.37)	2.23 (±0.24)
	1/*n*	0.35	0.31	0.45
	χ^2	6.62	10.52	10.42
	R^2	0.97	0.96	0.96

5.3.2.3. Adsorption Kinetics

Figure 5.8 shows the time–course variation of the C_t (mg/L) curves of the extruded composites: DE, ZTO-DE, and ZTO/La-DE. This figure indicates that the pseudo-second-order model was better than the pseudo-first-order model to describe the behavior of all composites. The figures show that the MB concentration in the solution decreased rapidly around the first 60 min, after which removal tended to become constant.

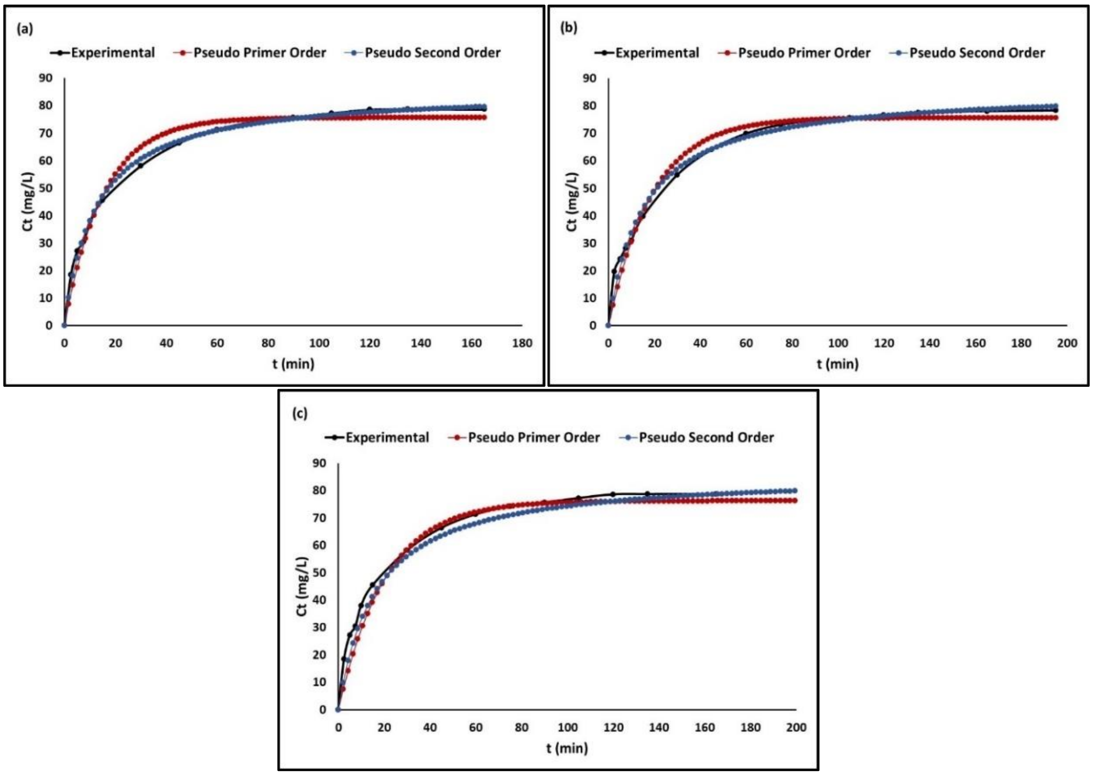

Figure 5. 8. Adsorption kinetics of (a) DE, (b) ZTO/La-DE, and (c) ZTO-DE

The intra-particle diffusion in Figure 5.9 indicates that two steps occurred in the adsorption process. The initial and the second portions in each plot may have been products in the boundary layer effect and intra-particle diffusion, respectively. The initial steep-slope portion is attributed to external surface adsorption or instantaneous adsorption, whereas the relatively flat-slope portion followed by the initial portion can be attributed to the gradual adsorption stage where intra-particle diffusion was the rate-limiting step [59,92].

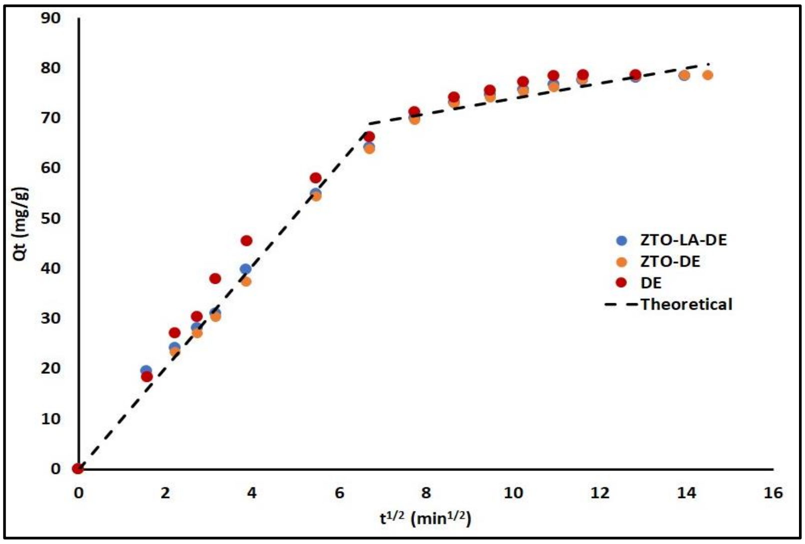

Figure 5. 9. Intra-particle diffusion plots for MB removal by the extrudates

Table 5.4 shows the equilibrium data of MB adsorption by extruded composites DE, ZTO-DE, and ZTO/La-DE.

Table 5. 4. Kinetic parameters for MB removal in composites

Kinetic Parameters		ZTO-DE	ZTO/LA-DE	DE
Pseudo-first order	q_{max} (mg g^{-1})	76.21 (±1.37)	75.62 (±1.53)	75.60 (±1.50)
	k_1 (min^{-1})	0.05 (±3.91 × 10^{-3})	0.05 (±4.61 × 10^{-3})	0.06 (±5.49 × 10^{-3})
	χ^2	14.69	16.83	15.87
	R^2	0.98	0.98	0.98
Pseudo-second order	q_{max} (mg g^{-1})	86.35 (±4.40)	85.96 (±1.53)	85.57 (±0.99)
	k_2 (g mg^{-1} min^{-1})	7.11 × 10^{-4} (±6.14 × 10^{-5})	7.63 × 10^{-4} (±7.06 × 10^{-5})	9.41 × 10^{-4} (±5.68 × 10^{-5})
	χ^2	6.29	6.79	2.89
	R^2	0.99	0.99	1.00

Intraparticle diffusion	k_3 (mg g^{-1} $min^{-1/2}$)	5.37 (±0.51)	5.66 (±0.52)	6.05 (±0.56)
	A	15.31 (±4.37)	14.68 (±4.21)	15.28 (±4.23)
	R^2	0.87	0.89	0.89
External-film diffusion	*Df* (m^2 min^{-1})	1.32×10^{-11}	1.27×10^{-11}	1.37×10^{-11}
	R^2	0.97	0.98	0.93
Internal-pore diffusion	*Dp* (m^2 min^{-1})	1.20×10^{-17}	1.24×10^{-17}	2.00×10^{-17}
	R^2	0.99	0.99	0.90

5.3.3. Photocatalytic Degradation of MB

Photocatalysts can efficiently decompose organic substances because of their strong oxidizing ability, which is generated when the photocatalysts are irradiated by light. In this paper, the photocatalytic activity of ZTO, ZTO/La, ZTO-DE, and ZTO/La-DE composites was tested by the decomposition of methylene blue (MB) in water using solar light. Figure 5.10 shows the results obtained in the test.

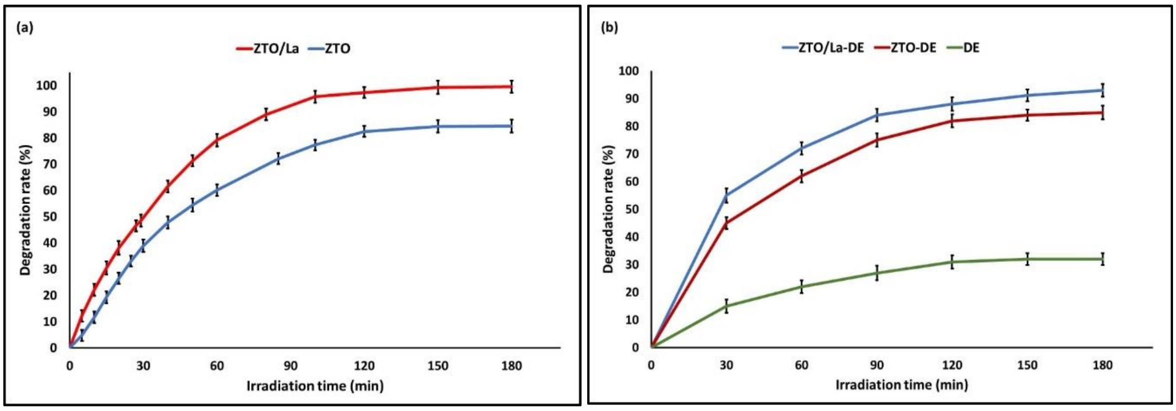

Figure 5. 10. Photocatalytic degradation of MB by (a) a photocatalyst and (b) a supported photocatalysts

Figure 5.11(a) shows that DE had a higher capacity for adsorption of the MB dye than supported semiconductors. Moreover, ZTO-DE and ZTO/La-DE had higher photocatalytic activity than DE. Figure 5.11(b) shows that DE-supported photocatalysts had higher efficiency for MB removal in aqueous systems.

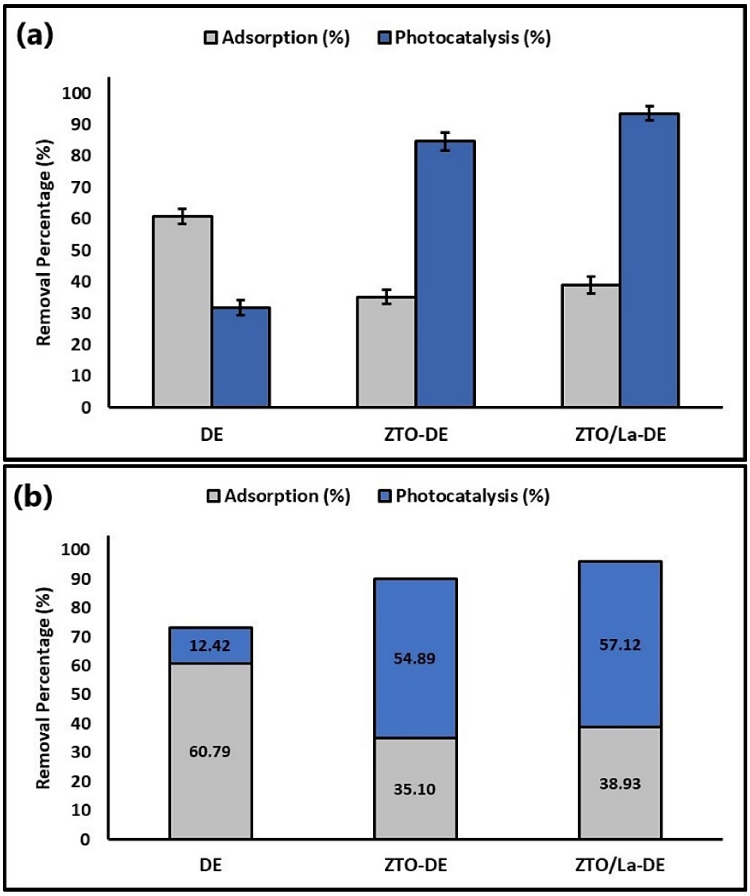

Figure 5. 11. Percentage of (a) individual and (b) accumulated MB adsorbed and photodegraded by the composites

5.3.4. Reuse of the Composites

As the stability and recyclability of the photocatalysts are considered important factors for their application on a large scale, five consecutive removal runs were carried out for the DE, ZTO-DE, and ZTO/La-DE extrudates. Figure 5.12 shows the efficiency (removal percentage) of these materials for five cycles.

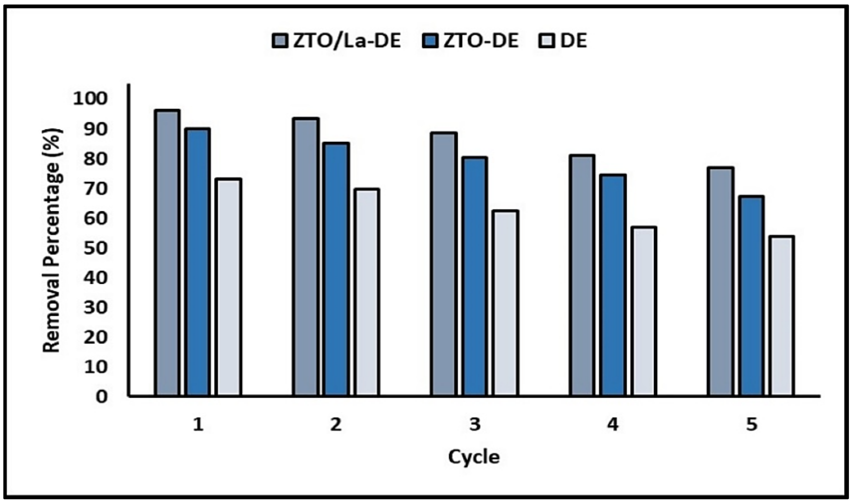

Figure 5. 12. Percentage of MB removal during five successive adsorption-photocatalysis cycles

Figure 5.12 clearly shows that the percentage of MB removal decreased slightly with increasing cycle times. However, after five cycles the synthesized materials still had high activity and could efficiently degrade MB in aqueous solution.

5.4. Discussion

5.4.1. Characterization of the Samples

5.4.1.1. XRD and XRF Analysis

Figure 5.1 illustrates the XRD pattern of diatomaceous earth (DE), in which the high content of SiO_2 in the form of quartz is clear, as well as other mineralogical phases consistent with the XRF results (Table 5.1). The chemical and mineralogical composition of DE is in accordance with that reported in the literature [26]. In Figure 5.2, it is observed that the La ion significantly reduced the intensity of the zinc titanate ($ZnTiO_3$) and anatase peaks of the doped compound (ZTO/La). According to the literature, the La ion has an ionic radius of 1.03 Å and could therefore not replace Ti cations with an ionic radius of 0.64 Å, but could potentially be located on the surface of $ZnTiO_3$ crystallites and anatase in small amounts [72]. The presence of Ti-O-La on the surface of the hybrid catalyst's crystallites can contribute to the decrease in the intensities of the diffraction peaks [64]. This is because segregation of doping cations on the crystallites' surface inhibits their growth by restricting direct contact with neighboring crystallites, which leads to the stabilization of small crystalline particles [60,67]. The rutile phase is not present in the doped compound, probably because the La ion would greatly delay transformation from the anatase phase to the rutile phase [93,94]. No diffraction peaks of lanthanide oxides in the ZTO/La patterns were observed. This is probably due to the low amount of La ions (~1%) and also to the fact that the lanthanide oxides would be well dispersed in the $ZnTiO_3$ and anatase phases [55].

5.4.1.2. Optical and Photoelectric Properties

The UV-vis optical absorption spectra of ZTO and ZTO/La heterojunctions are shown in Figure 5.3(a). With respect to the undoped ZTO, it is clear that the absorption threshold was slightly shifted to the visible light region. Various authors have also reported a red-shift in UV to visible light absorption caused by La^{3+} doping into TiO_2 [47,95]. However, other authors have reported a blue-shift in the absorption profile of La-doped TiO_2 [96] and even an unchanged absorption spectrum for La-doped TiO_2 relative to pure TiO_2 [97]. Furthermore, plots of $(\alpha h v)^2$ versus hv in Figure 5.3(b) reveal that the bandgap (Eg) values of ZTO and ZTO/La were estimated at 3.07 and 3.04 eV, respectively. The bandgap plays a critical role in the photocatalytic activity of photocatalysts due to the fact that it participates in determining the e^-/h^+ recombination rate [11]. From the result observed, the bandgap of ZTO decreased when it was doped with La^{3+}. Therefore, it is shown that ZTO/La is more active than ZTO under solar irradiation, probably due to the lesser separation between occupied and unoccupied bands [34].

5.4.1.3. SEM and EDS Analysis

The SEM photographs and EDX spectra in Figures 5.4 and 5.5, respectively, confirm the immobilization of ZTO and ZTO/La in DE. Photocatalysts immobilized in DE were relatively uniform, with some agglomerations that could have been covering the characteristic DE skeletons. The use of DE to immobilize nanostructured semiconductors was an effective alternative to obtain porous photocatalysts with better active surface and adsorption capacity than isolated semiconductors, keeping their electronic and structural properties for their application in the MB degradation under solar irradiation.

5.4.1.4. Specific Surface Area (SSA) Analysis

The specific surface area (SSA) was estimated by nitrogen adsorption at a low temperature (−196°C). The result listed in Table 5.2 shows that ZTO/La had a higher specific surface area, around 126.45 m^2/g, compared to the ZTO compound, whose specific surface area was 105.84 m^2/g. The increase in the surface area of ZTO/La was probably due to the decrease in the size of the primary crystallites, as well as the different phase composition of these samples [98]. Table 5.2 also shows that the extrudates had a lower specific surface area than the powdered materials. The decrease in the surface area of the extruded adsorbents after heat treatment is essentially attributed to the elimination of the physically adsorbed water as well as to the surface hydroxyl groups loosely bound to the DE structure [99–101]. Dehydration creates additional spaces within the DE porous structure, which probably contracts, causing the internal surface area to decrease. The relatively high surface area of the DE-immobilized ZTO/La nanocomposite could be a promising material for adsorption and photocatalysis, as well as for other applications. In fact, preliminary studies on the adsorption capacity and photocatalytic activity of the ZTO compound showed promising results for methylene blue (MB) removal in aqueous systems under irradiation with ultraviolet light [83,90]. Although the powdered materials usually have a higher SSA, in this study, the extrudates were chosen to adsorb MB due to their appropriate mechanical and chemical stability, which facilitated their recovery at the end of the process and their reuse after several cycles.

5.4.2. MB Adsorption

Batch adsorption of MB was performed from an aqueous solution to investigate the adsorption properties of ZTO-DE, ZTO/La-DE, and DE. Although the extrudates showed a lower specific surface area, they were also effective in removing MB from the aqueous solution, probably through other mechanisms, including electrostatic interaction, chemical reactions such as complexation, or ion exchange between adsorbent and MB [82].

Consequently, despite the reduction in the specific surface area of the extrudates, the surface chemistry of these materials was also an important factor controlling MB adsorption. The extruded DE showed a pH_{PZC} value of around 4.4 and the adsorption tests were carried out at pH = 7.0; therefore, the surface of these materials was negatively charged, improving adsorption of the cationic dye. In addition, according to XRF, DE contained various cations, such as Mg, K, Ca, and Fe, that could promote the cation exchange capacity of the extruded composites prepared to improve their MB adsorption capacity [102]. Likewise, there are several parameters that determine the effectiveness of the adsorption process. In this study, experiments were developed by varying the following parameters: initial pH of the MB solution, initial MB concentration, and contact time.

5.4.2.1. Effect of pH

During the adsorption process, pH can affect the surface charge of the adsorbent, the electrical charge of the dye, and the degree of ionization. Adsorption is expected to increase with pH, particularly for an adsorbate of a cationic nature [103]. Several authors have suggested that at pH values above pH_{PZC}, the surface has a net negative charge and tends to accumulate cationic dye molecules due to the electrostatic attraction between the cationic dye molecule and the negatively charged surface or the extrudate [104]. However, MB adsorption is reduced at pH values lower than pH_{PZC} due to the net positive charge on the surface, which causes electrostatic repulsion. As shown in Figure 6, the rate of MB adsorbed improved as pH increased from 3.0 to 9.0. However, the adsorption rate at pH values between 7.0 and 9.0 was relatively lower than that observed at pH values between 3.0 and 7.0. As reported in the literature, the high adsorption capacity observed at alkaline pH values is due to the increase in hydroxyl ions and, therefore, to the increase in electrostatic attraction between the positive and negative charges of the adsorption sites [91]. However, at very alkaline pH levels, it appears that OH ions form a complex with other ions within alkaline pH ranges, which affects the dye–adsorbent interaction [105]. This leads to the precipitation of MB on the adsorbent surface, since the adsorption process is probably a combination of factors, such as electrostatic attraction, adsorption, and precipitation [106].

5.4.2.2. Adsorption Isotherm

Adsorption isotherm studies show that using the extrudates, the MB removal rate first increases from 0.25 to 20 mg L^{-1}, and then decreases when the initial MB concentration (20–30 mg L^{-1}) is increased. This can be explained by the fact that at higher concentrations, more MB molecules compete for the active sites available on the surface of the adsorbent material. These active sites, which are limited in amount, quickly become saturated as the concentration of MB increases. Therefore, the initial concentration of dye provides a significant driving force to overcome the mass transfer resistance of the dye between the aqueous solution and the surface of the extrudates [107].

The experimental data of adsorption were fitted to the Langmuir and Freundlich isotherm models. The parameters corresponding to the fit of these results are summarized in Table 5.3. The correlation coefficients in both isotherm models were close to 1, indicating that the two models fit the experimental data well [108]. However, as shown in Figure 5.7, the Langmuir isotherm model fit better than the Freundlich isotherm model. It can be concluded that MB adsorption onto these adsorbents can be considered monolayer adsorption rather than multilayer adsorption. This fact supposes that MB adsorption on extrudates occurs as a phenomenon of electrostatic attraction in which the adsorption energy is uniform [109]. During this adsorption process, the cationic dye tends to move through the pores and channels of the extrudates, replacing the exchangeable cations present in the synthesized materials, which are shown in Figure 5.5.

5.4.2.3. Adsorption Kinetics

Although the adsorption models help to establish efficiency in the process, it is also important to determine the kinetic mechanism. The adsorption kinetic models express the contact time required for complete adsorption of the chemical species. From them, we can establish the optimal conditions for a process of continuous dye removal and/or scaling at an industrial level. Figure 5.8 illustrates the MB concentration in an aqueous solution at different contact times. For all adsorbents, it was observed that the MB concentration decreased rapidly at the beginning, and tended to be constant after 60 min. From this trend, we can conclude that equilibrium was reached at the contact time of around 180 min. The rapid initial adsorption stage resulted from the presence of the vacant adsorption sites, as well as from the presence of a high concentration gradient. On the one hand, adsorption by all extrudates can be attributed to the negative surface charge of these materials, which leads to a high electrostatic attraction between the negatively charged sorbents and the positively charged cationic MB [110]. On the other hand, the efficiency of extrudates to adsorb dissolved MB dye molecules is also attributed to the combination of active sites provided by the diatomaceous earth, which acts as a support, and the photocatalysts nanoparticles immobilized on the surface.

The adsorption kinetic parameters are summarized in Table 5.4. In this study, the highest correlation coefficient (R^2) was obtained for the pseudo-second-order model, which assumed chemical adsorption o the cationic dye in the extrudates [111]. The adjustment of experimental data to the intraparticle diffusion model shown in Figure 5.9 allowed for the identification of two linear regions, which suggests that the MB adsorption process could be described by external-film diffusion followed by internal-pore diffusion. Table 5.4 also summarizes the linear regression analysis for the diffusion kinetic models. The highest values of the regression coefficient (R^2) were found for the external-film diffusion; furthermore, the values of A were relatively high. Therefore, surface adsorption was the rate-limiting step [112].

5.4.3. Photocatalytic Degradation of MB

It is clear from Figure 5.10 that the photocatalytic activity of ZTO/La was the highest probably due to it having a high surface area and low bandgap. The results show that the photocatalytic activities of the ZTO/La nanoparticles increased and the bandgap value decreased. This is due to the fact that the energy ($h\nu$) required is directly proportional to the bandgap and hence reduces the energy needed to excite electrons from the valence band to the conduction band [11].

The use of DE-supported photocatalysts (ZTO-DE and ZTO/La-DE) allowed for an efficient degradation of the MB solution, probably due to the following two main reasons. First, the unique mesoporous structure and higher surface area of DE would significantly improve the adsorption capacity of the material, providing a more active adsorption site towards the target molecules. Second, the incorporation of $ZnTiO_3/TiO_2$ and $ZnTiO_3/TiO_2$/La photocatalysts could facilitate transfer of photogenerated electrons from the bulk to the surface and thus inhibit the recombination of electron pairs and holes under solar irradiation [38]. As is known, under illumination, the electrons of a photocatalyst can be excited and then immediately transferred from the valence band (VB) to the conduction band (CB), generating an electron-hole pair (e^-/h^+) and leaving a hole (h^+) in the VB (reaction 1). The electron-hole pairs can recombine immediately (reaction 2); some of them can also migrate to the surface of the catalyst and react separately with other species adsorbed on the surface, such as H_2O, OH^-, O_2, and other molecules (R), as MB dye. The holes at the semiconductor VB can oxidize adsorbed water or hydroxyl ions to form highly reactive hydroxyl radicals (reactions 3 and 4). On the other hand, the generated electrons at the CB can react with adsorbed oxygen molecules to produce OH radicals via a succession of reactions (reactions 5–8). These formed hydroxyl radicals have a strong ability to degrade organic dyes such as methylene blue (MB) (reaction 9). Furthermore, direct oxidation of MB could also occur by reaction with holes (reaction 10) [79]. The following reactions represent the probable mechanism of MB photodegradation on the surfaces of ZTO-DE and ZTO/La-DE.

$$(semiconductor) \xrightarrow{hv} semiconductor + e^-_{CB} + h^+_{VB} \qquad (1)$$

$$e^-_{CB} + h^+_{vb} \rightarrow heat \qquad (2)$$

$$H_2O_{ads} + h^+_{VB} \rightleftharpoons (H^+ + OH^-)_{ads} + h^+_{VB} \rightarrow OH^{\bullet}_{ads} \qquad (3)$$

$$OH^-_{ads} + h^+_{VB} \rightarrow OH^{\bullet}_{ads} \qquad (4)$$

$$(O_2)_{ads} + e^-_{BC} \rightarrow O_2^{\bullet -} \qquad (5)$$

$$O_2^{\bullet -} + H^+ \rightarrow HO_2^{\bullet} \qquad (6)$$

$$2HO_2^{\bullet} \rightarrow H_2O_2 + O_2 \qquad (7)$$

$$H_2O_2 + e^- \rightarrow OH^{\bullet} + OH^- \qquad (8)$$

$$R + OH^{\bullet}_{ads} \rightarrow R'^{\bullet}_{ads} + H_2O \rightarrow degradation\ products \qquad (9)$$

$$R_{ads} + h^+_{VB} \rightarrow R^{\bullet +}_{ads} \rightarrow degradation\ products \qquad (10)$$

When the ZTO/La is irradiated by solar light, the electrons of La_2O_3—which is wrapped on the surface of ZTO—may be excited from ground state to 4*f* orbital. Generally, the photoexcited state of La_2O_3 is generated by the absorption of light, corresponding to the transition of the electrons situated in the inner 4*f* orbital to the 5*d* orbitals (4*f*–5*d* transition) or to other 4*f* orbitals (*f*–*f* transition). As a result, the electrons can be freely transported along the surface, leading to better photoelectrochemical and photocatalytic performances of ZTO/La under solar light [39].

5.4.4. Reuse of the Composites

Figure 5.11 shows the efficiency obtained in the present study for the adsorption and photocatalytic degradation of MB from aqueous solutions. Although DE has low photocatalytic activity, its adsorption capacity is greater and allows for the immobilization of the photocatalyst to facilitate its handling and recovery in the process.

Mechanical stability is an especially important property, which is directly related to the useful life of the supported photocatalyst. When mechanical stability is poor, the photocatalyst will gradually flake away from the support into the reaction solution during the process; consequently, the supported photocatalyst loses its activity prematurely, and causes both secondary contamination and waste of the photocatalyst. Some research results showed that mechanical stability of the material is correlated with the calcination temperature [113]. Consequently, increasing the calcination temperature produces better mechanical stability, although there is an optimal calcination temperature to achieve maximum mechanical stability. In the present paper, a maximum calcination temperature of the extrudates of 500 °C was used to avoid the crystalline phase change of the synthesized photocatalysts. On average, the loss of activity in the materials did not exceed 20% at the end of the fifth cycle. Thus, 500 °C is the optimum calcination temperature to achieve adequate photocatalytic activity and reuse property, under the operating conditions used in this study.

5.4.5. MB Adsorption Capacity and Photocatalytic Activity of the Synthesized Materials Compared to Other Materials Described in the Literature

The results from this paper indicate that diatomaceous earth is a valuable support for photocatalysts, as it contributes with active sites that improve adsorption of dyes for its subsequent photodegradation. Table 5.5 summarizes the MB adsorption capacity of the synthesized compounds in comparison with other materials reported in the literature.

Table 5. 5. MB adsorption capacity of synthesized materials and of other materials reported in the literature

Material	q_e (mg/g)	References
Activated lignin–chitosan composite extrudates	36.25	[114]
TiO_2/montmorillonite–albumin nanocomposite	18.18	[115]
Carboxymethyl cellulose/ZSM-5/ZIF-8	10.49	[116]
ZSM-5 zeolite	105.82	[117]
NaX zeolite	127.13	[118]
Chitosan/clay microspheres	152.20	[119]
Magnetic chitosan/clay beads	82.00	[120]
Activated carbon–clay composite	178.64	[121]
Hydroxysodalite	10.82	[122]
Kaolin	21.41	[123]
Nonporous silica	91.10	[124]
a-TiO_2/$ZnTiO_3$	16.00	[86]
a-TiO_2	15.00	[86]
Natural clay	15.40	[125]
Raw coal fly ash	5.06	[126]
Activated carbon	6.43	[127]
DE	77.05	This study
$ZnTiO_3$/TiO_2/DE	37.32	This study
$ZnTiO_3$/TiO_2/La-DE	40.11	This study

Similarly, the composites synthesized in this study could be used efficiently to photodegrade dyes in aqueous effluents. Table 5.6 summarizes the operating and process conditions applied in different research studies that photodegraded MB using various doped TiO_2. The conditions are described by four factors, including initial MB concentration, type of light used, reaction time, and MB removal efficiency.

Table 5. 6. Different operating conditions and efficiency for the photocatalytic oxidation of MB by different doping agents

Type of Dopant	MB (mg/L)	Type of Light	Reaction Time (min)	Efficiency (%)	Reference
TiO_2/La	0.1	UV irradiation	120	85	[128]
TiO_2/Fe	0.1	UV irradiation	120	75	[128]
TiO_2/La	0.1	Visible irradiation	120	20	[128]
TiO_2/Fe	0.1	Visible irradiation	120	26	[128]
TiO_2/Ce	32	Visible irradiation	180	90	[129]
TiO_2/Au	12	Visible irradiation	48	92	[130]
TiO_2/Sb	100	Visible irradiation	60	100	[131]
TiO_2/N	10	Solar light	120	97	[132]
TiO_2/I	8	Solar light	120	45	[133]
TiO_2/F	10	Solar light	120	55	[133]
TiO_2/C	28.5	Visible irradiation	420	70	[134]
TiO_2/Fe/La	0.1	Visible irradiation	120	91	[128]
TiO_2/C/N	10	Visible irradiation	180	85	[135]
TiO_2/N/F	5.74	Visible irradiation	140	16	[136]
TiO_2/Mn/Fe	10	Visible irradiation	150	85	[137]
$ZnTiO_3$/PANI/Ag	10	Visible irradiation	25	96	[138]
$ZnTiO_3$/Ag	10	UV irradiation	150	93	[14]
$ZnTiO_3$/TiO_2/La	20	Solar light	150	100	This study
$ZnTiO_3$/TiO_2 (not doped)	20	Solar light	150	87	This study
$ZnTiO_3$/TiO_2/La-DE	20	Solar light	150	93	This study
$ZnTiO_3$/TiO_2-DE (not doped)	20	Solar light	150	85	This study

Finally, the synthesized DE-supported composite reported in this paper could be an efficient alternative to remove dyes in aqueous effluents and the most probable reason is the combined effects of several factors, such as specific surface area, crystal size and crystallization phases, absorption capacity, photocatalytic activity, and mechanical stability.

5.5. Conclusions

In summary, according to the results obtained, it can be concluded that the sol-gel method is suitable for preparing La-doped ZTO of nanometric size and with high photocatalytic activity. Diatomaceous earth was effectively used to immobilize the nanocatalyst and incorporate various active sites on the surface of the compound. The supported catalysts were adapted into extrudates and then successfully used for the adsorption and photocatalytic removal of MB in aqueous systems. In general, the experimental adsorption isotherms were fitted to the Langmuir model, which describes monolayer adsorption on a surface containing an indefinite number of identical sites. This model was correlated with the one found in the pseudo-second-order kinetic model, which indicates a chemisorption process in the adsorbent. On the other hand, the La ion exerted a significant effect on the gap band and particle size of the ZTO hybrid catalyst. These physical chemistry changes improved efficiency in the absorption and photodegradation under solar irradiation of MB [144,145].

ZTO/La-DE was found to be highly efficient (96.05%) when compared to ZTO-DE (89.99%) and DE (73.21%) in adsorbing and photodegrading MB dye. In addition, it was observed that composite materials can be recycled up to five times with a total 20% reduction in the MB removal capacity. Finally, the MB removal capacity of the materials synthesized in this study open a door to the potential generation of efficient and ecological technologies that can be used on an industrial scale from available natural resources.

5.6. References

[1] Chen, F.; Yu, C.; Wei, L.; Fan, Q.; Ma, F.; Zeng, J.; Yi, J.; Yang, K.; Ji, H. Fabrication and characterization of $ZnTiO_3/Zn_2Ti_3O_8/ZnO$ ternary photocatalyst for synergetic removal of aqueous organic pollutants and Cr(VI) ions. *Sci. Total. Environ.* **2020**, *706*, 136026, doi:10.1016/j.scitotenv.2019.136026.

[2] Wang, B.; De Godoi, F.C.; Zheng, S.; Gentle, I.; Li, C. Enhanced photocatalytic properties of reusable TiO_2 -loaded natural porous minerals in dye wastewater purification. *Powder Technol.* **2016**, *302*, 426–433, doi:10.1016/j.powtec.2016.09.003.

[3] Al-Mamun, M.; Kader, S.; Islam, M.; Khan, M. Photocatalytic activity improvement and application of UV-TiO_2 photocatalysis in textile wastewater treatment: A review. *J. Environ. Chem. Eng.* **2019**, *7*, doi:10.1016/j.jece.2019.103248.

[4] Zangeneh, H.; Zinatizadeh, A.; Habibi, M.; Akia, M.; Isa, M.H. Photocatalytic oxidation of organic dyes and pollutants in wastewater using different modified titanium dioxides: A comparative review. *J. Ind. Eng. Chem.* **2015**, *26*, 1–36, doi:10.1016/j.jiec.2014.10.043.

[5] Omer, O.S.; Hussein, M.A.; Hussein, B.; Mgaidi, A. Adsorption thermodynamics of cationic dyes (methylene blue and crystal violet) to a natural clay mineral from aqueous solution between 293.15 and 323.15 K. *Arab. J. Chem.* **2018**, *11*, 615–623, doi:10.1016/j.arabjc.2017.10.007.

[6] Tavakoli-Azar, T.; Mahjoub, A.R.; Sadjadi, M.S.; Farhadyar, N.; Sadr, M.H. Improving the photocatalytic performance of a perovskite $ZnTiO_3$ through $ZnTiO_3$@S nanocomposites for degradation of Crystal violet and Rhodamine B pollutants under sunlight. *Inorg. Chem. Commun.* **2020**, *119*, 108091, doi:10.1016/j.inoche.2020.108091.

[7] Wu, A.; Wang, D.; Wei, C.; Zhang, X.; Liu, Z.; Feng, P.; Ou, X.; Qiang, Y.; Garcia, H.; Niu, J. A comparative photocatalytic study of TiO_2 loaded on three natural clays with different morphologies. *Appl. Clay Sci.* **2019**, *183*, 105352, doi:10.1016/j.clay.2019.105352.

[8] Ahmed, M.; El-Katori, E.E.; Gharni, Z.H. Photocatalytic degradation of methylene blue dye using Fe_2O_3/TiO_2 nanoparticles prepared by sol–gel method. *J. Alloy. Compd.* **2013**, *553*, 19–29, doi:10.1016/j.jallcom.2012.10.038.

[9] Shahid, M.; El Saliby, I.; McDonagh, A.; Chekli, L.; Tijing, L.D.; Kim, J.-H.; Shon, H.K. Adsorption and Photocatalytic Degradation of Methylene Blue Using Potassium Polytitanate and Solar Simulator. *J. Nanosci. Nanotechnol.* **2016**, *16*, 4342–4349, doi:10.1166/jnn.2016.10998.

[10] Ong, C.B.; Ng, L.Y.; Mohammad, A.W. A review of ZnO nanoparticles as solar photocatalysts: Synthesis, mechanisms and applications. *Renew. Sustain. Energy Rev.* **2018**, *81*, 536–551.

[11] El-Bahy, Z.M.; Ismail, A.A.; Mohamed, R.M. Enhancement of titania by doping rare earth for photodegradation of organic dye (Direct Blue). *J. Hazard. Mater.* **2009**, *166*, 138–143, doi:10.1016/j.jhazmat.2008.11.022.

[12] Mazierski, P.; Lisowski, W.; Grzyb, T.; Winiarski, M.; Klimczuk, T.; Mikołajczyk, A.; Flisikowski, J.; Hirsch, A.; Kołakowska, A.; Puzyn, T.; et al. Enhanced photocatalytic properties of lanthanide-TiO_2 nanotubes: An experimental and theoretical study. *Appl. Catal. B: Environ.* **2017**, *205*, 376–385, doi:10.1016/j.apcatb.2016.12.044.

[13] Cai, H.; Chen, X.; Li, Q.; He, B.; Tang, Q. Enhanced photocatalytic activity from Gd, La codoped TiO_2 nanotube array photocatalysts under visible-light irradiation. *Appl. Surf. Sci.* **2013**, *284*, 837–842, doi:10.1016/j.apsusc.2013.08.018.

[14] Abirami, R.; Kalaiselvi, C.; Kungumadevi, L.; Senthil, T.; Kang, M. Synthesis and characterization of $ZnTiO_3$ and Ag doped $ZnTiO_3$ perovskite nanoparticles and their enhanced photocatalytic and antibacterial activity. *J. Solid State Chem.* **2020**, *281*, 121019, doi:10.1016/j.jssc.2019.121019.

[15] El-Sharkawy, E.; Soliman, A.Y.; Al-Amer, K.M. Comparative study for the removal of methylene blue via adsorption and photocatalytic degradation. *J. Colloid Interface Sci.* **2007**, *310*, 498–508, doi:10.1016/j.jcis.2007.02.013.

[16] Mahamadi, C.; Mawere, E. Kinetic Modeling of Methylene Blue and Crystal Violet Dyes Adsorption on Alginate-Fixed Water Hyacinth in Single and Binary Systems. *Am. J. Anal. Chem.* **2013**, *04*, 17–24, doi:10.4236/ajac.2013.410A3003.

[17] Nourmoradi, H.; Ghiasvand, A.; Noorimotlagh, Z. Removal of methylene blue and acid orange 7 from aqueous solutions by activated carbon coated with zinc oxide (ZnO) nanoparticles: equilibrium, kinetic, and thermodynamic study. *DESALINATION Water Treat.* **2015**, *55*, 252–262, doi:10.1080/19443994.2014.914449.

[18] Chen, Y.; Xiang, Z.; Wang, D.; Kang, J.; Qi, H. Effective photocatalytic degradation and physical adsorption of methylene blue using cellulose/GO/TiO_2 hydrogels. *RSC Adv.* **2020**, *10*, 23936–23943, doi:10.1039/d0ra04509h.

[19] Salazar-Rábago, J.J.; Leyva-Ramos, R.; Rivera-Utrilla, J.; Perez, R.O.; Cerino-Cordova, F. Biosorption mechanism of Methylene Blue from aqueous solution onto White Pine (Pinus durangensis) sawdust: Effect of operating conditions. *Sustain. Environ. Res.* **2017**, *27*, 32–40, doi:10.1016/j.serj.2016.11.009.

[20] Subramaniam, M.N.; Goh, P.S.; Abdullah, N.; Lau, W.J.; Ng, B.C.; Ismail, A.F. Adsorption and photocatalytic degradation of methylene blue using high surface area titanate nanotubes (TNT) synthesized via hydrothermal method. *J. Nanoparticle Res.* **2017**, *19*, 220, doi:10.1007/s11051-017-3920-9.

[21] Laysandra, L.; Sari, M.W.M.K.; Soetaredjo, F.E.; Foe, K.; Putro, J.N.; Kurniawan, A.; Ju, Y.-H.; Ismadji, S. Adsorption and photocatalytic performance of bentonite-titanium dioxide composites for methylene blue and rhodamine B decoloration. *Heliyon* **2017**, *3*, e00488, doi:10.1016/j.heliyon.2017.e00488.

[22] Tsai, W.-T.; Lai, C.-W.; Hsien, K.-J. Characterization and adsorption properties of diatomaceous earth modified by hydrofluoric acid etching. *J. Colloid Interface Sci.* **2006**, *297*, 749–754, doi:10.1016/j.jcis.2005.10.058.

[23] Lutyński, M.; Sakiewicz, P.; Lutyńska, S. Characterization of Diatomaceous Earth and Halloysite Resources of Poland. *Miner.* **2019**, *9*, 670, doi:10.3390/min9110670.

[24] Jia, Y.; Han, W.; Xiong, G.; Yang, W. Diatomite as high performance and environmental friendly catalysts for phenol hydroxylation with H2O*Sci. Technol. Adv. Mater.* **2007**, *8*, 106–109, doi:10.1016/j.stam.2006.10.003.

[25] Tokarský, J.; Matějka, V.; Neuwirthová, L.; Vontorová, J.; Kutláková, K.M.; Kukutschová, J.; Čapková, P. A low-cost photoactive composite quartz sand/TiO, *Chem. Eng. J.* **2013**, *222*, 488–497, doi:10.1016/j.cej.2013.02.056.

[26] Ibrahim, S. S. and Selim, A. Q. *Heat treatment of natural diatomite*, Physicochem. Probl. Miner. Process., Wrocław, Poland; vol. 48, no. 2, pp. 413–424, **2012**, doi: 10.5277/ppmp120208.

[27] Upadhyay, G.K.; Rajput, J.K.; Pathak, T.K.; Kumar, V.; Purohit, L. Synthesis of ZnO:TiO_2 nanocomposites for photocatalyst application in visible light. *Vac.* **2019**, *160*, 154–163, doi:10.1016/j.vacuum.2018.11.026.

[28] Irani, M.; Mohammadi, T.; Mohebbi, S. Photocatalytic Degradation of Methylene Blue with ZnO Nanoparticles; a Joint Experimental and Theoretical Study. *J. Mex. Chem. Soc.* **2017**, *60*, 218–225, doi:10.29356/jmcs.v60i4.115.

[29] Ozturk, B.; Soylu, G.S.P. Promoting role of transition metal oxide on $ZnTiO_3$–TiO_2 nanocomposites for the photocatalytic activity under solar light irradiation. *Ceram. Int.* **2016**, *42*, 11184–11192, doi:10.1016/j.ceramint.2016.04.027.

[30] Siwińska-Stefańska, K.; Kubiaka, A.; Piasecki, A.; Goscianska, J.; Nowaczyk, G.; Jurga, S.; Jesionowski, T. TiO_2-ZnO Binary Oxide Systems: Comprehensive Characterization and Tests of Photocatalytic Activity. *Mater.* **2018**, *11*, 841, doi:10.3390/ma11050841.

[31] Belver, C.; Hinojosa, M.; Bedia, J.; Tobajas, M.; Alvarez, M.A.; Rodríguez-González, V.; Rodriguez, J.J. Ag-Coated Heterostructures of ZnO-TiO_2/Delaminated Montmorillonite as Solar Photocatalysts. *Mater.* **2017**, *10*, 960, doi:10.3390/ma10080960.

[32] Nešić, J.; Manojlović, D.D.; Anđelković, I.; Dojčinović, B.P.; Vulić, P.J.; Krstić, J.; Roglić, G.M. Preparation, characterization and photocatalytic activity of lanthanum and vanadium co-doped mesoporous TiO_2 for azo-dye degradation. *J. Mol. Catal. A: Chem.* **2013**, *378*, 67–75, doi:10.1016/j.molcata.2013.05.018.

[33] Wang, M.; Xu, X.; Lin, L.; He, D. Gd–La codoped TiO_2 nanoparticles as solar photocatalysts. *Prog. Nat. Sci.* **2015**, *25*, 6–11, doi:10.1016/j.pnsc.2015.01.002.

[34] Sridevi, A.; Ramji, B.; Venkatesan, G.P.; Sugumaran, V.; Selvakumar, P. A facile synthesis of TiO2/BiOCl and TiO2/BiOCl/La2O3 heterostructure photocatalyst for enhanced charge separation efficiency with improved UV-light catalytic activity towards Rhodamine B and Reactive Yellow *Inorg. Chem. Commun.* **2021**, *130*, 108715, doi:10.1016/j.inoche.2021.108715.

[35] Daou, I.; Zegaoui, O.; Elghazouani, A. Physicochemical and photocatalytic properties of the ZnO particles synthesized by two different methods using three different precursors. *Comptes Rendus Chim.* **2017**, *20*, 47–54, doi:10.1016/j.crci.2016.04.003.

[36] Chen, J.; Qiu, F.; Xu, W.; Cao, S.; Zhu, H. Recent progress in enhancing photocatalytic efficiency of TiO_2 -based materials. *Appl. Catal. A: Gen.* **2015**, *495*, 131–140, doi:10.1016/j.apcata.2015.02.013.

[37] Shwetharani, R.; Sakar, M.; Chandan, H.; Balakrishna, R.G. Observation of simultaneous photocatalytic degradation and hydrogen evolution on the lanthanum

modified TiO2 nanostructures. *Mater. Lett.* **2018**, *218*, 262–265, doi:10.1016/j.matlet.2018.02.031.

[38] Yu, L.; Yang, X.; He, J.; He, Y.; Wang, D. A fluorine free method to synthesize nitrogen and lanthanum co-doped TiO_2 nanocrystals with exposed {001} facets for enhancing visible-light photocatalytic activity. *J. Mol. Catal. A: Chem.* **2015**, *399*, 42–47, doi:10.1016/j.molcata.2015.01.022.

[39] Nie, J.; Mo, Y.; Zheng, B.; Yuan, H.; Xiao, D. Electrochemical fabrication of lanthanum-doped TiO_2 nanotube array electrode and investigation of its photoelectrochemical capability. *Electrochimica Acta* **2013**, *90*, 589–596, doi:10.1016/j.electacta.2012.12.049.

[40] Peng, H.; Cui, J.; Zhan, H.; Zhang, X. Improved photodegradation and detoxification of 2,4,6-trichlorophenol by lanthanum doped magnetic TiO*Chem. Eng. J.* **2015**, *264*, 316–321, doi:10.1016/j.cej.2014.11.122.

[41] Dal'Toé, A.T.; Colpani, G.L.; Padoin, N.; Fiori, M.A.; Soares, C. Lanthanum doped titania decorated with silver plasmonic nanoparticles with enhanced photocatalytic activity under UV-visible light. *Appl. Surf. Sci.* **2018**, *441*, 1057–1071, doi:10.1016/j.apsusc.2018.01.291.

[42] Du, J.; Li, B.; Huang, J.; Zhang, W.; Peng, H.; Zou, J. Hydrophilic and photocatalytic performances of lanthanum doped titanium dioxide thin films. *J. Rare Earths* **2013**, *31*, 992–996, doi:10.1016/s1002-0721(13)60019-8.

[43] Nasir, M.; Xi, Z.; Xing, M.; Zhang, J.; Chen, F.; Tian, B.; Bagwasi, S. Study of Synergistic Effect of Ce- and S-Codoping on the Enhancement of Visible-Light Photocatalytic Activity of TiO*J. Phys. Chem. C* **2013**, *117*, 9520–9528, doi:10.1021/jp402575w.

[44] Djellabi, R.; Ordonez, M.F.; Conte, F.; Falletta, E.; Bianchi, C.L.; Rossetti, I. A review of advances in multifunctional $XTiO_3$ perovskite-type oxides as piezo-photocatalysts for environmental remediation and energy production. *J. Hazard. Mater.* **2022**, *421*, 126792, doi:10.1016/j.jhazmat.2021.126792.

[45] Kumar, R.D.; Thangappan, R.; Jayavel, R. Synthesis and characterization of $LaFeO_3/TiO_2$ nanocomposites for visible light photocatalytic activity. *J. Phys. Chem. Solids* **2017**, *101*, 25–33, doi:10.1016/j.jpcs.2016.10.005.

[46] Ruzimuradov, O.; Hojamberdiev, M.; Fasel, C.; Riedel, R. Fabrication of lanthanum and nitrogen—co-doped $SrTiO_3$—TiO_2 heterostructured macroporous monolithic

materials for photocatalytic degradation of organic dyes under visible light. *J. Alloys Compd.* **2017**, *699*, 144–150, doi:10.1016/j.jallcom.2016.12.355.

[47] Ako, R.T.; Ekanayake, P.; Tan, A.L.; Young, D.J. La modified TiO_2 photoanode and its effect on DSSC performance: A comparative study of doping and surface treatment on deep and surface charge trapping. *Mater. Chem. Phys.* **2016**, *172*, 105–112, doi:10.1016/j.matchemphys.2015.12.066.

[48] Jaimy, K.B.; Ghosh, S.; Warrier, K.G. Enhanced visible light activity of nano-titanium dioxide doped with multiple ions: Effect of crystal defects. *J. Solid State Chem.* **2012**, *196*, 465–470, doi:10.1016/j.jssc.2012.06.048.

[49] Umar, K.; Haque, M.; Muneer, M.; Harada, T.; Matsumura, M. Mo, Mn and La doped TiO_2: Synthesis, characterization and photocatalytic activity for the decolourization of three different chromophoric dyes. *J. Alloy. Compd.* **2013**, *578*, 431–438, doi:10.1016/j.jallcom.2013.06.083.

[50] Zhou, X.; Zhang, X.; Feng, X.; Zhou, J.; Zhou, S. Preparation of a La/N co-doped TiO_2 film electrode with visible light response and its photoelectrocatalytic activity on a Ni substrate. *Dye. Pigment.* **2016**, *125*, 375–383, doi:10.1016/j.dyepig.2015.10.044.

[51] Zhang, Z.; Li, G.; Cui, Z.; Zhang, K.; Feng, Y.; Meng, S. Influence of difference quantity La-doped TiO_2 photoanodes on the performance of dye-sensitized solar cells: A strategy for choosing an appropriate doping quantity. *J. Solid State Chem.* **2016**, *237*, 242–247, doi:10.1016/j.jssc.2016.02.005.

[52] Raza, W.; Haque, M.; Muneer, M.; Fleisch, M.; Hakki, A.; Bahnemann, D.B.D. Photocatalytic degradation of different chromophoric dyes in aqueous phase using La and Mo doped TiO2 hybrid carbon spheres. *J. Alloy. Compd.* **2015**, *632*, 837–844, doi:10.1016/j.jallcom.2015.01.222.

[53] Chai, Y.; Lin, L.; Zhang, K.; Zhao, B.; He, D. Efficient visible-light photocatalysts from Gd–La codoped TiO_2 nanotubes. *Ceram. Int.* **2014**, *40*, 2691–2696, doi:10.1016/j.ceramint.2013.10.054.

[54] Rafieh, A.I.; Ekanayake, P.; Tan, A.L.; Lim, C.M. Effects of ionic radii of co-dopants (Mg, Ca, Al and La) in TiO_2 on performance of dye-sensitized solar cells. *Sol. Energy* **2017**, *141*, 249–255, doi:10.1016/j.solener.2016.11.052.

[55] Armaković, S.J.; Grujić-Brojčin, M.; Šćepanović, M.; Armaković, S.; Golubović, A.; Babić, B.; Abramović, B.F. Efficiency of La-doped TiO_2 calcined at different temperatures in photocatalytic degradation of β-blockers. *Arab. J. Chem.* **2019**, *12*, 5355–5369, doi:10.1016/j.arabjc.2017.01.001.

[56] Grujić-Brojčin, M.; Armaković, S.; Tomic, N.; Abramović, B.; Golubović, A.; Stojadinović, B.; Kremenovic, A.; Babić, B.; Dohčević-Mitrović, Z.; Šćepanović, M. Surface modification of sol–gel synthesized TiO_2 nanoparticles induced by La-doping. *Mater. Charact.* **2014**, *88*, 30–41, doi:10.1016/j.matchar.2013.12.002.

[57] Lan, X.; Wang, L.; Zhang, B.; Tian, B.; Zhang, J. Preparation of lanthanum and boron co-doped TiO_2 by modified sol–gel method and study their photocatalytic activity. *Catal. Today* **2014**, *224*, 163–170, doi:10.1016/j.cattod.2013.10.062.

[58] Elsellami, L.; Lachheb, H.; Houas, A. Synthesis, characterization and photocatalytic activity of Li-, Cd-, and La-doped TiO*Mater. Sci. Semicond. Process.* **2015**, *36*, 103–114, doi:10.1016/j.mssp.2015.03.032.

[59] Guo, H.; Chen, J.; Weng, W.; Zheng, Z.; Wang, D. Adsorption behavior of Congo red from aqueous solution on La_2O_3-doped TiO_2 nanotubes. *J. Ind. Eng. Chem.* **2014**, *20*, 3081–3088, doi:10.1016/j.jiec.2013.11.047.

[60] Zhang, Y.; Xu, H.; Xu, Y.; Zhang, H.; Wang, Y. The effect of lanthanide on the degradation of RB in nanocrystalline Ln/TiO_2 aqueous solution. *J. Photochem. Photobiol. A: Chem.* **2005**, *170*, 279–285, doi:10.1016/j.jphotochem.2004.09.001.

[61] Coelho, L.L.; Hotza, D.; Estrella, A.S.; de Amorim, S.M.; Puma, G.L.; Moreira, R.D.F.P.M. Modulating the photocatalytic activity of TiO_2 (P25) with lanthanum and graphene oxide. *J. Photochem. Photobiol. A: Chem.* **2019**, *372*, 1–10, doi:10.1016/j.jphotochem.2018.11.048.

[62] Shi, H.; Zhang, T.; Wang, H. Preparation and photocatalytic activity of La^{3+} and Eu^{3+} co-doped TiO_2 nanoparticles: photo-assisted degradation of methylene blue. *J. Rare Earths* **2011**, *29*, 746–752, doi:10.1016/s1002-0721(10)60535-2.

[63] Prakash, J.; Samriti; Kumar, A.; Dai, H.; Janegitz, B.C.; Krishnan, V.; Swart, H.C.; Sun, S. Novel rare earth metal–doped one-dimensional TiO_2 nanostructures: Fundamentals and multifunctional applications. *Mater. Today Sustain.* **2021**, *13*, 100066, doi:10.1016/j.mtsust.2021.100066.

[64] Zhang, J.; Zhao, Z.-Y.; Wang, X.; Yu, T.; Guan, J.; Yu, Z.; Li, Z.; Zou, Z. Increasing the Oxygen Vacancy Density on the TiO_2 Surface by La-Doping for Dye-Sensitized Solar Cells. *J. Phys. Chem. C* **2010**, *114*, 18396–18400, doi:10.1021/jp106648c.

[65] Hafez, H.; Wu, J.; Lan, Z.; Li, Q.; Xie, G.; Lin, J.; Huang, M.; Huang, Y.; Abdel-Mottaleb, M.S. Enhancing the photoelectrical performance of dye-sensitized solar cells using TiO_2:Eu_3 +nanorods. *Nanotechnol.* **2010**, *21*, 415201, doi:10.1088/0957-4484/21/41/415201.

[66] Saif, M. Luminescence based on energy transfer in silica doped with lanthanide titania ($Gd_2Ti_2O_7$:Ln^{3+}) [Ln^{3+}=Eu^{3+} or Dy^{3+}]. *J. Photochem. Photobiol. A: Chem.* **2009**, *205*, 145–150, doi:10.1016/j.jphotochem.2009.04.020.

[67] Wang, B.; Zhang, G.; Sun, Z.; Zheng, S.; Frost, R.L. A comparative study about the influence of metal ions (Ce, La and V) doping on the solar-light-induced photodegradation toward rhodamine B. *J. Environ. Chem. Eng.* **2015**, *3*, 1444–1451, doi:10.1016/j.jece.2015.05.007.

[68] Priyanka, K.; Revathy, V.; Rosmin, P.; Thrivedu, B.; Elsa, K.; Nimmymol, J.; Balakrishna, K.; Varghese, T. Influence of La doping on structural and optical properties of TiO_2 nanocrystals. *Mater. Charact.* **2016**, *113*, 144–151, doi:10.1016/j.matchar.2016.01.015.

[69] Khalid, N.; Ahmed, E.; Hong, Z.; Ahmad, M. Synthesis and photocatalytic properties of visible light responsive La/TiO_2-graphene composites. *Appl. Surf. Sci.* **2012**, *263*, 254–259, doi:10.1016/j.apsusc.2012.09.039.

[70] Li, H.; Feng, B. Visible-light-driven composite La_2O_3/TiO_2 nanotube arrays: Synthesis and improved photocatalytic activity. *Mater. Sci. Semicond. Process.* **2016**, *43*, 55–59, doi:10.1016/j.mssp.2015.11.021.

[71] Mazierski, P.; Mikołajczyk, A.; Bajorowicz, B.; Malankowska, A.; Zaleska-Medynska, A.; Nadolna, J. The role of lanthanides in TiO2-based photocatalysis: A review. *Appl. Catal. B: Environ.* **2018**, *233*, 301–317, doi:10.1016/j.apcatb.2018.04.019.

[72] Tanyi, A.R.; Rafieh, A.I.; Ekaneyaka, P.; Tan, A.L.; Young, D.; Zheng, Z.; Chellappan, V.; Subramanian, G.S.; Chandrakanthi, R. Enhanced efficiency of dye-sensitized solar cells based on Mg and La co-doped TiO_2 photoanodes. *Electrochimica Acta* **2015**, *178*, 240–248, doi:10.1016/j.electacta.2015.07.172.

[73] Zhang, Y.; Zhang, H.; Xu, Y.; Wang, Y. Significant effect of lanthanide doping on the texture and properties of nanocrystalline mesoporous TiO*J. Solid State Chem.* **2004**, *177*, 3490–3498, doi:10.1016/j.jssc.2004.05.026.

[74] Xu, A.-W.; Gao, Y.; Liu, H.- Q. The Preparation, Characterization, and their Photocatalytic Activities of Rare-Earth-Doped TiO_2 Nanoparticles. *J. Catal.* **2002**, *207*, 151–157, doi:10.1006/jcat.2002.3539.

[75] Ranjit, K.T.; Willner, I.; Bossmann, A.S.H.; Braun, A.M. Lanthanide Oxide-Doped Titanium Dioxide Photocatalysts: Novel Photocatalysts for the Enhanced Degradation ofp-Chlorophenoxyacetic Acid. *Environ. Sci. Technol.* **2001**, *35*, 1544–1549, doi:10.1021/es001613e.

[76] Lin, L.; Yang, Y.; Men, L.; Wang, X.; He, D.; Chai, Y.; Zhao, B.; Ghoshroy, S.; Tang, Q. A highly efficient TiO2@ZnO n–p–n heterojunction nanorod photocatalyst. *Nanoscale* **2013**, *5*, 588–593, doi:10.1039/c2nr33109h.

[77] Fu, R.; Wang, Q.; Gao, S.; Wang, Z.; Huang, B.; Dai, Y.; Lu, J. Effect of different processes and Ti/Zn molar ratios on the structure, morphology, and enhanced photoelectrochemical and photocatalytic performance of Ti3+ self-doped titanium–zinc hybrid oxides. *J. Power Sources* **2015**, *285*, 449–459, doi:10.1016/j.jpowsour.2015.03.070.

[78] Pengkalsinan, K.; Tio,Z.; and Melalui, F. *Effect of Calcination Temperature on ZnO / TiO_2 Composite in Photocatalytic Treatment of Phenol under Visible Light*, Malaysian Analytical Sciences Society, Selangor, Malaysia; vol. 21, no. 1, pp. 173–181, **2017**.

[79] Khaki, M.R.D.; Shafeeyan, M.S.; Raman, A.A.A.; Daud, W.M.A.W. Enhanced UV–Visible photocatalytic activity of Cu-doped ZnO/TiO_2 nanoparticles. *J. Mater. Sci. Mater. Electron.* **2018**, *29*, 5480–5495, doi:10.1007/s10854-017-8515-9.

[80] K. C. L. Khang, M. H. M. Hatta, S. L. Lee, and L. Yuliati, Photocatalytic removal of phenol over mesoporous ZnO/TiO2 composites. *J. Tekno.* **2018**, *80*, 153–160, doi:10.11113/jt.v80.11209.

[81] Chorfi, H.; Saadoun, M.; Bousselmi, L.; Bessaïs, B. TiO_2-ITO and TiO_2-ZnO nanocomposites: application on water treatment. In *Proceedings of the EPJ Web of Conferences, Sousse, Tunisie, 6-10 September 2011*, EDP Sciences, **2012**; Vol. 29, p. 00015.

[82] Jaramillo-Fierro, X.V.; Zambrano, C.; Fernández, F.; Saenz-Puche, R.; Costa, C.; Guerrero, V.; Gonzalez, S. Synthesis, characterization and theoretical calculations of Cu(I) complex of trithiocyanuric acid [Cu(ttc)3]. *Univ. Sci.* **2018**, *23*, 241–266, doi:10.11144/javeriana.sc23-2.scat.

[83] Jaramillo-Fierro, X.; González, S.; Montesdeoca-Mendoza, F.; Medina, F. Structuring of $ZnTiO_3$/TiO_2 Adsorbents for the Removal of Methylene Blue, Using Zeolite Precursor Clays as Natural Additives. *Nanomater.* **2021**, *11*, 898, doi:10.3390/nano11040898.

[84] Jaramillo-Fierro, X.; Capa, L.; Medina, F.; González, S. DFT Study of Methylene Blue Adsorption on $ZnTiO_3$ and TiO_2 Surfaces (101). *Mol.* **2021**, *26*, 3780, doi:10.3390/molecules26133780.

[85] Wang, R.; An, S.; Zhang, J.; Song, J.; Wang, F. Existence form of lathanum and its improving mechanism of visible-light-driven La-F co-doped TiO*J. Rare Earths* **2020**, *38*, 39–45, doi:10.1016/j.jre.2019.02.011.

[86] Ke, S.; Cheng, X.; Wang, Q.; Wang, Y.; Pan, Z. Preparation of a photocatalytic TiO_2/$ZnTiO_3$ coating on glazed ceramic tiles. *Ceram. Int.* **2014**, *40*, 8891–8895, doi:10.1016/j.ceramint.2014.01.027.

[87] Holzwarth, U.; Gibson, N. The Scherrer equation versus the 'Debye-Scherrer equation'. *Nat. Nanotechnol.* **2011**, *6*, 534, doi:10.1038/nnano.2011.145.

[88] Mehrabi, M.; Javanbakht, V. Photocatalytic degradation of cationic and anionic dyes by a novel nanophotocatalyst of TiO_2/$ZnTiO_3$/αFe_2O_3 by ultraviolet light irradiation. *J. Mater. Sci. Mater. Electron.* **2018**, *29*, 9908–9919, doi:10.1007/s10854-018-9033-0.

[89] García-Ramírez, E.; Mondragón-Chaparro, M.; Zelaya-Angel, O. Band gap coupling in photocatalytic activity in ZnO–TiO_2 thin films. *Appl. Phys. A* **2012**, *108*, 291–297, doi:10.1007/s00339-012-6890-x.

[90] Jaramillo-Fierro, X.; Pérez, S.G.; Jaramillo, X.; Cabello, F.M. Synthesis of the $ZnTiO_3$/TiO_2 Nanocomposite Supported in Ecuadorian Clays for the Adsorption and Photocatalytic Removal of Methylene Blue Dye. *Nanomater.* **2020**, *10*, 1891, doi:10.3390/nano10091891.

[91] Fan, S.; Tang, J.; Wang, Y.; Li, H.; Zhang, H.; Tang, J.; Wang, Z.; Li, X. Biochar prepared from co-pyrolysis of municipal sewage sludge and tea waste for the adsorption of

methylene blue from aqueous solutions: Kinetics, isotherm, thermodynamic and mechanism. *J. Mol. Liq.* **2016**, *220*, 432–441, doi:10.1016/j.molliq.2016.04.107.

[92] Gil, A.; Assis, F.; Albeniz, S.; Korili, S. Removal of dyes from wastewaters by adsorption on pillared clays. *Chem. Eng. J.* **2011**, *168*, 1032–1040, doi:10.1016/j.cej.2011.01.078.

[93] Hanaor, D.A.H.; Sorrell, C.C. Review of the anatase to rutile phase transformation. *J. Mater. Sci.* **2011**, *46*, 855–874, doi:10.1007/s10853-010-5113-0.

[94] Hwang, D.W.; Lee, J.S.; Li, W.; Oh, S.H. Electronic Band Structure and Photocatalytic Activity of $Ln_2Ti_2O_7$ (Ln = La, Pr, Nd). *J. Phys. Chem. B* **2003**, *107*, 4963–4970, doi:10.1021/jp034229n.

[95] Li, L.; Zhuang, H.; Bu, D. Characterization and activity of visible-light-driven TiO_2 photocatalyst codoped with lanthanum and iodine. *Appl. Surf. Sci.* **2011**, *257*, 9221–9225, doi:10.1016/j.apsusc.2011.06.007.

[96] Smitha, V.S.; Manjumol, K.A.; Baiju, K.V.; Ghosh, S.; Perumal, P.; Warrier, K.G.K. Sol–gel route to synthesize titania-silica nano precursors for photoactive particulates and coatings. *J. Sol-Gel Sci. Technol.* **2010**, *54*, 203–211, doi:10.1007/s10971-010-2178-9.

[97] Choi, J.; Park, H.; Hoffmann, M.R. Effects of Single Metal-Ion Doping on the Visible-Light Photoreactivity of TiO*J. Phys. Chem. C* **2010**, *114*, 783–792, doi:10.1021/jp908088x.

[98] Yang, P.; Lu, C.; Hua, N.; Du, Y. Titanium dioxide nanoparticles co-doped with Fe^{3+} and Eu^{3+} ions for photocatalysis. *Mater. Lett.* **2002**, *57*, 794–801, doi:10.1016/s0167-577x(02)00875-3.

[99] Sanabria, N.; Avila, P.; Yates, M.; Rasmussen, S.; Molina, R.; Moreno, S. Mechanical and textural properties of extruded materials manufactured with AlFe and AlCeFe pillared bentonites. *Appl. Clay Sci.* **2010**, *47*, 283–289, doi:10.1016/j.clay.2009.11.029.

[100] Grande, C.; Águeda, V.I.; Spjelkavik, A.; Blom, R. An efficient recipe for formulation of metal-organic Frameworks. *Chem. Eng. Sci.* **2015**, *124*, 154–158, doi:10.1016/j.ces.2014.06.048.

[101] Cárdenas-Ramírez, C.; Jaramillo, F.; Fernández, A.G.; Cabeza, L.F.; Gómez, M.A. Influence of thermal treatments on the absorption and thermal properties of a clay mineral support used for shape-stabilization of fatty acids. *J. Energy Storage* **2021**, *36*, 102427, doi:10.1016/j.est.2021.102427.

[102] El-Kousy, S.M.; El-Shorbagy, H.G.; El-Ghaffar, M.A. Chitosan/montmorillonite composites for fast removal of methylene blue from aqueous solutions. *Mater. Chem. Phys.* **2020**, *254*, 123236, doi:10.1016/j.matchemphys.2020.123236.

[103] Chen, L.; Zhu, Y.; Cui, Y.; Dai, R.; Shan, Z.; Chen, H. Fabrication of starch-based high-performance adsorptive hydrogels using a novel effective pretreatment and adsorption for cationic methylene blue dye: Behavior and mechanism. *Chem. Eng. J.* **2021**, *405*, 126953, doi:10.1016/j.cej.2020.126953.

[104] Wang, G.; Li, G.; Huan, Y.; Hao, C.; Chen, W. Acrylic acid functionalized graphene oxide: High-efficient removal of cationic dyes from wastewater and exploration on adsorption mechanism. *Chemosphere* **2020**, *261*, 127736, doi:10.1016/j.chemosphere.2020.127736.

[105] Badeenezhad, A.; Azhdarpoor, A.; Bahrami, S.; Yousefinejad, S. Removal of methylene blue dye from aqueous solutions by natural clinoptilolite and clinoptilolite modified by iron oxide nanoparticles. *Mol. Simul.* **2019**, *45*, 564–571, doi:10.1080/08927022.2018.1564077.

[106] An, F.; Liu, J.; Xu, Z.; Zheng, S. Efficient removal of three dyes using porous covalent triazine frameworks: adsorption mechanism and role of pore distribution. *Water Sci. Technol.* **2020**, *82*, 3023–3031, doi:10.2166/wst.2020.550.

[107] Sarici-Ozdemir, C. Adsorption and desorption kinetics behaviour of methylene blue onto activated carbon, *Physicochem. Probl. Miner. Process*. **2012**, *48(2)*, 441–454, doi: 10.5277/ppmp120210.

[108] Malatji, N.; Makhado, E.; Ramohlola, K.E.; Modibane, K.D.; Maponya, T.C.; Monama, G.R.; Hato, M.J. Synthesis and characterization of magnetic clay-based carboxymethyl cellulose-acrylic acid hydrogel nanocomposite for methylene blue dye removal from aqueous solution. *Environ. Sci. Pollut. Res.* **2020**, *27*, 44089–44105, doi:10.1007/s11356-020-10166-8.

[109] Al-Degs, Y.; El-Barghouthi, M.; El-Sheikh, A.; Walker, G. Effect of solution pH, ionic strength, and temperature on adsorption behavior of reactive dyes on activated carbon. *Dye. Pigment.* **2008**, *77*, 16–23, doi:10.1016/j.dyepig.2007.03.001.

[110] Al-Ghouti, M.; Khraisheh, M.; Allen, S.; Ahmad, M. The removal of dyes from textile wastewater: a study of the physical characteristics and adsorption mechanisms of

diatomaceous earth. *J. Environ. Manag.* **2003**, *69*, 229–238, doi:10.1016/j.jenvman.2003.09.005.

[111] Afroze, S.; Sen, T.K.; Ang, M.; Nishioka, H. Adsorption of methylene blue dye from aqueous solution by novel biomassEucalyptus sheathianabark: equilibrium, kinetics, thermodynamics and mechanism. *DESALINATION Water Treat.* **2016**, *57*, 5858–5878, doi:10.1080/19443994.2015.1004115.

[112] Hosseini, S.; Khan, M.A.; Malekbala, M.R.; Cheah, W.; Choong, T.S. Carbon coated monolith, a mesoporous material for the removal of methyl orange from aqueous phase: Adsorption and desorption studies. *Chem. Eng. J.* **2011**, *171*, 1124–1131, doi:10.1016/j.cej.2011.05.010.

[113] Shi, J.-W.; Chen, S.-H.; Wang, S.-M.; Ye, Z.-L.; Wu, P.; Xu, B. Favorable recycling photocatalyst TiO_2/CFA: Effects of calcination temperature on the structural property and photocatalytic activity. *J. Mol. Catal. A: Chem.* **2010**, *330*, 41–48, doi:10.1016/j.molcata.2010.06.029.

[114] Hu, X.-S.; Liang, R.; Sun, G. Super-adsorbent hydrogel for removal of methylene blue dye from aqueous solution. *J. Mater. Chem. A* **2018**, *6*, 17612–17624, doi:10.1039/c8ta04722g.

[115] Varmazyar, A.; Sedaghat, S.; Khalaj, M. Highly efficient removal of methylene blue by a synthesized TiO_2/montmorillonite-albumin nanocomposite: kinetic and isothermal analysis in water. *RSC Adv.* **2017**, *7*, 37214–37219, doi:10.1039/c7ra07096a.

[116] Marsiezade, N.; Javanbakht, V. Novel hollow beads of carboxymethyl cellulose/ZSM-5/ZIF-8 for dye removal from aqueous solution in batch and continuous fixed bed systems. *Int. J. Biol. Macromol.* **2020**, *162*, 1140–1152, doi:10.1016/j.ijbiomac.2020.06.229.

[117] Ji, Y.; Xu, F.; Wei, W.; Gao, H.; Zhang, K.; Zhang, G.; Xu, Y.; Zhang, P. Efficient and fast adsorption of methylene blue dye onto a nanosheet MFI zeolite. *J. Solid State Chem.* **2021**, *295*, 121917, doi:10.1016/j.jssc.2020.121917.

[118] Zhao, Y.-P.; Guo, D.-X.; Li, S.-F.; Cao, J.-P.; Wei, X.-Y. Removal of methylene blue by NaX zeolites synthesized from coal gasification fly ash using an alkali fusion-hydrothermal method. *Desalination Water Treat.* **2020**, *185*, 355–363, doi:10.5004/dwt.2020.25424.

[119] Xu, R.; Mao, J.; Peng, N.; Luo, X.; Chang, C. Chitin/clay microspheres with hierarchical architecture for highly efficient removal of organic dyes. *Carbohydr. Polym.* **2018**, *188*, 143–150, doi:10.1016/j.carbpol.2018.01.073.

[120] Bée, A.; Obeid, L.; Mbolantenaina, R.; Welschbillig, M.; Talbot, D. Magnetic chitosan/clay beads: A magsorbent for the removal of cationic dye from water. *J. Magn. Magn. Mater.* **2017**, *421*, 59–64, doi:10.1016/j.jmmm.2016.07.022.

[121] Marrakchi, F.; Bouaziz, M.; Hameed, B. Activated carbon–clay composite as an effective adsorbent from the spent bleaching sorbent of olive pomace oil: Process optimization and adsorption of acid blue 29 and methylene blue. *Chem. Eng. Res. Des.* **2017**, *128*, 221–230, doi:10.1016/j.cherd.2017.10.015.

[122] Woolard, C.; Strong, P.J.; Erasmus, C. Evaluation of the use of modified coal ash as a potential sorbent for organic waste streams. *Appl. Geochem.* **2002**, *17*, 1159–1164, doi:10.1016/s0883-2927(02)00057-4.

[123] El-Mekkawi, D.; Ibrahim, F.A.; Selim, M.M. Removal of methylene blue from water using zeolites prepared from Egyptian kaolins collected from different sources. *J. Environ. Chem. Eng.* **2016**, *4*, 1417–1422, doi:10.1016/j.jece.2016.01.007.

[124] Ge, S.; Geng, W.; He, X.; Zhao, J.; Zhou, B.; Duan, L.; Wu, Y.; Zhang, Q. Effect of framework structure, pore size and surface modification on the adsorption performance of methylene blue and Cu^{2+} in mesoporous silica. *Colloids Surfaces A: Physicochem. Eng. Asp.* **2018**, *539*, 154–162, doi:10.1016/j.colsurfa.2017.12.016.

[125] Sahoo, S.; Uma; Banerjee, S.; Sharma, Y.C. Application of natural clay as a potential adsorbent for the removal of a toxic dye from aqueous solutions. *Desalination Water Treat.* **2013**, *52*, 6703–6711, doi:10.1080/19443994.2013.816872.

[126] Li, H.; Dai, M.; Dai, S.; Dong, X.; Li, F. Methylene blue adsorption properties of mechanochemistry modified coal fly ash. *Hum. Ecol. Risk Assessment: Int. J.* **2018**, *24*, 2133–2141, doi:10.1080/10807039.2018.1440527.

[127] Nayeri, D.; Mousavi, S.A.; Fatahi, M.; Almasi, A.; Khodadoost, F. Dataset on adsorption of methylene blue from aqueous solution onto activated carbon obtained from low cost wastes by chemical-thermal activation – modelling using response surface methodology. *Data Brief* **2019**, *25*, 104036, doi:10.1016/j.dib.2019.104036.

[128] Wang, Q.; Xu, S.; Shen, F. Preparation and characterization of TiO_2 photocatalysts co-doped with iron (III) and lanthanum for the degradation of organic pollutants. *Appl. Surf. Sci.* **2011**, *257*, 7671–7677, doi:10.1016/j.apsusc.2011.03.157.

[129] Xie, J.; Jiang, D.; Chen, M.; Li, D.; Zhu, J.; Lü, X.; Yan, C. Preparation and characterization of monodisperse Ce-doped TiO_2 microspheres with visible light photocatalytic activity. *Colloids Surfaces A: Physicochem. Eng. Asp.* **2010**, *372*, 107–114, doi:10.1016/j.colsurfa.2010.09.037.

[130] Li, X.Z.; Li, F.B. Study of Au/Au^{3+}-TiO_2 Photocatalysts toward Visible Photooxidation for Water and Wastewater Treatment. *Environ. Sci. Technol.* **2001**, *35*, 2381–2387, doi:10.1021/es001752w.

[131] Moon, J.; Takagi, H.; Fujishiro, Y.; Awano, M. Preparation and characterization of the Sb-doped TiO_2 photocatalysts. *J. Mater. Sci.* **2001**, *36*, 949–955, doi:10.1023/a:1004819706292.

[132] Rattanakam, R.; Supothina, S. Visible-light-sensitive N-doped TiO_2 photocatalysts prepared by a mechanochemical method: effect of a nitrogen source. *Res. Chem. Intermed.* **2009**, *35*, 263–269, doi:10.1007/s11164-009-0030-z.

[133] Wen, C.; Zhu, Y.-J.; Kanbara, T.; Zhu, H.-Z.; Xiao, C.-F. Effects of I and F codoped TiO_2 on the photocatalytic degradation of methylene blue. *Desalination* **2009**, *249*, 621–625, doi:10.1016/j.desal.2009.01.028.

[134] Chen, D.; Jiang, Z.; Geng, J.; Wang, Q.; Yang, D. Carbon and Nitrogen Co-doped TiO_2 with Enhanced Visible-Light Photocatalytic Activity. *Ind. Eng. Chem. Res.* **2007**, *46*, 2741–2746, doi:10.1021/ie061491k.

[135] Yang, X.; Cao, C.; Erickson, L.; Hohn, K.; Maghirang, R.; Klabunde, K. Synthesis of visible-light-active TiO_2-based photocatalysts by carbon and nitrogen doping. *J. Catal.* **2008**, *260*, 128–133, doi:10.1016/j.jcat.2008.09.016.

[136] Chen, D.; Jiang, Z.; Geng, J.; Zhu, J.; Yang, D. A facile method to synthesize nitrogen and fluorine co-doped TiO_2 nanoparticles by pyrolysis of (NH4)2TiF*J. Nanoparticle Res.* **2009**, *11*, 303–313, doi:10.1007/s11051-008-9383-2.

[137] Zhang, N.; Zeng, F. Characterization, activity and mechanisms of a visible light driven photocatalyst: Manganese and iron co-modified TiO_2 nanoparticles. *Russ. J. Phys. Chem. A* **2011**, *85*, 1825–1831, doi:10.1134/s0036024411100347.

[138] Faisal, M.; Jalalah, M.; Harraz, F.A.; El-Toni, A.M.; Labis, J.P.; Al-Assiri, M. A novel Ag/PANI/$ZnTiO_3$ ternary nanocomposite as a highly efficient visible-light-driven photocatalyst. *Sep. Purif. Technol.* **2021**, *256*, 117847, doi:10.1016/j.seppur.2020.117847.

[139] Krupskaya, V.V.; Zakusin, S.V.; Tyupina, E.A.; Dorzhieva, O.V.; Zhukhlistov, A.P.; Belousov, P.E.; Timofeeva, M.N. Experimental Study of Montmorillonite Structure and Transformation of Its Properties under Treatment with Inorganic Acid Solutions. *Miner.* **2017**, *7*, 49, doi:10.3390/min7040049.

[140] Benkacem, T.; Hamdi, B.; Chamayou, A.; Balard, H.; Calvet, R. Physicochemical characterization of a diatomaceous upon an acid treatment: a focus on surface properties by inverse gas chromatography. *Powder Technol.* **2016**, *294*, 498–507, doi:10.1016/j.powtec.2016.03.006.

[141] Benjelloun, M.; Miyah, Y.; Evrendilek, G.A.; Zerrouq, F.; Lairini, S. Recent Advances in Adsorption Kinetic Models: Their Application to Dye Types. *Arab. J. Chem.* **2021**, *14*, 103031, doi:10.1016/j.arabjc.2021.103031.

[142] Bello, M.O.; Abdus-Salam, N.; Adekola, F.A.; Pal, U. Isotherm and kinetic studies of adsorption of methylene blue using activated carbon from ackee apple pods. *Chem. Data Collect.* **2021**, *31*, 100607, doi:10.1016/j.cdc.2020.100607.

[143] Zhang, L.; Liu, N.; Yang, L.; Lin, Q. Sorption behavior of nano-TiO2 for the removal of selenium ions from aqueous solution. *J. Hazard. Mater.* **2009**, *170*, 1197–1203, doi:10.1016/j.jhazmat.2009.05.098.

[144] Milanovic, M.; Nikolic, L.M. Modification of TiO2 nanoparticles through lanthanum doping and peg templating. *Process. Appl. Ceram.* **2014**, *8*, 195–202, doi:10.2298/pac1404195m.

[145] Ambigadevi, J.; Kumar, P.S.; Vo, D.-V.N.; Haran, S.H.; Raghavan, T.S. Recent developments in photocatalytic remediation of textile effluent using semiconductor based nanostructured catalyst: A review. *J. Environ. Chem. Eng.* **2021**, *9*, 104881, doi:10.1016/j.jece.2020.104881.

CHAPTER 6

DFT STUDY OF METHYLENE BLUE ADSORPTION ON $ZnTiO_3$ AND TiO_2 SURFACES (101)

6.1. Introduction

Over the past decade, Ti- and Zn-based oxides have received much attention due to their competitive cost, non-toxicity, excellent stability, availability, and ability to produce highly oxidizing radicals [1–4]. Titanium oxide (TiO_2) and zinc oxide (ZnO) are two well-known semiconductors that have been widely used to construct electron transport channels due to their appropriate bandgaps, efficient electron mobilities, and simple synthesis methods [5–8]. In addition, these oxides are promising semiconductors to eliminate organic pollutants with incomparable efficiency due to their tunable surface and structural functionality [9]. The ZnO–TiO_2 composite system has even more superior properties than the individual oxides due to the high separation rate of photogenerated carriers and the wide optical response range [10]. Several syntheses and characterization studies of the ZnO–TiO_2 system have shown that there are three compounds in this binary system, including $ZnTiO_3$ (cubic, hexagonal), Zn_2TiO_4 (cubic, tetragonal), and $Zn_3Ti_3O_8$ (cubic) [11–13].

$ZnTiO_3$ has many similar physical properties to TiO_2 and ZnO, including high electron mobility [14–16]. This ternary oxide has been widely used because of its outstanding properties and potential scientific and technical applications [17]. $ZnTiO_3$ has been investigated in a variety of applications as an antibacterial, catalyst, nanofiber, white pigment, microwave dielectric, gas sensor, nonlinear optical, corrosion inhibitor, and luminescent material [18–23], but its application in adsorption has not been sufficiently studied, despite the fact that the literature indicates that due to its great specific area, it could have an important potential as an adsorbent [24,25].

$ZnTiO_3$ is a polar oxide of the $LiNbO_3$-type (LN-type) with both cations coordinated octahedrally in a three-dimensional framework of the octahedron perovskite (Pv) that shares corners [26]. In this structure, both cations move along the trigonal axis c, thus producing a spontaneous polarization reinforced by a second-order Jahn–Teller (SOJT) distortion due to Ti^{4+} (d^0) [27]. The paraelectric parent structure of $ZnTiO_3$ is the ilmenite (Il)-type phase (hexagonal space group *R-3*), which is the stable phase under ambient conditions [28]. The crystalline and phase transformation behaviors of $ZnTiO_3$ have systematically been investigated by various authors regarding several synthesis methods, Ti:Zn precursor molar ratios, and calcination temperatures [29–35]. Furthermore, the literature agrees that obtaining $ZnTiO_3$ as a pure phase at a low processing temperature is a challenge in materials chemistry [36–38].

In a previous experimental paper, we reported the synthesis and characterization of the $ZnTiO_3/TiO_2$ nanocomposite. This heterostructure was indexed to a hexagonal phase with space group R-3(148) for $ZnTiO_3$ and a tetragonal phase with space group $I4_1/amd(141)$ for TiO_2 (anatase) [39,40]. In these studies, we also reported the ability of $ZnTiO_3/TiO_2$ to remove the methylene blue (MB) dye in aqueous systems, and it was contrasted with the results obtained for pure TiO_2 (anatase). The results showed that the heterostructure has better photocatalytic adsorption and degradation capacity than anatase alone, probably due to a synergistic effect. This synergistic effect between semiconductors has been extensively studied, showing that the presence of a second semiconductor can provide special active sites to enhance the adsorption and photocatalysis of various compounds [41].

Although several properties of $ZnTiO_3$ have been extensively studied experimentally, a proper description of its electronic, optical, and adsorptive properties remains an active research area from a theoretical point of view [42] since, up to date, this ternary oxide has scarcely been studied with quantum methods [43]. Therefore, the computational study of the molecular interaction between $ZnTiO_3$ and methylene blue could contribute to clarifying the adsorption and degradation mechanism of this dye, favoring the development of materials for the treatment of waters contaminated with MB.

The elimination of MB in wastewater is an extremely important task in environmental protection because it has caused serious contamination in many countries of the world [44]. Methylene blue, known as methylthioninium chloride is a basic cationic dye widely used in the printing, plastics, paper, leather, food, pharmaceutical, and textile industries [45–47]. The discharge of wastewater effluents from these industries, with a high content of MB without efficient degradation, results in harmful effects for humans and animals [48].

Various technologies have been used to treat wastewater contaminated with dyes [49]. Among these techniques, adsorption is easy to perform without pretreatment and is highly selective for removing dyes [50]. In addition, adsorption has been found to be superior to other techniques for wastewater treatment in terms of initial cost, simplicity of design, ease of operation, and insensitivity to toxic substances [24]. Although there are several experimental studies of MB adsorption on different surfaces, some uncertainties remain due to lack of understanding at the molecular level of the MB adsorption mechanism on the $ZnTiO_3$ surface. As is well known, computational calculations of the electronic structure in an isolated molecule can achieve the desired chemical precision as long as a sufficiently large basis set is used, the electronic correlation is sufficiently described, and the relativistic effects in the calculation are adequately included [51]. Therefore, in this study, Density Functional Theory (DFT) computational calculations were used to characterize the electronic structure of $ZnTiO_3$ and TiO_2 (anatase) and also to investigate the feasibility of using both oxides as MB adsorbents. The results presented in this paper clarify the previously obtained experimental results and confirm that $ZnTiO_3$ is an excellent adsorbent and that it has high potential for future technological and environmental applications.

6.2. Materials and Methods

All Density Functional Theory (DFT) calculations were performed using the Viena Ab initio Simulation Package (VASP), version 5.3.3 [15,74]. The Perdew–Burke–Ernzerhof (PBE) exchange–correlation functional in the generalized gradient approximation (GGA) proposed by Perdew et al. [75] was employed. The augmented plane wave (PAW) method was used to describe the electron–ion interactions [15]. The cutoff energy to the plane waves was set to 500 eV. The Kohn–Sham equations [76,77] were solved self-consistently until the energy variation between cycles was less than 10^{-5} eV. The first Brillouin zone was sampled using Monkhorst–Pack [78] *k*-point meshes to calculate the bulk properties of $ZnTiO_3$ and TiO_2, in particular, 3 × 7 × 5 and 3 × 3 × 1, respectively. All atomic positions were fully relaxed until the forces on each atom were below 0.01 eV/Å. The computational parameters were selected seeking the best balance between computational cost and precision. The tested values were as follows: energy cutoff points = 450, 475, 500, and 515 eV; force convergence criterion for ionic relaxation

= 0.08, 0.04, 0.02, 0.01, and 0.005 eV/Å and number of k-points corresponding to k-spacing in each axe = 0.35, 0.30, 0.25, 0.20, and 0.15. The parameters were optimized until the difference between the energy values of the system was lower than 10^{-4} eV.

The Gaussian smearing method with $\sigma = 0.10$ eV was applied to band occupations in order to improve total energy convergence [15]. A Hubbard U approximation term was adopted to describe the strong on-site Coulomb repulsion in order to accurately explain the electronic structures [62], which is not correctly described by the PBE functional [58]. Population analyses were estimated using Bader's charge analysis code, which provided important information on bonding behaviors from the atomic charge values [79–81]. All calculations were non-spin polarized and all molecular models were created and visualized using BioVia Material Studio, version 5.5.

To study MB adsorption, an optimized molecular structure was used [68]. The bulk of both $ZnTiO_3$ and TiO_2 crystals was cleaved on the surface (101), since it is the most stable surface according to the literature [54,57,62,66,82]. The slab model of $ZnTiO_3$ (101) was a supercell p(2 × 3) with three atomic layers, which includes 36 Zn atoms, 36 Ti atoms, and 108 O atoms. On the other hand, the TiO_2 (101) surface model has seven atomic layers with a p(3 × 3) structure of the original unit cell, which includes 168 Ti atoms and 336 O atoms.

An appropriate vacuum thickness of each structure was chosen by calculating the surface energy. For both $ZnTiO_3$ and TiO_2 surface models, a vacuum of 20 Å was added. The surface energies (γ_s) were calculated using the following equation [83]:

$$\gamma_s = \frac{(E_{slab} - n \times \ E_{bulk})}{2A} \tag{6.1}$$

where E_{slab} is the total energy of the slab material (eV), E_{bulk} is the total energy of the bulk material (eV), n is the number of atoms contained in the slab, and A is the surface area (Å^2). The values for the surface energies (γ_s) of the $ZnTiO_3$ and TiO_2 structures with a vacuum distance of 20 Å were 0.076 eV/Å^2 (7.30 kJ/Å^2) and 0.062 eV/Å^2 (5.98 kJ/Å^2), respectively.

Adsorption calculation was initiated with the MB molecule placed close to the surface of each oxide in at least one of the following orientations, horizontal (H) and semi-perpendicular (SP), with respect to the surface.

The adsorption energy (ΔE_{ads}) of the MB molecule on the surface of both $ZnTiO_3$ and TiO_2 oxides was calculated using the following equation [84]:

$$\Delta E_{ads} = E_{MB/oxide} - E_{oxide} - E_{MB} \qquad \textbf{(6.2)}$$

where $E_{MB/oxide}$ is the energy of the supersystem formed by the adsorbed molecule on the surface (eV), E_{oxide} is the energy of the clean oxide (eV), and E_{MB} is the energy of the isolated molecule in vacuum (eV).

6.3. Results

6.3.1. Optimization and Electronic Structure of $ZnTiO_3$ and TiO_2

The adsorption of the methylene blue molecule on the surface of both $ZnTiO_3$ and TiO_2 was modeled using the following parameters: hexagonal $ZnTiO_3$ with a cell = 5.148 Å × 5.148 Å × 13.937 Å < 90° × 90° × 120° > and tetragonal TiO_2 with a cell = 3.821 Å × 3.821 Å × 9.697 Å < 90° × 90° × 90° >, as shown in Figure 6.1. The coordinates of the optimized $ZnTiO_3$ and TiO_2 structures are detailed in Appendices (Table C1 and C2) and the corresponding optimization energy values are included in Appendices (Figure C1).

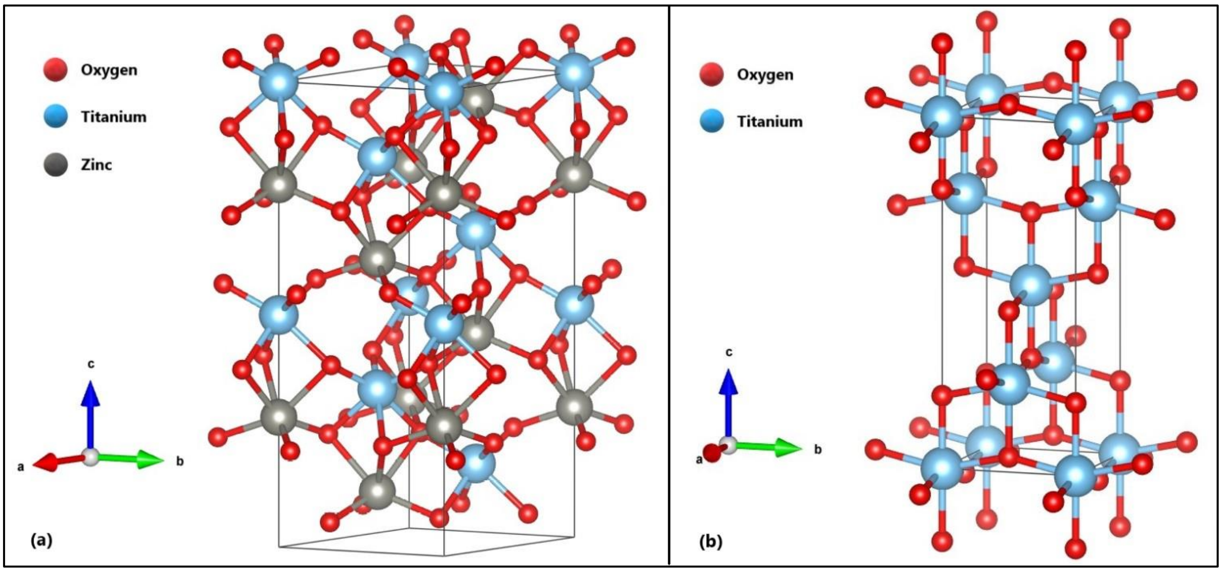

Figure 6. 1. Optimized structures of (a) $ZnTiO_3$ and (b) TiO_2.

The selection of the high symmetry points and lines in the first Brillouin zone [52] and the results of the calculation of the electronic band structure of $ZnTiO_3$ and TiO_2 are shown in Figures 6.2(a) and 6.2(b), respectively.

Figures 6.2(a) and 6.2(b) show that the indirect bandgap energy values of the $ZnTiO_3$ and TiO_2 structures calculated by the exchange–correlation functional in the generalized gradient approximation (GGA-PBE) method were 2.20 and 2.31 eV, respectively. However, the indirect bandgap values were also calculated by the GGA+U method, that is, incorporating the Hubbard *U* approximation term. Indirect bandgap calculations using GGA+U resulted in 3.16 eV (U = 2.5) and 3.21 eV (U = 4.0) for $ZnTO_3$ and TiO_2, respectively. These results are in good agreement with the experimental results reported in the literature: 3.18 eV for $ZnTiO_3$ [15] and 3.20 eV for TiO_2 [53].

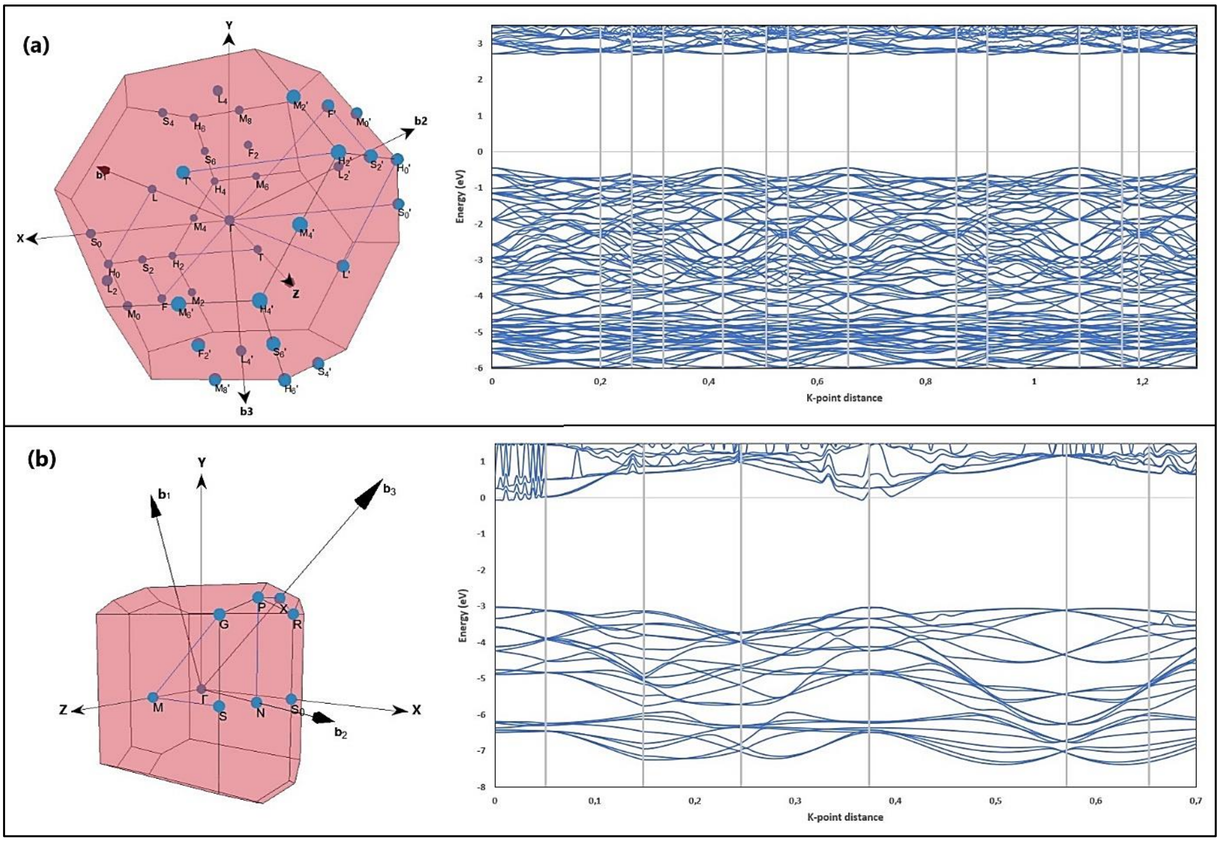

Figure 6. 2. Band structures of (a) $ZnTiO_3$ and (b) TiO_2 along the high symmetry directions in the Brillouin zone.

The total and partial density of states (DOS) of $ZnTiO_3$ and TiO_2 are illustrated in Figures 6.3 and 6.4, respectively. Figure 6.3(a) shows that the total density of state (TDOS) of $ZnTiO_3$ has two main zones: an upper conduction band (CB) zone from 2.5 to 6.2 eV, and a lower valence band (VB) zone, from –6.0 to –0.2 eV. The CB is dominated by the contribution of Ti, while the VB is dominated by the contribution of Zn and O. Figures 6.3(b), 6.3(c), and 6.3(d) show the partial density of state (PDOS) of $ZnTiO_3$. As can be seen in Figure 6.3(b), the main contribution of Ti in the CB is through the 3*d* orbital. On the other hand, Figure 6.3(c) shows that Zn contributes mainly to the VB through the 3*d* orbital while O interacts with Zn in this band through the 2*p* orbital shown in Figure 6.3(d).

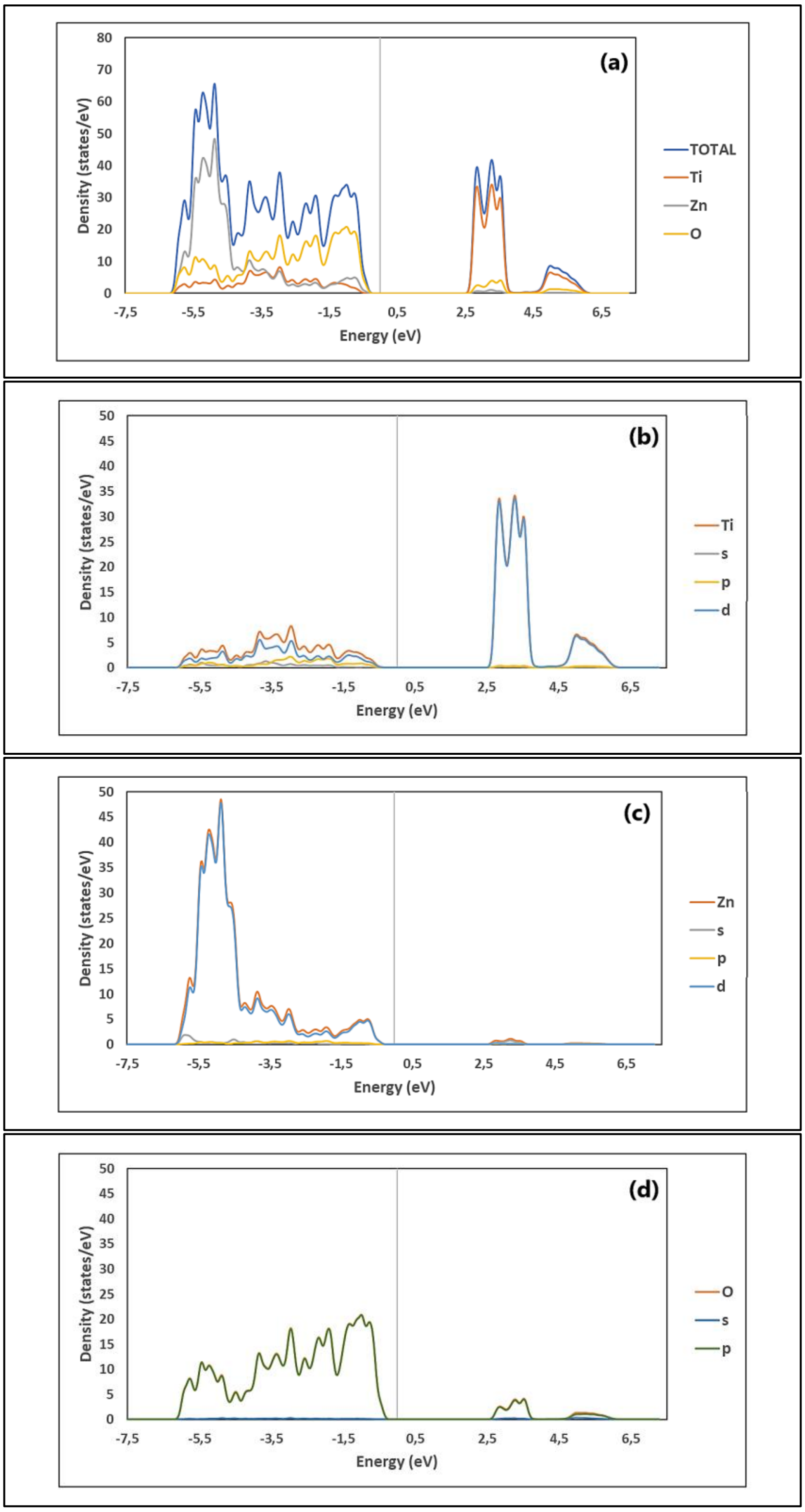

Figure 6. 3. Density of states (DOSs) of $ZnTiO_3$: (a) total, and partial: (b) Ti, (c) Zn and (d) O.

Likewise, Figure 6.4(a) shows that the total density of state (TDOS) of TiO_2 has two main zones: an upper conduction band (CB) zone from −0.1 to 3.8 eV, and a lower valence band (VB) zone, from −7.6 to −2.8 eV. The CB is dominated by the contribution of Ti, while the VB is dominated by the contribution of O. Figures 6.4(b) and 6.4(c) show the partial density of state (PDOS) of TiO_2. As can be seen in Figure 6b, the main contribution of Ti in the CB is through the 3*d* orbital. On the other hand, Figure 6.4(c) shows that O contributes mainly to the VB through the 2*p* orbital.

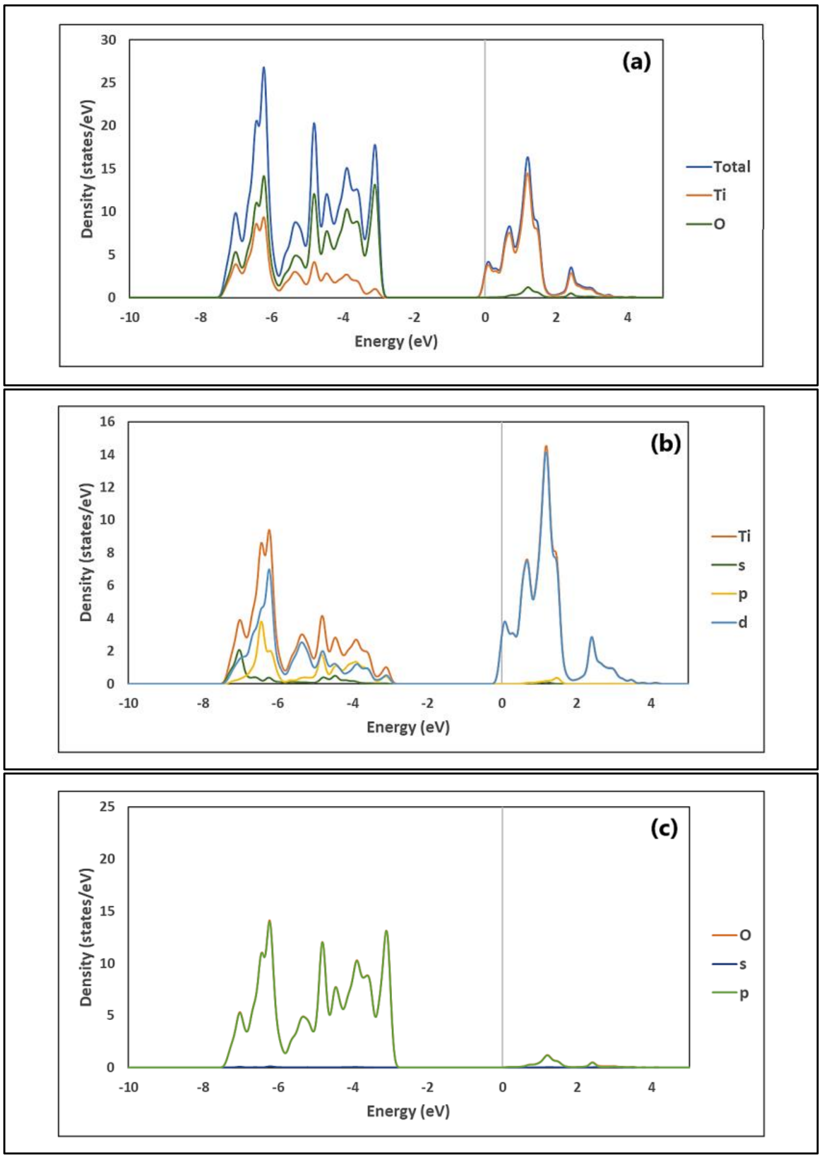

Figure 6. 4. Density of states (DOSs) of TiO_2: (a) total, and partial: (b) Ti and (c) O.

In both structures, $ZnTiO_3$ and TiO_2, the valence band maximum (VBM) is bordered by the oxygen atom, while the Ti atom determines the conduction band maximum (CBM). Consequently, $ZnTiO_3$ has an energy bandgap quite similar to that of TiO_2, due to the fact that $ZnTiO_3$ involves both ZnO and TiO_2. Our calculated results agree with the literature [5,18,54].

In order to further understand the chemical bonding of hexagonal $ZnTiO_3$ and tetragonal TiO_2, the population analyses were estimated by the Bader method. For $ZnTiO_3$, the net charge of Ti (+2.6*e*) was 1.4*e*, much smaller than its +4*e* formal charge, whereas the Zn atom had a positive charge of +1.4*e* and the O atom had a negative charge of −1.3*e*, which are less than their +2*e* and −2*e* formal charges by 0.6*e* and 0.7*e*, respectively. For TiO_2, the net charges of the Ti and O atoms were similar to those calculated for the Ti and O atoms of $ZnTiO_3$. These results agree with those reported by other authors [55]. Since the charges on the different bonds can reflect the covalent and ionic properties of the molecule, we concluded that the Ti–O bond is typically covalent for both $ZnTiO_3$ and TiO_2 and that the Zn–O bond for $ZnTiO_3$ is typically ionic; these results coincide with those reported in the literature [42,56].

6.3.2. Adsorption of the MB Dye on the Structures

The orientations of the MB molecule on the $ZnTiO_3$ and TiO_2 surfaces are shown in Figure 6.5. Figure 6.5(a) shows the horizontal orientation of the MB molecule on the $ZnTiO_3$ surface, while Figures 6.5(b) and 6.5(c) show the semi-perpendicular orientation of the MB molecule on the $ZnTiO_3$ and TiO_2 surfaces, respectively. The adsorption of the MB molecule on the $ZnTiO_3$ surface with the molecule placed in semi-perpendicular orientation ($E_{ads} = -2.916$ eV) was more energetically favored than in the horizontal orientation ($E_{ads} = -1.310$ eV). Therefore, we studied the adsorption of MB on the TiO_2 surface only with the semi-perpendicular orientation. The calculated adsorption energy for the TiO_2 surface ($E_{ads} = -0.113$ eV) was less favorable than the calculated adsorption energy for the $ZnTiO_3$ surface.

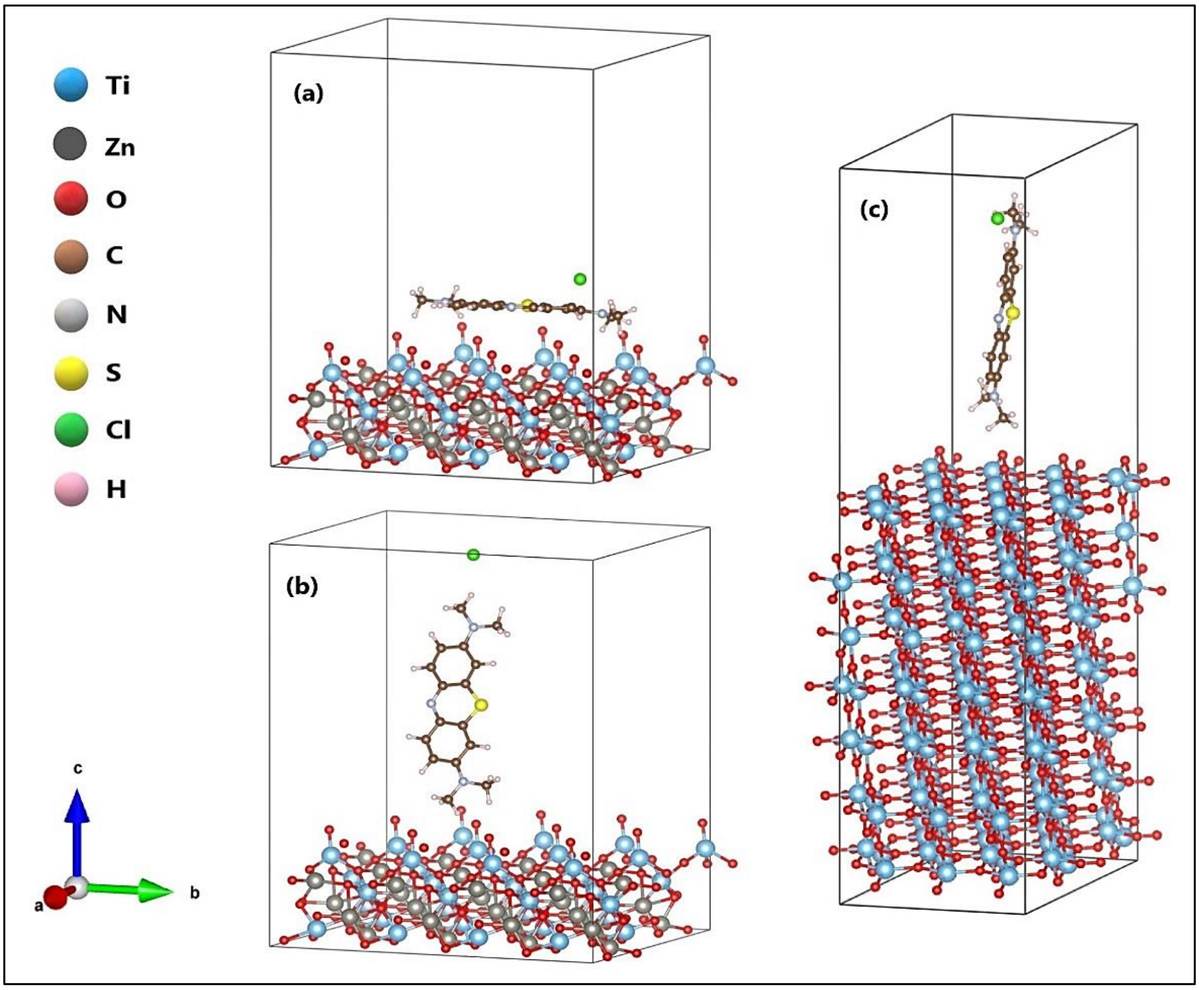

Figure 6. 5. Methylene blue (MB) molecule in (a) horizontal and (b) semi-perpendicular orientation on the $ZnTiO_3$ surface, and (c) semi-perpendicular orientation on the TiO_2 surfaces.

The anchoring modes of the MB molecule on the $ZnTiO_3$ and TiO_2 surfaces are shown in Figure 6.6. Adsorption of the dye on the $ZnTiO_3$ and TiO_2 surfaces occurs in a bidentate chelating (BC) adsorption model [57] with two protons oriented toward the nearest surface oxygen [58].

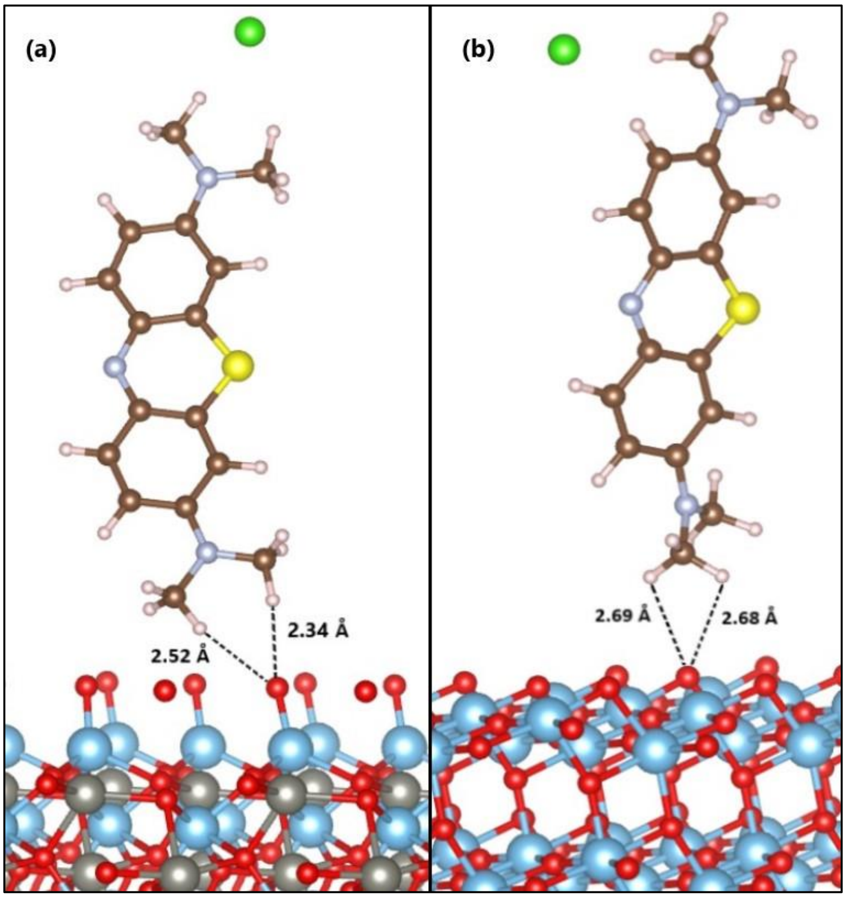

Figure 6. 6. Anchoring modes of the MB molecule on the surface of (a) $ZnTiO_3$ and (b) TiO_2.

The calculated adsorption energy value indicates that the MB molecule is strongly adsorbed on the $ZnTiO_3$ surface. The average distances from the hydrogen atoms of the MB molecule (H_{MB}) to the surface plane of $ZnTiO_3$ are $O_{(oxide)}$-H_{MB} = 2.34 Å and $O_{(oxide)}$-H_{MB} = 2.52 Å. Moreover, the adsorption energy value of the MB molecule on the TiO_2 surface indicates a weaker interaction than on $ZnTiO_3$ (E_{ads} = −0.113 eV). The average distances from the hydrogen atoms of the molecule to the plane of the TiO_2 surface are $O_{(oxide)}$-H_{MB} = 2.68 Å and $O_{(oxide)}$-H_{MB} = 2.69 Å.

6.4. Discussion

6.4.1. Optimization and Electronic Structure of $ZnTiO_3$ and TiO_2

The description of the electronic structure of materials involving transition metals with DFT is often complicated due to correlation effects involving 3*d* electrons [59]. However, since the transition metals of the oxides studied in this paper are formally in the $3d^0$ or $3d^{10}$, neither TiO_2 nor $ZnTiO_3$ are strongly correlated materials; consequently, a simple DFT approach allowed us to accurately calculate the conduction and valence bands of $ZnTiO_3$ and TiO_2.

The literature shows that $ZnTiO_3$ has a relatively wide bandgap (E_g = 2.73–3.70 eV), the value of which depends on the synthesis conditions [60,61]. In our study, the $ZnTiO_3$ and TiO_2 structures presented indirect bandgap values of 2.20 and 2.31 eV, respectively, which were calculated by the GGA-PBE method. In contrast with the experimental data, 3.18 eV for $ZnTiO_3$ [15] and 3.20 eV for TiO_2 [53], the theoretical values are lower, and this may be due to the widely known DFT-underestimation of the bandgap in most materials [1,15]. Therefore, a Hubbard *U* approximation term was adopted to accurately describe the electronic structures [12,62]. The new indirect bandgap values calculated by GGA+U were 3.16 and 3.21 eV for $ZnTiO_3$ and TiO_2, respectively, which are consistent with the aforementioned experimental data. As can be seen, mixed oxide $ZnTiO_3$ has lower bandgap energy than TiO_2. According to the literature, this occurs due to the replacement of Ti ($3d^0$) atoms with Zn ($3d^{10}$) that induce O 2*p*-Zn $3d^{10}$ repulsion [21,63]. Table 6.1 shows the comparison of the bandgap energy values of the $ZnTiO_3$ and TiO_2 calculated in this study with other energy values reported in the literature.

Table 6. 1. Calculated bandgap energy of $ZnTiO_3$ and TiO_2 and other values reported in the literature.

Adsorbent	Software Used	Basis Set Used/ Functional Used	Bandgap (eV)	Reference
$ZnTiO_3$	CASTEP	GGA/SP-PBE	3.14	[1]
$ZnTiO_3$	CASTEP	GGA+U	3.28	[1]
$ZnTiO_3$	MS-DMol3	GGA/PBE	3.10	[5]
$ZnTiO_3$	MS-DMol3	GGA/PPE-grime	3.53	[5]
$ZnTiO_3$	MS-DMol3	GGA/PPE-TS	3.12	[5]
$ZnTiO_3$	Experimental		3.18	[15]
$ZnTiO_3$	VASP	GGA/PBE	2.96	[15]
$ZnTiO_3$	CASTEP	GGA/PW91	3.47	[18]
$ZnTiO_3$	ABINIT	HSE06	4.25	[56]
$ZnTiO_3$	ABINIT	GGA/NC	3.25	[56]
$ZnTiO_3$	ABINIT	LDA/NC	3.05	[56]

$ZnTiO_3$	ABINIT	GGA/ultrasoft	2.96	[56]
$ZnTiO_3$	ABINIT	LDA/ultrasoft	2.86	[56]
$ZnTiO_3$	VASP	GGA/PBE+U	3.16	This study
$ZnTiO_3$	VASP	GGA/PBE	2.20	This study
TiO_2	VASP	HSE06	3.20	[62]
TiO_2	VASP	GGA/PBE	2.55	[58]
TiO_2	VASP	GGA/PBE+U	3.11	[58]
TiO_2	Experimental		3.20	[53]
TiO_2	CASTEP	GGA/PBE	2.70	[53]
TiO_2	CASTEP	GGA/PBE+U	3.34	[53]
TiO_2	ABINIT	GGA/PBE	2.08	[64]
TiO_2	ABINIT	GW	3.71	[64]
TiO_2	VASP	GGA/PBE	2.31	This study
TiO_2	VASP	GGA/PBE+U	3.21	This study

The main character of the electronic structure of $ZnTiO_3$ originates mainly from the hybridization between the Ti-3*d* and O-2*p* states. The Zn-3*d* and O-2*p* hybridization and the Ti-3*d* and O-2*p* hybridization as well as nonbonding O-2*p* states are observed at the upper valence bands (VBs). The localized Zn-3*d* states indicate weak Zn-3*d* and O-2*p* hybridization. The states at the lower conduction bands (CBs) are attributed to antibonding states from Ti-3*d* and O-2*p*. These results agree with those reported by other authors [42]. Similarly, the main character of the electronic structure of TiO_2 originates from the hybridization between the Ti-3*d* and O-2*p* states. This hybridization, as well as nonbonding O-2*p* states, is observed at the upper valence bands (VBs), while the states at the lower conduction bands (CBs) are attributed to antibonding states from Ti-3*d* and O-2*p*. In both structures, the lowest-energy states are due to the isolated Ti-3*s*, Ti-3*p*, and O-2*s* states. These results also agree with those reported by other authors [5,54,65].

6.4.2. Adsorption of the MB Dye on the Oxide Models

Several experimental studies of MB removal in aqueous systems have shown that this cationic dye can be easily adsorbed on the $ZnTiO_3$ and TiO_2 surfaces, due to electrostatic attraction [49]. Therefore, the surface oxygen atoms of both oxides probably generate negatively charged sites that easily attract positive regions of the MB molecule, favoring molecular adsorption.

Our results indicated that the semi-perpendicular orientation of the MB molecule with respect to both oxide surfaces is more favored. In fact, the MB molecule oriented parallel to the surface shows a strong preference for the methyl group of the molecule, while the aromatic ring bends slightly away from the surface due to electrostatic repulsion between the N and S atoms from the aromatic ring and surface oxygen (see Appendices, Figure C2). This is consistent with several studies reporting good adsorption results for dye molecules oriented perpendicular to the adsorbent surface [57,66,67]. Greathouse et al. mentioned that at very high concentrations, this dye forms aggregates that are adsorbed vertically to the surface [68]. Our results suggested that this orientation of the MB molecule on the surface is caused by the balance between electrostatic repulsion between adjacent ions and the strong hydrophobic MB–MB and MB–surface interactions [69].

The MB molecule was adsorbed on the $ZnTiO_3$ surface (101) with higher negative energy (E_{ads} = −2.92 eV) than on the TiO_2 surface (101) (E_{ads} = −0.12 eV), and the average adsorption distances (O–H) were 2.43 and 2.68 Å for $ZnTiO_3$ and TiO_2, respectively. According to the optimized configurations, in both cases, the approach is from the two H atoms of the methyl group of the MB molecule to an O atom of each surface. In agreement with the literature, hydrogen bonding can increase the stability of the interaction of a dye with the $ZnTiO_3$ and TiO_2 surfaces during the adsorption process [70,71]. The Bader charge analysis in Appendices (Table C3) indicates no significant electronic exchange between the MB molecule and the oxides surface [72]. The results obtained in this theoretical study suggest that MB adsorption is more stable (higher negative adsorption energy) on the $ZnTiO_3$ surface than on the TiO_2 surface, which is consistent with previous experimental studies.

Pastore et al. suggested three typical coordination schemes: monodentate, bidentate chelating, and bidentate bridging [57]. In our study, we found that the MB molecule is adsorbed on the $ZnTiO_3$ and TiO_2 surfaces (101) in a bidentate chelating mode, which, according to several authors, produces more stable adsorption with more exothermic adsorption energy [70,73]. The shape of the dye molecules anchored to the oxide significantly affects the molecular adsorption energy. Therefore, calculating the adsorption energy value gives insight into the adherence strength and shape of molecule–surface bonding [66]. The higher the adsorption energy, the higher the retention of the dye on the oxide surface, this being a desirable condition to apply to subsequent photosensitive processes.

In the literature, not enough computational studies of MB adsorption on semiconductors were found; consequently, in Table 6.2, the results obtained in the present study are compared with those results reported in the literature for the adsorption of other dyes on $ZnTiO_3$ (101) and TiO_2 (101).

Table 6. 2. Calculated adsorption energy of $ZnTiO_3$ and TiO_2 and other values reported in the literature.

Adsorbent	Dye	Software Used	Basis set/ Functional Used	Adsorption eV	Adsorption kJ/mol	References
$ZnTiO_3$ (101)	**TPA-1**	**CASTEP**	**GGA/PBE**	−1.41	−136.39	[66]
$ZnTiO_3$ (101)	TPA-2	CASTEP	GGA/PBE	−1.63	−157.47	[66]
$ZnTiO_3$ (101)	TPA-3	CASTEP	GGA/PBE	−5.82	−561.33	[66]
$ZnTiO_3$ (101)	TPA-4	CASTEP	GGA/PBE	−2.37	−228.19	[66]
$ZnTiO_3$ (101) (H)	MB	VASP	GGA/PBE	−1.31	−126.76	This study
$ZnTiO_3$ (101) (SP)	MB	VASP	GGA/PBE	−2.92	−282.05	This study
TiO_2 (101)	R4-BT	VASP	GGA/PBE	−1.40	−135.46	[58]
TiO_2 (101)	R4-F2BT	VASP	GGA/PBE	−1.39	−134.50	[58]
TiO_2 (101)	R4-BO	VASP	GGA/PBE	−1.39	−134.50	[58]
TiO_2 (101)	R6-Bz	VASP	GGA/PBE	−1.40	−135.46	[58]
TiO_2 (101)	R6-BT	VASP	GGA/PBE	−1.38	−133.53	[58]
TiO_2 (101)	R6-F2BT	VASP	GGA/PBE	−1.37	−132.56	[58]
TiO_2 (101)	R6-B0	VASP	GGA/PBE	−1.37	−132.56	[58]
TiO_2 (101)	R6-Bz	VASP	GGA/PBE	−1.38	−133.53	[58]
TiO_2 (101) (SP)	MB	VASP	GGA/PBE	−0.12	−11.61	This study

Other research studies should analyze and apply these results to implement adsorptive systems for dyes or similar molecules.

6.5. Conclusions

The aim of this comparative study was to use molecular simulation to address unresolved issues related to the adsorption mechanism of methylene blue on both $ZnTiO_3$ and TiO_2. DFT calculations of MB adsorption on the surface (101) of both $ZnTiO_3$ and TiO_2 indicated that adsorption on $ZnTiO_3$ was stronger than on TiO_2. The semi-perpendicular orientation was the most probable molecular approach to the oxide surfaces. Electrostatic repulsion due to the proximity of adjacent S and N atoms when MB was in high concentration was overcome by the much stronger interactions between the methyl groups and the surface oxygen atoms of $ZnTiO_3$ and TiO_2.

Finally, we computationally corroborated the feasibility of using $ZnTiO_3$ as an MB adsorbent material, as experimentally found. Theoretically, we forecast the appealing prospect for this material according to the adsorption energy and the large bandgap calculated by DFT, which is in addition to the experimental results that we reported in a previous paper. Our study verifies that $ZnTiO_3$ has better MB adsorption energy than TiO_2 in the anatase phase, which is important to enhance a subsequent degradation process. The large bandgap obtained by DFT calculations also shows that $ZnTiO_3$ can potentially be used as a photocatalyst, allowing for complete degradation of the dye after being adsorbed. Therefore, considering only the band structure, $ZnTiO_3$ fully meets the necessary requirements to be a photocatalyst. As already mentioned, however, in addition to the band structure, the adsorption capacity is also very important for photocatalytic materials. In this way, $ZnTiO_3$ constitutes an efficient alternative material for various technological and environmental applications.

6.6. References

[1] Obodo, K.O.; Noto, L.L.; Mofokeng, S.J.; Ouma, C.N.M.; Braun, M.; Dhlamini, M.S. Influence of Tm, Ho and Er dopants on the properties of Yb activated $ZnTiO_3$ perovskite: A density functional theory insight. *Mater. Res. Express* **2018**, *5*, doi:10.1088/2053-1591/aadaf2.

[2] Li, L.; Zhang, X.; Zhang, W.; Wang, L.; Chen, X.; Gao, Y. Microwave-assisted synthesis of nanocomposite Ag/ZnO-TiO_2 and photocatalytic degradation Rhodamine B with different modes. *Colloids Surf. A Physicochem. Eng. Asp.* **2014**, *457*, 134–141, doi:10.1016/j.colsurfa.2014.05.060.

[3] Ozturk, B.; Soylu, G.S.P. Promoting role of transition metal oxide on $ZnTiO_3$-TiO_2 nanocomposites for the photocatalytic activity under solar light irradiation. *Ceram. Int.* **2016**, *42*, 11184–11192, doi:10.1016/j.ceramint.2016.04.027.

[4] Grabis, J.; Letlena, A.; Sīpola, I. Preparation and properties of photocalysts in ZnO/TiO_2 system. *Key Eng. Mater.* **2019**, *800,* 170–174, doi:10.4028/www.scientific.net/KEM.800.170.

[5] Cherifi, K.; Cheknane, A.; Benghia, A.; Hilal, H.S.; Rahmoun, K.; Benyoucef, B.; Goumri-Said, S. Exploring N3 ruthenium dye adsorption onto $ZnTiO_3$ (101) and (110) surfaces for dye sensitized solar cell applications: Full computational study. *Mater. Today Energy* **2019**, *13*, 109–118, doi:10.1016/j.mtener.2019.04.013.

[6] Lee, C.-G.; Na, K.-H.; Kim, W.-T.; Park, D.-C.; Yang, W.-H.; Choi, W.-Y. TiO_2/ZnO nanofibers prepared by electrospinning and their photocatalytic degradation of methylene blue compared with TiO_2 nanofibers. *Appl. Sci.* **2019**, *9*, 3404, doi:10.3390/app9163404.

[7] Irani, M.; Mohammadi, T.; Mohebbi, S. Photocatalytic degradation of methylene blue with zno nanoparticles; a joint experimental and theoretical study. *J. Mex. Chem. Soc.* **2017**, *60*, 218–225, doi:10.29356/jmcs.v60i4.115.

[8] Sinha, D.; De, D.; Goswami, D.; Mondal, A.; Ayaz, A. ZnO and TiO2 nanostructured dye sensitized solar photovoltaic cell. *Mater. Today Proc.* **2019**, *11*, 782–788, doi:10.1016/j.matpr.2019.03.043.

[9] Ranjith, K.S.; Uyar, T. ZnO-TiO2 composites and ternary ZnTiO3 electrospun nanofibers: The influence of annealing on the photocatalytic response and reusable functionality. *CrystEngComm* **2018**, *20*, 5801–5813, doi:10.1039/c8ce00920a.

[10] Chen, F.; Yu, C.; Wei, L.; Fan, Q.; Ma, F.; Zeng, J.; Yi, J.; Yang, K.; Ji, H. Fabrication and characterization of $ZnTiO_3$/$Zn_2Ti_3O_8$/ZnO ternary photocatalyst for synergetic removal of aqueous organic pollutants and Cr(VI) ions. *Sci. Total Environ.* **2020**, *706*, 136026, doi:10.1016/j.scitotenv.2019.136026.

[11] Zalani, N.M.; Kaleji, B.K.; Mazinani, B. Synthesis and characterisation of the mesoporous ZnO-TiO_2 nanocomposite; Taguchi optimisation and photocatalytic methylene blue degradation under visible light. *Mater. Technol.* **2019**, *35*, 281–289, doi:10.1080/10667857.2019.1678087.

[12] Dutta, D.P.; Singh, A.; Tyagi, A. Ag doped and Ag dispersed nano $ZnTiO_3$: Improved photocatalytic organic pollutant degradation under solar irradiation and antibacterial activity. *J. Environ. Chem. Eng.* **2014**, *2*, 2177–2187, doi:10.1016/j.jece.2014.09.015.

[13] Fu, R.; Wang, Q.; Gao, S.; Wang, Z.; Huang, B.; Dai, Y.; Lu, J. Effect of different processes and Ti/Zn molar ratios on the structure, morphology, and enhanced photoelectrochemical and photocatalytic performance of Ti^{3+} self-doped titanium-zinc hybrid oxides. *J. Power Sources* **2015**, *285*, 449–459, doi:10.1016/j.jpowsour.2015.03.070.

[14] Li, X.; Xiong, J.; Huang, J.; Feng, Z.; Luo, J. Novel g-C_3N_4/h′$ZnTiO_3$-a′TiO_2 direct Z-scheme heterojunction with significantly enhanced visible-light photocatalytic activity. *J. Alloys Compd.* **2019**, *774*, 768–778, doi:10.1016/j.jallcom.2018.10.034.

[15] Yu, J.; Li, N.; Zhu, L.; Xu, X. Application of $ZnTiO_3$ in quantum-dot-sensitized solar cells and numerical simulations using first-principles theory. *J. Alloys Compd.* **2016**, *681*, 88–95, doi:10.1016/j.jallcom.2016.04.224.

[16] Sarkar, M.; Sarkar, S.; Biswas, A.; De, S.; Kumar, P.R.; Mothi, E.M.; Kathiravan, A. Zinc titanate nanomaterials—Photocatalytic studies and sensitization of hydantoin derivatized porphyrin dye. *Nano-Struct. Nano-Objects* **2020**, *21*, 100412, doi:10.1016/j.nanoso.2019.100412.

[17] Baamran, K.S.; Tahir, M. Ni-embedded TiO2-$ZnTiO_3$ reducible perovskite composite with synergistic effect of metal/support towards enhanced H2 production via phenol steam reforming. *Energy Convers. Manag.* **2019**, *200*, 112064, doi:10.1016/j.enconman.2019.112064.

[18] Liu, Q.-J.; Zhang, N.-C.; Liu, F.-S.; Wang, H.-Y.; Liu, Z.-T. Theoretical study of structural, elastic, electronic properties, and dispersion of optical functions of hexagonal $ZnTiO_3$. *Phys. Status Solidi Basic Res.* **2013**, *250*, 1810–1815, doi:10.1002/pssb.201349093.

[19] Yan, X.; Zhao, C.-L.; Zhou, Y.-L.; Wu, Z.-J.; Yuan, J.-M.; Li, W.-S. Synthesis and characterization of $ZnTiO_3$ with high photocatalytic activity. *Trans. Nonferrous Met. Soc. China Engl. Ed.* **2015**, *25*, 2272–2278, doi:10.1016/S1003-6326(15)63841-9.

[20] Li, M.; Jiao, B. Synthesis and photoluminescence properties of $ZnTiO_3$:Eu^{3+} red phosphors via sol-gel method. *J. Rare Earths* **2015**, *33*, 231–238, doi:10.1016/S1002-0721(14)60408-7.

[21] Lv, J.; Tang, M.; Quan, R.; Chai, Z. Synthesis of solar heat-reflective $ZnTiO_3$ pigments with novel roof cooling effect. *Ceram. Int.* **2019**, *45*, 15768–15771, doi:10.1016/j.ceramint.2019.05.081.

[22] Sowmyashree, A.; Somya, A.; Kumar, C.P.; Rao, S. Novel nano corrosion inhibitor, integrated zinc titanate nano particles: Synthesis, characterization, thermodynamic and electrochemical studies. *Surf. Interfaces* **2021**, *22*, 100812, doi:10.1016/j.surfin.2020.100812.

[23] Tavakoli-Azar, T.; Mahjoub, A.R.; Sadjadi, M.S.; Farhadyar, N.; Sadr, M.H. Improving the photocatalytic performance of a perovskite $ZnTiO_3$ through $ZnTiO_3$@S nanocomposites for degradation of Crystal violet and Rhodamine B pollutants under sunlight. *Inorg. Chem. Commun.* **2020**, *119*, 108091, doi:10.1016/j.inoche.2020.108091.

[24] Raveendra, R.; Prashanth, P.; Krishna, R.H.; Bhagya, N.; Nagabhushana, B.; Naika, H.R.; Lingaraju, K.; Nagabhushana, H.; Prasad, B.D. Synthesis, structural characterization of nano $ZnTiO_3$ ceramic: An effective azo dye adsorbent and antibacterial agent. *J. Asian Ceram. Soc.* **2014**, *2*, 357–365, doi:10.1016/j.jascer.2014.07.008.

[25] Kurajica, S.; Minga, I.; Blazic, R.; Muzina, K.; Tominac, P. Adsorption and degradation kinetics of methylene blue on as-prepared and calcined titanate nanotubes. *Athens, J. Sci.* **2018**, *5*, 7–22, doi:10.30958/ajs.5-1-1.

[26] Sahu, A.; Chaurasiya, R.; Hiremath, K.; Dixit, A. Nanostructured zinc titanate wide band gap semiconductor as a photoelectrode material for quantum dot sensitized solar cells. *Sol. Energy* **2018**, *163*, 338–346, doi:10.1016/j.solener.2018.01.092.

[27] Inaguma, Y.; Aimi, A.; Shirako, Y.; Sakurai, D.; Mori, D.; Kojitani, H.; Akaogi, M.; Nakayama, M. High-pressure synthesis, crystal structure, and phase stability relations of a LiNbO3-type polar titanate ZnTiO3 and its reinforced polarity by the second-order Jahn-Teller effect. *J. Am. Chem. Soc.* **2013**, *136*, 2748–2756, doi:10.1021/ja408931v.

[28] Ruiz-Fuertes, J.; Winkler, B.; Bernert, T.; Bayarjargal, L.; Morgenroth, W.; Koch-Müller, M.; Refson, K.; Milman, V.; Tamura, N. Ferroelectric soft mode of polar ZnTiO3 investigated by Raman spectroscopy at high pressure. *Phys. Rev. B Condens. Matter Mater. Phys.* **2015**, *91*, 214110, doi:10.1103/PhysRevB.91.214110.

[29] Pawar, R.C.; Kang, S.; Park, J.H.; Kim, J.-H.; Ahn, S.; Lee, C.S. Evaluation of a multi-dimensional hybrid photocatalyst for enrichment of H2 evolution and elimination of dye/non-dye pollutants. *Catal. Sci. Technol.* **2017**, *7*, 2579–2590, doi:10.1039/c7cy00466d.

[30] Salavati-Niasari, M.; Soofivand, F.; Sobhani-Nasab, A.; Shakouri-Arani, M.; Faal, A.Y.; Bagheri, S. Synthesis, characterization, and morphological control of $ZnTiO_3$ nanoparticles through sol-gel processes and its photocatalyst application. *Adv. Powder Technol.* **2016**, *27*, 2066–2075, doi:10.1016/j.apt.2016.07.018.

[31] Ke, S.; Cheng, X.; Wang, Q.; Wang, Y.; Pan, Z. Preparation of a photocatalytic $TiO_2/ZnTiO_3$ coating on glazed ceramic tiles. *Ceram. Int.* **2014**, *40*, 8891–8895, doi:10.1016/j.ceramint.2014.01.027.

[32] Acosta-Silva, Y.D.J.; Castanedo-Perez, R.; Torres-Delgado, G.; Méndez-López, A.; Zelaya-Angel, O. Analysis of the photocatalytic activity of $CdS+ZnTiO_3$ nanocomposite films prepared by sputtering process. *Superlattices Microstruct.* **2016**, *100*, 148–157, doi:10.1016/j.spmi.2016.09.018.

[33] Yadav, B.; Yadav, A.; Singh, S.; Singh, K. Nanocrystalline zinc titanate synthesized via physicochemical route and its application as liquefied petroleum gas sensor. *Sens. Actuators B Chem.* **2013**, *177*, 605–611, doi:10.1016/j.snb.2012.11.045.

[34] Tahay, P.; Khani, Y.; Jabari, M.; Bahadoran, F.; Safari, N.; Zamanian, A. Synthesis of cubic and hexagonal ZnTiO3 as catalyst support in steam reforming of methanol: Study of physical and chemical properties of copper catalysts on the H2 and CO selectivity and coke formation. *Int. J. Hydrog. Energy* **2020**, *45*, 9484–9495, doi:10.1016/j.ijhydene.2020.01.149.

[35] Edalatfar, M.; Yazdani, F.; Salehi, M.B. Synthesis and identification of $ZnTiO_3$ nanoparticles as a rheology modifier additive in water-based drilling mud. *J. Pet. Sci. Eng.* **2021**, *201*, 108415, doi:10.1016/j.petrol.2021.108415.

[36] Bhagwat, U.O.; Wu, J.J.; Asiri, A.M.; Anandan, S. Synthesis of $ZnTiO_3@TiO_2$ heterostructure nanomaterial as a visible light photocatalyst. *ChemistrySelect* **2019**, *4*, 6106–6112, doi:10.1002/slct.201901083.

[37] Lei, S.; Fan, H.; Ren, X.; Fang, J.; Ma, L.; Liu, Z. Novel sintering and band gap engineering of $ZnTiO_3$ ceramics with excellent microwave dielectric properties. *J. Mater. Chem. C* **2017**, *5*, 4040–4047, doi:10.1039/c7tc00815e.

[38] Pantoja-Espinoza, J.C.; Domínguez-Arvizu, J.L.; Jiménez-Miramontes, J.A.; Hernández-Majalca, B.C.; Meléndez-Zaragoza, M.J.; Salinas-Gutiérrez, J.M.; Herrera-Pérez, G.M.; Collins-Martínez, V.H.; López-Ortiz, A. Comparative study of $Zn_2Ti_3O_8$ and $ZnTiO_3$ photocatalytic properties for hydrogen production. *Catalysts* **2020**, *10*, 1372, doi:10.3390/catal10121372.

[39] Jaramillo-Fierro, X.; Pérez, S.G.; Jaramillo, X.; Cabello, F.M. Synthesis of the $ZnTiO_3/TiO_2$ nanocomposite supported in ecuadorian clays for the adsorption and photocatalytic removal of methylene blue dye. *Nanomaterials* **2020**, *10*, 1891, doi:10.3390/nano10091891.

[40] Jaramillo-Fierro, X.; González, S.; Montesdeoca-Mendoza, F.; Medina, F. Structuring of zntio3/tio2 adsorbents for the removal of methylene blue, using zeolite precursor clays as natural additives. *Nanomaterials* **2021**, *11*, 898, doi:10.3390/nano11040898.

[41] Zhang, Z.; Yates, J.J.T. Band bending in semiconductors: Chemical and physical consequences at surfaces and interfaces. *Chem. Rev.* **2012**, *112*, 5520–5551, doi:10.1021/cr3000626.

[42] Xiao-Chao, Z.; Cai-Mei, F.; Zhen-Hai, L.; Pei-De, H. Electronic structures and optical properties of ilmenite-type hexagonal $ZnTiO_3$. *Wuli Huaxue Xuebao/Acta Phys. Chim. Sin.* **2011**, *27*, 47–51, doi:10.3866/pku.whxb20110102.

[43] Conesa, J.C. Band structures and nitrogen doping effects in zinc titanate photocatalysts. *Catal. Today* **2013**, *208*, 11–18, doi:10.1016/j.cattod.2012.08.039.

[44] Gil, A.; Assis, F.; Albeniz, S.; Korili, S. Removal of dyes from wastewaters by adsorption on pillared clays. *Chem. Eng. J.* **2011**, *168*, 1032–1040, doi:10.1016/j.cej.2011.01.078.

[45] Laysandra, L.; Sari, M.W.M.K.; Soetaredjo, F.E.; Foe, K.; Putro, J.N.; Kurniawan, A.; Ju, Y.-H.; Ismadji, S. Adsorption and photocatalytic performance of bentonite-titanium dioxide composites for methylene blue and rhodamine B decoloration. *Heliyon* **2017**, *3*, e00488, doi:10.1016/j.heliyon.2017.e00488.

[46] Mehrabi, M.; Javanbakht, V. Photocatalytic degradation of cationic and anionic dyes by a novel nanophotocatalyst of $TiO_2/ZnTiO_3/\alpha Fe_2O_3$ by ultraviolet light irradiation. *J. Mater. Sci. Mater. Electron.* **2018**, *29*, 9908–9919, doi:10.1007/s10854-018-9033-0.

[47] Subramaniam, M.N.; Goh, P.S.; Abdullah, N.; Lau, W.J.; Ng, B.C.; Ismail, A.F. Adsorption and photocatalytic degradation of methylene blue using high surface area titanate nanotubes (TNT) synthesized via hydrothermal method. *J. Nanoparticle Res.* **2017**, *19*, 220, doi:10.1007/s11051-017-3920-9.

[48] Abdellah, M.; Nosier, S.; El-Shazly, A.; Mubarak, A. Photocatalytic decolorization of methylene blue using TiO_2/UV system enhanced by air sparging. *Alex. Eng. J.* **2018**, *57*, 3727–3735, doi:10.1016/j.aej.2018.07.018.

[49] Sutanto, N.; Saharudin, K.A.; Sreekantan, S.; Kumaravel, V.; Akil, H.M. Heterojunction catalysts g-C_3N_4/-3ZnO-c-$Zn_2Ti_3O_8$ with highly enhanced visible-light-driven photocatalytic activity. *J. Sol-Gel Sci. Technol.* **2020**, *93*, 354–370, doi:10.1007/s10971-019-05101-4.

[50] Zhao, Q.; Zhang, L.; Wang, X.; Jia, X.; Xu, P.; Zhao, M.; Dai, R. Simultaneous efficient adsorption and photocatalytic degradation of methylene blue over iron(III)-based metal–organic frameworks: A comparative study. *Transit. Met. Chem.* **2019**, *44*, 789–797, doi:10.1007/s11243-019-00349-9.

[51] Chang-Guo, Z. Development and application of first-principles electronic structure approach for molecules in solution based on fully polarizable continuum model. *Wuli Huaxue Xuebao/Acta Phys. Chim. Sin.* **2011**, *27*, 1–10, doi:10.3866/pku.whxb20110101.

[52] Hinuma, Y.; Pizzi, G.; Kumagai, Y.; Oba, F.; Tanaka, I. Band structure diagram paths based on crystallography. *Comput. Mater. Sci.* **2017**, *128*, 140–184, doi:10.1016/j.commatsci.2016.10.015.

[53] Zhang, R.; Zhao, J.; Yang, Y.; Lu, Z.; Shi, W. Understanding electronic and optical properties of La and Mn co-doped anatase TiO_2. *Comput. Condens. Matter* **2016**, *6*, 5–17, doi:10.1016/j.cocom.2016.03.001.

[54] Qi, K.; Selvaraj, R.; Al Fahdi, T.; Al-Kindy, S.; Kim, Y.; Wang, G.-C.; Tai, C.-W.; Sillanpää, M. Enhanced photocatalytic activity of anatase-TiO_2 nanoparticles by fullerene modification: A theoretical and experimental study. *Appl. Surf. Sci.* **2016**, *387*, 750–758, doi:10.1016/j.apsusc.2016.06.134.

[55] Koch, D.; Golub, P.; Manzhos, S. Stability of charges in titanium compounds and charge transfer to oxygen in titanium dioxide. *J. Phys. Conf. Ser.* **2018**, *1136*, 012017, doi:10.1088/1742-6596/1136/1/012017.

[56] Zhang, J.; Xu, B.; Wang, Y.-S.; Qin, Z.; Ke, S.-H. First-principles investigation of the ferroelectric, piezoelectric and nonlinear optical properties of LiNbO$_3$-type ZnTiO$_3$. *Sci. Rep.* **2019**, *9*, 1–14, doi:10.1038/s41598-019-53986-6.

[57] Pastore, M.; De Angelis, F. Computational modelling of TiO$_2$ surfaces sensitized by organic dyes with different anchoring groups: Adsorption modes, electronic structure and implication for electron injection/recombination. *Phys. Chem. Chem. Phys.* **2012**, *14*, 920–928, doi:10.1039/c1cp22663k.

[58] Samanta, P.K.; English, N.J. Opto-electronic properties of stable blue photosensitisers on a TiO$_2$ anatase-101 surface for efficient dye-sensitised solar cells. *Chem. Phys. Lett.* **2019**, *731*, 136624, doi:10.1016/j.cplett.2019.136624.

[59] Cramer, C.J.; Truhlar, D. Density functional theory for transition metals and transition metal chemistry. *Phys. Chem. Chem. Phys.* **2009**, *11*, 10757–10816, doi:10.1039/b907148b.

[60] Wang, J.; Wang, D.; Zhang, X.; Zhao, C.; Zhang, M.; Zhang, Z.; Wang, J. An anti-symmetric dual (ASD) Z-scheme photocatalytic system: (ZnIn$_2$S$_4$/Er$^{3+:}$Y$_3$Al$_5$O$_{12}$@ZnTiO$_3$/CaIn$_2$S$_4$) for organic pollutants degradation with simultaneous hydrogen evolution. *Int. J. Hydrog. Energy* **2019**, *44*, 6592–6607, doi:10.1016/j.ijhydene.2019.01.214.

[61] Wang, Y.-W.; Yuan, P.-H.; Fan, C.-M.; Wang, Y.; Ding, G.-Y.; Wang, Y.-F. Preparation of zinc titanate nanoparticles and their photocatalytic behaviors in the photodegradation of humic acid in water. *Ceram. Int.* **2012**, *38*, 4173–4180, doi:10.1016/j.ceramint.2012.01.078.

[62] Khan, S.; Cho, H.; Kim, D.; Han, S.S.; Lee, K.H.; Cho, S.-H.; Song, T.; Choi, H. Defect engineering toward strong photocatalysis of Nb-doped anatase TiO2: Computational predictions and experimental verifications. *Appl. Catal. B Environ.* **2017**, *206*, 520–530, doi:10.1016/j.apcatb.2017.01.039.

[63] McLeod, J.A.; Moewes, A.; Zatsepin, D.A.; Kurmaev, E.Z.; Wypych-Puszkarz, A.; Bobowska, I.; Opasinska, A.; Cholakh, S.O. Predicting the band gap of ternary oxides containing 3d10 and 3d0 metals. *Phys. Rev. B Condens. Matter Mater. Phys.* **2012**, *86*, 195207, doi:10.1103/PhysRevB.86.195207.

[64] Zhu, T.; Gao, S.-P. The stability, electronic structure, and optical property of tio 2 polymorphs. *J. Phys. Chem. C* **2014**, *118*, 11385–11396, doi:10.1021/jp412462m.

[65] Hossain, F.M.; Evteev, A.V.; Belova, I.V.; Nowotny, J.; Murch, G.E. First-principles calculations of a corrugated anatase TiO2 surface. *Comput. Mater. Sci.* **2012**, *51*, 78–82, doi:10.1016/j.commatsci.2011.07.018.

[66] Cherifi, K.; Cheknane, A.; S.Hilal, H.; Benghia, A.; Rahmoun, K.; Benyoucef, B. Investigation of triphenylamine-based sensitizer characteristics and adsorption behavior onto $ZnTiO_3$ perovskite (1 0 1) surfaces for dye-sensitized solar cells using first-principle calculation. *Chem. Phys.* **2020**, *530*, 110595, doi:10.1016/j.chemphys.2019.110595.

[67] Zhu, H.-C.; Li, C.-F.; Fu, Z.-H.; Wei, S.-S.; Zhu, X.-F.; Zhang, J. Increasing the open-circuit voltage and adsorption stability of squaraine dye binding onto the TiO_2 anatase (1 0 1) surface via heterocyclic anchoring groups used for DSSC. *Appl. Surf. Sci.* **2018**, *455*, 1095–1105, doi:10.1016/j.apsusc.2018.06.081.

[68] Greathouse, J.A.; Geatches, D.L.; Pike, D.Q.; Greenwell, H.; Johnston, C.T.; Wilcox, J.; Cygan, R.T. Methylene blue adsorption on the basal surfaces of kaolinite: Structure and thermodynamics from quantum and classical molecular simulation. *Clays Clay Miner.* **2015**, *63*, 185–198, doi:10.1346/CCMN.2015.0630303.

[69] Zhong, L.; Hu, Y.; Xing, D. Adsorption orientation of methylene blue (MB+) on the silver colloid: SERS and DFT studies. In Proceedings of the 2009 Conference on Lasers & Electro Optics & The Pacific Rim Conference on Lasers and Electro-Optics, Shanghai, China, 30 August–3 September 2009; pp. 1–2, doi:10.1109/CLEOPR.2009.5292661.

[70] Orellana, W. D-π-A dye attached on TiO2(101) and TiO2(001) surfaces: Electron transfer properties from ab initio calculations. *Sol. Energy* **2021**, *216*, 266–273, doi:10.1016/j.solener.2020.12.061.

[71] Qin, H.-C.; Qin, Q.-Q.; Luo, H.; Wei, W.; Liu, L.-X.; Li, L.-C. Theoretical study on adsorption characteristics and environmental effects of dimetridazole on TiO_2 surface. *Comput. Theor. Chem.* **2019**, *1150*, 10–17, doi:10.1016/j.comptc.2019.01.002.

[72] Kuganathan, N.; Chroneos, A. Hydrogen adsorption on Ru-encapsulated, -doped and -supported surfaces of C60. *Surfaces* **2020**, *3*, 408–422, doi:10.3390/surfaces3030030.

[73] Mathew, S.; Yella, A.; Gao, P.; Humphry-Baker, R.; Curchod, B.F.E.; Ashari-Astani, N.; Tavernelli, I.; Rothlisberger, U.; Nazeeruddin, K.; Graetzel, M. Dye-sensitized solar

cells with 13% efficiency achieved through the molecular engineering of porphyrin sensitizers. *Nat. Chem.* **2014**, *6*, 242–247, doi:10.1038/nchem.1861.

[74] Kresse, G.; Furthmüller, J. Efficient iterative schemes for ab initio total-energy calculations using a plane-wave basis set. *Phys. Rev. B Condens. Matter Mater. Phys.* **1996**, *54*, 11169–11186, doi:10.1103/PhysRevB.54.11169.

[75] Perdew, J.P.; Burke, K.; Ernzerhof, M. Generalized gradient approximation made simple. *Phys. Rev. Lett.* **1996**, *77*, 3865–3868, doi:10.1103/PhysRevLett.77.3865.

[76] Kohn, W.; Sham, L. Quantum density oscillations in an inhomogeneous electron gas. *Phys. Rev.* **1965**, *137*, A1697–A1705, doi:10.1103/PhysRev.137.A1697.

[77] Wang, Y.A.; Xiang, P. From the Hohenberg-Kohn theory to the Kohn-Sham equations. In *Recent Progress in Orbital-free Density Functional Theory*; World Scientific: Singapore, 2013; pp. 3–12.

[78] Monkhorst, H.J.; Pack, J.D. Special points for Brillouin-zone integrations. *Phys. Rev. B* **1976**, *13*, 5188–5192, doi:10.1103/PhysRevB.13.5188.

[79] Voityuk, A.A.; Stasyuk, A.J.; Vyboishchikov, S.F. A simple model for calculating atomic charges in molecules. *Phys. Chem. Chem. Phys.* **2018**, *20*, 23328–23337, doi:10.1039/c8cp03764g.

[80] Yu, M.; Trinkle, D.R. Accurate and efficient algorithm for Bader charge integration. *J. Chem. Phys.* **2011**, *134*, 064111, doi:10.1063/1.3553716.

[81] Kumar, P.S.V.; Raghavendra, V.; Subramanian, V. Bader's Theory of Atoms in Molecules (AIM) and its Applications to Chemical Bonding. *J. Chem. Sci.* **2016**, *128*, 1527–1536, doi:10.1007/s12039-016-1172-3.

[82] Martinez, J.; Sinnott, S.B.; Phillpot, S.R. Adhesion and diffusion at TiN/TiO_2 interfaces: A first principles study. *Comput. Mater. Sci.* **2017**, *130*, 249–256, doi:10.1016/j.commatsci.2016.11.017.

[83] German, E.; Faccio, R.; Mombrú, A.W. Comparison of standard DFT and Hubbard-DFT methods in structural and electronic properties of TiO_2 polymorphs and H-titanate ultrathin sheets for DSSC application. *Appl. Surf. Sci.* **2018**, *428*, 118–123, doi:10.1016/j.apsusc.2017.09.141.

[84] Pillai, R.S.; Khan, I.; Titus, E. C_2-Hydrocarbon Adsorption in Nano-porous Faujasite: A DFT Study. *Mater. Today Proc.* **2015**, *2*, 436–445, doi:10.1016/j.matpr.2015.04.053.

CHAPTER 7

MAIN CONCLUSIONS

Twelve Ecuadorian clays were collected, purified and characterized. $Clay_6$ (or G-Clay due to its gray color) proved to be a good adsorbent, probably due to the presence of the metahalloysite phase that was identified by X-ray Diffraction (XRD). On the other hand, $Clay_{12}$ (or R-Clay, due to its red color) exhibited photocatalytic activity, probably due to the presence of TiO_2 and Fe_2O_3 in its composition, which was verified by X-ray Fluorescence (XRF). From these clays, FAU and LTA zeolites, respectively, with good morphological and adsorbent characteristics, could be synthesized hydrothermally.

The mixed oxide of Zn and Ti, perovskite type, $ZnTiO_3/TiO_2$ and $ZnTiO_3/TiO_2/La$ were synthesized by the sol-gel method with a molar ratio of Ti:Zn of 3:1 and final calcination at 500 °C for 5 hours. $ZnTiO_3/TiO_2$ and $ZnTiO_3/TiO_2/La$ showed better activity than TiO_2 (anatase) for the elimination of methylene blue dye from aqueous solutions, with high degradation under UV-C light and solar light.

Various extrudates in the form of cylinders were prepared by combining clays, zeolites and photocatalysts. Although these materials had a lower surface area than the corresponding powders, the extrudates efficiently removed methylene blue from aqueous solutions, with the additional advantage of easy handling and recovery, making them ideal for industrial applications.

The adsorption studies as a function of pH showed that the adsorption of the cationic dye increases, as the pH increases, due to the greater electrostatic attraction between the positive charges of the dye and the negative charges of the adsorption sites. However, at very alkaline pH levels (pH > 9), it appears that the OH ions formed a complex with other ions within alkaline pH ranges, which affected the adsorption of the dye on the adsorbents. In this way, it is inferred that the adsorption process probably occurred through a combination of electrostatic attraction, sorption and precipitation.

On the other hand, the adsorption studies also showed that the prepared materials eliminated methylene blue following a behavior described by the Langmuir model and with pseudo second-order kinetics. Film diffusion was also found to be the limiting step during adsorption of the colorant on the surface of the extrudates. After 3-5 adsorption cycles in batch reactors, the extrudates maintained their shape and also had a high efficiency for the removal of methylene blue in aqueous solutions.

Due to the difficulty of obtaining pure $ZnTiO_3$, computational studies were carried out to theoretically determine its electronic properties and the adsorption capacity of methylene blue, compared to TiO_2 (anatase phase). DFT calculations of methylene blue adsorption on the surface (101) of $ZnTiO_3$ and TiO_2 showed that the adsorption on $ZnTiO_3$ is much stronger than on TiO_2. Adsorption was favored by placing the methylene blue molecule in a semi-perpendicular orientation on the surface of each oxide, where adsorption occurred in a bidentate chelating (BC) pattern with two protons oriented toward the closest surface oxygen. Finally, the feasibility of using $ZnTiO_3$ as an adsorbent material for the removal of methylene blue due to the high calculated adsorption energy was computationally demonstrated. Likewise, the large band gap obtained by DFT calculations showed that $ZnTiO_3$ can potentially be used as a photocatalyst, which would allow complete degradation of the dye after being adsorbed on the surface.

Therefore, considering the experimental and theoretical results obtained in this thesis, it is inferred that $ZnTiO_3$ constitutes an efficient alternative material for various technological and environmental applications.

CHAPTER 8

PUBLICATIONS & COMMUNICATIONS

7.1. Published Articles

Jaramillo-Fierro, X.; González, S.; Jaramillo, H.A.; Medina, F. Synthesis of the $ZnTiO_3/TiO_2$ Nanocomposite Supported in Ecuadorian Clays for the Adsorption and Photocatalytic Removal of Methylene Blue Dye. ***Nanomaterials*** 2020, *10(9)*, 1891. https://doi.org/10.3390/nano10091891

Jaramillo-Fierro, X.; González, S.; Montesdeoca-Mendoza, F.; Medina, F. Structuring of ZnTiO3/TiO2 Adsorbents for the Removal of Methylene Blue, Using Zeolite Precursor Clays as Natural Additives. ***Nanomaterials*** 2021, *11(4)*, 898. https://doi.org/10.3390/nano11040898

Jaramillo-Fierro, X.; Capa, L.F.; Medina, F.; González, S. DFT Study of Methylene Blue Adsorption on $ZnTiO_3$ and TiO_2 Surfaces (101). ***Molecules*** 2021, *26(13)*, 3780. https://doi.org/10.3390/molecules26133780

Jaramillo-Fierro, X.; González, S.; Medina, F. La-Doped $ZnTiO_3/TiO_2$ Nanocomposite Supported on Ecuadorian Diatomaceous Earth as a Highly Efficient Photocatalyst Driven by Solar Light. ***Molecules*** 2021, *26(20)*, 6232. https://doi.org/10.3390/molecules26206232

7.2. Oral Communications

Jaramillo-Fierro, X.; González, S.; Medina, F. (2019). *Preparación de materiales fotocatalíticos para la remoción de contaminantes en sistemas acuosos a partir de óxido de titanio y arcillas de la región Sur del Ecuador*. Oral presentation at I Simposio de Ciencias Ambientales "Energía, Ambiente y Desarrollo Sostenible", UTPL, Loja, Ecuador.

Jaramillo-Fierro, X.; González, S.; Medina, F. (2019). *Preparación de materiales fotocatalíticos para la remoción de contaminantes en sistemas acuosos a partir de óxido de titanio y arcillas de la región Sur del Ecuador*. Oral presentation at VIII Investiga, UTPL, Loja, Ecuador.

Jaramillo-Fierro, X.; González, S.; Medina, F. (2021). *Synthesis of* $ZnTiO_3/TiO_2$ *nanocomposite supporting in Ecuadorian clays for the adsorption and photocatalytic degradation of Methylene Blue*. Oral presentation at First Annual Congress of doctorate students of the Miguel Hernández University, MH, Elche, Spain.

Jaramillo-Fierro, X.; González, S.; Medina, F. (2021). *Desarrollo de materiales adsorbentes y fotocatalíticos a partir de arcillas ecuatorianas*. Oral presentation at Primer Congreso de Ciencias Biológicas y Biomédicas, UTPL, Loja, Ecuador.

Jaramillo-Fierro, X.; González, S.; Medina, F. (2021). *Synthesis of* $ZnTiO_3/TiO_2$ *nanocomposite supporting in Ecuadorian clays for the adsorption and photocatalytic degradation of Methylene Blue*. Oral presentation at 2nd Advanced Materials Science World Congress, Berlin, Germany.

Jaramillo-Fierro, X.; González, S.; Medina, F. (2021). *Synthesis of* $ZnTiO_3/TiO_2$ *nanocomposite supporting in Ecuadorian clays for the adsorption and photocatalytic degradation of Methylene Blue*. Oral presentation at 34º Congreso Latinoamericano de Química CLAQ 2020, Cartagena de Indias, Colombia.

Jaramillo-Fierro, X.; González, S.; Medina, F. (2021). *Synthesis and characterization of adsorbent and photocatalytic materials for the removal of methylene blue in wastewater*. Oral presentation at VIII Congreso Internacional de Investigación, Ambato, Ecuador.

Jaramillo-Fierro, X.; González, S.; Medina, F. (2021). *Synthesis of* $ZnTiO_3/TiO_2$ *nanocomposite supporting in Ecuadorian clays for the adsorption and photocatalytic degradation of Methylene Blue (MB) in aqueous systems*. Oral presentation at International Workshop NanoAndes 2021, Lima, Perú.

Jaramillo-Fierro, X.; González, S.; Medina, F. (2021). *Síntesis y caracterización de materiales adsorbentes y fotocatalíticos para la remoción de azul de metileno en aguas residuales*. Oral presentation at II Simposio de Ciencias Ambientales "Energía, Ambiente y Desarrollo Sostenible", UTPL, Loja, Ecuador.

7.3. Poster Presentation

Jaramillo-Fierro, X.; González, S.; Medina, F. (2021). *DFT Study of Methylene Blue Adsorption on $ZnTiO_3$ and TiO_2 Surfaces (101).* Poster presentation at International Summer School "Ab initio Modeling in Solid State Chemistry – MSSC2021", Imperial College London, London, UK.

APPENDICES

Appendix A: Additional Figures/Tables from Chapter 3

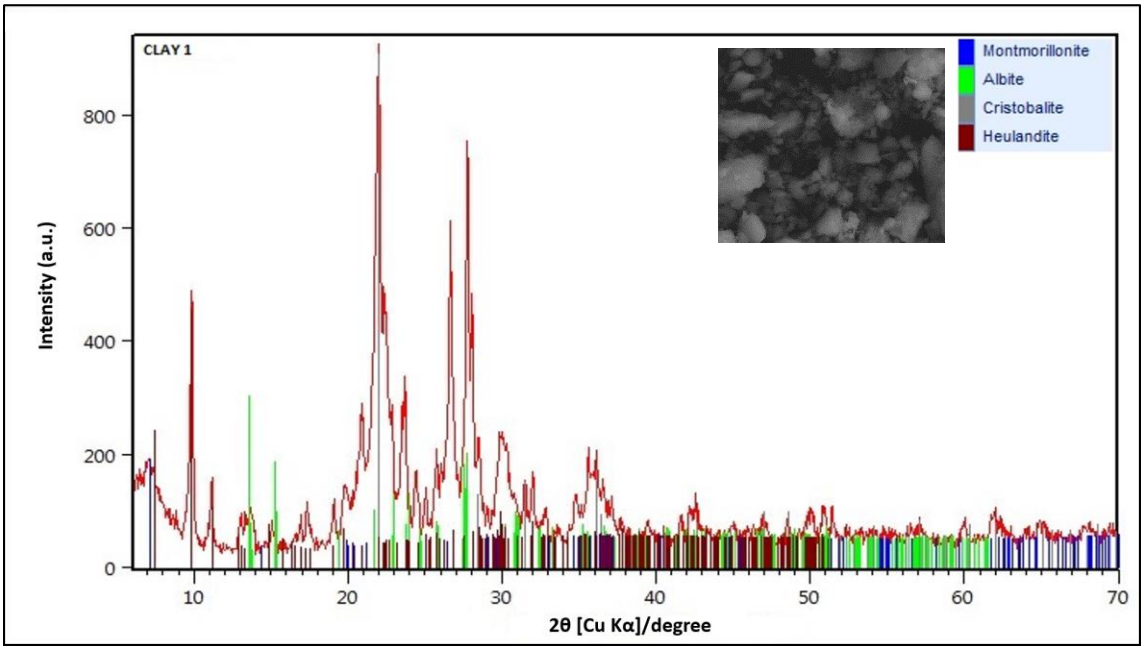

Figure A1. XRD pattern and SEM (insert) image of $Clay_1$

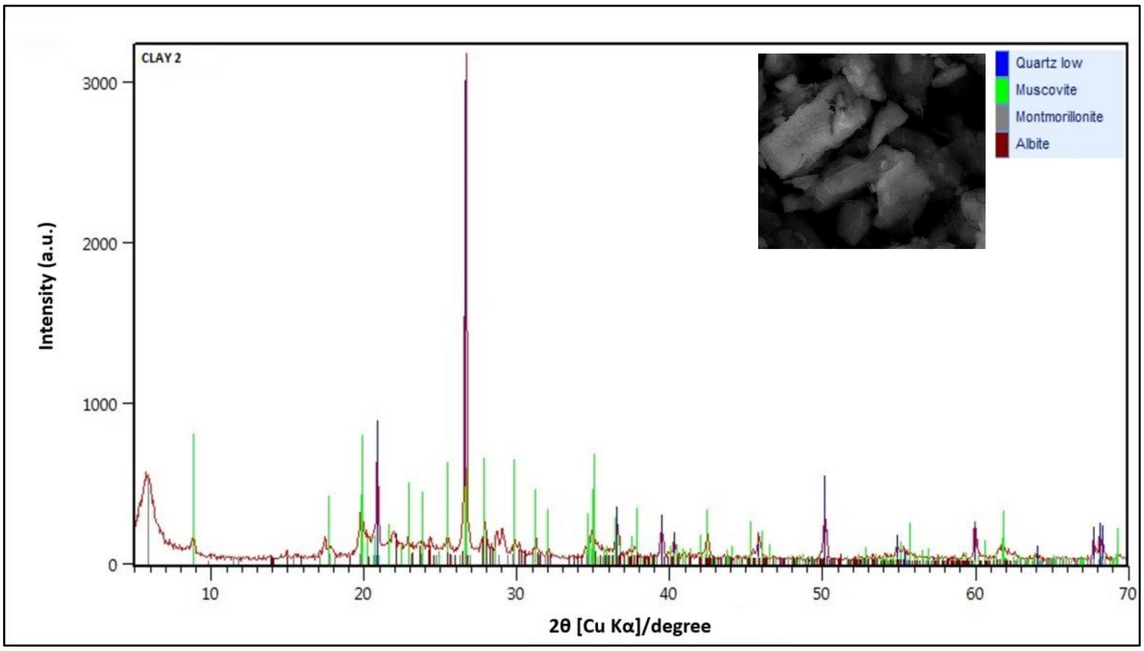

Figure A2. XRD pattern and SEM (insert) image of $Clay_2$

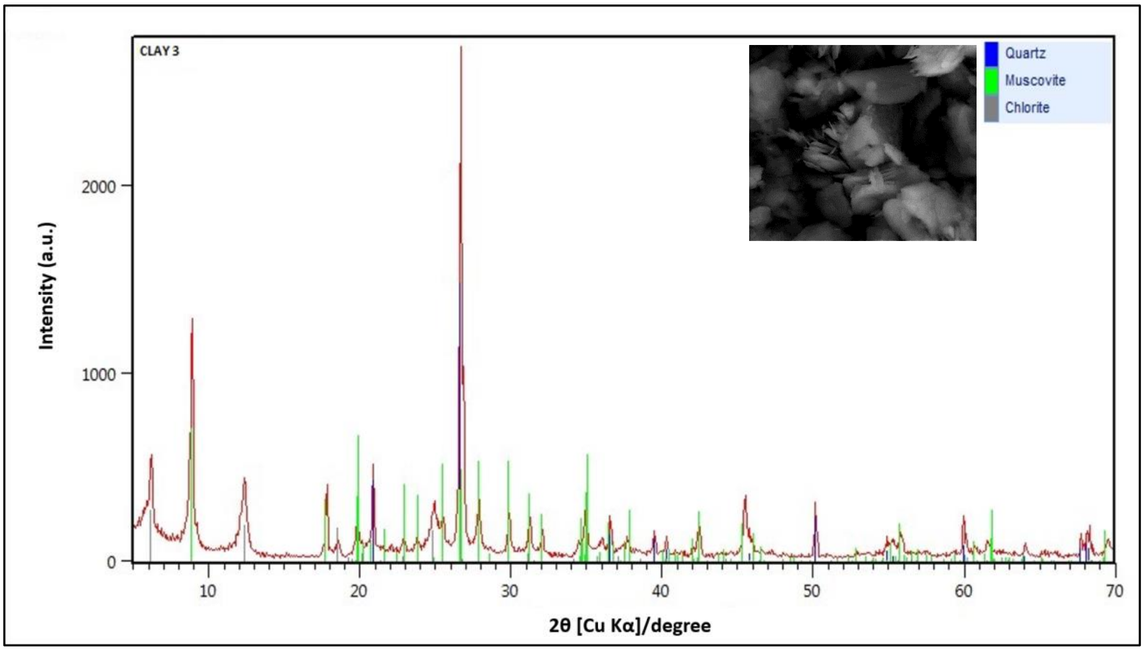

Figure A3. XRD pattern and SEM (insert) image of $Clay_3$

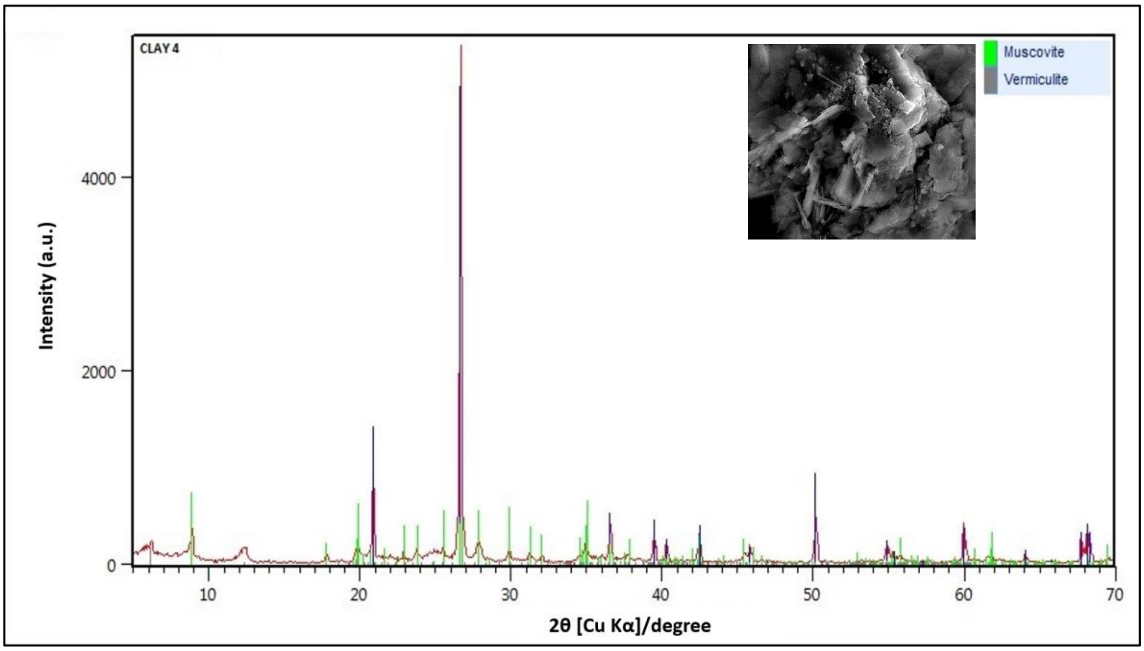

Figure A4. XRD pattern and SEM (insert) image of $Clay_4$

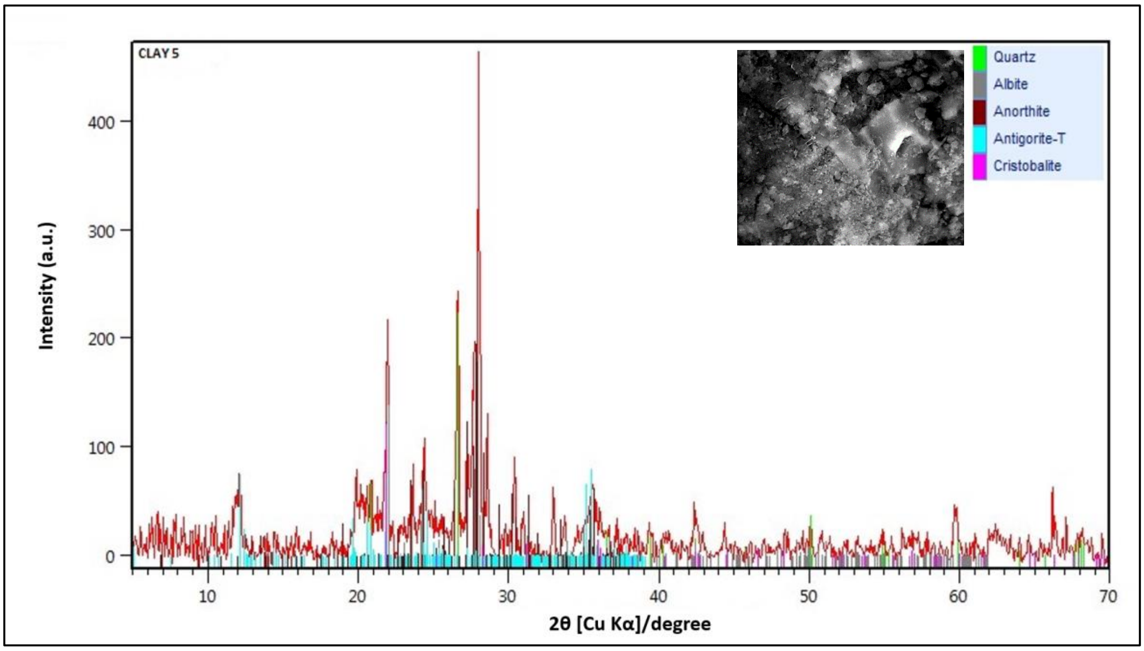

Figure A5. XRD pattern and SEM (insert) image of Clay5

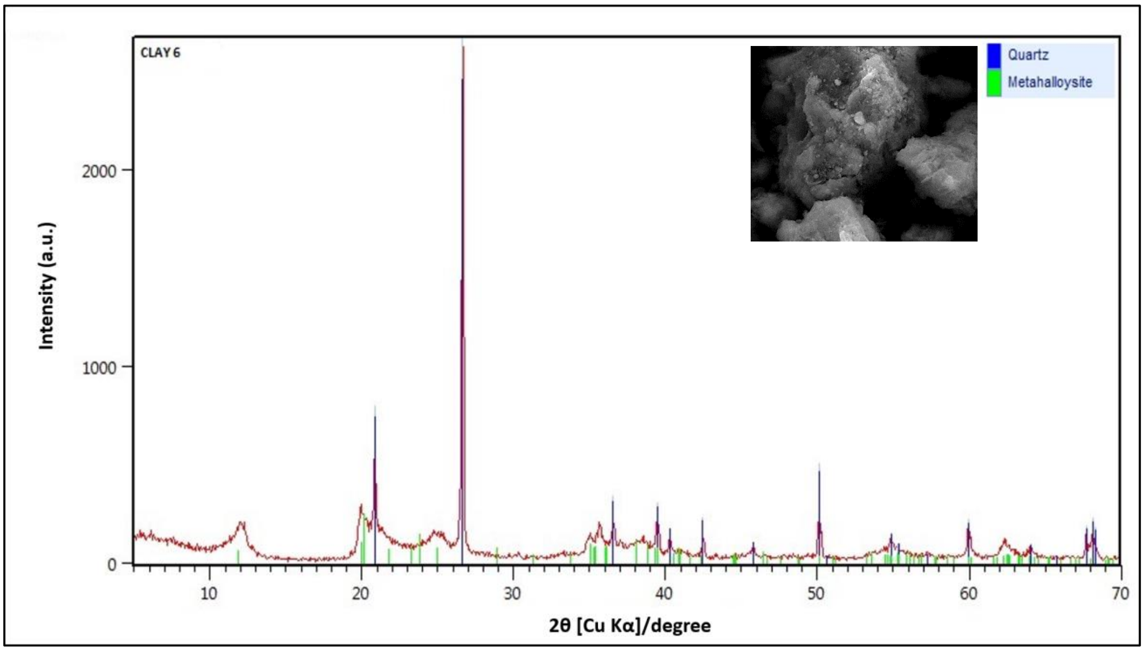

Figure A6. XRD pattern and SEM (insert) image of Clay6

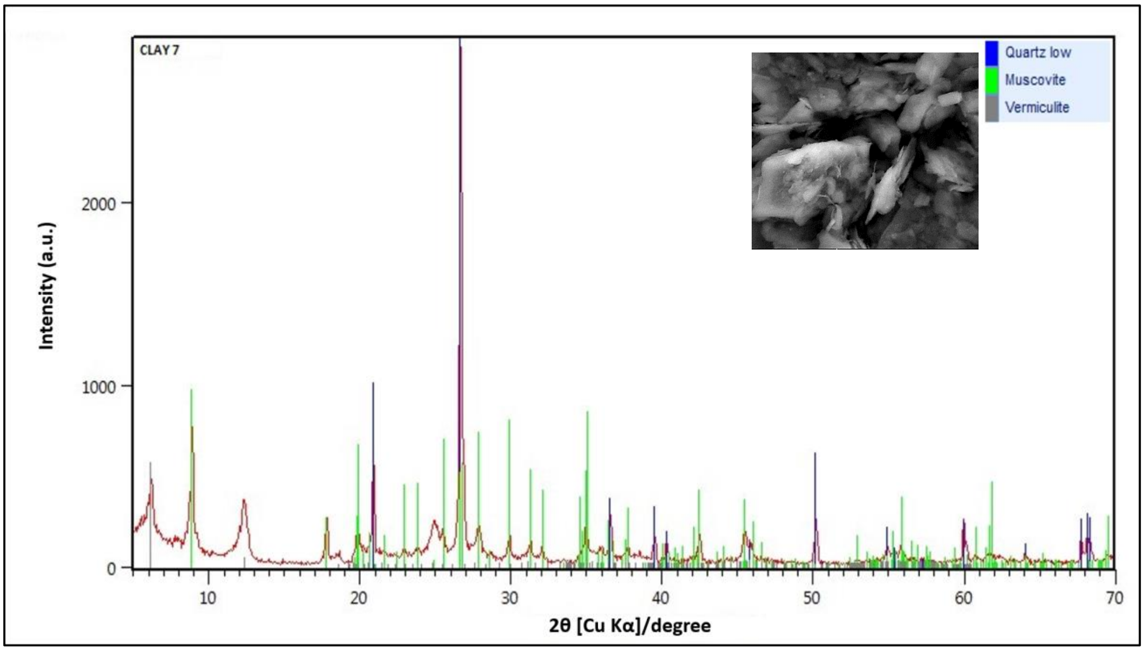

Figure A7. XRD pattern and SEM (insert) image of Clay7

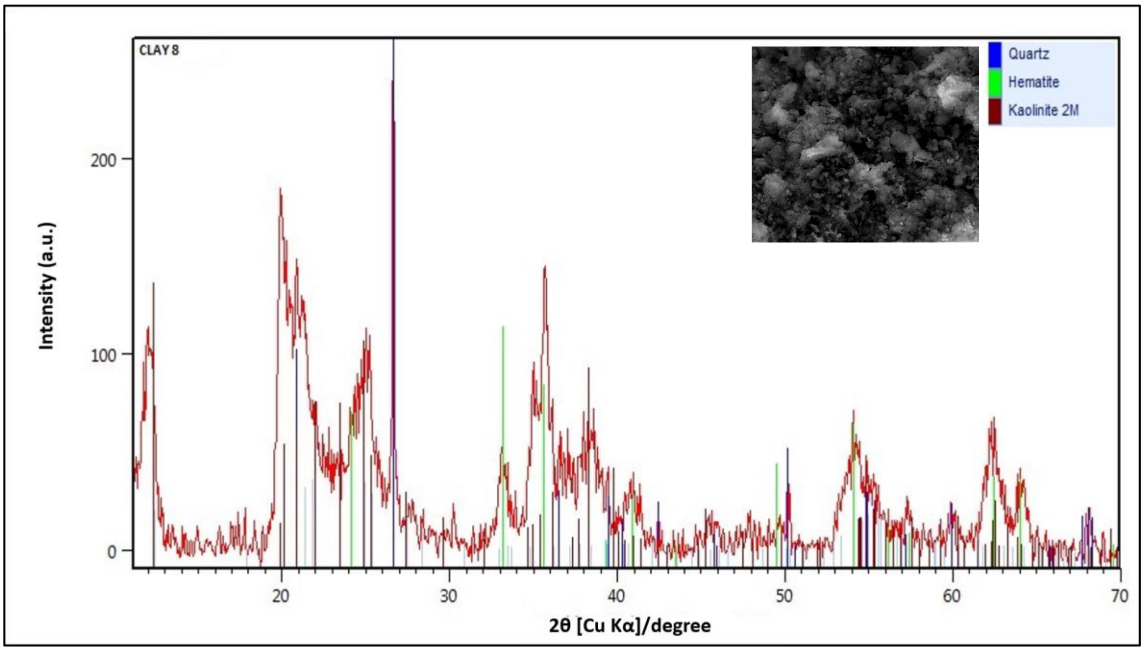

Figure A8. XRD pattern and SEM (insert) image of Clay8

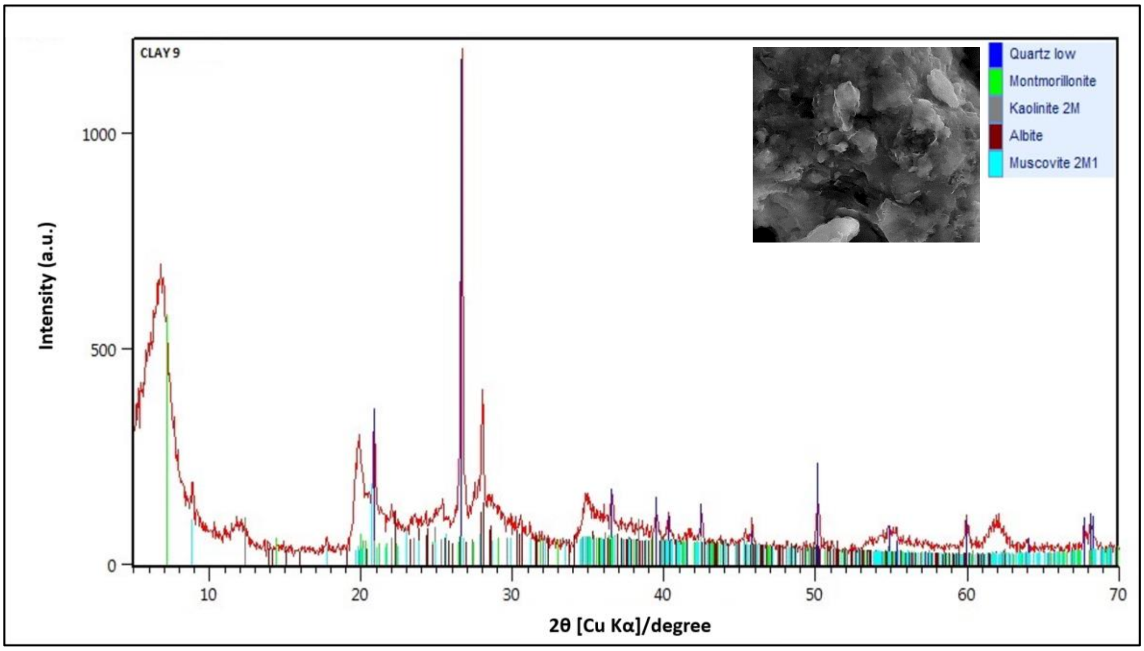

Figure A9. XRD pattern and SEM (insert) image of $Clay_9$

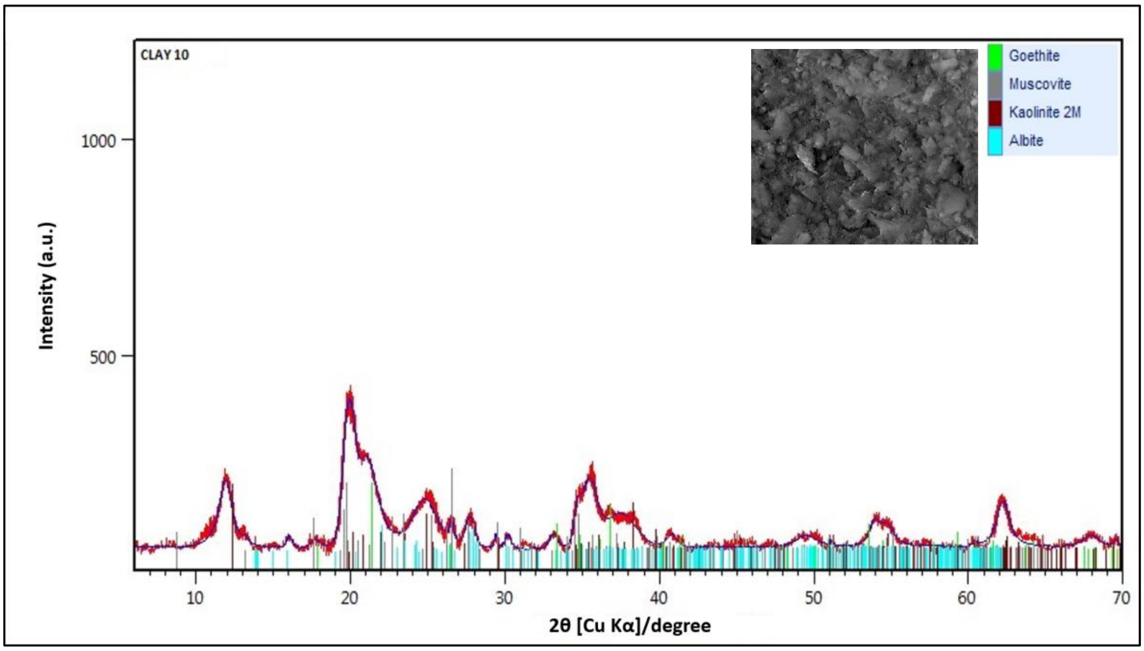

Figure A10. XRD pattern and SEM (insert) image of $Clay_{10}$

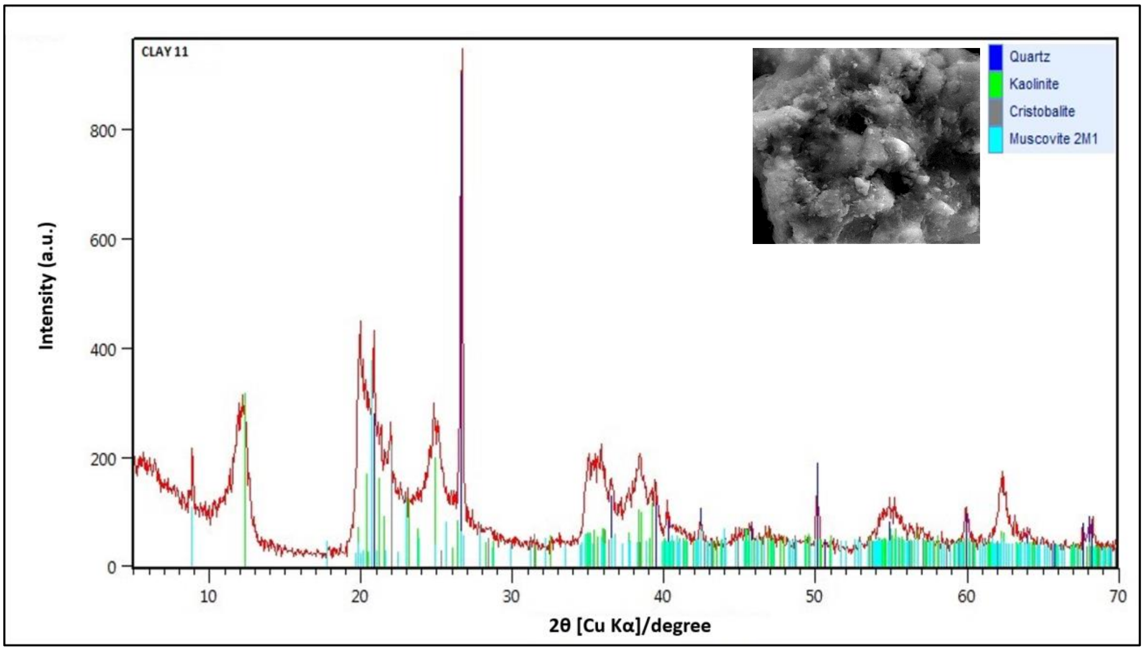

Figure A11. XRD pattern and SEM (insert) image of Clay11

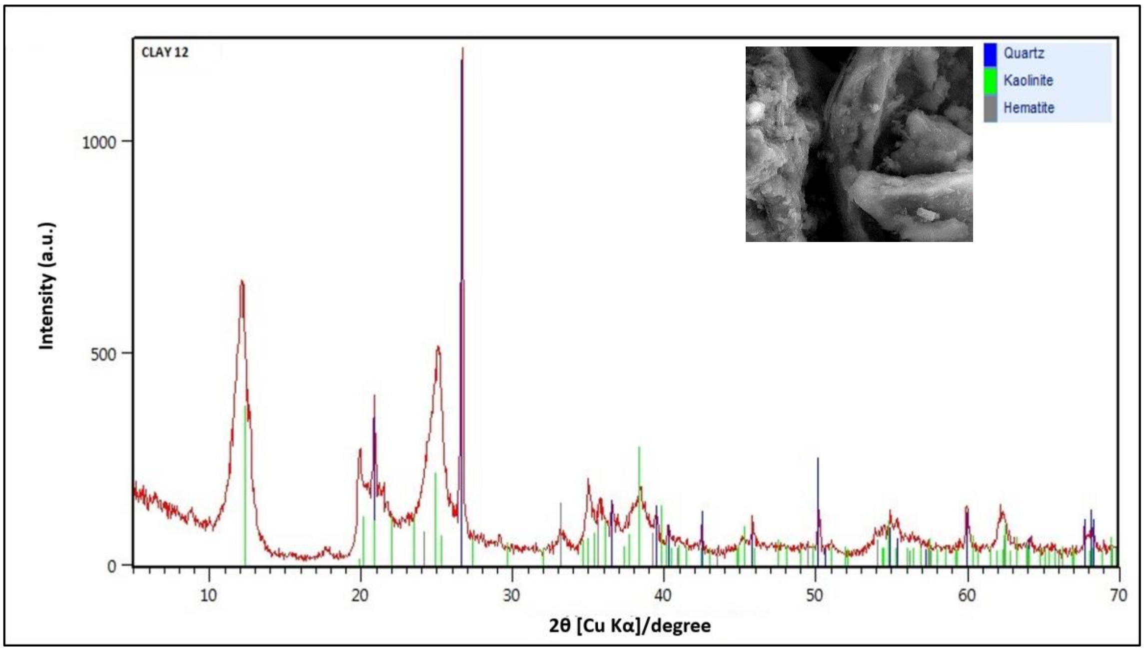

Figure A12. XRD pattern and SEM (insert) image of Clay12

Appendix B: Additional Figures/Tables from Chapter 4

Table B1. 2θ values of the diffraction peaks and planes assigned to the peaks

Compounds	2θ values	Planes
LTA zeolite	7.18°, 10.16°, 12.45°, 16.09°, 17.64°, 20.40°, 21.34°, 21.65°, 22.84°, 23.97°, 26.09°, 27.09°, 29.00°, 29.92°, 30.81°, 32.52°, 33.34°, 34.16°, 35.71°, 36.48°, 37.97°, 40.10°, 41.48°, 42.15°, 42.83°, 43.47°, 44.12°, 47.25°, 47.86°, 49.07°, 49.67°, 51.97°, 52.55°, 53.11°, 54.23°, 54.79°, 56.40°, 57.48° and 58.56°	(2 0 0), (2 2 0), (2 2 2), (4 2 0), (4 2 2), (4 4 0), (5 3 1), (6 0 0), (6 2 0), (6 2 2), (6 4 0), (6 4 2), (8 0 0), (6 4 4), (6 6 0), (8 4 0), (8 4 2), (6 6 4), (8 4 4), (10 0 0), (10 2 2), (10 4 2), (8 8 0), (10 4 4), (10 6 0), (10 6 2), (12 0 0), (10 8 0), (10 8 2), (12 4 4), (10 8 4), (12 6 4), (10 10 0), (14 2 2), (12 8 2), (14 4 2), (10 8 8), (10 10 6), and (12 10 0)
FAU zeolite	6.11°, 9.99°, 11.72°, 15.42°, 17.34°, 18.40°, 20.05°, 20.98°, 22.45°, 23.29°, 23.56°, 24.63°, 25.39°, 26.63°, 27.35°, 29.18°, 30.27°, 30.92°, 31.13°, 31.96°, 32.77°, 33.56°, 34.14°, 35.11°, 36.59°, 37.31°, 40.76°, 41.25°, 42.55°, 43.34°, 46.43°, 47.02°, 48.62°, 49.79°, 50.49°, 50.92°, 51.59°, 53.11°, 57.32°, 58.36°, 59.01° and 59.39°	(1 1 1), (2 2 0), (3 1 1), (3 3 1), (4 2 2), (5 1 1), (4 4 0), (5 3 1), (6 2 0), (5 3 3), (6 2 2), (4 4 4), (5 5 1), (6 4 2), (5 3 1), (7 3 3), (8 2 2), (1 5 7), (6 6 2), (8 4 0), (8 4 2), (6 6 4), (9 3 1), (8 4 4), (2 6 8), (10 2 2), (8 8 0), (11 3 1), (11 3 3), (8 8 4), (12 4 2), (10 8 2), (9 7 7), (13 3 3), (8 8 8), (13 5 1), (14 2 0), (11 9 3), (11 11 1), (1 9 13), (16 0 0) and (3 5 15)
Na-P1 zeolite	12.47°, 17.73°, 21.65°, 28.18°, 33.44°, 35.63°, 40.31°, 42.31°, 44.13°, 44.29°, 46.14°, 49.87°, 51.48°, 51.67°, 53.09°, 53.28°, 54.87°, 55.06°, 56.29°, 56.42°, 56.69°, 57.91°, 58.27°, 59.63°, 59.89°, 61.42°, 62.61°, 62.90°, 62.99°, 64.35°, 65.50°, 65.75°, 66.00°, 67.33°, 67.49°, 68.59° and 68.87°	(1 0 1), (2 0 0), (1 1 2), (3 0 1), (3 1 2), (0 0 4), (4 0 2), (3 3 2), (2 2 4), (4 2 2), (3 1 4), (5 1 2), (4 0 4), (4 4 0), (3 0 5), (4 3 3), (4 2 4), (6 0 0), (1 1 6), (3 2 5), (6 1 1), (2 0 6), (6 0 2), (4 1 5), (5 4 1), (6 2 2), (3 1 6), (6 1 3), (6 3 1), (4 4 4), (1 0 7), (4 3 5), (5 4 3), (6 0 4), (6 4 0), (3 3 6) and (6 3 3)
$ZnTiO_3$	23.92°, 32.79°, 35.31°, 40.45°, 48.93°, 53.44°, 56.82°, 61.79° and 63.39°	(0 1 2), (1 0 4), (1 1 0), (1 1 3), (0 2 4), (1 1 6), (0 1 8), (2 1 4) and (3 0 0)
Anatase ($TiO_{2\text{-a}}$)	25.28°, 36.95°, 37.80°, 38.58°, 48.05°, 53.89°, 55.06°, 62.12°, 62.69° and 68.76°	(1 0 1), (1 0 3), (0 0 4), (1 1 2), (2 0 0), (1 0 5), (2 1 1), (2 1 3), (2 0 4) and (1 1 6)
Rutile ($TiO_{2\text{-r}}$)	27.45°, 36.09°, 41.23°, 54.32°, 56.64° and 69.01°	(1 1 0), (1 0 1), (1 1 1), (2 1 1), (2 2 0) and (3 0 1)

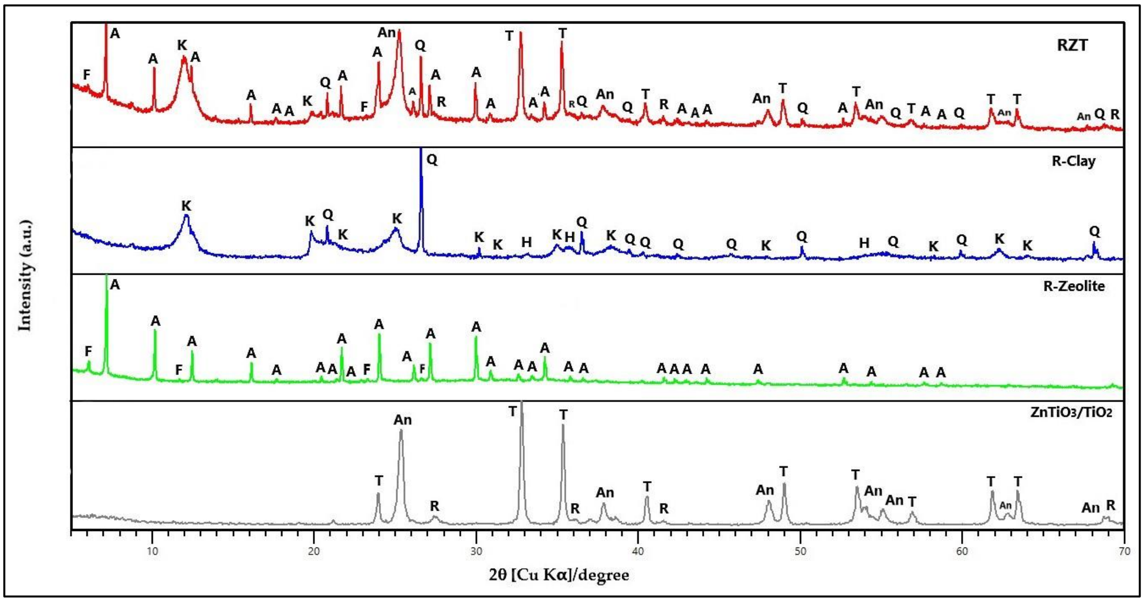

Figure B1. Comparison of the diffraction pattern of the RZT extrudate with the diffraction pattern of its individual components.

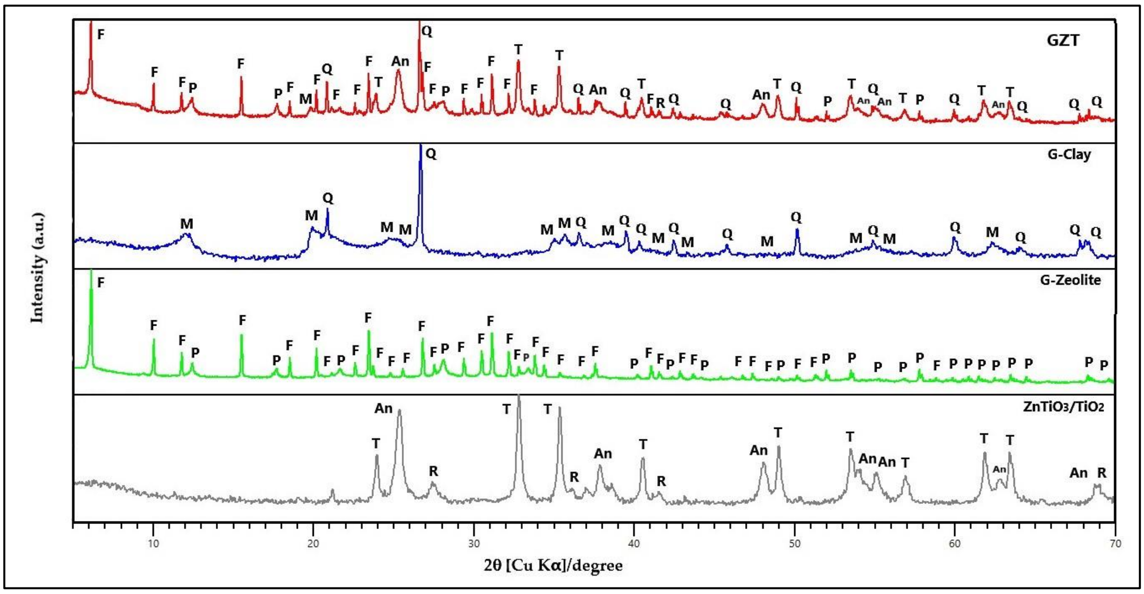

Figure B2. Comparison of the diffraction pattern of the GZT extrudate with the diffraction pattern of its individual components.

Appendix C: Additional Figures/Tables from Chapter 6

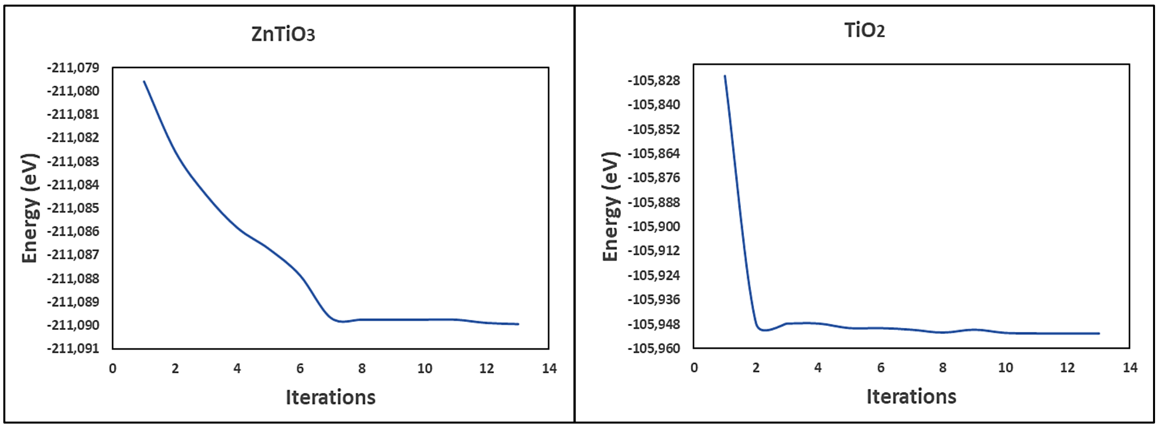

Figure C1. Optimization energies of (a) $ZnTiO_3$ and (b) TiO_2

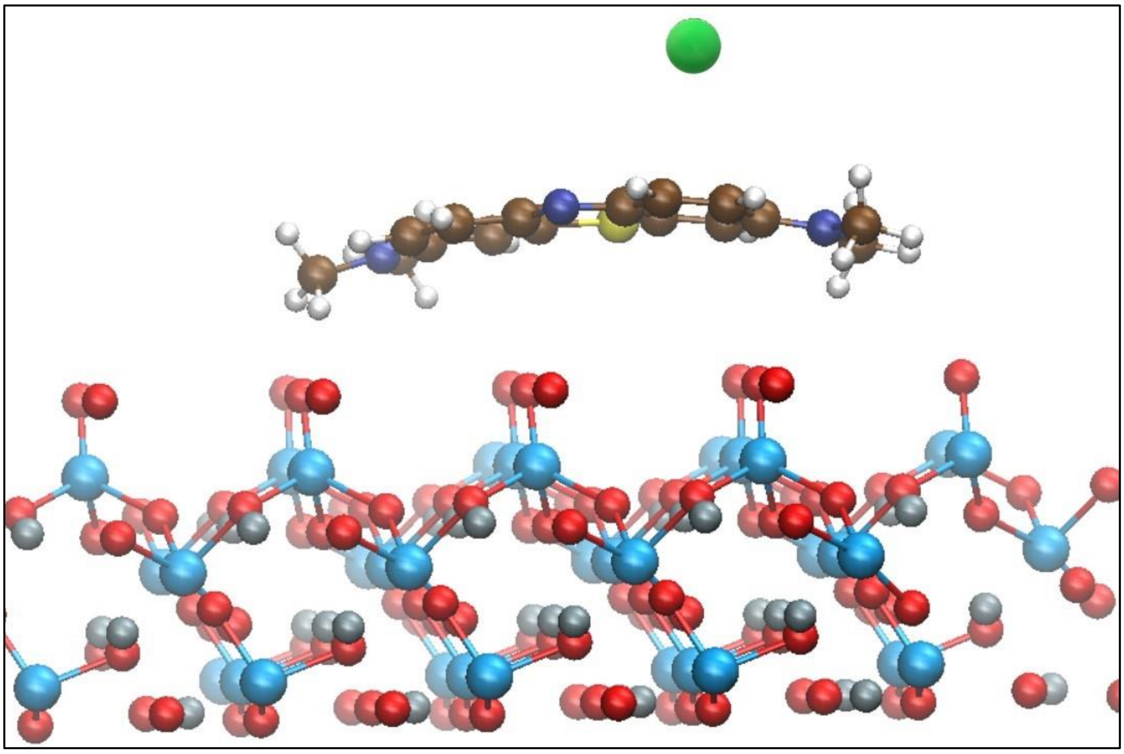

Figure C2. Aromatic ring of MB bent slightly on the $ZnTiO_3$ surface (101)

Table C1. Coordinates of the optimized $ZnTiO_3$ structure

$ZnTiO_3$	**Element**	**Coordinates**		
		X	**Y**	**Z**
a = 5.14797	O 1	0.0436517776555294	0.3434519311655431	0.0618327064818351
b = 5.14797	O 2	0.6565480388344616	0.7001998274899882	0.0618327064818351
c = 13.93750	O 3	0.2998001425100092	0.9563482113444732	0.0618327064818351
α = 90.0000	O 4	0.6565480388344616	0.9563482113444732	0.5618327214818327
β = 90.0000	O 5	0.2998001425100092	0.3434519311655431	0.5618327214818327
γ = 120.0000	O 6	0.0436517776555294	0.7001998274899882	0.5618327214818327
	O 7	0.7103184156555318	0.6767852741655427	0.3951660354818335
	O 8	0.3232147258344573	0.0335331784899886	0.3951660354818335
	O 9	0.9664667985100132	0.2896815543444728	0.3951660354818335
	O 10	0.3232147258344573	0.2896815543444728	0.8951660354818335
	O 11	0.9664667985100132	0.6767852741655427	0.8951660354818335
	O 12	0.7103184156555318	0.0335331784899886	0.8951660354818335
	O 13	0.3769851026555275	0.0101185981655372	0.7284993484818306
	O 14	0.9898814118344565	0.3668665144899912	0.7284993484818306
	O 15	0.6331334855100089	0.6230148973444725	0.7284993484818306
	O 16	0.9898814118344565	0.6230148973444725	0.2284993784818331
	O 17	0.6331334855100089	0.0101185981655372	0.2284993784818331
	O 18	0.3769851026555275	0.3668665144899912	0.2284993784818331
	Zn 1	0.0000000000000000	-0.0000000000000000	0.2790581887331681
	Zn 2	0.0000000000000000	-0.0000000000000000	0.7790581887331682
	Zn 3	0.6666666870000029	0.3333333429999996	0.6123915017331654
	Zn 4	0.6666666870000029	0.3333333429999996	0.1123915247331636
	Zn 5	0.3333333429999996	0.6666666870000029	0.9457248747331675
	Zn 6	0.3333333429999996	0.6666666870000029	0.4457248457331685
	Ti 1	0.0000000000000000	-0.0000000000000000	0.9988437118213425
	Ti 2	0.0000000000000000	-0.0000000000000000	0.4988437118213426
	Ti 3	0.6666666870000029	0.3333333429999996	0.3321770548213422
	Ti 4	0.6666666870000029	0.3333333429999996	0.8321770248213396
	Ti 5	0.3333333429999996	0.6666666870000029	0.6655103988213453
	Ti 6	0.3333333429999996	0.6666666870000029	0.1655103838213406

Table C2. Coordinates of the optimized TiO_2 structure

TiO_2	**Element**	**Coordinates**		
		X	**Y**	**Z**
a = 3.82060	Ti 1	-0.0000000000000000	0.0000000000000000	0.0000000000000000
b = 3.82060	Ti 2	0.5000000000000000	0.5000000000000000	0.5000000000000000
c = 9.69652	Ti 3	0.0000000000000000	0.5000000000000000	0.2500000000000000
α = 90.0000	Ti 4	0.5000000000000000	-0.0000000000000000	0.7500000000000000
β = 90.0000	O 1	-0.0000000000000000	0.0000000000000000	0.2066838593974745
γ = 90.0000	O 2	0.5000000000000000	0.5000000000000000	0.7066838893974697
	O 3	-0.0000000000000000	0.5000000000000000	0.4566838593974745
	O 4	0.5000000000000000	0.0000000000000000	0.9566838893974697
	O 5	0.5000000000000000	-0.0000000000000000	0.5433161106025303
	O 6	0.0000000000000000	0.5000000000000000	0.0433161406025255
	O 7	0.5000000000000000	0.5000000000000000	0.2933161406025255
	O 8	0.0000000000000000	-0.0000000000000000	0.7933161106025303

Table C3. Bader`s charge analysis of the Methylene Blue molecule

Atom	**MB**				**MB absorbed on $ZnTiO_3$**				**MB absorbed on TiO_2**			
	X	**Y**	**Z**	**Charge (-*e*)**	**X**	**Y**	**Z**	**Charge (-*e*)**	**X**	**Y**	**Z**	**Charge (-*e*)**
CL	6.6723	5.4913	18.1256	3.9473	5.7841	6.8665	18.8427	4.0377	8.5502	6.3036	37.8262	4.0165
C	6.6883	6.9248	18.2492	2.9801	5.4537	8.2487	19.0343	2.9038	7.1274	6.1282	37.9076	2.9116
C	6.8113	7.7022	17.0778	3.7228	5.5389	9.1145	17.9135	3.8886	6.3672	5.9423	36.7213	3.9439
C	6.8381	4.9031	16.9023	4.0263	6.1899	6.4038	17.6162	4.0043	9.0968	6.2958	36.5683	3.9895
C	6.9903	7.1050	15.8404	4.4306	5.9565	8.6387	16.6753	4.2272	6.9541	5.9232	35.4362	4.1712
C	7.0214	5.6667	15.7039	2.6235	6.3054	7.2586	16.4816	2.6376	8.4054	6.0825	35.3271	2.6542
C	7.4012	7.0194	13.1881	4.2267	6.6400	8.8226	14.0368	4.2430	7.1262	5.6325	32.7208	4.1458
C	7.6017	7.5508	11.9115	3.9548	6.8412	9.4525	12.8237	3.9190	6.6611	5.3793	31.4157	4.0569
C	7.7943	6.7163	10.7922	2.9653	7.3367	8.7318	11.6975	2.7809	7.5400	5.2562	30.3197	2.9217
C	7.7791	5.2961	10.9951	3.9989	7.6129	7.3252	11.8614	4.102	8.9224	5.3489	30.5791	3.9441
C	7.5841	4.7715	12.2459	3.9766	7.3997	6.7069	13.0583	3.8457	9.4304	5.5405	31.8646	4.0569
C	7.3901	5.5967	13.3925	2.632	6.9072	7.4076	14.2087	2.5409	8.5204	5.7274	32.9874	2.6496
C	8.0476	8.6800	9.3573	3.3209	7.2135	10.7579	10.3305	3.3619	5.9685	4.1045	28.7949	3.2969
C	8.1623	6.3644	8.3904	3.2358	8.1032	8.6179	9.3682	3.4622	7.6270	5.7136	27.888	3.4016
C	6.3617	6.7509	20.6746	3.2311	5.0669	7.8474	21.4312	3.3437	7.3591	6.2087	40.3865	3.3551
C	6.6204	8.9880	19.5700	3.3401	4.6740	10.1103	20.4200	3.2829	5.0623	5.8367	39.2665	3.7745
C	7.1937	8.1669	14.4764	5.6016	6.0469	9.7703	15.3638	5.7591	5.9774	5.7813	34.0176	5.7675
S	7.2001	4.9769	14.5721	7.7963	6.7432	6.7090	15.3311	7.8003	9.1383	5.9281	34.1814	7.7280
N	7.9923	7.2378	9.5422	7.4915	7.5403	9.3424	10.5148	7.4025	7.1210	4.9650	29.0625	7.4757
N	6.6024	7.5282	19.4673	7.4619	5.0720	8.7171	20.2557	7.4840	6.5601	6.1084	39.1715	7.0200

N	7.8071	10.6069	16.2128	7.7365	7.4174	9.9721	25.4704	7.6694	11.3226	6.5800	40.5672	7.5771
H	6.5464	4.8632	19.0063	0.9519	5.7058	6.1701	19.6745	0.9410	9.2393	6.4583	38.7013	0.8427
H	6.8463	3.8182	16.793	0.9123	6.4397	5.3533	17.4678	0.9051	10.2034	6.3392	36.4626	0.9552
H	6.8474	8.8004	17.1014	0.8673	5.2899	10.1698	18.0158	0.9714	5.2548	5.9168	36.7093	0.9938
H	7.6063	8.6347	11.8008	0.9618	6.6248	10.5151	12.7307	0.9768	5.5971	5.3471	31.2078	0.9224
H	7.9277	4.6224	10.1538	0.9834	7.9801	6.7477	11.0159	0.9303	9.6273	5.1718	29.7369	0.9330
H	7.5780	3.6933	12.4092	0.9595	7.5939	5.6415	13.1844	0.9355	10.4563	5.5461	32.1510	0.8849
H	8.2348	8.9005	8.3018	0.9762	7.3761	11.0287	9.28130	0.8688	6.2252	3.2788	28.0652	0.9363
H	7.0996	9.1625	9.6475	0.9452	6.1601	10.9473	10.5846	0.9927	5.6256	3.6424	29.726	0.9630
H	8.8571	9.1316	9.9535	0.9439	7.8548	11.3926	10.9641	0.9680	5.0539	4.6016	28.4023	0.9802
H	9.0590	5.7301	8.4852	0.9984	9.0775	8.1775	9.6186	0.9366	8.3192	6.4883	28.2325	0.9457
H	7.2886	5.7092	8.2442	0.9748	7.4344	7.8141	9.0297	0.9029	8.1160	4.9767	27.2684	0.9655
H	8.2768	6.9802	7.4928	0.9921	8.2389	9.3251	8.5457	0.9121	6.7832	6.1443	27.3016	0.9375
H	7.1440	5.9919	20.827	0.9953	6.0342	7.3406	21.5525	0.9403	7.8858	7.2124	40.3901	0.9220
H	6.3730	7.4256	21.5362	0.9362	4.8969	8.4559	22.3239	0.9438	6.7805	6.1236	41.3176	0.9454
H	5.3834	6.2424	20.6494	1.0190	4.2714	7.0867	21.3713	0.9804	8.1100	5.3704	40.3904	0.9415
H	5.6571	9.4259	19.2583	0.9799	3.8413	10.3684	19.7462	0.9596	4.8377	4.8672	38.7948	0.9633
H	6.8133	9.2656	20.6118	0.9741	4.3430	10.269	21.4511	0.9617	4.7315	5.8259	40.3284	0.8965
H	7.4023	9.4243	18.9325	0.9280	5.5117	10.797	20.2196	0.9732	4.6073	6.6687	38.7085	0.9543